Micromechanical Study of Capillary Regime Transitions in Partially Saturated Granular Soilss

Nabil Younes

UNIVERSITÉ DE LA ROCHELLE

ÉCOLE DOCTORALE EUCLIDE 618

Thèse présentée par :

Nabil YOUNES

Soutenue le : **03/11/2023**

pour obtenir le grade de : **Docteur de l'Université de La Rochelle**

Laboratoires : **LaSIE La Rochelle, *University of Calgary* et INRAE Aix-en-Provence**

Discipline : **Génie civil**

Étude micromécanique de la transition des régimes hydriques dans les sols granulaires partiellement saturés

Micromechanical Study of Capillary Regime Transitions in Partially Saturated Granular Soils

---

JURY :

Vanessa MAGNANIMO	*University of Twente, Netherlands*	Rapportrice
Farhang RADJAI	Université de Montpellier	Rapporteur
Ioannis STEFANOU	École Centrale de Nantes	Examinateur
François NICOT	Université Savoie Mont Blanc	Examinateur
Olivier MILLET	Université de La Rochelle	Directeur de thèse
Richard WAN	*University of Calgary, Canada*	Co-directeur de thèse
Antoine WAUTIER	INRAE Aix-en-Provence	Co-directeur de thèse

"Success consists of stumbling from failure to failure with no loss of enthusiasm."
"Le succès consiste à aller d'échec en échec sans perdre son enthousiasme."
Winston Churchill

"Sic Parvis Magna."
"Greatness from Small Beginnings."
Sir Francis Drake

Acknowledgement

First and foremost, I wish to express my sincere gratitude to my three supervisors—Olivier Millet, Richard Wan, and Antoine Wautier—for their invaluable guidance and infinite support throughout the journey of my Ph.D. thesis conducted in three different locations: La Rochelle, Aix-en-Provence, and Calgary, spanning two continents far away from each other. What made my collaboration with them truly enjoyable was the fact that they regarded me not only as their "Student" but as a colleague. I am tremendously thankful for their early confidence in my work and their huge support since day one. Their expertise, rigorous scientific approach, and particular attention to detail have played a pivotal role in shaping me into the researcher I am today. This thesis would not have been possible without their guidance and assistance during these challenging three years. I extend a special thanks to Olivier and Richard for providing me with the opportunity to teach at both the University of La Rochelle and the University of Calgary, contributing to the scientific life of both institutions in both theoretical and experimental aspects. A profound appreciation goes to Antoine, who generously hosted me at INRAE Aix-en-Provence for almost eight months, allowing me to collaborate with him on the complicated numerical aspects of my thesis. Their collective support has been instrumental in my academic and professional development, and for that, I am truly grateful! Even though François Nicot—the president of my jury—was not officially my supervisor, I want to express my gratitude to him here in this paragraph. Despite the distance, he followed my work, especially during our Ph.D. meetings that brought together students from different continents. His support and interest meant a lot to me, and I appreciate his contributions to my academic journey.

I would also like to extend my genuine thanks to all the members of my jury for their diligent examination of my thesis and the invaluable insights they provided during the defense: Vanessa Magnanimo, Farhang Radjaï, and Ioannis Stefanou. I am particularly grateful to Vanessa and Farhang for graciously accepting the challenging task of reviewing my thesis dissertation. Their willingness to undertake this responsibility is deeply appreciated. I express my sincere gratitude for the detailed feedback they offered after the presentation, shedding light on crucial aspects and pointing out avenues for future exploration.

I cannot proceed without expressing my gratitude to my *comité de suivi* members Aziz Hamdouni and Fabian Dedecker for their guidance and support throughout my work.

Huge thanks to all my friends and colleagues—from Lebanon to La Rochelle to Aix-en-Provence and finally to Calgary. I'm incredibly grateful to each one of you for transforming what could have been a stressful thesis journey into an enjoyable and memorable experience. Your presence made it all so much more cheerful and fulfilling!

Sending a big thanks to my amazing brothers for being by my side and supporting me throughout this thesis, despite the vast distances that separate us! Your unwavering support means the world to me. Biggest thanks and endless love to the most special person in my life! Even though she teasingly thought my thesis was all about sandcastles (:D), she stood by me, cheered me on, and kept me going through the toughest moments. Despite the miles between us, her infinite support and encouragement shaped me into the person I am today: a Doctor! She's my rock, my inspiration, my little red car, and the symphony of my heart!

Last but certainly not least, a huge shoutout to the most incredible beings in my life—the ones who have been my pillars of strength from the very beginning: my amazing

mom and dad! The story of my journey started long before my Ph.D., and it's because of their boundless love and tireless motivation day and night that I stand here today, not just as an Engineer, but as a Doctor in Engineering—a dream that has become a reality. My love for you knows no bounds, and I cannot express enough how your support and presence have shaped every part of my life. You both are the beating hearts of my world!

Résumé

Les digues en remblai jouent un rôle crucial dans la protection des communautés côtières contre les inondations. En général, elles sont construites à partir de matériaux granulaires compactés et se trouvent souvent dans des conditions de saturation partielle, ce qui confère à leurs matériaux une certaine cohésion bénéfique pour leur résistance mécanique. Cependant, lorsque ces matériaux granulaires, situés à la surface de la digue, sont exposés à des cycles de séchage et de mouillage, typiquement provoqués par la variation de pression entre l'amont et l'aval de la digue, elles peuvent devenir vulnérables. Ces fluctuations sont généralement causées par plusieurs facteurs, notamment des précipitations intenses et des canicules, les cycles de marées hautes et marées basses ou les tempêtes. Ces phénomènes deviennent, malheureusement, de plus en plus fréquents dans un contexte de changement climatique.

La présente thèse s'inscrit dans le cadre du projet StabDigue, financé pour une durée de cinq ans par la région Nouvelle-Aquitaine, pour l'étude de la stabilité des digues en remblai partiellement saturées.

Plus précisément, ce travail de thèse est consacré à l'étude microstructurale des matériaux non-saturés pour des degrés de saturation variables. Pour ce faire, nous proposons un couplage entre la méthode aux éléments discrets dite DEM pour simuler le squelette solide en forme de particules sphériques et la méthode de Boltzmann sur réseau dite LBM afin de modéliser les ponts capillaires eau-air entre les particules solides. Grâce à cette modélisation à pointe de l'état de l'art, nous avons pu mettre en évidence les mécaniques complexes à l'oeuvre dans les matériaux granulaires partiellement saturés.

Avant de s'attaquer à l'étude du matériau en considérant un volume élémentaire représentatif (VER), plusieurs benchmarks et validations ont été nécessaires pour le modèle LBM, notamment en ce qui concerne la prédiction précise de la forme des ponts capillaires ainsi que les forces associées. A l'équilibre mécanique de la simulation LBM, les formes des ponts capillaires entre deux grains solides sphériques coïncident parfaitement avec la solution théorique de l'équation de Young-Laplace. De plus, les résultats trouvés par la LBM montrent qu'elle est capable de retrouver l'inversion de signe de la courbure moyenne H quand la distance de séparation entre les deux particules augmente. En outre, une nouvelle expression numérique pour le calcul des forces capillaires entre des grains sphériques a été proposée. Cette nouvelle formulation a montré ses capacités à calculer de façon assez précise les forces capillaires résultant des ponts capillaires isolés et coalescents entre deux et trois particules sphériques, en les comparant avec des résultats expérimentaux et numériques dans la littérature. L'avantage de l'approche LBM est sa capacité à modéliser la fusion des ponts capillaires de façon intrinsèques sans avoir besoin de passer par des critères de fusion géométrique. Ainsi, ces résultats montrent que la LBM est capable de modéliser le passage du régime pendulaire au régime funiculaire.

Ensuite, le couplage DEM-LBM est mis en place pour explorer les caractéristiques des assemblages granulaires partiellement saturés pour tous les régimes capillaires. Nous avons pu retrouver la forme classique de la courbe de rétention qui est définie par l'évolution de la succion en fonction du degré de saturation. De plus, l'évolution de la contrainte capillaire moyenne, qui pourrait être considérée comme étant la cohésion apparente, a été tracée en fonction du degré de saturation. Nous observons une augmentation de la contrainte capillaire moyenne avec l'augmentation du degré de saturation jusqu'à un certain seuil au-delà duquel la contrainte capillaire moyenne diminue pour atteindre zéro lorsque le système devient complètement saturé. Par ailleurs, nous avons également démontré que le

paramètre de Bishop pour les contraintes effectives n'est jamais égal au degré de saturation. Ces derniers résultats ont été comparé avec des données numériques déjà existantes dans la littérature.

Nous avons enfin exploité la pleine capacité du couplage DEM-LBM pour simuler des cycles de séchage (évaporation) et de mouillage (condensation) dans les sols non-saturés. Cela a été réalisé à la fois sur de petits assemblages granulaires composés de trois et quatre particules sphériques, ainsi que sur des VER constitués de quelques milliers de grains. Nous avons réussi à reproduire les sauts (chutes) des forces capillaires au moment de la coalescence (rupture) des ponts capillaires dans le cas des petits assemblages granulaires. A l'échelle du VER, nous avons mis en évidence que la succion et la contrainte moyenne sont plus élevées lors de l'évaporation que celles qui ont été observées lors la condensation. Nous avons également montré que la contrainte capillaire moyenne (cohésion apparente) devient nulle quand le système devient complétement sec ou saturé, comme observé précédemment.

Pour conclure, le couplage DEM-LBM a prouvé ses capacités à retrouver les phénomènes physiques complexes des assemblages granulaires non-saturés. Les résultats observés sont prometteurs pour des études plus avancées, notamment les études de stabilité à l'échelle des digues.

Mots clés : DEM, LBM, micromécanique, cycles séchage/mouillage, mouillabilité, courbe de rétention, contrainte capillaire.

Abstract

Earthen dikes play a vital role in safeguarding coastal communities from flooding events. Typically constructed by compacting granular soils under unsaturated conditions, capillarity confers them with additional strength to resist potential failure against these events that generally involve large hydraulic gradients. On the other hand, shallow unsaturated regions in both upstream and downstream of the dike are also being continually subjected to drying and wetting cycles due to fluctuating conditions such as heatwaves, low tides, intense rainfall, and high tides, all tied to the phenomenon of Climatic Change. The drying and wetting cycles lead to changes in moisture content that will adversely impact the mechanical strength and deformation behaviors of the dikes to eventually cause their collapse. One of the characteristics of this type of failure originates in the changes in both the pore and fluid structures within the unsaturated soil.

This Ph.D. work is a part of the *StabDigue* project, funded for a five-year duration by the *Nouvelle-Aquitaine* region, for investigating earthen dike mechanical stabilities. As alluded to above, the physics of the problem resides at the pore and grain scales. Thus, this Ph.D. work is dedicated to studying the microstructure of unsaturated soils across the entire range of saturation levels. By combining two mesoscale models, namely the Discrete Element Method (DEM) for modeling solid particle interactions with the phase-field-based Lattice Boltzmann Method (LBM) for capturing the formation of air-water capillary bridges within a Representative Elementary Volume (REV), we can gain a deep understanding of the intricate mechanics governing unsaturated soils.

Before delving into the behavior of REVs, multiple validations are conducted. For instance, in the LBM framework, the formation of capillary bridges between two-particle (doublet) configurations and the comparison of their geometries with the Young-Laplace solution within the pendular regime are examined. Not only the capillary bridge shapes are replicated, but also the inversion of the mean curvature H sign is well captured when increasing the separation distance between the two particles. Furthermore, the capillary force arising from the water interaction with a curved solid surface is formulated along with a numerical integration scheme. This scheme goes further to compute the capillary forces resulting from isolated and coalesced capillary bridges in two- and three-spherical particle configurations (doublets and triplets, respectively), thus illustrating the pendular regime and its transition to the funicular regime. The numerical results in this thesis align well with available experimental and numerical data in doublet and triplet configurations of particles, respectively. These results indicate that the proposed phase-field-base LBM model and the integration scheme for the capillary force calculations are viable for pendular and funicular regimes, making them suitable for larger systems *via* the REV scale for a large range of saturation levels.

Then, a DEM-LBM algorithm is developed to explore the characteristics of partially saturated granular assemblies over a large range of degrees of saturation. Multiple results are found, including the capture of the Soil-Water Characteristics Curve (SWCC) which is defined as the evolution of the suction in terms of degrees of saturation or volumetric water content. Moreover, the evolution of the mean capillary stress, which can be referred to as the *apparent cohesion*, is also plotted in terms of degrees of saturation. It has been shown that the mean capillary stress increases with the degree of saturation up to a certain threshold beyond which the mean capillary stress drops and approaches zero as the system reaches full saturation conditions. Moreover, it is proven that Bishop's effective stress parameter is never equal to the degree of saturation. These findings have

been compared to other existing numerical data in the literature to ensure their validity.

Finally, a novel method was formulated to simulate drying (evaporation) and wetting (condensation) cycles within unsaturated soils on small granular assemblies composed of three and four particles, and within an REV composed of thousands of spherical grains. With this new technique, jumps (drops) in capillary forces during the coalescence (rupture) of capillary bridges were successfully reproduced for the small granular assemblies. At the REV scale, it is highlighted that the suction and the mean capillary stress are higher during evaporation compared to condensation. It is also shown that the system loses its apparent cohesion when it is dry or fully saturated as shown before.

In conclusion, the proposed DEM-LBM model has proven its capabilities in capturing multiple physical phenomena of unsaturated soils. It is believed that the devised model holds significant potential for the thorough study of instabilities at the REV scale, paving the way for its broader application in more complicated systems, including earthen dikes.

Keywords: DEM, LBM, micromechanics, wetting-drying cycles, wettability, SWCC, capillary stress.

Contents

List of Figures

List of Tables

Introduction

General context

The planet Earth has been experiencing climate change ever since the industrial revolution in the 18th century with an ongoing rise of the sea water level (Chu et al., 2012) which will certainly pose risks to coastal communities and coastlines. In order to avoid potential catastrophic failures, human beings have come up with the idea of building protective structures known as maritime dikes or *levees* to withstand any flooding event. Dikes are one of the solutions used to protect populations against these risks. For instance, to illustrate the magnitude of the challenges at stake, consider the possibility of severe flooding in the Netherlands resulting from major dike failures, which could lead to the disappearance of two-thirds of the country. As such, to understand the reasons behind these failures, it is vital to understand the construction process of dikes as well as the mechanical strength of materials and their interaction with water.

Earthen dikes are constructed by adding and compacting soil layers in lifts. For optimal compaction, the soil should remain wet within an optimum water saturation level of around 80% (Budhu, 2015). Consequently, during and after dike construction, the soil is under unsaturated conditions where air, water, and solid phases coexist simultaneously as illustrated in Figure (1).

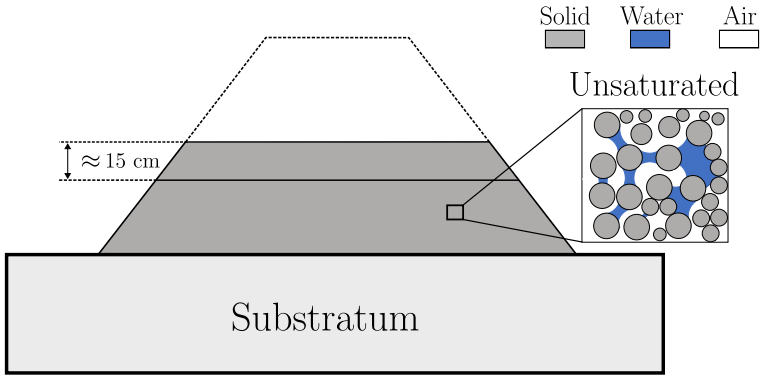

Figure 1: Typical dike or levee construction in successive compacted lifts.

Once the dike construction is completed and water impounded, seepage within the dike will occur due to the pressure differences between the upstream and downstream sides of the geostructure (Budhu, 2015). Figure (2) provides a visual example of a typical levee with impounding water.

Over time, civil, geotechnical, and even mining engineers invested themselves in improving the design of dikes. Despite cautions taken by engineers, and due to severe climatic conditions, there are instances where disasters are unavoidable, and these supposedly protective structures fail occasionally. It comes therefore as no surprise that this issue must be addressed carefully. According to Bonelli (2012), France holds a vast network of protective structures of 9,000 km against flooding, a significant network of dikes spanning over 8,000 km for navigation canals, and about 1,000 km of hydro-power canals. Several dam/dike failures have been reported in the past, such as the river erosion in *Arroux* in 2001, the *Ouches* dam in 2002, and the coastal line failures due to *Xynthia* storm in 2010. Likewise, in Canada, the residents of *British Columbia* have not forgotten the disaster that resulted from the *Mount Polley* tailings dam failure where 17 million cubic meters of polluted water and 8 million cubic meters of tailings and materials essentially went down

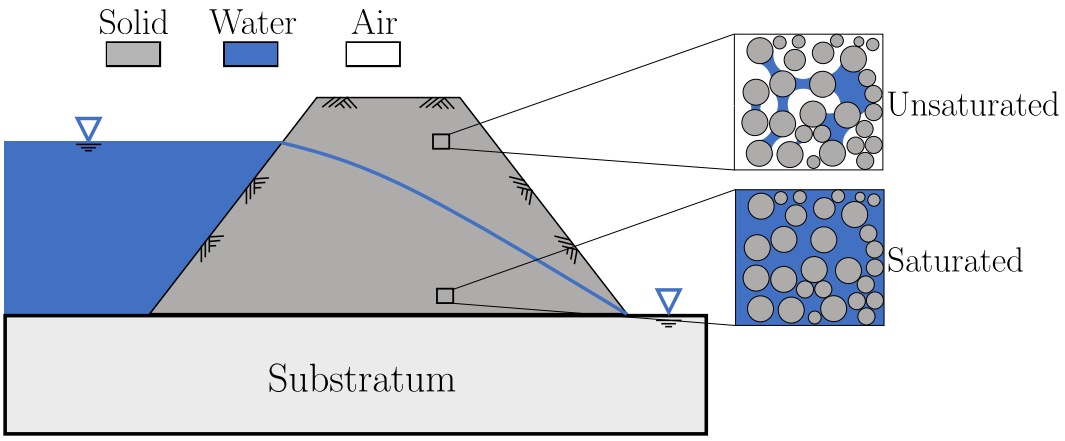

Figure 2: Typical maritime dike section showing different degrees of water-saturated zones.

into the *Polley* Lake. While, fortunately, no casualties were reported in the latter example, the environmental impact caused by the incident was profoundly catastrophic. The consequences induced by dam, dike, or tailings dike failures are substantial, especially the loss of lives, not to mention the cost of damages that can often reach billions of dollars. It is, therefore, necessary to anticipate these collapses and provide the best maintenance for preventing potential disasters from happening, or in the worst-case scenario to evacuate the residents living around these hydraulic structures to avoid casualties.

As illustrated in Figure (2), earthen dikes exhibit a zone where the material is under unsaturated conditions. It is well-known that in such unsaturated zones, capillary effects increase soil strength with respect to the dry or fully saturated soils (Likos and Lu, 2004b; Fredlund and Rahardjo, 1993). A simple yet illustrative example can be shown in Figure (3) whereby an initially wet cylindrical sand sample is being dried over time in an oven at a temperature of $T = 80\,^{\circ}\mathrm{C}$. As can be seen, Figure (3a) shows that the sample does not collapse even without having any lateral support because it is wet. As time passes by, the sample crumbles gradually to become ultimately a pile of sand as shown in Figure (3e).

Climate change may alter the saturation degree of dikes with potential impacts on mechanical stability. For instance, heatwaves, low tides, intense rainfall, and high tides may change the water content inside the dikes and make them vulnerable. Figure (4) shows an illustrative example of how climatic fluctuations can affect dike stability. In the figure, the red squares indicate potential failures that may occur during the wetting or drying processes as shown in (a) and (b), respectively. These failures represent points of vulnerability in the system, where changes in moisture conditions could affect the stability of the structure.

Within the context of the *StabDigue* project, funded for a duration of five years by the *Nouvelle-Aquitaine* region to investigate dike stabilities, this Ph.D. study is motivated by several key questions that will be addressed:

- Can we model and predict the consequences of a change in water saturation on the mechanical stability of granular soils?

- How will the wetting/drying cycles, resulting from climatic changes, affect the hydro-mechanical properties of a given soil?

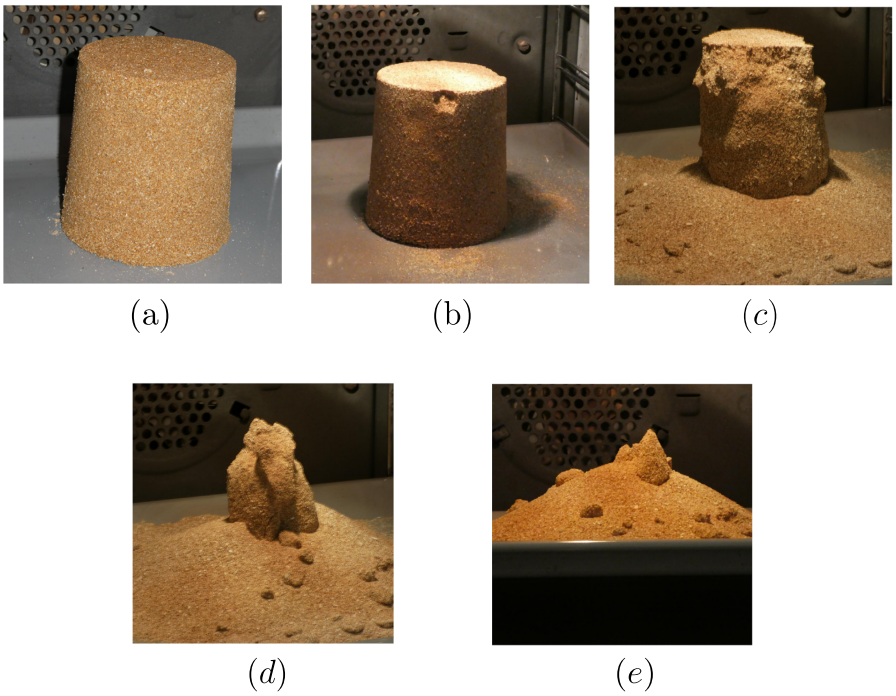

Figure 3: An initially wet cylindrical sand sample is being dried over time in an oven at a temperature of $T = 80\,^{\circ}\mathrm{C}$. (a) $t = 0$ h, (b) $t \approx 5$ h, (c) $t \approx 9$ h, (d) $t \approx 13$ h, and (e) $t \approx 16$ h. These photos are taken from (Maranha et al., 2022).

- Can we interpret these changes in terms of the underlying microstructure and its evolution?

Available approaches for predicting instabilities

Analytical methods

Over the years, researchers and engineers have developed analytical methods made simple using various assumptions for analyzing slope stability. These lead to the Bishop's and Janbu's methods (Janbu et al., 1956; Bishop, 1955; Khan and Wang, 2020) conventionally used by geotechnical engineers in practice. Alternatively, so-called stability charts for dry, saturated and unsaturated soils (Bishop and Morgenstern, 1960; Michalowski, 2002; Michalowski and Nadukuru, 2013; Steward et al., 2011; Yang and VANAPALLI, 2019) have been used. Despite the simplicity of these approaches, they are usually limited to a few engineering applications since they are based on many simplifying assumptions that vitiate the solution to the problem.

Numerical methods

Macro-scale models

To circumvent these assumptions and through the advances in computer technologies, researchers and engineers have developed numerical modeling approaches to tackle complex problems. Two strategies can be employed to describe the behavior of dikes: macro-scale and micro-scale approaches. In the former case, several methods can be put under the same umbrella, amongst others: Finite Element Method (FEM), Finite Difference Method (FDM), and so forth (Liu et al., 2020a; Yang et al., 2017; Shivamanth et al.,

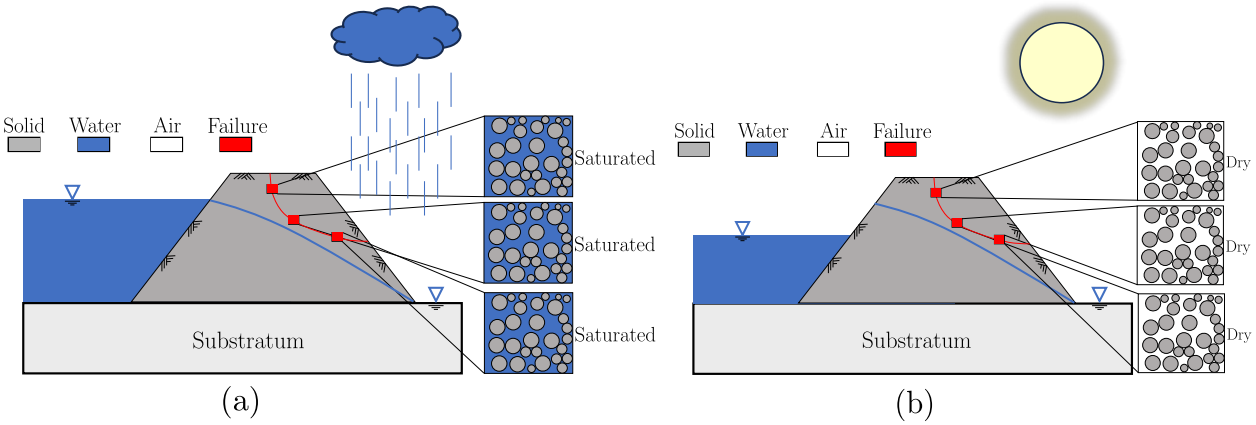

Figure 4: Potential failures within a dike when it is experiencing (a) severe rainfall events and (b) long drought periods due to Climate Change.

2015; Sorgatz and Nuber, 2017). These methods are also known as phenomenological approaches[1]. Although these techniques are tremendously reliable and practical for engineering applications, they still, unfortunately, fall short in many aspects, including but not limited to the calibration of parameters: in some cases, they do not possess any physical meaning. Furthermore, these *purely numerical* parameters are determined based on limited experimental tests which can limit the model's applicability to conditions outside of the observed data, especially for unsaturated soils. Moreover, phenomenological methods are not capable of taking into account the underlying behavior of the micro-structure of the soil being addressed. Furthermore, unsaturated conditions are not yet well modeled at this scale. Thus, capturing extreme conditions may seem grueling for these approaches.

Micro-scale models

To overcome these problems, researchers have come up with the idea of modeling soils at the micro-scale whereby deep insights into the fundamental mechanical behavior of soils can be acquired, namely grain-to-grain interactions and the motion of the fluid through pores. Also at that scale, the various micro-physica are additive. Micro-scale modeling is, therefore, certainly a great candidate to gain a deep understanding of the micro-structure features responsible for the instability of protective structures for varying saturation levels.

As mentioned earlier, unsaturated soils are composed of three components, solid, air, and liquid phases. Consequently, any micro-scale model should account for solid particles as well as their interactions with a two-phase flow model. Therefore, the chosen models for this work are given following the phase in question:

1. Solid: it can be modeled using the Discrete Element Method (DEM) which can be credited to Dr. Peter Cundall and Professor Otto Strack in their pioneering work (Cundall and Strack, 1979);

2. Air and water (fluid): the Lattice Boltzmann Method (LBM) is definitely one the best candidates to simulate fluids at the pore scale which is attributed to the famous physicist Ludwig Boltzmann.

[1]Phenomenological approaches are referred to the methods that are based on experimental observations.

The two aforementioned methods will be coupled together in order to simulate unsaturated soils for various saturation levels.

Outline and structure of the current work

The manuscript represents three years of extensive research conducted at three different locations: La Rochelle University (France), INRAE Aix-en-Provence (France), and the University of Calgary (Canada) under the Joint-Ph.D. Program between both La Rochelle University and the University of Calgary.

This research effort has led to the publication of three papers in international journals and numerous presentations at both international and national conferences as well as international workshops. The thesis is structured as follows.

- **Chapter 1:**
  The first chapter covers the fundamental aspects of unsaturated soils. It delves into concepts such as suction s, effective stress $\boldsymbol{\sigma}'$, and capillary stress $\boldsymbol{\sigma}^{\text{cap}}$. The literature review involves a thorough investigation of experimental, numerical, and analytical models to gain a deeper understanding of the main features of unsaturated soils. Additionally, this chapter recalls the extensive previous research work devoted to the description of the shapes of capillary bridges and the resulting forces affecting small granular assemblies—doublets, triplets, and quadruplets of particles. Numerical, experimental, and analytical methods and models are provided. The literature review in this chapter concludes by highlighting significant gaps in existing studies which have often focused solely on *pendular* regimes. This Ph.D. work contributes to addressing this point by providing a numerical tool encompassing all regimes, *e.g.*, *pendular*, *funicular*, and *capillary* regimes.

- **Chapter 2:**
  Simulating unsaturated soils requires modeling the various fluid components. Out of numerous models available in the literature, the Lattice Boltzmann Method (LBM) has been recognized as an exceptionally promising and versatile approach to simulating water-air interfaces in partially saturated granular assemblies. While multi-phase models are essential for this study, it is crucial and informative to comprehend the historical context of the LBM that solves the Boltzmann equation, derived by the physicist *Ludwig Boltzmann* for single-phase flows. Therefore, this chapter offers an introduction to the **single-phase** LBM to understand the underlying mathematical principles behind this approach.

- **Chapter 3:**
  A quick literature review of the available multi-phase LBM models is introduced in this chapter. The phase-field-based LBM model has been selected for this Ph.D. work along with a wetting condition, thus allowing the modeling of capillary bridges (Liang et al., 2018, 2019).

- **Chapter 4:**
  In this chapter, numerical validations and benchmarks of the LBM are presented, such as the Rayleigh-Taylor instability, capillary rise (Jurin's law), liquid drops on spherical and flat surfaces, the shapes of capillary bridges, and capillary forces of doublets and triplets of particles. Results about capillary forces within doublets and triplets of spherical particles as well as Jurin's law benchmark were published

in 2022 in *Phase-field Lattice Boltzmann model for liquid bridges and coalescence in wet granular media* (Younes et al., 2022). The findings regarding the shapes of capillary bridges will be forthcoming in the paper entitled *A relevant phase-field-based Lattice-Boltzmann method for water-air capillary interfaces* (Younes et al., 2023a).

- **Chapter 5:**
  In this chapter, the Discrete Element Method (DEM), describing the particle dynamics and interactions, is first reviewed. Afterward, the coupling algorithm between the devised DEM-LBM coupling is explained and thoroughly detailed, presenting original results that bridge the gap in the literature, such as a qualitative validation of the DEM-LBM coupling, calculating the suction and capillary stress from a micro-structural perspective, and demonstrating that Bishop's effective stress parameter χ is never equal to the degree of saturation S_r of the specimen. This chapter also explores the fluid dynamics within the specimen for different saturation levels using the Flood-Fill algorithm. A part of these results has been published in 2023 in: *DEM-LBM coupling for partially saturated granular materials* (Younes et al., 2023d).

- **Chapter 6:**
  In this chapter, a primary motivation of the Ph.D. project is tackled by examining the wetting (condensation) and drying (evaporation) processes of granular assemblies. In this chapter, a novel method for condensation and evaporation is introduced and thoroughly validated based on small granular assemblies by capturing the so-called capillary force jumps when capillary bridges merge within a triplet of particles. This phenomenon is also known as *Haines* jumps. These results will be submitted soon in the paper entitled: *Hysteresis phenomenon within unsaturated granular assemblies: capillary forces and matric suction* (Younes et al., 2023c). Then, the new condensation and evaporation technique along with DEM-LBM are applied altogether in order to investigate the *hysteresis* phenomenon of suction as well the capillary stress as a specimen undergoes wetting and drying processes. These aforementioned results will also be submitted soon in a paper entitled: *On the hysteresis phenomenon of unsaturated granular assemblies using DEM-LBM coupling* (Younes et al., 2023b).

Chapter 1

Physics and Mechanics of Unsaturated Soils

1.1 Introduction

The aim of this chapter is to provide readers with a foundational understanding of key concepts and a literature review about unsaturated soils, which are essential for comprehending this Ph.D. work. We start with a brief definition of basic geotechnical parameters and variables. We will next explore theoretical, numerical, and experimental aspects of small granular assemblies at the pore scale, namely: the evolution of capillary bridge shapes and forces in terms of water levels and separation distances. Once these definitions are covered, we have the basis to dive into the aspects of unsaturated soils at both macro and micro scales such as the matric suction, Terzaghi's and Bishop's effective stress, capillary stress, contact stress, and the mechanical behavior of unsaturated soils.

1.2 Definition of geotechnical parameters and variables

1.2.1 Basic geotechnical parameters

Unsaturated soils are defined when there are three phases that exist at the same time, namely: solid, liquid, and gas as illustrated in Figure (1.1)

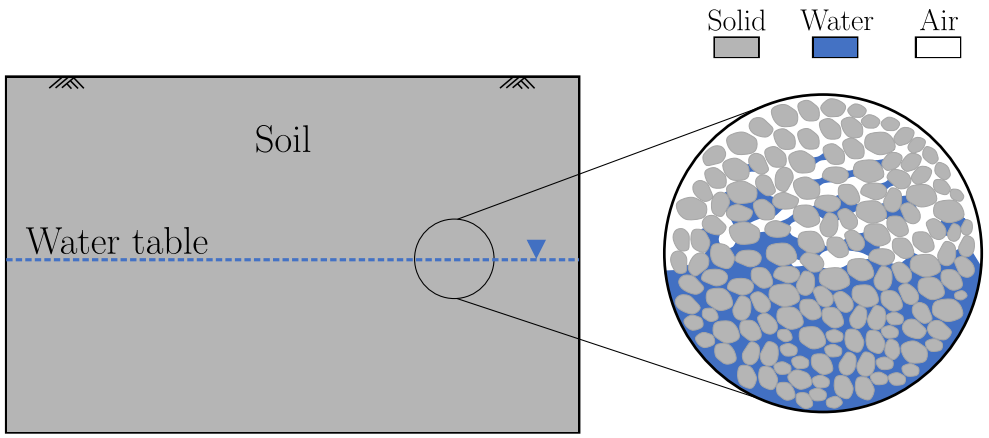

Figure 1.1: Illustration of a typical soil with a water table (depicted as a blue dashed line), along with a zoomed-in view of unsaturated soils at the micro-scale.

In Figure (1.2), referring to the idealized phase diagram from an actual soil cross-section, we define the following canonical volumes, V_a, V_w, and V_s which correspond to air, water, and solid volumes, respectively. The total volume V is determined by the sum of all three volumes such that $V = V_a + V_w + V_s$. The void volume V_v is defined as the sum of air and water volumes, i.e., $V_v = V_a + V_w$.

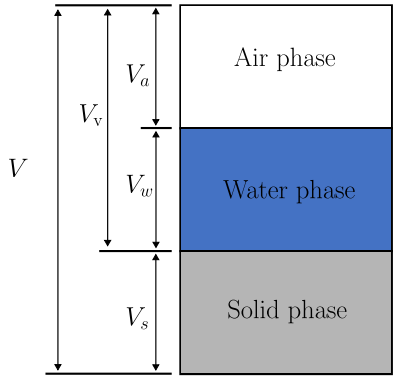

Figure 1.2: Typical phase diagram of soil in which air, water, and solid phases are shown.

One can derive numerous basic parameters via the aforementioned volumes that will be frequently used later in the thesis, such as:

- porosity: $\phi^p = \dfrac{V_\mathrm{v}}{V}$
- void ratio: $e = \dfrac{V_\mathrm{v}}{V_s} = \dfrac{\phi^p}{1-\phi^p}$;
- degree of (water) saturation: $S_r = \dfrac{V_w}{V_\mathrm{v}}$;
- volumetric water content: $\theta_w = \phi^p S_r$.

Depending on the degree of saturation, three principal capillary regimes can be distinguished:

- Pendular regime: capillary bridges are all isolated between each pair of particles. In this case, the gaseous phase is continuous within the sample in the form of large air clusters as illustrated in Figure (1.3a);
- Funicular regime: capillary bridges start to merge and connect more than two particles. The air phase remains mostly continuous, as shown in Figure (1.3b), (it percolates through the sample);
- Capillary regime: the water phase becomes continuous, and the air phase can be only found as air-trapped bubbles as seen in Figure (1.3c).

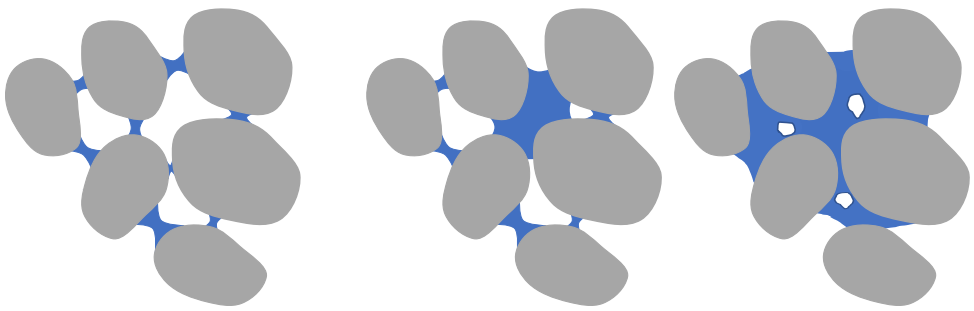

(a) (b) (c)

Figure 1.3: (a) Pendular regime, (b) Funicular regime, and (c) Capillary regime.

1.2.2 Wettability

Wettability, in its broadest definition, refers to the ability of a liquid to spread or adhere to a solid surface or so-called substrate. The origin of *wettability* finds its roots in microscopic effects due to interaction forces at this scale. It is characterized by a surface tension γ and a contact angle θ.

1.2.2.1 Surface tension γ

Generally speaking, fluids are composed of molecules that interact with each other. Fluids become condensed due to the weak forces of attraction known as van der Waals forces. When two immiscible fluids are in contact, *e.g.*, air and water, an unbalanced force is created due to different molecular forces of different fluids resulting in creating a sort of an elastic membrane or a *stretched elastic sheet* at the interface separating water from air, that can be characterized by the introduction of a surface tension γ.

An illustrative example is shown in Figure (1.4a) in which the 'black' molecule is surrounded by other similar molecules, and hence subjected to van der Waals forces in all directions. This results in the molecule being in equilibrium. On the contrary, the 'red' molecule (that lies on the interface) is subject to van der Waals forces only directed towards the water phase, giving rise to an unbalanced force that puts the water-air interface in tension. The surface tension counteracts this unbalance of van der Waals forces. Another widely known example is the rectangular film formed in a wire frame with a moving rod, as illustrated in Figure (1.4b). The force needed to keep it in equilibrium is related to the surface tension of the liquid. In passing, it is the surface tension that makes pond skaters walk and float on water without sinking.

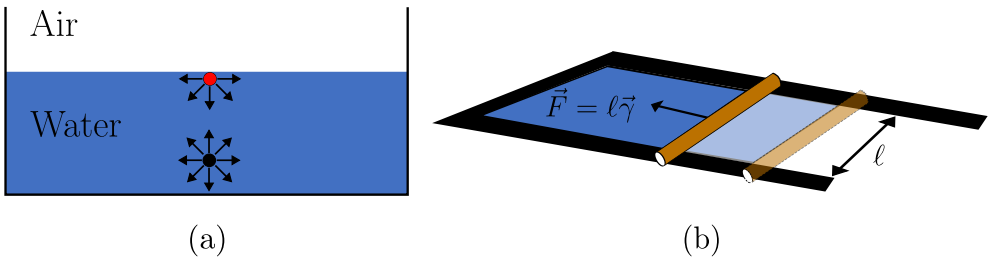

Figure 1.4: (a) surface tension as a result of membrane forces acting on a molecule at the air-water interface, (b) rectangular film formed by a moving rod in equilibrium with surface tension force.

From the above, surface tension originates from intermolecular interactions resulting from the interactions. An increase of the interface by ΔA requires an energy ΔW_{int}. The interfacial energy is the surface tension γ defined as:

$$\gamma = \frac{\Delta W_{int}}{\Delta A} \tag{1.1}$$

The surface tension is considered as a force per unit length [N.m^{-1}]. The surface tension of water and air is about $\gamma^{\text{wa}} = 0.072$ N.m^{-1} at a temperature of $T = 20\,^{\circ}$C. For water and air, the surface tension is usually estimated in terms of temperature using the following formula (Molenkamp and Nazemi, 2003; Edlefsen et al., 1943)

$$\gamma^{\text{wa}}(T) = 0.1171 - 0.0001516T \tag{1.2}$$

where T is the temperature expressed in Kelvin K.

1.2.2.2 Contact angle θ

If one were to place a drop of liquid on a flat surface, an equilibrium would be held between air, water, and solid phases to give a spherical cap-like as shown in Figure (1.5). The contact angle θ is related to the existence of different surface tensions for the three types of interfaces: liquid/gas, solid/liquid, and solid/gas.

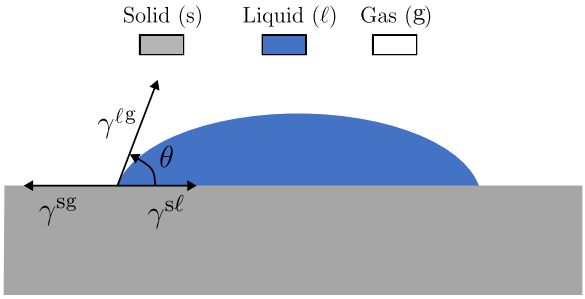

Figure 1.5: Liquid droplet on a flat surface. γ^{sg}, $\gamma^{\ell g}$, $\gamma^{s\ell}$ are the surface tensions of solid-gas, liquid-gas, and solid-liquid, respectively.

The established mechanical equilibrium at the solid-liquid-gas interface is attributed to the English scientist Thomas Young, who first formulated back in 1805 the following equation known as Young's equation (Young, 1805):

$$\cos\theta = \frac{\gamma^{sg} - \gamma^{s\ell}}{\gamma^{\ell g}}. \tag{1.3}$$

Generally speaking, depending on the value of θ, we distinguish two cases: hydrophilic $\theta < 90°$, e.g., water, and hydrophobic $\theta > 90°$, e.g., mercury, as shown in Figure (1.6).

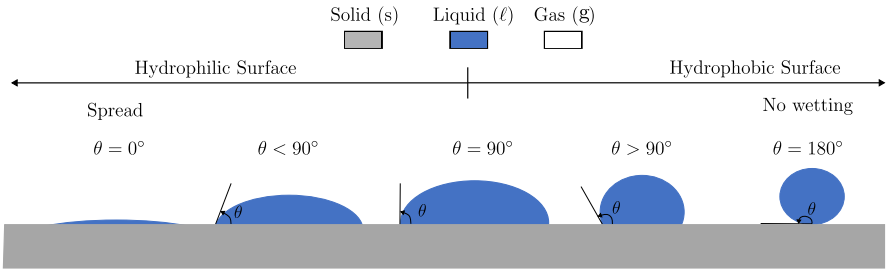

Figure 1.6: Different wettabilities of liquid droplets on a flat solid surface.

For the sake of brevity, γ refers to the surface tension $\gamma^{\ell g}$ in the following.

1.2.2.3 Capillary action

The existence of the surface tension γ and the contact angle θ explains why water can rise in a small tube as illustrated in Figure (1.7). This phenomenon is known as Jurin's law, named in honor of the late English physicist *James Jurin*. The height h is expressed as follows

$$h = \frac{2\gamma\cos\theta}{\Delta\rho g r} \tag{1.4}$$

where $\Delta\rho = \rho_\ell - \rho_g$, r is the tube radius, γ is the surface tension, and g is the acceleration due to gravity.

Laplace pressure:

An interesting aspect that can be observed from the air-water capillary rise example is the curving phenomenon that occurs on the top of the tube—red curve—known as a meniscus as shown in the zoomed illustration of Figure (1.7). This curve results in a pressure difference $\Delta P = P_w - P_a$, known as the Laplace pressure (Gennes et al., 2004).

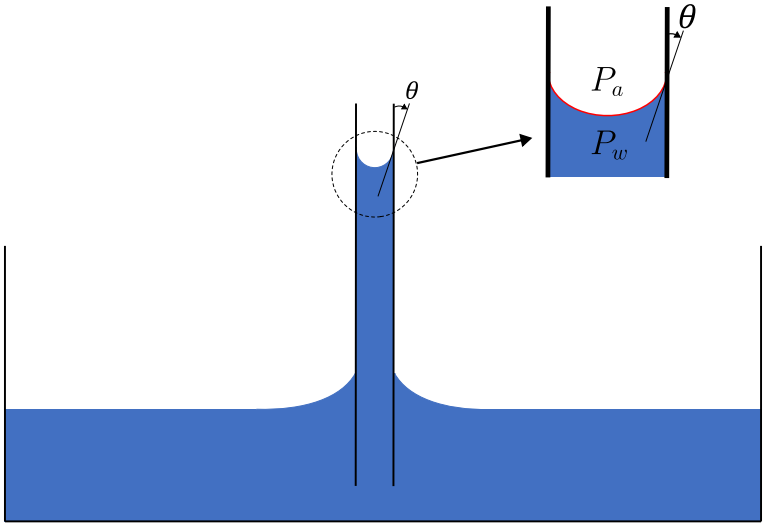

Figure 1.7: A visualization of air-water capillary rise with a magnified view of the meniscus.

According to Laplace, the relation between the curvature and the pressure difference is

$$\Delta P = \gamma \kappa \tag{1.5}$$

where κ is defined as the curvature.
As we will see in the next section, the curvature κ can be positive or negative depending on the orientation of the normal vector of the liquid-gas interface. The curvature κ is related to the principal radii of curvature R_1 and R_2 as follows:

$$\kappa = \frac{1}{R_1} + \frac{1}{R_2}. \tag{1.6}$$

In this particular case of the capillary tube, the principal radii of curvature happened to be equal, i.e., $R_1 = R_2$, hence Eq. (1.5) becomes:

$$\Delta P = \frac{2\gamma}{R}. \tag{1.7}$$

1.2.2.4 Hysteresis phenomenon

Historically, the term *hysteresis* was first introduced by Sir *James Alfred Ewing* in the late 19$^{\text{th}}$ century while he was studying magnetic fields (Encyclopedia Britannica, 2023). Etymologically speaking, *hysteresis* originates from the Greek word *hysterẽsis* which means *lagging* in English. In simple terms, if a material responds in a specific way when subjected to an external action, it will exhibit a different response if the action is reversed.

Practically, *hysteresis* can be observed in various systems and materials, such as magnetic materials, mechanical systems, and unsaturated soils. The phenomenon of *hysteresis* is characterized by a *delay* or *lag* between the changing input and the corresponding output, forming a loop-like pattern when the input is reversed.

Listed below are the two main origins of hysteresis in unsaturated soils:

- Non-homogeneous pore size distribution: this mechanism is usually referred to as the *Ink-Bottle* effect, which was first introduced by Haines (1929); and
- Wetting angle θ hysteresis.

Ink-Bottle effect:
To better understand this mechanism, one can use an analogy and imagine different pore sizes as non-uniform capillary tubes as depicted in Figure (1.8) with R and r representing the larger and the smaller tube radii, respectively.

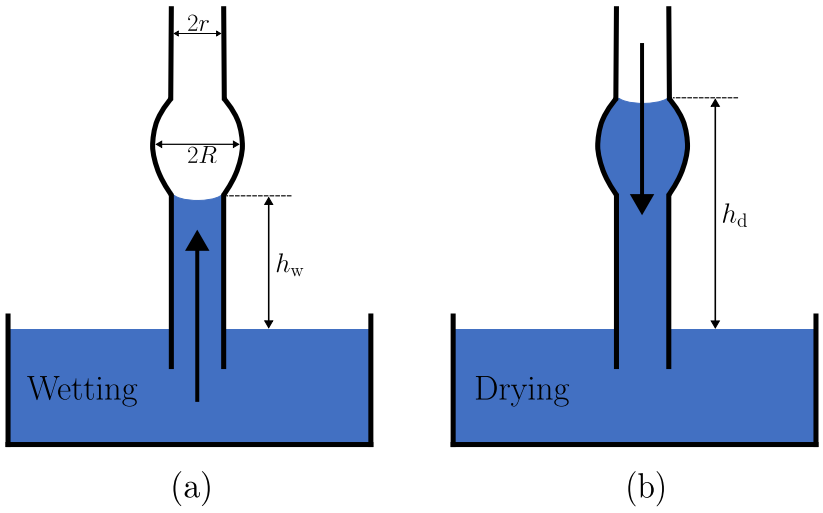

Figure 1.8: Schematic depicting the Ink-Bottle effect: (a) represents the wetting process while (b) shows the drying process. Inspired by (Likos and Lu, 2004b).

In Figure (1.8a) where the wetting is taking place, the maximum suction is controlled by the smaller tube, that is, r which gives $\Delta P_w = \frac{2\gamma}{r}$. However, if the tube is initially filled with liquid (water) and it is experiencing a drying process, as shown in Figure (1.8b), the maximum suction would also be $\Delta P_d = \frac{2\gamma}{r}$ as the water is stuck at the tube having a radius r.

The main idea is that even though the pressure difference or suction during both wetting and drying processes remains the same, the actual heights reached in the capillary tube system differ, with h_d being greater than h_w, as illustrated in Figure (1.8). The difference in heights corresponds to two different moisture contents or degrees of water saturation in the system. In simpler words, even with the same pressure driving the movement, the amount of moisture retained by the capillary tubes differs during the wetting and drying processes (Likos and Lu, 2004a,b).

Wetting angle θ hysteresis:
If one were to place a water droplet on a tilted surface, due to gravity, the droplet would slide down, as shown in Figure (1.9). In this case, the advancing wetting angle θ_w at the front (right side) is observed to be larger than the receding contact angle θ_d at the rear (left side). The reason behind the phenomenon is that the droplet advances on a dry surface while simultaneously wetting the surface behind it. Consequently, the rear side of the droplet slides on a wet surface, resulting in $\theta_w > \theta_d$. In unsaturated soils, the behavior during wetting and drying processes shares similarities with the mechanism previously described (Likos and Lu, 2004b,a).

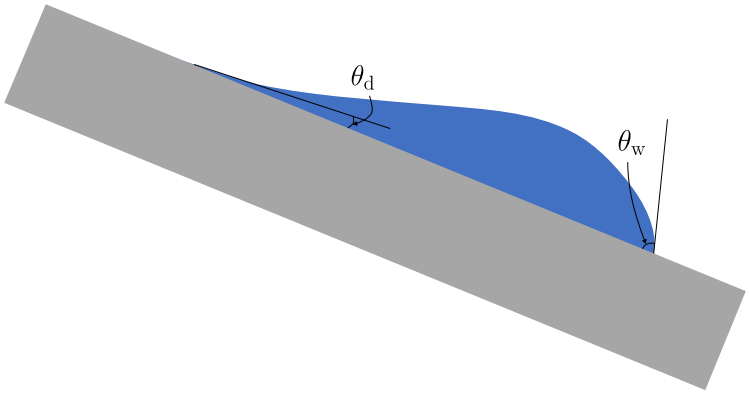

Figure 1.9: Schematic depicting the wetting angle hysteresis. Inspired by (Likos and Lu, 2004b).

1.3 Capillary bridges and forces

Capillary bridges between different solids result in the creation of forces acting on them. Consequently, capillary forces play a crucial role in modifying the behavior of partially saturated granular assemblies (Richefeu et al., 2009; Mielniczuk et al., 2015; Dörmann and Schmid, 2017; Wang et al., 2017; Louati et al., 2017; Grof et al., 2008). At the macro-scale, these capillary forces give to the material an *apparent cohesion*. As the liquid content increases until saturation, the capillary cohesion may be lost and the sample may collapse, for instance, the sandcastle (Lu et al., 2007; Hornbaker et al., 1997; Pakpour et al., 2012). For stability analysis, it is vital to quantify accurately the capillary forces acting within partially saturated granular materials.

Numerous studies have been carried out to explore the characteristics of capillary bridges and forces in various regimes, including *pendular* and *funicular*. This section provides a comprehensive overview of capillary bridges and their associated capillary forces for doublets and triplets of particles.

1.3.1 Doublet of particles

If one were to place a small amount of liquid between two objects—spherical particles, flat surfaces, or even between a spherical particle and a flat surface—a capillary bridge would be established, as shown in Figure (1.10a), (b), and (c), respectively.

A capillary bridge is defined as the free surface separating immiscible fluids due to the interactions of molecules between them along with the solid interface. The capillary bridge will adopt a shape that minimizes its gas-liquid under the constraint of an imposed liquid volume.

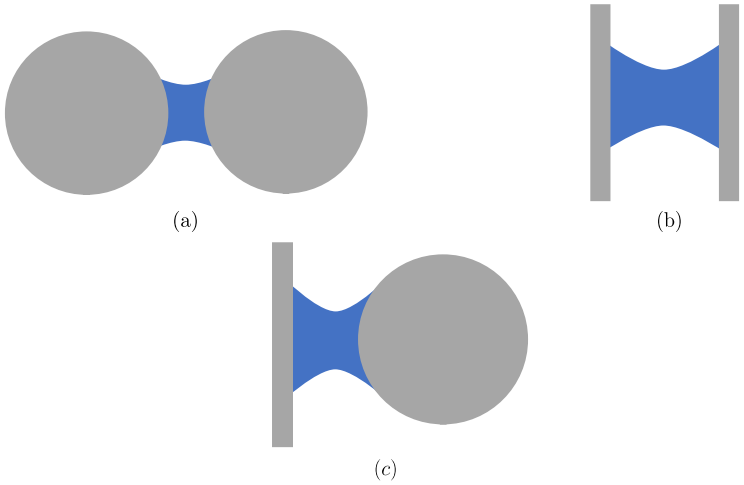

Figure 1.10: Capillary bridges between (a) two spherical particles, (b) two flat surfaces, and (c) a flat surface and a spherical particle.

1.3.1.1 Geometrical shapes

The equation that describes the shape of an axisymmetrical capillary bridge between two spherical grains has been defined by the scientists *Thomas Young* and *Pierre-Simon Laplace* in the 19$^{\text{th}}$ century. This equation is known as the Young-Laplace Equation (YLE) which reads (in the absence of gravity)

$$\frac{y''(x)}{(1+y'^2(x))^{3/2}} - \frac{1}{y(x)\sqrt{1+y'^2(x)}} = -\frac{\Delta P}{\gamma} = H \tag{1.8}$$

where $H = -\dfrac{\Delta P}{\gamma}$ is the mean curvature, and $y(x)$ is the meridian profile shown in Figure (1.11).

For axisymmetrical capillary bridges, the mean curvature H can be calculated as follows:

$$H = \frac{1}{R_1} + \frac{1}{R_2} \tag{1.9}$$

where R_1 and R_2 are the algebraic curvatures.

To understand the signs of curvatures, an example of a classical air-water capillary bridge is shown in Figure (1.12). From the latter figure, $\vec{n}_1$ and $\vec{n}_2$ are the normal unit vectors pointing outward of the air-water interface. If the normal unit vector points to the center of the circle, the curvature is then considered positive and *vice-versa* (with the convention that $R_1 > 0$ and $R_2 < 0$).

We also recall that the integration of the YLE leads to the non-linear first-order differential equation

$$1 + y'^2 = \frac{4y^2}{H^2\left(y^2 - \dfrac{2\lambda}{H}\right)^2} \tag{1.10}$$

where λ is the first integral of the Young-Laplace equation given by Gagneux and Millet (2014):

$$\lambda = \frac{y}{\sqrt{1+y'^2}} + \frac{Hy^2}{2}. \tag{1.11}$$

According to the signs of H and λ, Eq. (1.10) describes a Delaunay roulette (Delaunay, 1841)

$$1 + y'^2 = \frac{4a^2y^2}{(y^2 + \varepsilon b^2)^2} \tag{1.12}$$

where $\varepsilon = 1$ corresponds to a portion of unduloid, whereas $\varepsilon = -1$ corresponds to a portion of nodoid. Readers are invited to consult Gagneux and Millet (2014) for more details.

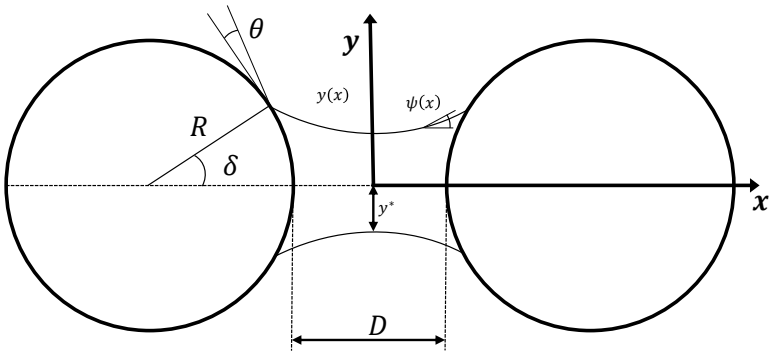

Figure 1.11: Capillary bridge profile between two particles. Parameters are: R is the particle radius, δ is the filling angle, y^* the neck radius, $\psi(x)$ angle between tangent and the x-axis, θ the contact angle, and D is the separation distance between grains.

1.3.1.2 Capillary force F^{cap}

The constant λ (the first integral of the YLE) takes the unit of a length. Thus, $2\pi\gamma\lambda$ will have a force unit. At static equilibrium, we can evaluate this quantity at the neck of the capillary bridge ($y = y^*$ and $y' = 0$), which gives the classical gorge expression of the capillary force (Gras et al., 2013; Gagneux and Millet, 2014):

$$F^{\text{cap}} = \underbrace{-\Delta p \pi y^{*2}}_{F_p} + \underbrace{2\pi\gamma y^*}_{F_{ad}}. \tag{1.13}$$

Note that, in the above expression, the capillary forces splits into two parts: a pressure force F_p and a surface tension force F_{ad}. As it is a first integral of Young–Laplace equation, the capillary force is constant at any point of the profile $y(x)$ and can also be calculated at the contact line[1] by Gagneux and Millet (2014)

$$F^{\text{cap}} = \underbrace{-\Delta p \pi R^2 \sin^2\delta}_{F_p} + \underbrace{2\pi\gamma R \sin\delta \sin(\delta + \theta)}_{F_{ad}} \tag{1.14}$$

where δ is the filling angle, and R is the radius of the particle.

Moreover, the capillary force can also be evaluated at any position along the capillary bridge and it expresses

$$F^{\text{cap}} = \underbrace{-\Delta p \pi y(x)^2}_{F_p} + \underbrace{2\pi\gamma y(x)\cos\psi}_{F_{ad}} \tag{1.15}$$

[1] At the contact line of abscissa x_c, $y(x_c) = r\sin\delta$ and $y'(x_c) = \cot(\delta + \theta)$.

where $\psi(x)$ denotes the angle between the tangent of the profile at point $(x, y(x))$ and the horizontal axis as illustrated in Figure (1.11).

It must be pointed out that Eqs. (1.13), (1.14), and (1.15) can only be applied for an isolated capillary bridge between two grains.

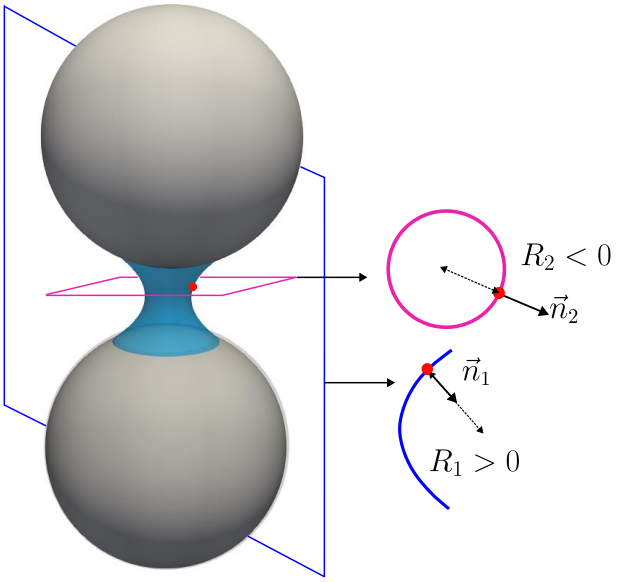

Figure 1.12: Illustration of the signs of curvatures within a typical capillary bridge between two spherical particles.

1.3.1.3 Topological approximations

Multiple experimental, analytical, and numerical studies have been conducted to investigate capillary bridge shapes between poly-dispersed and mono-dispersed spherical particles, two flat surfaces, and between a flat surface and a spherical particle.

Haines (Haines, 1925) is probably among the first who have approximated capillary forces using a circular arc. Capillary forces were calculated for low liquid volumes and very small contact angles θ. In this study, the aim of Haines was to try to understand and evaluate the order of magnitude of certain physical capillary forces named *cohesion forces* after Haines. The effect of the tension force was consciously omitted by Haines since it appeared to be small for low values of θ and particles in contact. One year later, Fisher extended Haines's work by using the same method, but incorporating the tension force term into the capillary force formulation (Fisher, 1926). Results reported by Fisher demonstrated that the tension force is indispensable in order to capture the *cohesion forces*.

Hotta et al. (1974) have improved the circular approximation to calculate the capillary forces of mono-dispersed spherical particles while taking into account gravity. The results reported in their study showed that the enhanced approximation is capable of capturing capillary forces for large volumes.

Melrose (1966) derived an exact analytical solution using a self-consistent thermodynamic theory for the meridian of the bridge between mono-dispersed spherical particles in contact. It must be pointed out that Melrose was among the firsts—maybe even the first—who have used the nodoid profile to describe capillary interfaces.

A semi-analytical method was proposed by Harireche et al. (2013) in which the capillary interface is approximated with a toroidal arc to calculate capillary forces for perfectly

wet poly-dispersed assemblies. The results reported by Harireche are in line with experimental data for a broad range of liquid volumes. This method can also be applied to a plane-sphere case. A closed-form equation was proposed by Willett et al. (2000) and calculated capillary forces between perfectly wet ($\theta = 0°$) mono-dispersed as well as poly-dispersed spherical particles in terms of separation distance.

A comparison of this method was conducted against the numerical resolution of the YLE. Good results were reported in their study, only for reasonable separation distances away from rupture. The same year, Pitois et al. (2000) proposed a simple closed-form expression of the total capillary force in terms of the separation distance, liquid bridge volume, particle radii, and contact angle, only for mono-dispersed spherical particles and in a quasi-static regime. This closed-form expression reads:

$$F^{\text{cap}} \approx 2\pi R\gamma \cos\theta \left[1 - \frac{1}{\sqrt{1 + \dfrac{2V}{\pi R D^2}}}\right]. \tag{1.16}$$

In addition to the proposed closed-form capillary bridge expression, the authors have also approximated the critical separation distance at which capillary bridges rupture and break into two parts. The proposed critical distance reads

$$D^{\text{crit}} \approx \left[1 + \frac{\theta}{2}\right] V^{1/3} \tag{1.17}$$

where θ is expressed in radians and V is the liquid bridge volume.

Also, Soulie et al. (2006) have proposed an exponential expression of capillary forces for poly-dispersed particles that yield

$$F^{\text{cap}} = \pi\gamma\sqrt{R_1 R_2}\left[c + \exp\left(a\frac{D}{R} + b\right)\right] \tag{1.18}$$

where $R = \max(R_1; R_2)$ and the dimensionless coefficients a, b, and c are expressed as follows:

$$\begin{aligned} a &= -1.1\left(\frac{V}{R^3}\right); \\ b &= \left[-0.148\ln\left(\frac{V}{R^3} - 0.96\right)\right]\theta^2 - 0.0082\ln\left(\frac{V}{R^3}\right) + 0.48; \\ c &= 0.0018\ln\left(\frac{V}{R^3}\right) + 0.078. \end{aligned} \tag{1.19}$$

These closed-form expressions provided great results with respect to the experimental data. Richefeu et al. (2006b) proposed an expression for the attractive capillary force between poly-dispersed particles with radii R_i and R_j as follows

$$F^{\text{cap}} = 2\pi R\gamma \cos\theta\, e^{-D/\eta} \tag{1.20}$$

where $R = \sqrt{R_i R_j}$ is the geometrical mean of particle radii, and η is a length scale defined as follows

$$\eta = h(r)\, c \left(\frac{V}{R'}\right)^{1/2}. \tag{1.21}$$

where r is the ratio between radii defined as $r = \left[\max\left(\frac{R_i}{R_j}\right); \max\left(\frac{R_j}{R_i}\right)\right]$, c is a fitting coefficient, $R' = \frac{2R_iR_j}{R_i + R_j}$ is the harmonic radius, and $h(r)$ is a function. After some fitting with the YLE, they concluded that $c \approx 0.9$ and $h(r) = r^{-1/2}$ are the best choices to capture the correct capillary forces.

An elliptic approximation was theoretically derived by Kruyt and Millet (2017) for mono-dispersed, perfectly wettable rigid spheres instead of the toroidal or circular arc approximations, to calculate forces and to determine the rupture distance of the capillary bridge. This approach showed to be accurate compared to the YLE. This method has been extended to poly-dispersed and to non-perfect wettable particles by Zhao et al. (2018, 2019).

Machine Learning approaches, especially Artificial Neural Networks (ANNs), have gained significant recognition in multiple fields. A recent study using ANN by (Argilaga and Zhao, 2023) has been carried out to predict capillary forces as well as the critical rupture distances of capillary bridges.

1.3.1.4 Experimental exploration of liquid bridge and capillary force measurement

Experimental investigations have also been carried out. Recently, Nguyen et al. (2020b, 2019b,d, 2020a) have devised a novel method to determine the exact shape of the capillary bridge and the associated capillary pressure ΔP involved in the YLE on the Right Hand Side (R.H.S.) of Eq. (4.11).

Figure (1.13) shows the experimental apparatus used in creating capillary bridges between two spherical rigid particles. The bottom particle is kept fixed, whereas the upper particle can only move in the vertical direction.

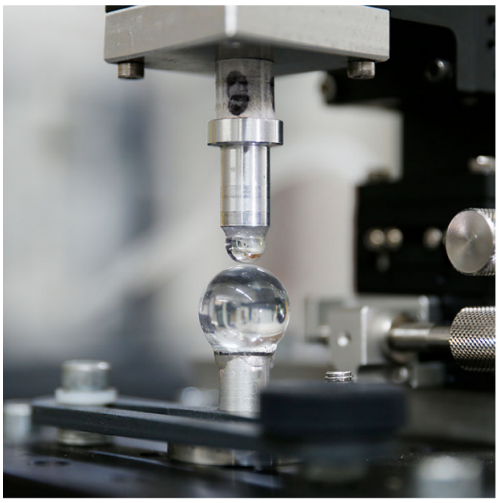

Figure 1.13: Experimental apparatus showing poly-dispersed particles used to create capillary bridges (Nguyen et al., 2019b).

Using a Basler ACE camera along with a telecentric lens, images of capillary bridges are taken and then analyzed using an in-house image processing code written in Matlab, as shown in Figure (1.14). This image-processing code is capable of determining multiple variables, such as the contact angles θ, filling angles δ, and the neck radius y^*. These latter are used to solve the YLE as an inverse problem, thus determining the shape of the

profile (a portion of nodoid, undoloid, catenoid, etc.) and the associated value of capillary pressure ΔP (Gagneux and Millet, 2014).

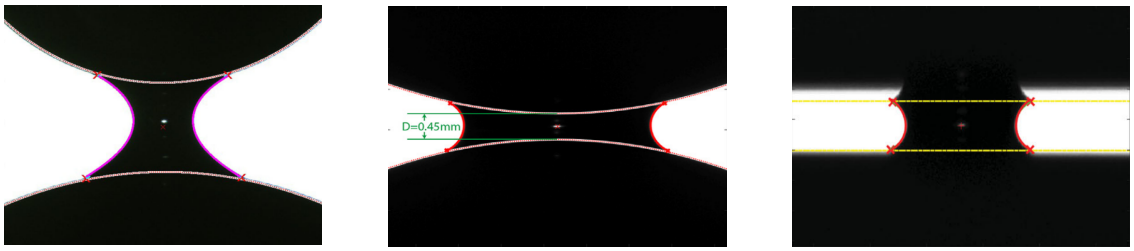

(a) (b) (c)

Figure 1.14: Experimental images of capillary bridges and their solutions. Red and purple curves are the Young-Laplace solution using the image-processing code for nodoid and undoloid, respectively. Green curves are the detected points on the air-water interface. (a) Poly-dispersed spherical particles (Nguyen et al., 2019b), (b) Mono-dispersed spherical particles (Nguyen et al., 2020b) and (c) Two parallel flat surfaces (Nguyen et al., 2020a).

1.3.1.5 Numerical resolutions

Numerical results have been well appreciated in the context of capillary bridges/interfaces. For instance, Duriez and Wan (2017) have solved the YLE numerically to calculate capillary forces between two spherical grains under suction-controlled conditions. Their findings were compared against experimental results and have found great similarities.

Another method to model capillary bridges between two grains has been pursued by Miot et al. (2021) in which an energy minimization technique was used. This minimization along with the virtual work principle has been employed to determine the shape of capillary bridges and calculate capillary forces. In this study, the open-source code Surface Evolver (Brakke, 1992) was used.

Furthermore, Sun and Sakai (2016) have combined the Volume Of Fluid (VOF) method with Immersed Boundary (IB), and Direct Numerical Simulation (DNS) to devise the VOF-IB-DNS method to solve the Navier-Stokes equations in order to determine the shape of gas-liquid interfaces. The Shan-Chen multi-phase Lattice Boltzmann Method (LBM) coupled with Carnahan-Starling Equation Of State (EOS) for the temperature have been employed in Benseghier et al. (2022) to investigate the capillary interfaces and their associated capillary forces. They have found that the Shan-Chen-based LBM model is capable of capturing the shapes of capillary bridges by comparing them with the image-processing technique using the same code used by Mielniczuk et al. (2018); Nguyen et al. (2019b) and Nguyen et al. (2019c,d, 2020b,a, 2021)—see Figure (1.15). They also succeeded in capturing the sign inversion of the dimensionless mean curvature $H^* = H \times R$ from nodoid ($H^* > 0$) to undoloid ($H^* < 0$) as seen in Figure (1.16). Lastly, they computed capillary forces and plotted them in terms of dimensionless liquid volumes V^* against other data, as depicted in Figure (1.17).

However, although the results seem to be accurate, multiple drawbacks can be reported. For instance, the Carnahan-Starling EOS is thermodynamically consistent only for high temperatures $T > 0.7T_C$ where T_C is defined as the critical temperature[2] which is equal to $T_C = 282.9°C$, which is non-physical (Huang et al., 2011, 2015). To prevent numerical noise, it is necessary to calculate capillary forces at a certain distance away from the spherical particle rather than in its immediate vicinity.

[2]The critical temperature is a temperature below which a liquid and its vapor coexist.

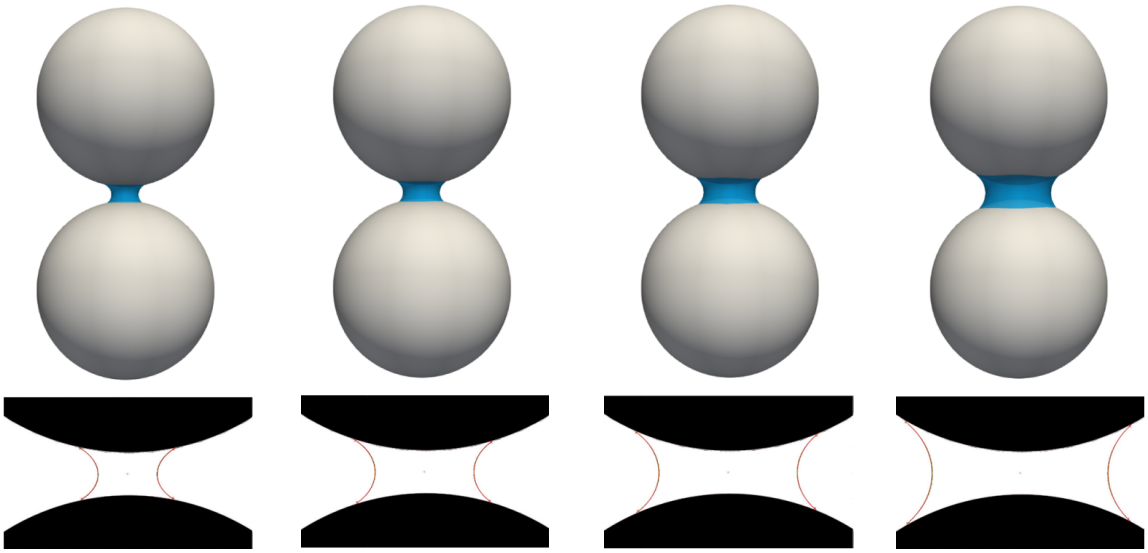

Figure 1.15: Numerical and theoretical shapes of capillary bridge profiles for different volumes on top and bottom, respectively. (a) $V^* = 0.016$, (b) $V^* = 0.041$, (c) $V^* = 0.085$, and (d) $V^* = 0.15$ (Benseghier et al., 2022).

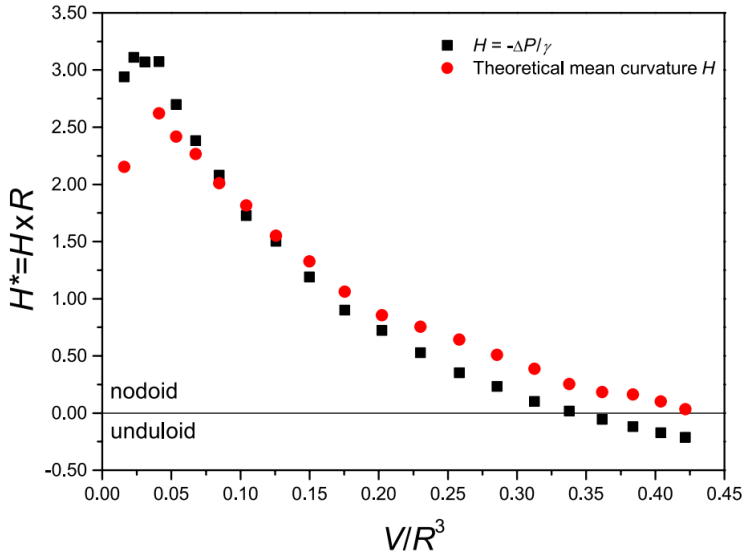

Figure 1.16: Evolution of the dimensionless mean curvature $H^* = H \times R$ of the capillary bridge between two spherical particles for various dimensionless liquid bridge volumes V^*. $H^* > 0$ refers to a portion of nodoid and $H^* < 0$ corresponds to a portion of undoloid shape (Benseghier et al., 2022).

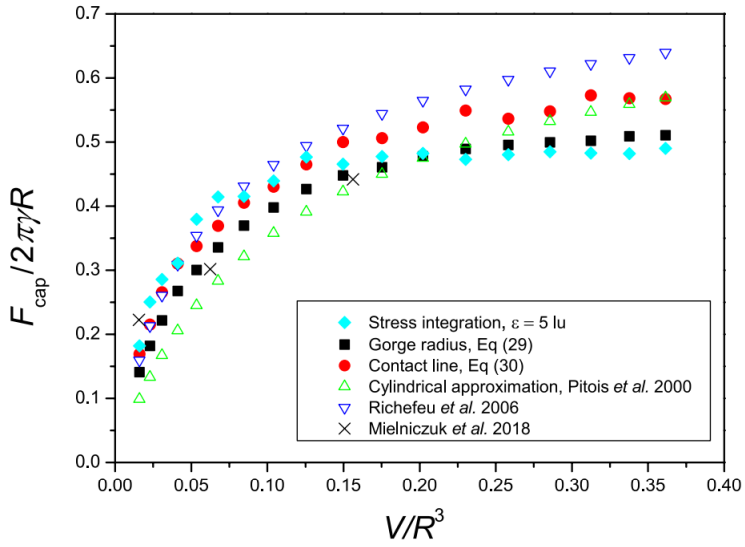

Figure 1.17: Evolution of the dimensionless capillary force for different dimensionless liquid bridge volumes V^*. Other analytical results and experimental data have been added for comparison (Benseghier et al., 2022).

1.3.2 Small granular assemblies: triplets or more

The funicular regime wherein capillary bridges start to merge is probably more prevalent than the pendular regime in practice. For this reason, an overview of the available studies of three particles or more will be provided.

1.3.2.1 Variation of capillary force with water volume from experiments

The experimental study conducted by (Gras, 2011) investigated the behavior of a coalesced capillary bridge between three spherical glass particles during an evaporation process. The findings are depicted in Figure (1.18). Over time, the capillary bridge undergoes significant changes. From stages (a) to (e), the bridge progressively shrinks. Eventually, in stage (f), the capillary bridge reaches a critical point and breaks down, leading to the formation of three separate and isolated capillary bridges connecting each pair of particles. As the process continues, these capillary bridges gradually disappear over time.

Figure (1.19) depicts the time evolution of capillary force acting on the top particle as the coalesced capillary bridge experiences an evaporation process. An intriguing observation is that when the coalesced capillary bridge ruptures in stage (f), the capillary force experiences a significant reduction, decreasing to approximately 30% of its value prior to coalescence. For several years, this particular observation regarding the reduction in capillary force after the rupture of the coalesced capillary bridge remained unexplained.

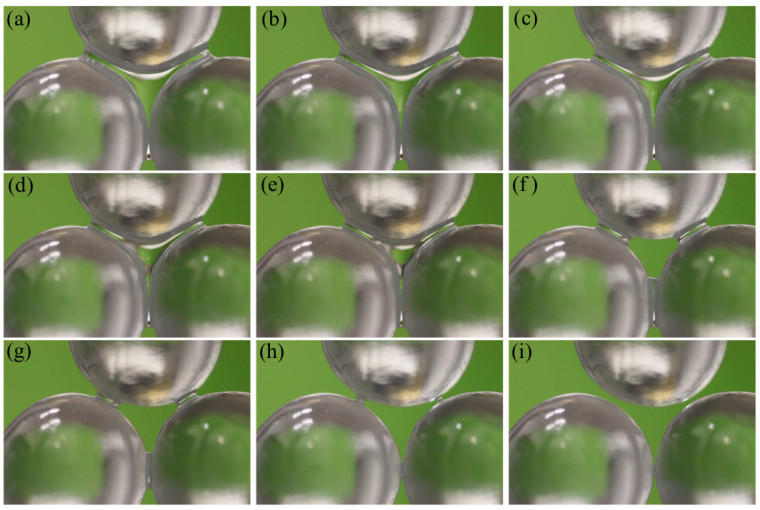

Figure 1.18: Photos of a coalesced capillary bridge between three spherical particles being evaporated (Gras, 2011).

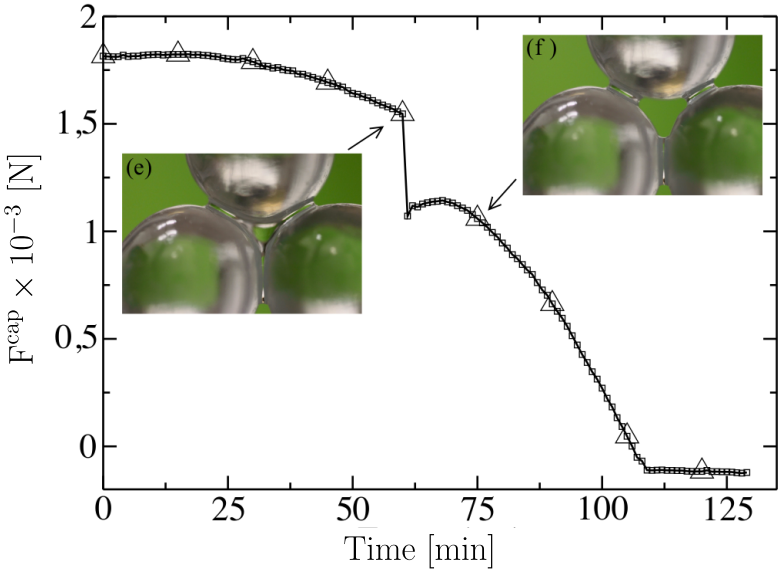

Figure 1.19: Time evolution of capillary force acting on the top particle in a triplet configuration (Gras, 2011).

Many years later, Gagneux et al. (2016) formulated a thorough analytical and geometrical explanation, providing a physical explanation for capillary forces drop after the rupture of a coalesced capillary bridge. In their work, they have proved that the dominant contribution of the change of capillary forces is due to the change in the Laplace pressure force denoted as F_p in Eq. (1.13) for a contact angle of $\theta = 50°$ which corresponds to the one deduced from Gras (2011). This significant alteration in capillary forces is attributed to the transition from *pendular* to *funicular* states and *vice-versa*, which is accompanied by a change in curvature.

An interesting investigation has been conducted by El Korchi (2017) wherein the author has investigated the variation of capillary forces in the context of water imbibition for a system of three and four glass spherical particles. Figure (1.20) describes the experimental setup in 2D used by El Korchi (2017).

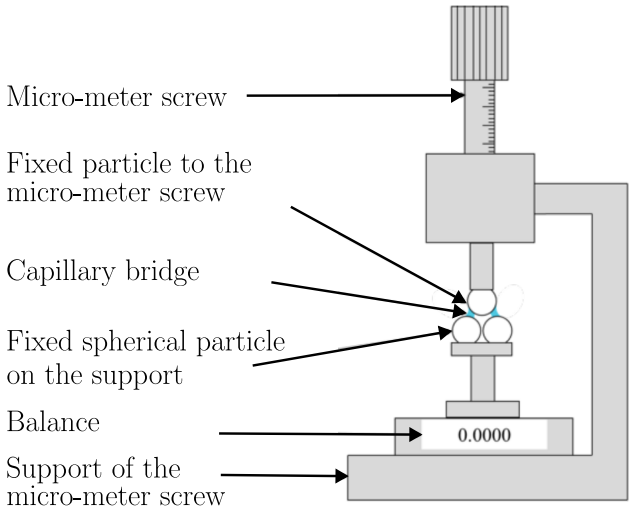

Figure 1.20: A sketch of the experimental setup used for triplets and quadruplets of spherical particles (El Korchi, 2017). Legends have been translated from French to English.

The author injected water between pairs of particles to form two equally isolated capillary bridges as shown in Figure (1.21a). As the water content increases, when capillary interfaces touch each other, a merging of capillary bridges takes place. Consequently, the isolated capillary bridges become one large cluster as shown in Figure (1.21b).

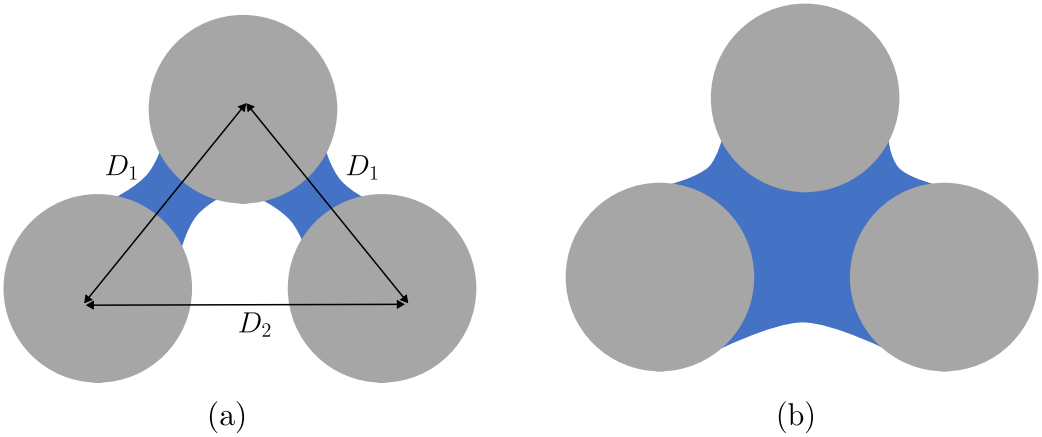

Figure 1.21: (a) Before coalescence and (b) after coalescence.

The author has reported that when capillary bridges merge, a jump in capillary forces is observed as shown in Figure (1.22). The same study has also been conducted, but for quadruplets of particles as shown in Figure (1.23).

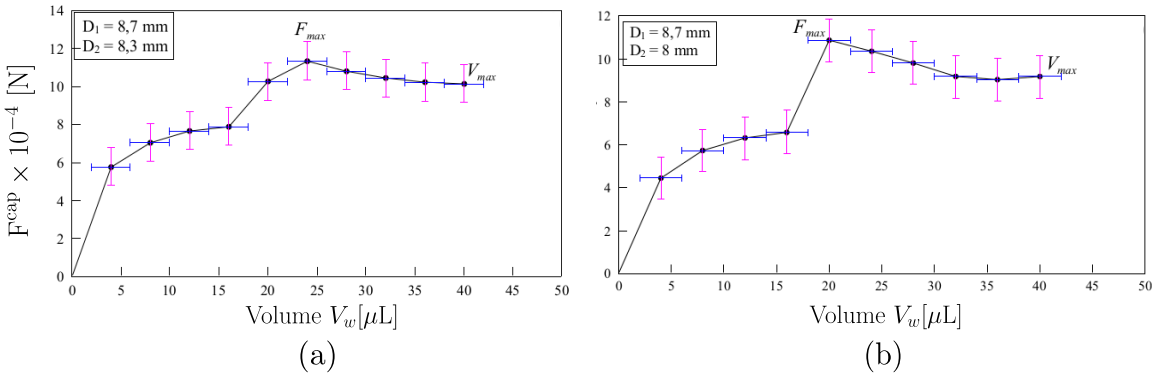

Figure 1.22: Capillary forces F^{cap} evolution in terms of water volumes V_w in triplet configurations for two different setups, $D_1 = 8.7$ mm for both (a) $D_2 = 8.3$ mm and (b) $D_2 = 8$ mm (El Korchi, 2017).

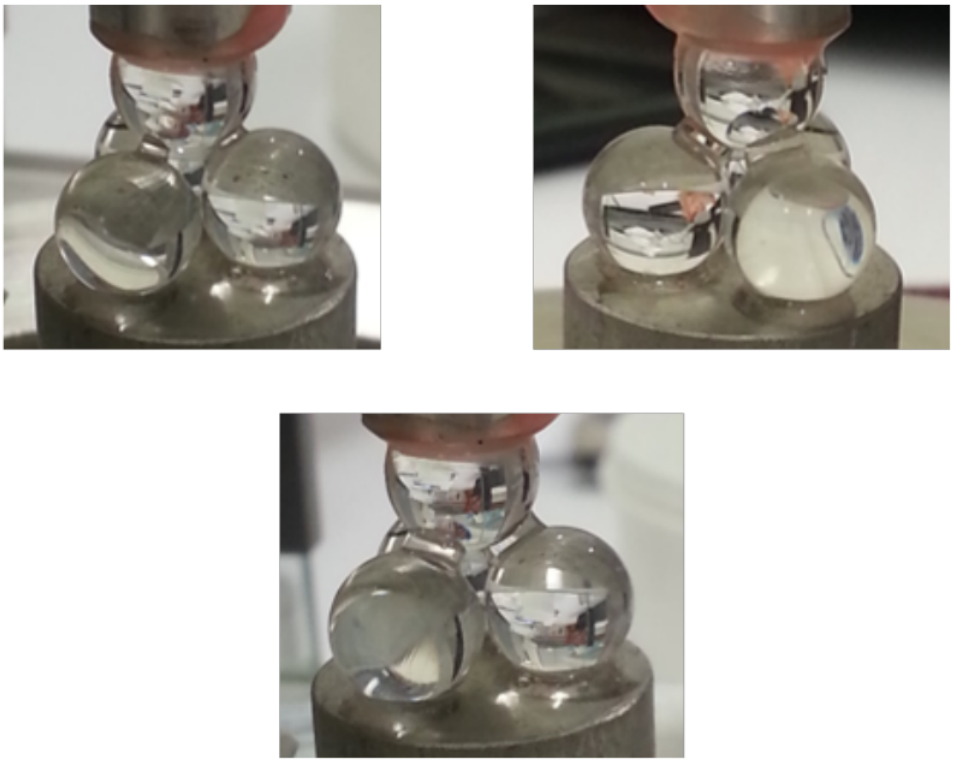

Figure 1.23: Different photos of the quadruplets used in the experiment with capillary bridges (El Korchi, 2017).

The reported findings indicate that the conclusion regarding capillary force jumps at coalescence remains consistent between the triplet and quadruplet cases, as shown in Figure (1.24).

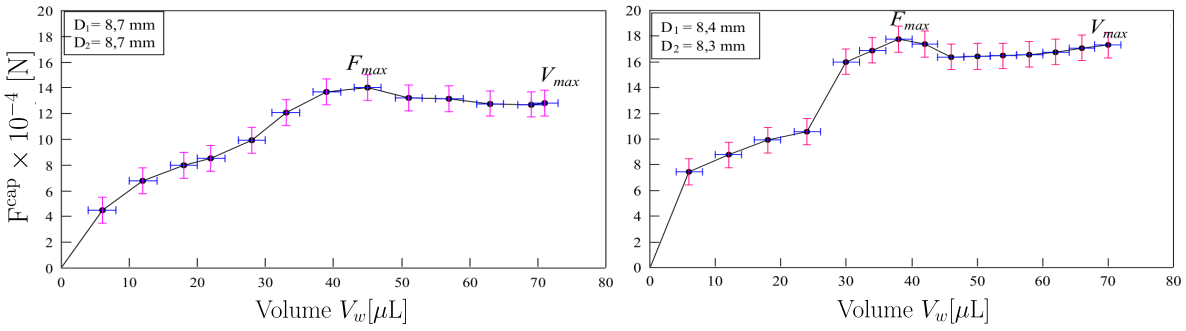

Figure 1.24: Capillary forces F^{cap} evolution in terms of water volumes V_w in quadruplet configurations for two different setups, for both (a) $D_1 = D_2 = 8.7$ mm and (b) $D_1 = 8.4$ mm and $D_2 = 8.3$ mm (El Korchi, 2017).

Using roughly the same experimental setup of Gras (2011), the study conducted by Hueckel et al. (2020) expands upon the research by investigating the evaporation of capillary bridges formed between three, four, and five particles. Remarkably, their findings align with those of the previous study, demonstrating consistent observations across different particle configurations as shown in Figures (1.25) and (1.26).

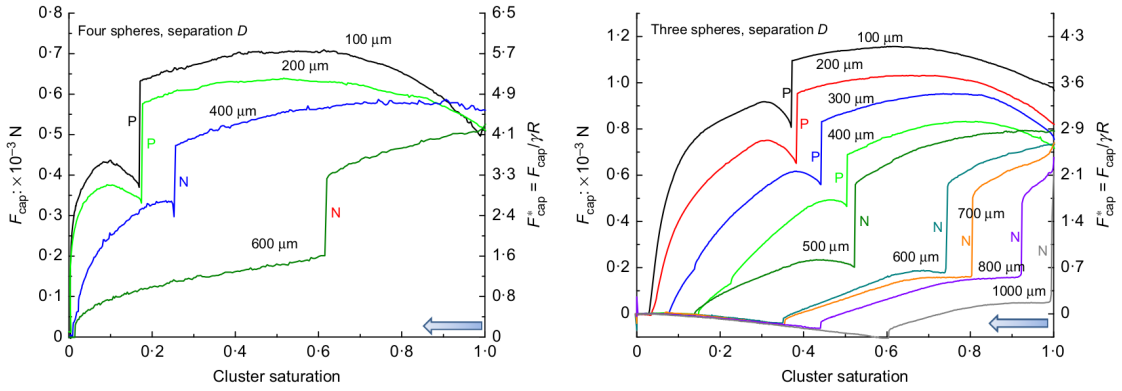

Figure 1.25: Capillary forces F^{cap} evolution in terms of cluster saturation in three- and four-particle configurations for different separation distances (Hueckel et al., 2020).

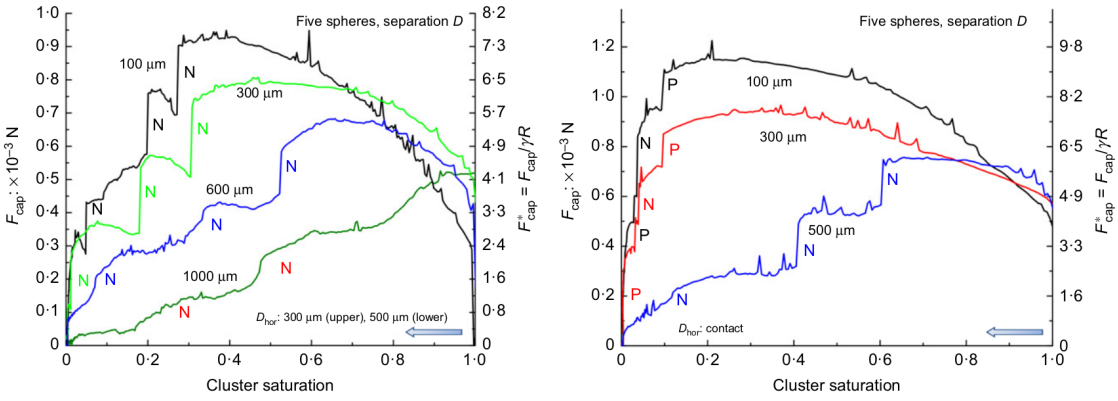

Figure 1.26: Capillary forces F^{cap} evolution in terms of cluster saturation in five-particle configurations for different separation distances (Hueckel et al., 2020).

1.3.2.2 Numerical investigation of capillary force with volumetric water content

In the numerical framework, Miot et al. (2021) used the surface energy minimization approach to address three-particle problems and compared them to the findings reported in El Korchi (2017). In the study conducted by Miot et al. (2021), notable results were reported. However, one limitation of their approach is the inability to simulate coalescence naturally. To overcome this limitation, they resorted to analytical criteria for merging capillary bridges and later had to reinitialize a coalesced capillary bridge between the three spherical particles. Similarly, the same method has also been employed by Di Renzo et al. (2020) to study the influence of the separation distances and water volumes on the capillary forces of three and four spherical particles.

Despite the valuable contributions made by various researchers in studying capillary forces and their dependence on factors such as particle configuration, separation distances, and water volumes, there is still a noticeable gap in the literature when it comes to considering coalescence as an intrinsic aspect of the phenomenon. The existing methods often resort to analytical criteria to simulate coalescence, which may limit the accuracy and realism of the results. Therefore, further research is warranted to develop comprehensive approaches that can naturally incorporate coalescence and capture its effects on capillary forces in unsaturated granular assemblies. This will contribute to a deeper understanding of the complex dynamics involved and provide more realistic models for studying capillary phenomena in the context of unsaturated soils.

1.4 Soil-Water Characteristic Curve and Suction s

One of the most important characteristics of unsaturated soil is its suction s which is defined as the negative pressure present in the pore spaces due to the triphasic interaction at the liquid-gas-solid interface. The suction s originates from two different components: matric and osmotic(Fredlund and Rahardjo, 1993). The matric suction, denoted by s_m, is a concept that arises solely in unsaturated soils, and it represents the difference between the air pressure u_a and water pressure u_w due to capillarity. The matric suction is also defined as the energy required to extract water from a given soil (Eyo et al., 2022).

Mathematically speaking, it can be expressed as (Leong and Abuel-Naga, 2018):

$$s_m = u_a - u_w. \tag{1.22}$$

The term *matric* is used to emphasize its connection to the interaction between fluids and the soil *matrix*. It must be pointed out that the $s = -\Delta P$, where ΔP is the pressure difference we have already in the YLE (4.11). The voids of a partially saturated granular material can be seen as a group of narrow tubes in which water can readily suspend as shown in Figure (1.27).
When solutes, such as salts, are dissolved in water, a chemical potential difference is created between the free water (water without solutes) and the water with dissolved solutes. This chemical potential difference is called osmotic suction and is denoted by s_o. The total suction s, on the other hand, is simply the algebraic sum of matric and osmotic suction (Fatahi et al., 2015):

$$s = s_o + s_m. \tag{1.23}$$

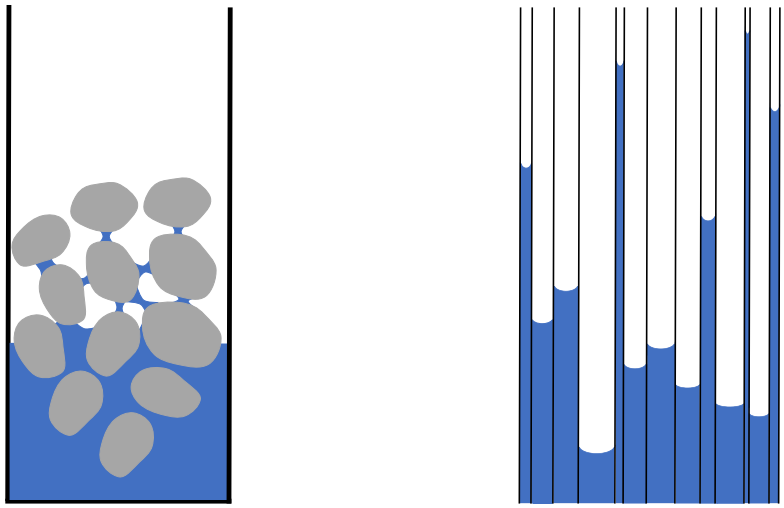

(a) (b)

Figure 1.27: (a) Illustrative picture of capillary rise within granular materials. (b) An analogy of a group of tubes with different radii representing the size of pores within the granular materials.

It is interesting to note that in this work, only the matric suction is to be considered, simply referred to as s.
The Soil-Water Characteristic Curve (SWCC) represents the relationship between the suction s in terms of degrees of saturation S_r, the volumetric water content θ_ω or even water content ω (Zhai and Rahardjo, 2012). Figure (1.28) illustrates a typical SWCC for the entire saturation range. In this figure, and for the drying curve (decreasing S_r, continuous line), three zones are presented (Eyo et al., 2022; Vanapalli, 1996; Vanapalli et al., 1999):

- Boundary-effect zone: At the beginning of this zone, the water phase is continuous and fills all the voids. Towards the end of this zone, the air phase becomes entrapped in the form of air bubbles. This zone corresponds to the *capillary* regime;
- Transition zone: As the water dries out, the air starts invading the larger pores, known as the Air-Entry Value suction (AEV), denoted as s_e. In this zone, the water phase gradually loses its continuity. This zone represents the *funicular* regime;

- Residual zone: In this zone, the water phase becomes discontinuous, and the air phase becomes continuous. The water phase exists in the form of isolated capillary bridges and will eventually vanish as the drying process continues. This zone is equivalent to the *pendular* regime.

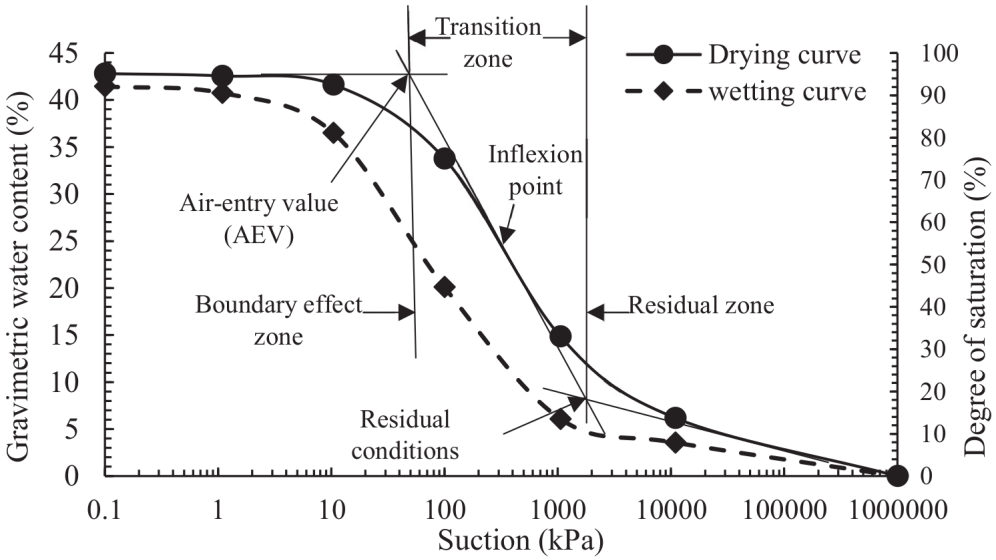

Figure 1.28: Typical SWCC for the entire saturation level (Eyo et al., 2022).

Numerous studies, whether experimental, numerical, or analytical, have been conducted to measure or calculate the suction.

1.4.1 Experimental measurement of SWCC

From an experimental perspective, numerous techniques are available in the literature such as contact filter paper, electrical or thermal conductivity sensors, and pressure cells. However, attention will be given to a specific method called the axis-translation technique. Figure (1.29) shows the apparatus used to measure the suction s. This apparatus is made of a box containing a soil specimen placed on top of a porous disk. This latter is known chosen with a High-Air-Entry material, similar to porous ceramic. Below the disk, there is a pressurized reservoir of water with a pressure of $P_\ell = u_w$, while above the disk there is air with pressure $P_a = u_a$. If one were to zoom in on the porous disk, the tubes would be saturated with formed menisci on the top allowing only for a finite suction $s = u_a - u_w$. If the pores are assumed to be tube-shaped with a minimum radius $r_{\min}$ and using the YLE, one can calculate the maximum pressure s allowed in this test, which is given by the following formula:

$$s_{\max} = \frac{2\gamma}{r_{\min}} \tag{1.24}$$

The advantage of this technique lies in the ability to separately control the apparent air and water pressures without allowing the air to enter the water reservoir as long as the following condition $u_a - u_w < s_{\max}$ is satisfied. Initially, the saturated soil specimen is placed on the top of the HAE disk as seen in (b). Then, the water is gradually drained until equilibrium is reached for an imposed suction s. This equilibrium state is achieved when the water pressure within the specimen matches that in the reservoir, as long as

the water coming from the reservoir is in contact with the water within the specimen, as depicted in (c).

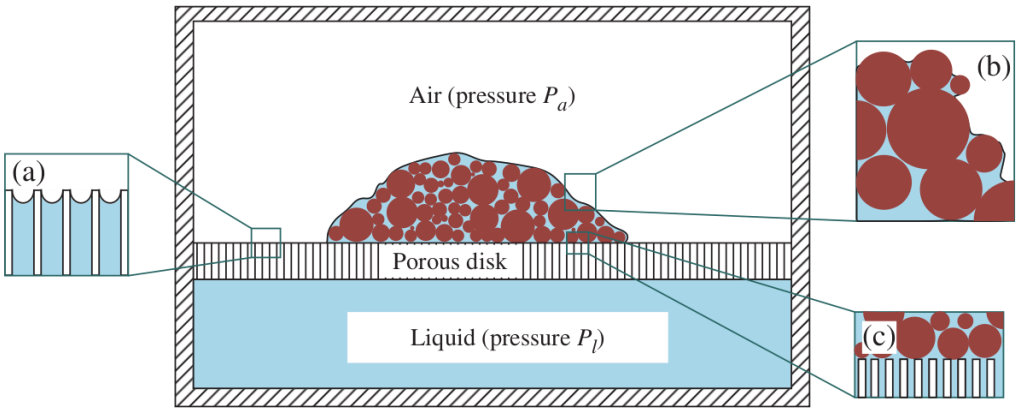

Figure 1.29: HAE Material (Mitarai and Nori, 2006).

1.4.2 Equations for fitting SWCC

Over the span of a century, numerous analytical models have been proposed by researchers to describe soil-water retention characteristics. For instance, Brooks (1965) introduced an equation that relates suction, air-entry-value suction, and the pore-size distribution parameter λ as follows:

$$S_r = \left(\frac{s_e}{s}\right)^{\lambda} \tag{1.25}$$

Here, s_e is the air-entry-value suction. However, this equation is only applicable when $s > s_e$.
Logarithmic models have also been proposed for certain Australian soils. Williams et al. (1983) presented one such model:

$$\ln(s) = a + b\ln(S_r) \tag{1.26}$$

The scientific community has recognized logarithmic relationships extensively, as reported in McQueen and Miller's work (McQueen and Miller, 1974).
Furthermore, the power model has been widely utilized and takes the form:

$$s = aS_r^b \tag{1.27}$$

This formulation has been acknowledged by Williams et al. (1983); Visser; Clapp and Hornberger (1978).
Exponential relationships have been proposed by McKee and Bumb (1984), also known as the Boltzmann distribution (Fredlund and Xing, 1994). Their model is given by:

$$S_r = \exp\left(\frac{a-s}{b}\right) \tag{1.28}$$

However, Eq. (1.28) is not valid for extreme cases, such as nearly fully saturated or dry soils. To overcome this limitation, McKee and Bumb (1987) introduced an alternative model based on the Fermi-Dirac distribution:

$$S_r = \frac{1}{1+\exp\left(\frac{s-a}{b}\right)} \tag{1.29}$$

Among the various models, the most widely used one is the van Genuchten model (Van Genuchten, 1980), which relies on three fitting parameters α, n, and m:

$$S_r = \left[\frac{1}{1+(\alpha s)^n}\right]^m \tag{1.30}$$

Recently, Wan et al. (2019); Pouragha et al. (2021) have addressed this issue by using a probabilistic approach to recover pore size distribution from grain size distribution and the physics of pore filling or drainage.

Indeed, many other models exist, but the ones mentioned above are some of the most notable in the field of SWCC.

1.5 Effective stress $\boldsymbol{\sigma}'$

While the definition of effective stress is well understood and accepted by geotechnical engineers and researchers for dry and fully saturated materials, its formulation for partially saturated soils has been a subject of ongoing debate for centuries now. The concept of effective stress corresponds to the possibility of describing the response of the wet material using the same constitutive law as in the dry case but with effective stress instead of total stress. The change in effective stress governs both the failure and deformation of the soil. Khalili et al. (2005) have proposed a unified expression for the effective stress averaged over the total volume as

$$\boldsymbol{\sigma}' = \boldsymbol{\sigma} - \sum_{i=1}^{n} \alpha_i u_i \boldsymbol{I} \tag{1.31}$$

where $\boldsymbol{\sigma}$ is the total stress, u_i is the pore fluid i pressure, n is the number of fluids within a sample, $\boldsymbol{I}$ is the identity matrix, and α_i are the coefficients that should be chosen in a way that takes into account how each individual fluid pressure u_i affects the overall behavior of the soil.

Eq. (1.31) represents a generalized form of effective stress applicable to porous media, geomaterials, and different fluid phases such as water and air. While the formulation is likely to be unique, the effective stress variable itself is not unique due to the possibility of coefficients α_i not being constants. Strictly speaking, a fully saturated soil is defined when $S_r = 1$, thus only water and solid phases exist at the same time. Whereas, soil is considered dry when the saturation level is nil, indicating the exclusive presence of air and solid phases—$S_r = 0$. In dry soils, and under the condition of compressible air and quasi-static loading regime, the effective stress is expected to be equal to the total stress, that is

$$\boldsymbol{\sigma}' = \boldsymbol{\sigma} \tag{1.32}$$

with α_a (air) is nil.

Indeed, several decades prior to Khalili et al. (2005), Karl von Terzaghi introduced a straightforward yet impressive expression for effective stress in his renowned book *Soil Mechanics in Engineering Practice* widely regarded as the *bible* of Soil Mechanics (Terzaghi, 1925). The formulation applies specifically to fully saturated soils—$\alpha_w = 1$ and reads:

$$\boldsymbol{\sigma}' = \boldsymbol{\sigma} - u_w \boldsymbol{I}. \tag{1.33}$$

Undoubtedly, Eq. (1.33) finds application in nearly all practical geotechnical engineering problems. Nevertheless, this formula is subject to certain conditions and assumptions that must be taken into account in order to ensure its proper and accurate application

- The grain-to-grain contacts must be point-wise so that the resultant force applied by the water on each grain is zero.
- Both water and grains must be considered incompressible, meaning that changes in water pressure do not lead to volumetric strain.
- Only quasi-static loading should be considered to prevent the transmission of shear stress in the water phase.

In extreme cases such as a very high confining pressure, the compressibility of grains cannot be neglected anymore. In this case, Skempton (1984); Nur and Byerlee (1971) have formulated an expression taking into account the compressibility of grains C_s and the drained compressibility of the skeleton C and reads:

$$\boldsymbol{\sigma}' = \boldsymbol{\sigma} - \left(1 - \frac{C_s}{C}\right) u_w \boldsymbol{I}. \tag{1.34}$$

For fully saturated conditions, the existence of effective stress is well established. For unsaturated soils, Eq. (1.33) is no longer valid as it does not take into account the air-water capillary interface. The concept of the effective stress for unsaturated soils was originally introduced by the Road Research Laboratory in Washington DC in their publication (Croney et al., 1958). The empirical formulation is expressed as follows:

$$\boldsymbol{\sigma}' = \boldsymbol{\sigma} - \beta' u_w \boldsymbol{I}. \tag{1.35}$$

In this equation, the parameter β' represents the bonding factor, acting as a measure of the water's ability to contribute to the shear strength of the soil through tension-induced bonding. Indeed, this parameter can be determined experimentally. Similar empirical formulae were proposed by (Jennings, 1961; Aitchison, 1961) during the Pore Pressure and Suction in Soils conference organized in London in 1961 (Pressure, 1960).

Several years later, Alan W. Bishop and Geoffrey E. Blight made notable extensions to Terzaghi's effective stress principle, introducing a novel formulation specifically designed for unsaturated soils (Bishop, 1959; Bishop and Blight, 1963). Their contributions have been widely recognized and well-received within the soil mechanics community. This formulation, known as Bishop's effective stress, is expressed as follows

$$\boldsymbol{\sigma}' = (\boldsymbol{\sigma} - u_a \boldsymbol{I}) + \chi \underbrace{(u_a - u_w)}_{s} \boldsymbol{I} \tag{1.36}$$

where u_a is the air pressure, u_w the water pressure in capillary bridges, the difference between them is the suction $s = u_a - u_w$, χ is some weighting parameter that controls the degree of saturation: χ=0 for dry soils, and $\chi = 1$ for saturated soils, to recover the Terzaghi's effective stress as seen in Eq. (1.33).

Bishop's effective stress in Eq. (1.36) is based on the idea of replacing u_w with $u_w = (1 - \chi)u_a + u_w\chi$ in Eq. (1.33) to take into account the air phase.
Many years later, Richards (1966) proposed an expression for the effective stress based on osmotic suction:

$$\boldsymbol{\sigma}' = (\boldsymbol{\sigma} - u_a \boldsymbol{I}) + \chi_s(s + u_a)\boldsymbol{I} + \chi_o(s_o + u_a)\boldsymbol{I} \tag{1.37}$$

where χ_s and χ_o are the effective stress parameters for matric and osmotic suction, respectively. Likewise, Aitchison and Peter (1973) suggested a modified version of Eq. (1.37) that reads:

$$\boldsymbol{\sigma}' = \boldsymbol{\sigma} + \chi_s s \boldsymbol{I} + \chi_o s_o \boldsymbol{I}. \tag{1.38}$$

The two equations mentioned earlier will not be taken into account since osmotic suction is not within the scope of this thesis.

The value of χ not only depends on the degree of saturation but also on other parameters, such as the Particle Size Distribution (PSD) of a given soil, as shown in Figure (1.30). Several attempts have been made to estimate the value of χ. For instance, Aitchison (1961) proposed a fitted expression which expresses

$$\chi = \begin{cases} 1 & \text{if } S_r = 1 \\ \left(\frac{\alpha}{s}\right) s_e & \text{if } S_r < 1 \end{cases} \tag{1.39}$$

where α is a coefficient that ranges between 0.3 and 0.35 and s_e represents the air entry suction. Also, Khalili and Khabbaz (1998) have proposed an expression similar to that in Eq. (1.39) that reads:

$$\chi = \begin{cases} 1 & \text{if } s \leq s_e \\ \left(\frac{s}{s_e}\right)^{-0.55} & \text{if } s > s_e \end{cases}. \tag{1.40}$$

Many years later, Russell and Khalili (2006) have modified Eq. (1.40) and proposed a new equation for $\frac{s}{s_e} > 25$—usually for sandy soils. This new equation reads:

$$\chi = \begin{cases} \left(\frac{s}{s_e}\right) & \text{if } \frac{s}{s_e} \leq 25 \\ 25^{0.45} \left(\frac{s_e}{s}\right) & \text{if } \frac{s}{s_e} > 25 \end{cases}. \tag{1.41}$$

Moreover, fitting expressions based on several soil characteristics can also be used

$$\chi = \left(\frac{\theta_w}{\theta_s}\right)^k \tag{1.42}$$

where θ_w is the volumetric water content, θ_s is the saturated volumetric water content, and k is a fitting parameter. Similarly, χ can also be expressed as follows

$$\chi = \frac{\theta_w - \theta_r}{\theta_s - \theta_r} \tag{1.43}$$

where θ_r is the residual volumetric water content.

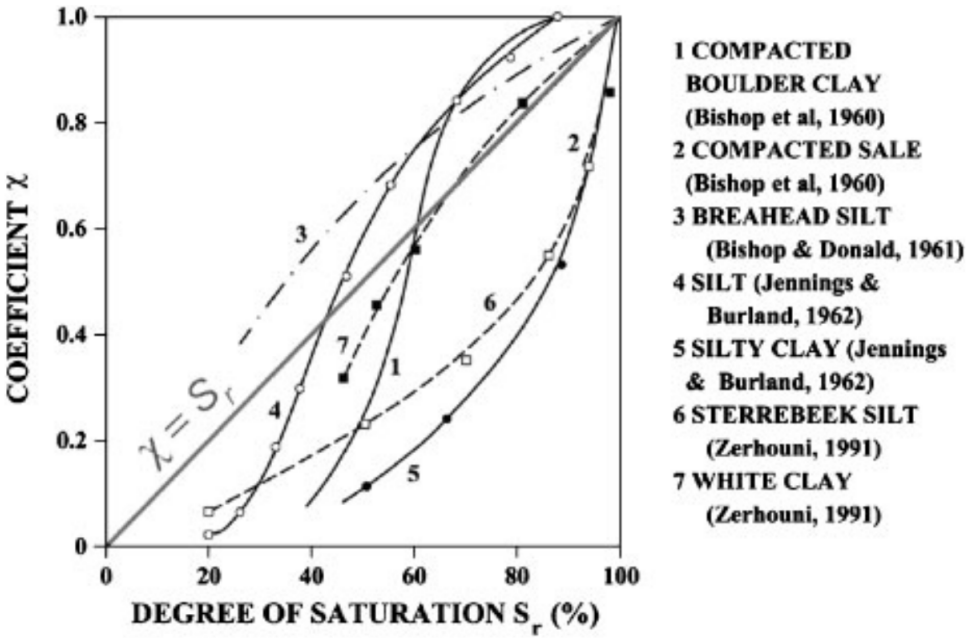

Figure 1.30: Evolution of Bishop's effective stress parameter χ in terms of water saturation S_r for various number of soils (Nuth and Laloui, 2008). This figure was originally plotted by Jennings and Burland (1962) which was updated by Zerhouni (1994)

Several studies within the numerical framework have made efforts to estimate the values of χ. Among these, Yuan et al. (2018) employed the 2PFV-DEM method for this purpose, but their findings indicated that $\chi = S_r$, revealing that the approach was not highly accurate. Following that, the DEM-Fabonnacci-Lattice points discretization has been utilized by Liu et al. (2020b), and it revealed great results when compared to experimental data as shown in Figure (1.31).

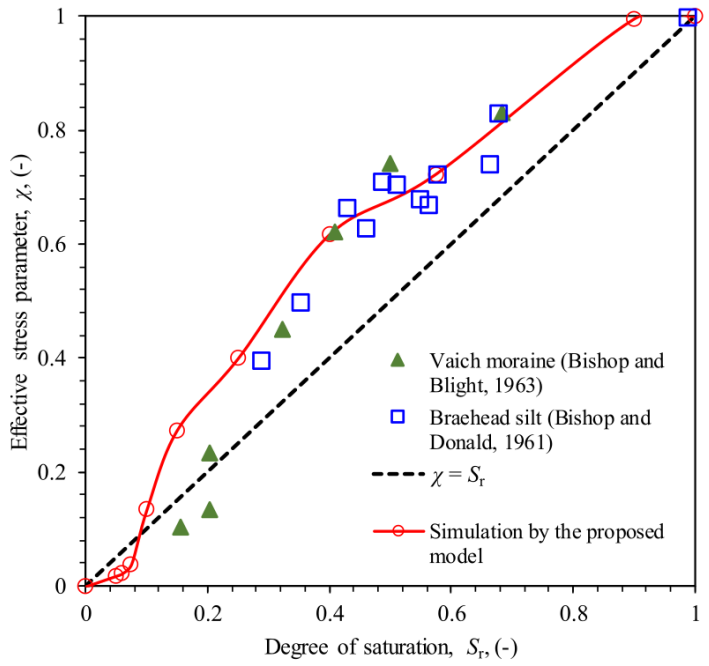

Figure 1.31: Evolution of numerical and experimental Bishop's effective stress parameter χ in terms of water saturation S_r (Liu et al., 2020b).

In addition, artificial neural networks have been successfully trained to predict the value of χ (Lee et al., 2003; Ajdari et al., 2012).

1.6 Capillary stress $\boldsymbol{\sigma}^{\text{cap}}$

In the framework of micro-mechanics, the total stress $\boldsymbol{\sigma}^{\text{tot}}$ can be formally decomposed as the sum of the skeleton contact stress $\boldsymbol{\sigma}^{\text{cont}}$ and the capillary stress $\boldsymbol{\sigma}^{\text{cap}}$ generated by capillary bridges:

$$\boldsymbol{\sigma}^{\text{tot}} = \boldsymbol{\sigma}^{\text{cont}} + \boldsymbol{\sigma}^{\text{cap}}. \tag{1.44}$$

The contact stress $\boldsymbol{\sigma}^{\text{cont}}$ is defined as the transmission of forces at the particle contacts within the solid skeleton. The contact stress tensor can then be calculated *via* the Love-Weber formula expressed as follows (Love, 2013; Weber, 1966)

$$\boldsymbol{\sigma}^{\text{cont}} = \frac{1}{V}\sum_{c} \boldsymbol{f}_{ij}^{c} \otimes \boldsymbol{\ell}_{ij}^{c} \tag{1.45}$$

where $\boldsymbol{f}_{ij}^{c}$ is the contact force between pair of grains (i and j) and $\boldsymbol{\ell}_{ij}^{c}$ is the branch vector from the center of i to that of j, $\otimes$ refers to dyadic product, and V is the total domain volume.

The capillary stress $\boldsymbol{\sigma}^{\text{cap}}$ is the stress responsible for providing unsaturated soils with the *apparent cohesion*. It is tempting to associate it with the second term of the R.H.S of Eq. (1.36) under the assumption that u_a is negligible compared to the total stress $\boldsymbol{\sigma}$. This equation can be re-written as follows:

$$\boldsymbol{\sigma}' = \boldsymbol{\sigma} + \overbrace{\chi(u_a - u_w)\boldsymbol{I}}^{\boldsymbol{\sigma}^{\text{cap}}?}. \tag{1.46}$$

When the capillary stress is not zero, the effective stress $\boldsymbol{\sigma}'$ will be larger than the total stress $\boldsymbol{\sigma}$ giving rise to the so-called *apparent cohesion* ($u_a - u_w > 0$). As mentioned earlier, the challenging task is to determine the values of χ in order to capture well the behavior of unsaturated soils. But the question that arises is: can we find another form of $\boldsymbol{\sigma}^{\text{cap}}$ without using χ?

Limited studies have been conducted to explore a novel form of capillary stress to avoid using the perplex parameter χ. For instance, Scholtès et al. (2009) introduced an innovative approach for modeling unsaturated soils within the context of micro-mechanics using DEM. The core idea of this method lies in treating capillary forces as localized forces at the points of contact between each pair of grains. Consequently, it is possible to see capillary effects as additional contact forces and generalize the Love-Weber equation, as defined in (5.11), except that it involves replacing contact forces with capillary forces. The total stress then becomes:

$$\boldsymbol{\sigma} = \overbrace{\frac{1}{V}\sum_{c} \boldsymbol{f}_{ij}^{c} \otimes \boldsymbol{\ell}_{ij}^{c}}^{\boldsymbol{\sigma}^{\text{cont}}} + \overbrace{\frac{1}{V}\sum_{c} \boldsymbol{f}_{ij}^{\text{cap},c} \otimes \boldsymbol{\ell}_{ij}^{c}}^{\boldsymbol{\sigma}^{\text{cap}}}. \tag{1.47}$$

The calculation of capillary forces in Eq.(1.47) is performed, under suction-imposed conditions and for perfectly wet particles $\theta = 0°$, using the so-called *gorge method* as outlined in Eq.(1.13).

Several years later, Duriez and Wan (2016, 2017, 2018) modeled unsaturated granular assemblies using DEM for non-zero contact angles by solving numerically the YLE—the same technique as in Eq. (1.47). Furthermore, the same authors proposed an analytical capillary stress tensor derived through stress homogenization of the medium. Its mathematical form for spherical particles is composed of four micro-structure tensors and can be expressed as follows

$$\boldsymbol{\sigma}^{\text{cap}} = \frac{1}{V}\left[s\left(\boldsymbol{\mu}_{V_w} + \boldsymbol{\mu}_{S_{sw}}\right) + \gamma\left(\boldsymbol{\mu}_{S_{nw}} + \boldsymbol{\mu}_{\Gamma}\right)\right] \tag{1.48}$$

Where:

$$\boldsymbol{\mu}_{V_w} = V_l \boldsymbol{I} \tag{1.49a}$$

$$\boldsymbol{\mu}_{S_{sw}} = \sum_p R_p \int_{S_{p,sl}} \boldsymbol{n} \otimes \boldsymbol{n} \mathrm{d}S \tag{1.49b}$$

$$\boldsymbol{\mu}_{S_{nw}} = \int_{S_{lg}} (\boldsymbol{I} - \boldsymbol{n} \otimes \boldsymbol{n})\, \mathrm{d}S \tag{1.49c}$$

$$\boldsymbol{\mu}_{\Gamma} = \sum_p R_p \int_{\Gamma_p} \boldsymbol{\nu} \otimes \boldsymbol{n} \mathrm{d}l \tag{1.49d}$$

In Eqs. (1.49), V_l is the liquid volume, R_p is the spherical particle radius, $\boldsymbol{n}$ is the unit normal vector to the interface, $\boldsymbol{I}$ is the identity tensor in $\mathbb{R}^3$, and $\boldsymbol{\nu}$ is the unit tangent vector to the interface as depicted in Figure (1.32).

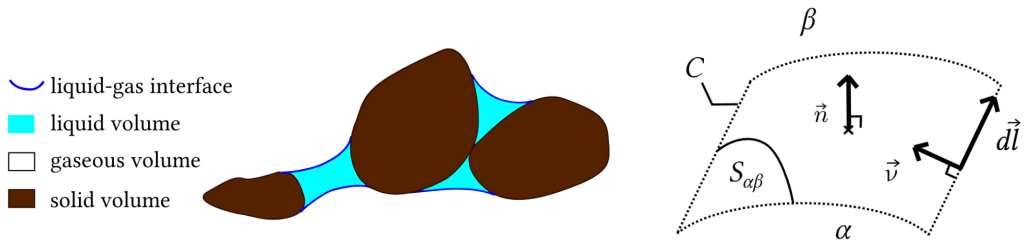

(a) (b)

Figure 1.32: (a) Illustration of several phases within an unsaturated soil. (b) Interface separating two phases α and β which represent air and liquid phases.

Eqs. (1.49a) and (1.49b) represent the effect of suction s along the wetted surfaces S_{sl}, whereas Eq. (1.49c) describes the surface tension contribution to the total liquid-gas interfaces. Furthermore, Eq. (1.49d) represents the contribution of the contour contact lines.

In their study, they proved that the analytical capillary stress matches the one computed using DEM—capillary force technique, thus demonstrating the accuracy of the homogenization technique and its effectiveness in delivering correct results. Unfortunately, computing the capillary stress tensor via capillary forces is restricted only to the *pendular* regime making it impossible to verify the validity of the analytical capillary stress beyond the *pendular* regime using DEM. Therefore, the validity of the analytical capillary stress remains elusive to this day for the *funicular* and *capillary* regimes.

1.7 Mechanical behavior of unsaturated media

Before delving into unsaturated soil conditions, it is essential to briefly recall the failure of saturated/dry soils. When a soil sample is subjected to a certain combination of external loads, it can fail if the internal shearing forces developed exceed the shearing resistance developed by virtue of its *strength*.

In the early 1900s, Professor Christian Otto Mohr proposed a theory of material/soil rupture that involves a combination of normal and shear stresses. Mathematically speaking, the shear strength τ_f of dry/fully saturated soils can be approximated as a linear relationship to the effective normal stress σ':

$$\tau_f = \sigma' \tan \phi' + c'. \tag{1.50}$$

Here, the shear strength has two contributions: (1) shear strength due to friction resulting from the friction angle ϕ' and (2) a cohesion shear strength originating from the cohesion c'. The former is the slope of the envelope, whereas the latter is the intersection with the y-axis. Under dry conditions of sandy soils, the cohesion is negligible. Note that the shear stress is equal to the effective shear stress as the fluid stress is spherical in quasi-static conditions.

For clarity, Figure (1.33) provides a graphical representation of the Mohr-Coulomb failure criterion. Here, the $\tau - \sigma'$ envelope is shown, but in soil mechanics, the $q - p'$ plane is usually used instead. q and p' represent the deviatoric and the mean effective stress (or the hydrostatic pressure), respectively. These aforementioned variables are known as the invariants of the stress tensor $\boldsymbol{\sigma}'$ and are defined as follows:

$$p' = \frac{1}{3}\mathrm{Tr}\left(\boldsymbol{\sigma}'\right), q = \begin{cases} \sqrt{\frac{3}{2}\boldsymbol{\sigma}'_{\mathrm{dev}} : \boldsymbol{\sigma}'_{\mathrm{dev}}} \\ \boldsymbol{\sigma}'_{\mathrm{dev}} = \boldsymbol{\sigma}' - p'\boldsymbol{I} \end{cases} \tag{1.51}$$

where the ":" refers to the double dot contraction product. We also define the volumetric strain ε_v which is defined as the change of the sample's volume and is expressed as:

$$\varepsilon_v = \mathrm{Tr}(\boldsymbol{\varepsilon}) \tag{1.52}$$

where $\boldsymbol{\varepsilon}$ is the strain tensor.

1.7.1 Notion of apparent cohesion

Let us now rewrite Eq. (1.50) in terms of total stress using Tezaghi's effective stress Eq. (1.33) for fully saturated conditions:

$$\tau_f = \sigma \tan \phi' + c' \underbrace{- u_w \tan \phi'}_{\text{apparent cohesion}}. \tag{1.53}$$

From the previous equation, the failure envelope is still the same as in Eq. (1.50). However, for fully saturated soils, the pore-water pressure is positive, resulting in a reduction in the *apparent cohesion*'s value ($-u_w \tan \phi' < 0$) which will reduce the value of τ_f for a given normal stress σ'.

If we extend Eq. (1.50) to unsaturated conditions, we find that the pore-water pressure is negative leading to an increase in shear strength. For both dry and fully saturated soils, cohesion is nill ($c' = 0$). However, the presence of capillary bridges introduced a negative pore-water pressure ($-u_w \tan \phi' > 0$) in sandy soils, giving rise to what is commonly

referred to as *apparent cohesion*. This is the reason why sandcastles remain standing without supports ($\sigma = 0$).

Many studies have been conducted to investigate the behavior of unsaturated soils, but only a few will be presented.

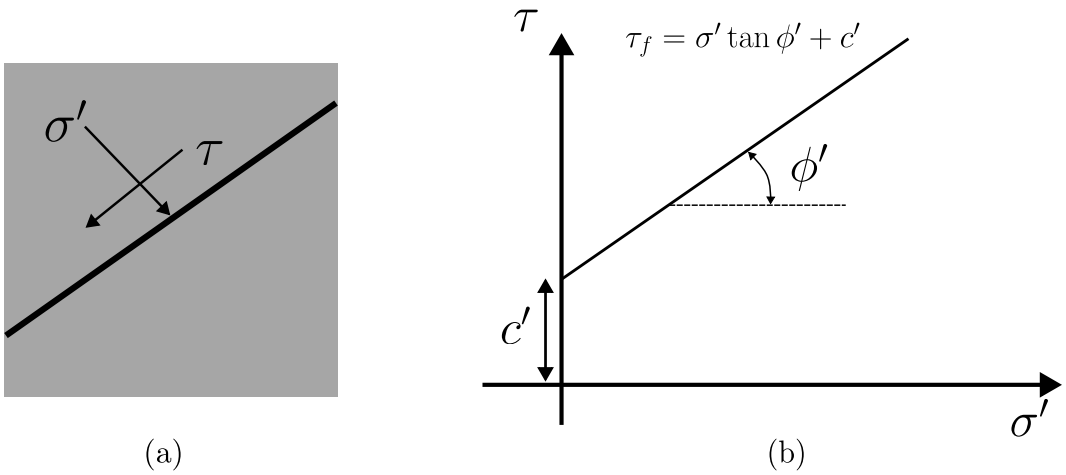

(a) (b)

Figure 1.33: (a) Conceptual sketch of failure plane within a soil and (b) conceptual sketch of a typical failure envelope of cohesive and frictional soils.

1.7.2 Experimental studies

In the experimental framework, for instance, Wang et al. (2002) have conducted a series of triaxial tests for unsaturated soils under suction-controlled conditions. They carried out the responses of deviatoric stresses q in terms of axial strain ε_a for multiple suctions and confining pressures as shown in Figure (1.34).

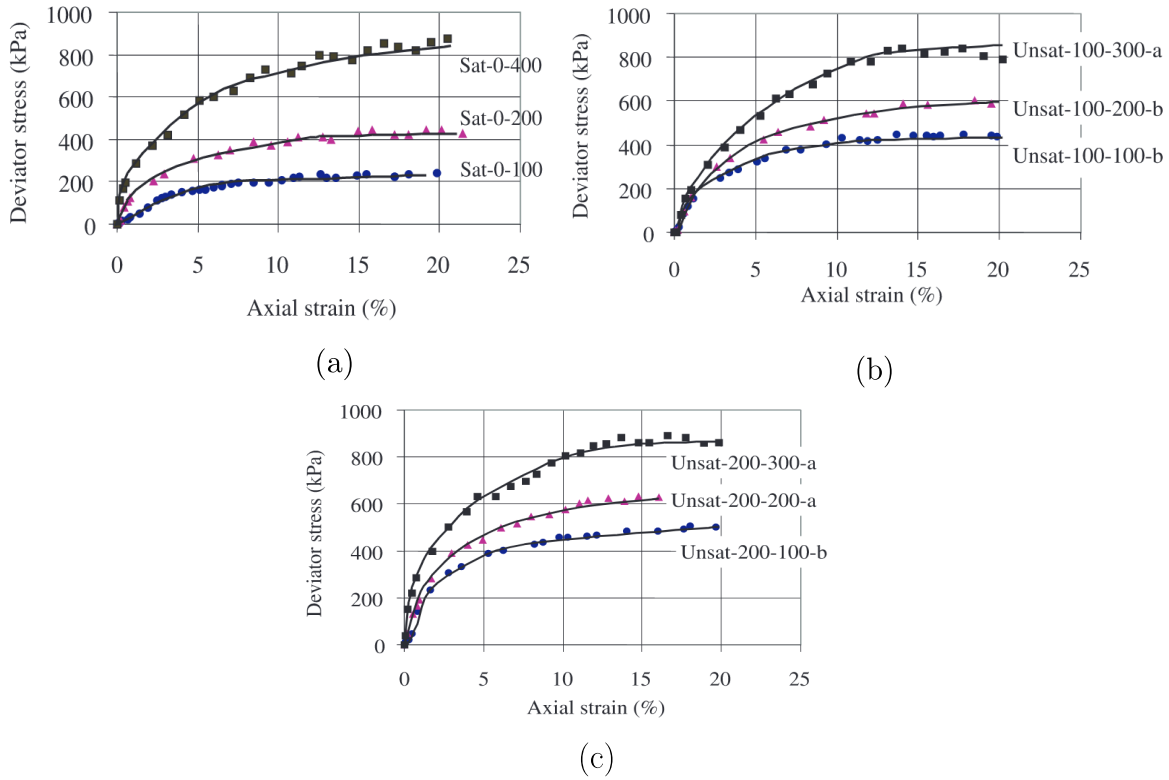

Figure 1.34: Evolution of the deviatoric stress q [kPa] in terms of the axial strain ε_a [%] for a series triaxial tests conducted on silty soils. (a) Saturated conditions with confining pressures of 100, 200, and 400 kPa. (b) and (c) Unsaturated conditions with a suction of 100 and 200 kPa, respectively, for confining pressures of 100, 200, and 300 kPa (Wang et al., 2002).

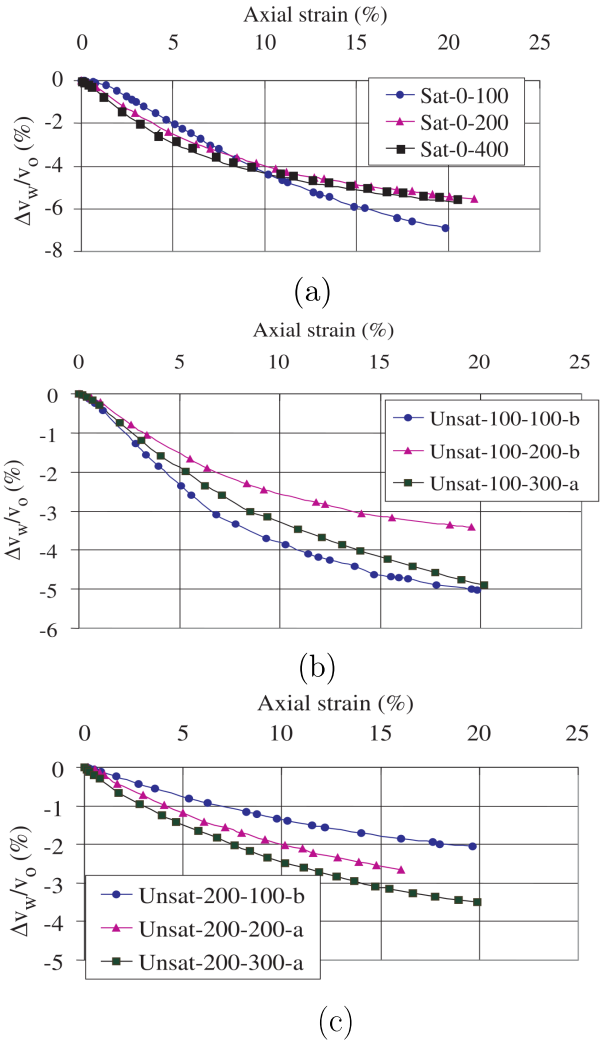

Figure 1.35: Evolution of the volumetric strain ε_v [%] in terms of the axial strain ε_a [%] for a series triaxial tests conducted on silty soils. (a) Saturated conditions with confining pressures of 100, 200, and 400 kPa. (b) and (c) Unsaturated conditions with a suction of 100 and 200 kPa, respectively, for confining pressures of 100, 200, and 300 kPa (Wang et al., 2002).

Not only do capillary bridges provide the soil with a certain cohesion as seen in Figure (1.34), but even the behavior changes in terms of the volumetric strain ε_v. Figure (1.35) shows that the unsaturated soils (b) and (c) deform less than saturated soils (a).

While it is clear in Figure (1.34) that unsaturated soils have more strength than saturated ones, Figure (1.36) shows the Critical State Lines (CSLs) in $q - p'$ plane[3] for both saturated and unsaturated soils. As the suction increases, the CSLs shift up while keeping the same slope, resulting in an increase in the soil's strength.

A compression test was conducted by Soulié (2005) on an unsaturated sample of glass beads for two different particle size distributions. Figure (1.37b) and (c) show the evolution of the breaking force [N] in terms of water contents ω [%]. It can be seen from both figures that the force increases as the amount of water increases because of the bonds created thanks to capillary bridges between the pores. Unfortunately, the study was only carried out for low water content $\omega < 13\%$.

[3]In Figure (1.36) the x-axis is labeled as p'' which is the same as p'.

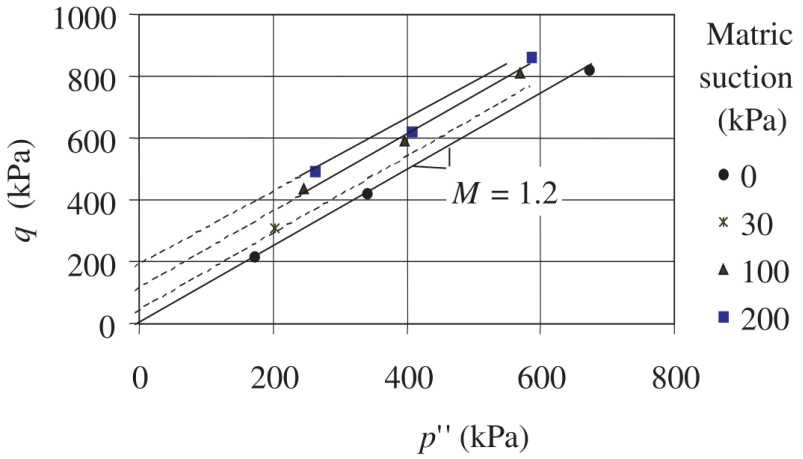

Figure 1.36: Critical State Lines (CSLs) of both saturated and unsaturated soils (Wang et al., 2002).

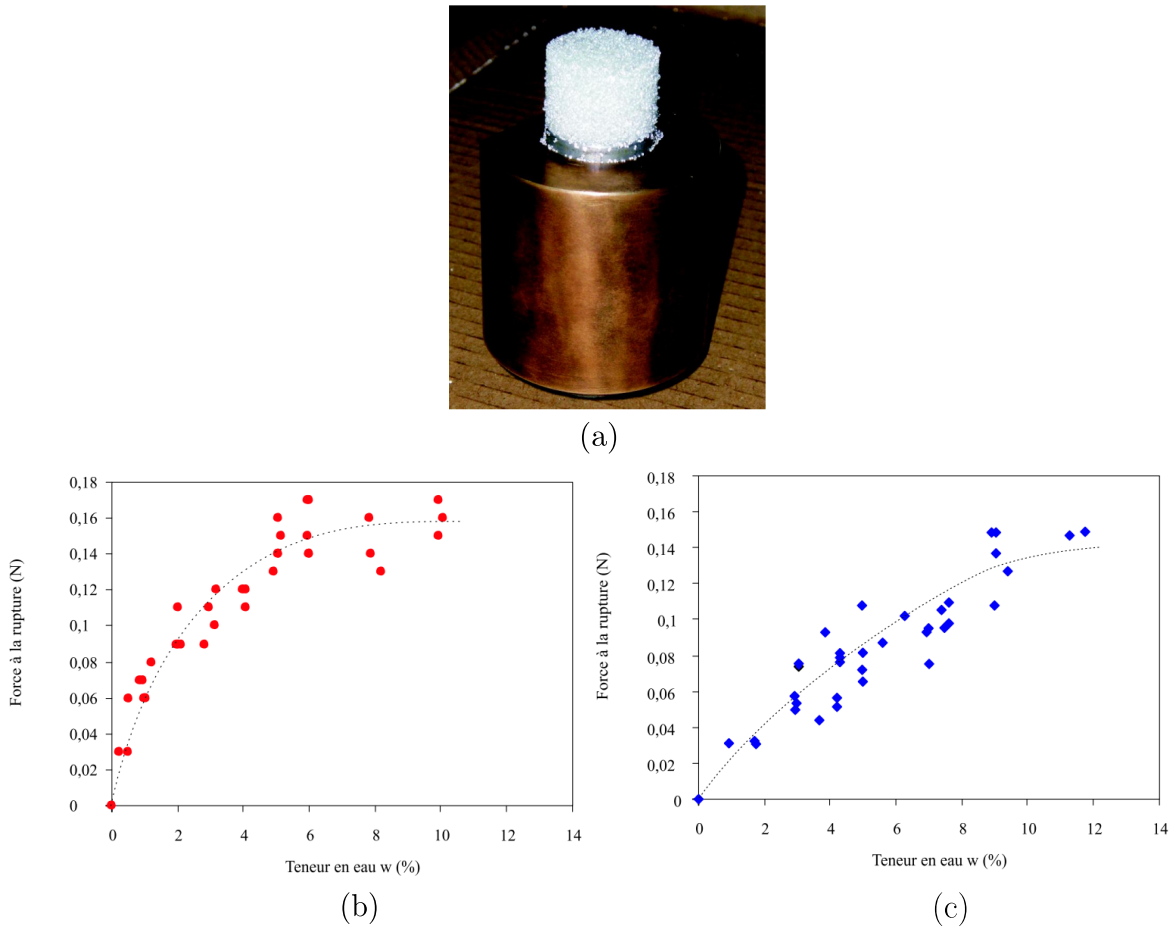

Figure 1.37: (a) A photo of the moist sample for $\omega = 3\%$ of glass beads with diameters ranging between [0.8; 1.3] mm. (b) and (c) Evolution of breaking force [N] in terms of water content ω [%] for two different ranges of diameters [0.8; 1.3] mm and [0.5; 1] mm, respectively (Soulié, 2005). *Force à la rupture* and *Teneur en eau* mean breaking force and water content, respectively.

In the same year, Richefeu (2005) carried out a simple shear test on several sandy and glass beads unsaturated samples and then plotted the Mohr-Coulomb failure in $\tau - \sigma$ plane for different types of samples and different water contents as shown in Figure (1.38). As

seen in the figure, the Mohr-Coulomb failure line shifts up as the water content increases, proving, once again, the importance of capillary bridges and forces within unsaturated soils. The only drawback of this study is the low amount of water $\omega < 5\%$.

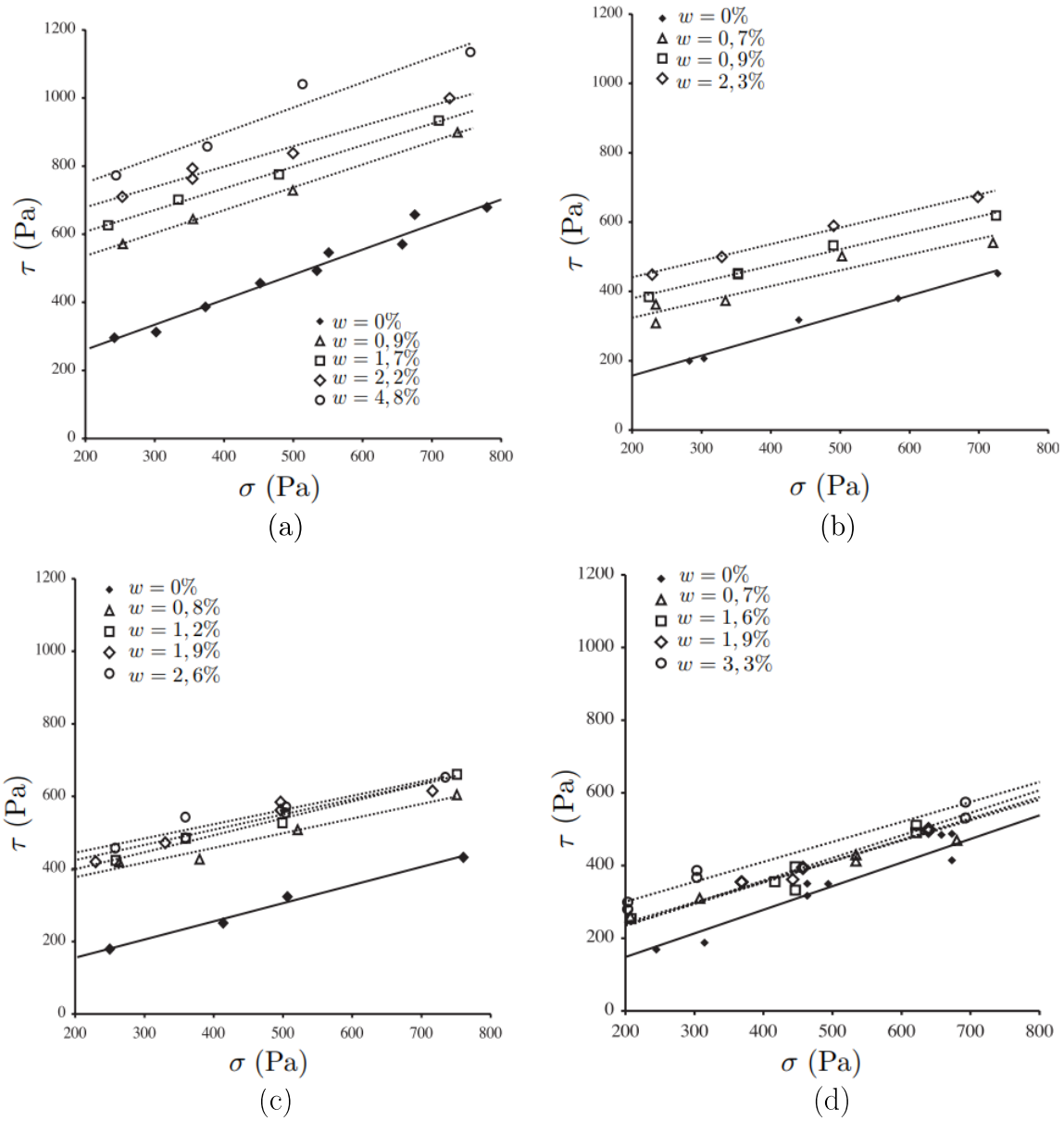

Figure 1.38: Mohr-Coulomb failure lines for different types of soils and different water contents. (a) Sandy soil. (b) and (c) poly-dispersed glass beads with diameters ranging between [0.4; 5] mm, [0.4; 8] mm. (d) Mono-dispersed glass beads of $D = 1$ mm (Richefeu, 2005).

1.7.3 Numerical studies

In the numerical framework, as seen earlier in Scholtès et al. (2009), Scholtès (2008) used DEM and incorporated capillary forces based on Eq.(1.13). Triaxial tests were conducted for a confining pressure of $\sigma^{\text{conf}} = 10$ kPa for different degrees of saturation as shown in Figure (1.39) where the deviatoric stress q [kPa]. As can be seen from the figure, the deviatoric stress q increases as the degree of saturation increases up to some point where the influence of the degree of saturation becomes nearly negligible $S_r = 10\%$. Once again, the drawback of this method is that it can only be applied to *pendular* regimes.

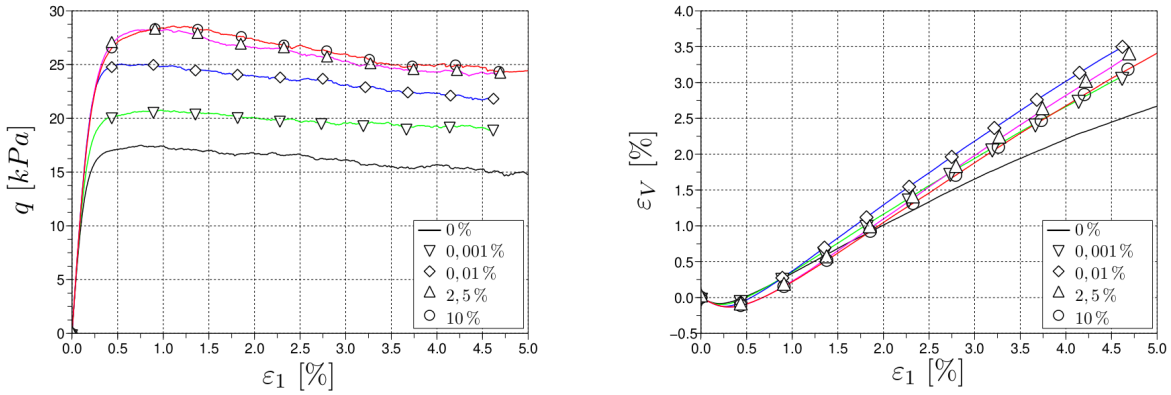

(a) (b)

Figure 1.39: Evolution of the (a) deviatoric stress q [kPa] and (b) the volumetric strain ε_v [%] in terms of the axial strain $\varepsilon_1 = \varepsilon_a$ for different degrees of saturation and for a confining pressure of $\sigma^{\text{conf}} = 10$ kPa (Scholtès, 2008).

Many other numerical models were proposed in the literature. For instance, Melnikov et al. (2016) have simulated triaxial tests for mono-dispersed unsaturated media for high values of degrees of saturation using the Contact Dynamics (CD) method to model the contacts between spherical grains, coupled with a Numerical Energy Minimization (NEM) software for accounting air-water interfaces and the associated capillary forces. They highlighted the impact of air-water capillary interfaces on the mechanical behavior of unsaturated media subjected to different water contents. However, using the NEM technique, one should select the shape of clusters (trimer, tetrahedral, heptamer, pentamer, and large) based on defined criteria (Melnikov et al., 2015). Therefore, re-meshing of clusters must be done once when they change shape. Also, Delenne et al. (2013, 2015) have used a 2D Single Component Shan-Chen LBM model along with Molecular Dynamics to investigate the ensuing apparent cohesive strength for a wide range of degrees of saturation. However, in the latter work, grain particles were fixed, supposing that capillary forces arising from the interstitial fluids are balanced by contact forces between the solid particles. In addition, Duriez and Wan (2016) have modeled unsaturated granular assemblies using DEM. Capillary bridges were incorporated in DEM calculations by numerically solving the Young-Laplace Equation (YLE) via Finite Differences to compute resulting capillary forces between pairs of grains. The authors highlighted the impact of small degrees of saturation on the mechanical response of soil subjected to triaxial tests. Finally, Liu et al. (2020b) have used a model that consists of using DEM coupled with Fabonnacci-Point Element discretization of the capillary bridge cap[4] to compute capillary forces. They were able to model capillary bridges for a wide range of degrees of saturation. Nevertheless, it is important to note that in the latter work, even though high values of degrees of saturation were reported, the coalescence of capillary bridges was not possible.

1.8 Literature Gaps and Research Motivations

The heart of the problem is that the physics of unsaturated soils lies at the pore and grain scales, which necessitates a microstructural investigation to evaluate the significance of the phases and their interactions in influencing unsaturated soil behavior. Thus, a series of analytical, numerical, and experimental studies that involved capillary actions

[4]Liquid-solid interface.

between pairs of grains and then extended to triplets were presented. One of the tenets of capillary action is the so-called capillary force, but there are challenges in its evaluation as the topology of liquid bridges evolves with the capillary regimes as volumetric water content changes in the soil. This leads to the question of how capillary action affects the strength and deformation of the unsaturated assembly and the stress partitioning in the different phases?

There are many gaps that have been identified in this literature review, but the main ones can be summarized in the following.

- The issue of the controlling stress variable that governs both the failure and deformation of unsaturated soils remains unresolved, even micromechanical studies exist in the literature where the tensorial form of the capillary stress is well-recognized.
- Current analytical and numerical macroscopic methods are efficient, but they may not be able to take into account finer aspects at the micro-scale such as the dynamics of fluid phase topology.
- Within the micromechanics framework, proposed methods are restricted to the *pendular* regime, which corresponds to very few case studies within unsaturated soils (Scholtès et al., 2009; Scholtes et al., 2009; Scholtès, 2008; Duriez and Wan, 2016, 2017; Duriez et al., 2017; Duriez and Wan, 2018).
- While several numerical studies have explored the *funicular* regime, they often rely on geometric criteria to model the merging and rupture of liquid bridges, along with the corresponding jumps and drops in capillary forces. The challenge arises from the fact that geometric criteria are typically defined for a maximum of three particles. Consequently, simulating large partially saturated media using these approaches becomes exceedingly sophisticated (Miot et al., 2021; Di Renzo et al., 2020).
- Distinctive capillary regimes can be modeled, but there are difficulties in continuously modeling the entire range of saturation levels and as such unreasonable assumptions have to be made, for instance, capillary bridges cannot merge together as is the case in Liu et al. (2020b).
- Although the kinematics of solid particles can be described numerically using a discrete element approach, on the contrary, the modeling of fluid phases and interface dynamics are not as well developed.

Based on the above, the purpose of this Ph.D. work is to develop a multi-scale numerical approach within which an unsaturated granular assembly can be modeled taking explicitly into account details of the physics of all the phases involved, including their interactions. More precisely, the micro-kinematics of the particles with the granular assembly will be coupled with the dynamics of the fluids (air and water) driven by interfacial physics as a function of external loads. The latter loads can be a combination of mechanical and hydraulic origin.

The numerical framework hinges on the Discrete Element and Lattice Boltzmann Method frameworks and their coupling. Indeed, the numerical effort touches on two major aspects. First, the traversing of the various water saturation regimes—pendular-funicular, and capillary—can be naturally modeled. Second, such modeling of the influences of the interactions of the various phases at play will naturally address the thorny issue of how unsaturated conditions affect the strength and deformation of wet granular materials or soils.

Chapter 2

Basics of Lattice Boltzmann Method for single-phase flow

2.1 Introduction

The most complicated physical problems, especially with complex geometries, are usually described by four-dimensional space-time Partially Differential Equations (PDEs), such as the Navier-Stokes Equations (NSEs). However, finding closed-form solutions to these equations is not always straightforward. Consequently, researchers have devoted a significant amount of time to numerically solving these PDEs by approximating real solutions as closely as possible. The most well-known methods for solving the NSE include, amongst others, the Finite Element Method (FEM), Finite Volume Method (FVM), and Finite Difference Method (FDM) (Zienkiewicz et al., 2013; Chung, 2002; Moukalled et al., 2016). This family of methods is known as Computational Fluid Dynamics, usually denoted as CFD, and they involve discretizing the NSE to find numerical solutions. Although these methods have shown to be effective, they have limitations, namely difficulty with irregular geometries and higher computational cost.
In contrast, the Lattice Boltzmann Method (LBM) is a computational technique employed to simulate fluid dynamics and solve complex fluid flow problems (Sukop, 2006; Timm et al., 2016). As will be shown later in this chapter, the LBM offers an alternative approach to solving the NSEs directly by solving the Boltzmann Equation that converges naturally to the NSEs. The LBM offers an important benefit by being highly parallelizable on Graphical Processing Units (GPUs). Readers may refer to Appendix B for more details about GPUs. Moreover, the LBM is known for its ease of handling complex boundary conditions.

In this chapter, a brief introduction to the Lattice Boltzmann Method (LBM) as well as the kinetic theory is presented. It will be demonstrated how the Boltzmann Equation (BE) can be solved in just two steps: (1) collision and (2) streaming. Furthermore, the convergence of the BE to the Navier-Stokes Equations (NSEs) is detailed, along with the classical boundary conditions that are employed in LBM.

2.2 Macroscale governing partial differential equations

Euler's equation must be amongst the first PDEs in the world established in 1757. It is ascribed to the Swiss mathematician and physicist *Leonhard Euler*:

$$\begin{aligned} \rho\left(\frac{\partial \boldsymbol{u}}{\partial t}+\boldsymbol{\nabla u}\cdot\boldsymbol{u}\right) &= -\boldsymbol{\nabla} p+\boldsymbol{G} \\ \boldsymbol{\nabla}\cdot\boldsymbol{u} &= 0. \end{aligned} \tag{2.1}$$

Eq. (2.1) describes the motion of non-viscous fluids—perfect incompressible fluid. Several years later, the Navier-Stokes Equations (NSE), originally established by Claude-Louis-Navier and George-Gabriel-Stokes, was formulated. It is the extension of Euler's equation for a viscous fluid which reads

$$\begin{aligned} \rho\left(\frac{\partial \boldsymbol{u}}{\partial t}+\boldsymbol{\nabla u}\cdot\boldsymbol{u}\right) &= -\boldsymbol{\nabla} p+\boldsymbol{\nabla}\cdot\left[\rho\nu\left(\boldsymbol{\nabla u}+\boldsymbol{\nabla u}^{T}\right)\right]+\boldsymbol{G} \\ \boldsymbol{\nabla}\cdot\boldsymbol{u} &= 0 \end{aligned} \tag{2.2}$$

where ρ, $\boldsymbol{u}$, p, ν, and $\boldsymbol{G}$, are density, velocity vector, pressure, kinematic viscosity, and body forces, respectively. $\boldsymbol{\nabla}\cdot$ denotes the divergence operator, also known as *nabla*.

2.3 Microscale modeling of fluids

In order to simulate a fluid at the microscale, the most popular method is the so-called Molecular Dynamics (MD). This latter studies the motion of molecules, as shown in Figure (2.1) at the microscale by solving Newton's Second Law

$$m_i \frac{\mathrm{d}\boldsymbol{v}_i}{\mathrm{d}t} = -\boldsymbol{\nabla}(U) \tag{2.3}$$

where m_i, $\boldsymbol{v}_i$, and U are the mass molecule, the microscopic velocity vector of i^{th}, and the interaction potential between molecules, respectively. The interactions between molecules are modeled through the potential U (Nijmeijer et al., 1992; Nie et al., 2004).

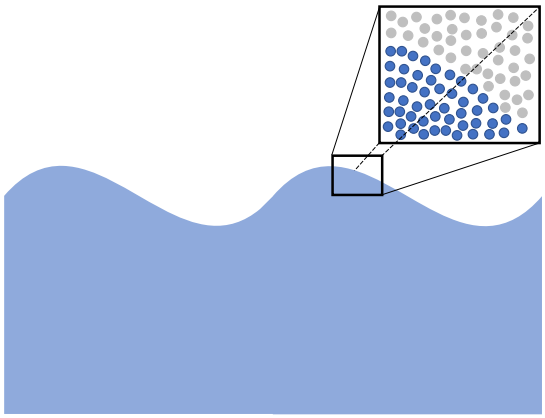

Figure 2.1: Molecular Dynamics representation. Blue particles are water molecules and the grey ones are air molecules.

Contrary to the macroscopic approaches, the MD is capable of capturing the physics occurring at the microscale. The only drawback of this approach, however, is the large amount of computational time. The following example reveals the complexity of this method. A water droplet generally weighs 0.05 grams, this is equivalent[1] to 3.10^{22} atoms in interaction. Working with a 2D simulation, every single molecule will have 2 degrees of freedom. Thus, the simulation of one single water droplet needs to consider $2 \times 3.10^{22} = 6.10^{22}$ degrees of freedom. This enormous number of degrees of freedom involved in these simulations would result in years of computation. Therefore, the MD method is definitely not a suitable candidate in the context of capillary bridges between solid particles.

To overcome this issue of computational time, and to take into account the microscopic scale effects, a solution is to use the so-called Lattice Boltzmann Method (LBM).

2.4 Mesoscale: resolution with LBM for Single-flow

Strictly speaking, the mesoscale is not a real scale as the two previously mentioned. It corresponds to the scale of the statistical models that (i) take into consideration the interactions between molecules and (ii) fill the gap between macro and micro scales in a reasonable computational time.

Before going through the LBM, several notions must be presented, such as the kinetic theory which is the fundamental idea of LBM, and the mathematical formulation of the Boltzmann Equation. But first, a brief historical perspective is given.

[1]Here, we used Avogrado's Number which is the number of atoms in 1 gram of a given material.

2.4.1 The Genesis of the Lattice Boltzmann Method

The origin of the Lattice Boltzmann Method (LBM) can be traced back to the concept of Lattice Gas Automata (LGA), which involves describing the discrete evolution of individual particles on a lattice in a boolean state (Timm et al., 2016; Frisch et al., 2019; Hardy et al., 1973; Wolf-Gladrow, 2004): particles, at a given position and time, can exist or not. The evolution of each particle is controlled by two main steps: streaming from one lattice site to another and collision with neighboring particles. However, LGA had limitations, such as an inability to accurately simulate high velocities and the presence of spurious velocities.
Several years later, McNamara and Zanetti (McNamara and Zanetti, 2019) abandoned the boolean approach and introduced the use of an average population ranging between 0 and 1 to overcome noisy results. However, this new formulation presented challenges in modeling particle collisions. To address this issue, Qian, D'Humières, and Lallemand (Qian et al., 1992) were the first to employ the single-relaxation time Bhatnagar-Gross-Krook (BGK) model to simulate collisions among the averaged particles. This innovation allowed them to recover the Navier-Stokes fluid behavior (Bhatnagar et al., 1954), giving rise to the Lattice Boltzmann Method as we know it today.
Additionally, it has been demonstrated that the Boltzmann Equation (BE) can be linked to the Navier-Stokes equation through the well-known Chapman-Enskog expansion theory (Timm et al., 2016; Chapman and Cowling, 1990).

2.4.2 Kinetic theory and statistical mechanics

The kinetic theory is a mathematical model of the fluid that postulates that molecules are always in a continuous agitation and in a ceaseless motion. Furthermore, kinetic theory, unlike MD, assumes that molecules are completely neutral[2]. Hence the molecular interactions between particles are not taken into account and only collisions between particles are considered. For an ideal fluid, the following assumptions are considered:

- a fluid is a set of elastic, identical, and rigid spheres;
- the molecules composing the fluid do not have any privileged directions when traveling;
- collisions, both between two molecules or between molecules and walls are perfectly elastic. Thus, the kinetic momentum is conserved.

Contrary to kinetic theory, statistical mechanics do not take into account every single piece of information of the particles but the averages[3] of the associated macroscopic properties through Probability Density Functions (PDFs). This latter can be seen as a representation of a particle distribution function $f(\boldsymbol{r}, \boldsymbol{\xi}, t)$ in the phase space[4], where $\boldsymbol{r} \in \{x, y, z\}$, $\boldsymbol{\xi} \in \{\xi_x, \xi_y, \xi_z\}$, and t are position, microscopic velocity, and time, respectively. The PDF $f(\boldsymbol{r}, \boldsymbol{\xi}, t)$ is the probability of finding a group of particles at the $\boldsymbol{r}$ position having a velocity $\boldsymbol{\xi}$ at time t (Timm et al., 2016).

[2]The potential U in MD models the inter-molecular interaction forces between molecules.
[3]As the number of molecules is tremendously large, the idea of averaging might be accepted.
[4]The phase space is defined as the phase containing the position and momentum coordinates.

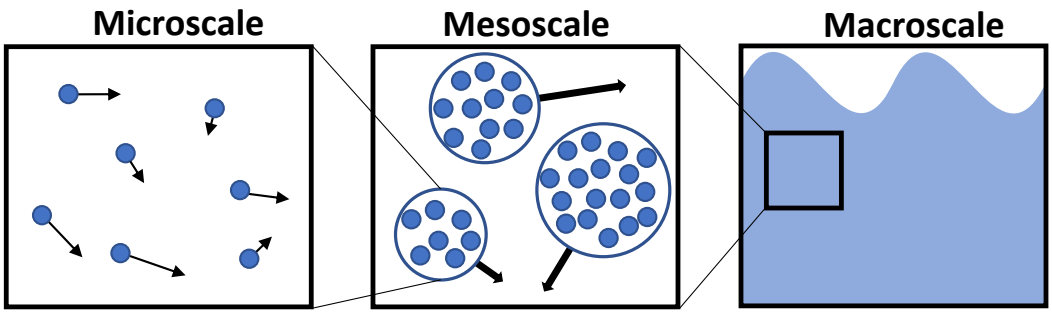

Figure 2.2: Representation of the micro, meso, and macro scales in a fluid.

By definition, the macroscopic mass density $\rho(\boldsymbol{r}, t)$ reads

$$\rho(\boldsymbol{r}, t) = \int f(\boldsymbol{r}, \boldsymbol{\xi}, t) \mathrm{d}^3\xi \tag{2.4}$$

where $\mathrm{d}^3\xi$ denotes the 3D integration in the microscopic velocity space. Eq. (2.4) indicates that the density $\rho(\boldsymbol{r}, t)$ is defined as the density for all possible microscopic velocities $\boldsymbol{\xi}$, at position $\boldsymbol{r}$ and at time t. Similarly, the momentum which depends on the macroscopic velocity $\boldsymbol{u}(\boldsymbol{r}, t)$ reads:

$$\rho(\boldsymbol{r}, t)\boldsymbol{u}(\boldsymbol{r}, t) = \int \boldsymbol{\xi} f(\boldsymbol{r}, \boldsymbol{\xi}, t) \mathrm{d}^3\xi. \tag{2.5}$$

2.4.3 Mathematical description of Boltzmann Equation

As previously described, the PDF $f(\boldsymbol{r}, \boldsymbol{\xi}, t)$ represents a certain probability of finding particles sharing, on average, the same microscopic velocities and the same position at time t. The Boltzmann Equation (BE) describes the time evolution of the aforementioned PDF. Ideally, in the absence of collisions between particles as shown in Figure 2.3(a), the evolution of $f(\boldsymbol{r}, \boldsymbol{\xi}, t)$ which is the total derivative with respect to time, reads:

$$\frac{\mathrm{d}f}{\mathrm{d}t} = 0. \tag{2.6}$$

Whereas, when collisions take place, the total derivative will not be nil anymore. The red particles shown in Figure 2.3(b) are the ones that have been dispersed due to collisions.

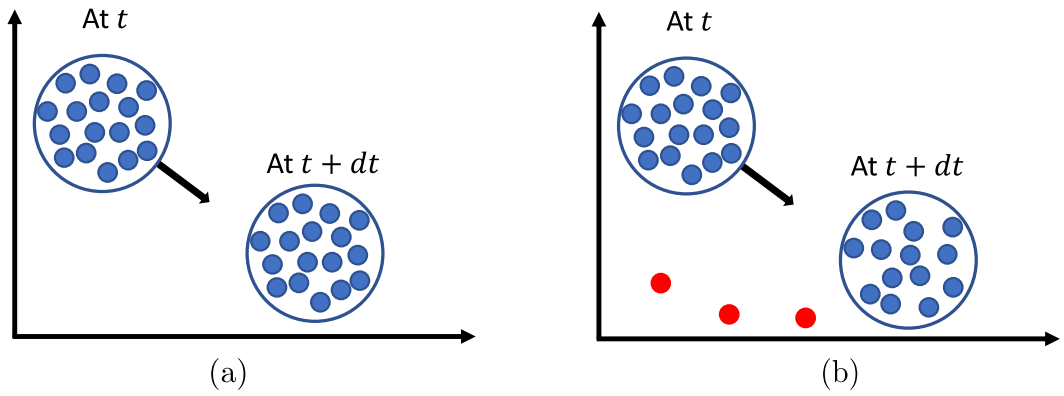

Figure 2.3: The evolution of $f(\boldsymbol{r}, \boldsymbol{\xi}, t)$ over time. (a) Without collisions and (b) with collisions between particles.

As a consequence, the change of $f(\boldsymbol{r}, \boldsymbol{\xi}, t)$ over time yields:

$$\frac{\mathrm{d}f}{\mathrm{d}t} = \overbrace{\left(\frac{\partial f}{\partial \boldsymbol{r}}\right)}^{\nabla f} \underbrace{\frac{\mathrm{d}\boldsymbol{r}}{\mathrm{d}t}}_{\boldsymbol{\xi}} + \left(\frac{\partial f}{\partial \boldsymbol{\xi}}\right) \overbrace{\frac{\mathrm{d}\boldsymbol{\xi}}{\mathrm{d}t}}^{\boldsymbol{F}/m} + \left(\frac{\partial f}{\partial t}\right) \underbrace{\frac{\mathrm{d}t}{\mathrm{d}t}}_{=1} . \tag{2.7}$$

It is worth noting that $\boldsymbol{F}$, which is the external vector forces applied to the system (Newton's second law), will be neglected for the sake of simplicity in the presentation of the method (this avoids sophisticated computations). Eq. (2.7) can be seen as a net difference of a collection of particles as seen in Figure (2.3) between two different time steps. Thus, this difference can be modeled with *Collision Operator* denoted as $\Omega(f)$ that depends on f. Therefore, Eq. (2.7) yields to the continuum free force Boltzmann Equation:

$$\underbrace{\frac{\partial f}{\partial t} + \boldsymbol{\xi} \cdot \boldsymbol{\nabla} f}_{\text{Streaming}} = \underbrace{\Omega(f)}_{\text{Collision}} . \tag{2.8}$$

Eq. (2.8) can be divided into 2 two steps. On the one hand, the L.H.S. term of the equation describes the streaming (propagation) of the particles inside the domain. On the other hand, the R.H.S. term denotes collision operator accounting for the impact between particles.

Multiple collision operator models have been proposed and used in the literature, amongst others, Multiple-Relaxation-Times (MRT) ((Timm et al., 2016; Huang et al., 2015; Fakhari and Lee, 2013; Suga et al., 2015; Yasuda et al., 2017)) or Two-Relaxation-Times TRT (Timm et al., 2016; Yan et al., 2017). But the most popular one is based on using a single relaxation time ascribed to Bhatnagar-Gross-Krook (BGK) (Zu and He, 2013; Liang et al., 2018, 2019). The mathematical description is defined as follows:

$$\Omega(f) = \frac{1}{\tau}(f^{\mathrm{eq}} - f). \tag{2.9}$$

This collision operator postulates that the distribution functions $f(\boldsymbol{r}, \boldsymbol{\xi}, t)$ evolve until they reach a certain equilibrium state f^{eq}. The speed of this evolution is controlled through the relaxation time τ when the fluid is in motion. The aforementioned equilibrium Maxwell-Boltzmann function for ideal fluids is defined as:

$$f^{\mathrm{eq}}(\rho, \boldsymbol{u}, \boldsymbol{\xi}) = \rho \left[\sqrt{\frac{1}{2\pi RT}}\right]^3 e^{-||\boldsymbol{u}-\boldsymbol{\xi}||^2/2RT}. \tag{2.10}$$

The equilibrium function represents the distribution of the microscopic velocity $\boldsymbol{\xi}$ of particles within a tank of fluid at a given temperature T moving at a macroscopic velocity $\boldsymbol{u}$, and R is the constant of ideal gases. Regardless of the chosen model, it has to obey the following conservation constraints:

$$\text{Mass Conservation:} \qquad \int \Omega(f) d\xi^3 = 0 \tag{2.11a}$$

$$\text{Momentum Conservation:} \qquad \int \boldsymbol{\xi}\Omega(f) d\xi^3 = \boldsymbol{0} \tag{2.11b}$$

$$\text{Energy conservation:} \qquad \int ||\boldsymbol{\xi}||^2 \Omega(f) d\xi^3 = 0 \tag{2.11c}$$

2.4.4 Discretization

The Boltzmann Equation possesses different variables: position vector $\boldsymbol{r}$, microscopic velocity vector $\boldsymbol{\xi}$, and time t. In this section, we show how the space velocity $\boldsymbol{\xi}$ is discretized into a finite number of discrete velocities ($\boldsymbol{\xi} \rightarrow \boldsymbol{c}_i$). Thus, to compute the moments in Eqs. (2.4) and (2.5), the integrals are transformed to sums over the microscopic velocity space $\boldsymbol{c}_i$. To do so, Harold Grad, an American mathematician, was the first to use the Hermite polynomials to approximate the equilibrium distribution function (Grad, 1949a,b; Shan et al., 2006). The coefficients of the Hermite polynomials match perfectly the moments of the Maxwellian distribution function. For more theoretical details about the Hermite polynomials, readers are invited to consult Appendix C.

2.4.4.1 Discretization of the Maxwellian function

The equilibrium function can be rewritten as follows

$$\begin{aligned} f^{\mathrm{eq}}(\rho, \boldsymbol{u}, \boldsymbol{\xi}) &= \rho \left[\sqrt{\frac{1}{2\pi RT}}\right]^3 \exp\left[-\frac{(\boldsymbol{u}-\boldsymbol{\xi})^2}{2RT}\right] \\ &= \underbrace{\frac{1}{(2\pi RT)^{3/2}} \exp\left(-\frac{\boldsymbol{\xi}^2}{2RT}\right)}_{\omega(\boldsymbol{\xi})} \underbrace{\rho \exp\left(\frac{2\boldsymbol{\xi}\boldsymbol{u}-\boldsymbol{u}^2}{2RT}\right)}_{f_T(\rho,\boldsymbol{u},\boldsymbol{\xi})} \end{aligned} \tag{2.12}$$

where $\omega(\boldsymbol{\xi})$ is the Gaussian weight function. $f_T(\rho, \boldsymbol{u}, \boldsymbol{\xi})$ can be decomposed into an infinite series of Hermite polynomials as follows

$$f_T(\rho, \boldsymbol{u}, \boldsymbol{\xi}) = \sum_{k=0}^{+\infty} \frac{\boldsymbol{b}^{\mathrm{eq},(k)}}{k!(RT)^k} \cdot \mathscr{H}^{(k)}(\boldsymbol{\xi}) \tag{2.13}$$

where the " $\cdot$ " is the generalization of scalar product[5] for k$^{\mathrm{th}}$-order tensors, $\boldsymbol{b}^{\mathrm{eq},(k)}$ are the k$^{\mathrm{th}}$-order tensor of coefficients, and $\mathscr{H}^{(k)}(\boldsymbol{\xi})$ are the k$^{\mathrm{th}}$-order tensor of Hermite polynomials which are defined as follows:

$$\mathscr{H}^{(k)}(\boldsymbol{\xi}) = (-RT)^k \frac{1}{\omega(\boldsymbol{\xi})} \boldsymbol{\nabla}^k \omega(\boldsymbol{\xi}) \tag{2.14}$$

Furthermore, the coefficients $\boldsymbol{b}^{\mathrm{eq},(k)}$ are determined based on Hermite polynomial k$^{\mathrm{th}}$ tensor:

$$\boldsymbol{b}^{\mathrm{eq},(k)} = \int f^{\mathrm{eq}}(\boldsymbol{\xi}) \mathscr{H}^{(k)}(\boldsymbol{\xi}) \mathrm{d}\xi. \tag{2.15}$$

Some tensors of $\boldsymbol{b}^{\mathrm{eq},(k)}$ and $\mathscr{H}^{(k)}(\boldsymbol{\xi})$ are shown below

$$\mathscr{H}^{(k)}(\boldsymbol{\xi}) = \begin{cases} \mathscr{H}^{(0)} & = 1, \\ \mathscr{H}_{\alpha}^{(1)} & = \xi_\alpha, \\ \mathscr{H}_{\alpha\beta}^{(2)} & = \xi_\alpha\xi_\beta - RT\delta_{\alpha\beta} \\ \mathscr{H}_{\alpha\beta\gamma}^{(3)} & = \xi_\alpha\xi_\beta\xi_\gamma - RT\left[\xi_\alpha\delta_{\beta\gamma}\right]_{\mathrm{cyc}} \\ & \vdots \end{cases} \qquad \boldsymbol{b}^{(\boldsymbol{k}),\mathrm{eq}} = \begin{cases} b^{\mathrm{eq},(0)} & = \rho, \\ b_{\alpha}^{\mathrm{eq},(1)} & = \rho u_\alpha, \\ b_{\alpha\beta}^{\mathrm{eq},(2)} & = \rho u_\alpha u_\beta \\ b_{\alpha\beta\gamma}^{\mathrm{eq},(3)} & = \rho u_\alpha u_\beta u_\gamma \\ & \vdots \end{cases} \tag{2.16}$$

[5] For tensors of order two, the " $\cdot$ " is equivalent to the double dot product ": ".

where the $[\xi_\alpha\delta_{\beta\gamma}]_{\text{cyc}} = \xi_\alpha\delta_{\beta\gamma} + \xi_\beta\delta_{\alpha\gamma} + \xi_\gamma\delta_{\alpha\beta}$.
As there is no need to compute an infinite series of polynomials to recover the equilibrium function, the Maxwellian distribution function will be truncated to the N$^{\text{th}}$ order as follows:

$$\begin{aligned} f^{\text{eq}}(\rho, \boldsymbol{u}, \boldsymbol{\xi}) &\approx \omega(\boldsymbol{\xi}) \sum_{k=0}^{N} \frac{\boldsymbol{b}^{\text{eq},(k)}}{k!(RT)^k} \cdot \mathscr{H}^{(k)}(\boldsymbol{\xi}) \\ &= \rho\omega(\boldsymbol{\xi}) \left[1 + \frac{\boldsymbol{\xi}\cdot\boldsymbol{u}}{RT} + \frac{(\boldsymbol{\xi}\cdot\boldsymbol{u})^2}{2(RT)^2} - \frac{\boldsymbol{u}\cdot\boldsymbol{u}}{2RT}\right] + \mathcal{O}(\boldsymbol{u}^2) \end{aligned} \tag{2.17}$$

where $N = 2$. Therefore the truncation stops at the 2$^{\text{nd}}$ order with respect to the macroscopic velocities $\boldsymbol{u}$.

The main objective is to compute the moments of the distribution functions, as shown in Eqs. (2.4) and (2.5), or even the n$^{\text{th}}$ order moments using the approximated equilibrium function formulated in Eq.(2.17). Therefore, the moments are approximated to

$$\int \mathcal{L}(\boldsymbol{\xi}) f^{\text{eq}}(\rho, \boldsymbol{u}, \boldsymbol{\xi}) \mathrm{d}\xi \approx \int \omega(\boldsymbol{\xi}) \overbrace{\mathcal{L}(\boldsymbol{\xi})\, \rho \left[1 + \frac{\boldsymbol{\xi}\cdot\boldsymbol{u}}{RT} + \frac{(\boldsymbol{\xi}\cdot\boldsymbol{u})^2}{2(RT)^2} - \frac{\boldsymbol{u}\cdot\boldsymbol{u}}{2RT}\right]}^{Q^M(\rho,\boldsymbol{\xi},\boldsymbol{u})} \mathrm{d}\xi \tag{2.18}$$

where $\mathcal{L}(\boldsymbol{\xi})$ is a tensor that corresponds to one of the following functions $\{1, \boldsymbol{\xi}, \boldsymbol{\xi}\otimes\boldsymbol{\xi}, ...\}$, and $Q^M(\rho, \boldsymbol{\xi}, \boldsymbol{u})$ is a M$^{\text{th}}$ order polynomial function. Eq.(2.18) will be computed in the next section by discretizing the continuum velocity space into discrete velocity vectors.

2.4.4.2 Velocity discretization

Contrary to the conventional methods, where only the space and the time are discretized, the Lattice Boltzmann Method (LBM) also introduced a discretization of the microscopic velocity space $\boldsymbol{\xi}$ into $\boldsymbol{c}_i$ as shown in Figure (2.5). In addition, all of the moments, summarized in Eq.(2.18), are integrals in the microscopic velocity space $\boldsymbol{\xi}$. It is therefore practical to transform these integrals into discretized sums for machine computation. By using the Gauss-Hermite Quadrature will be used[6] summarized in Eq. (2.18), they discretized as

$$\int \omega(\boldsymbol{\xi}) Q^M(\rho, \boldsymbol{\xi}, \boldsymbol{u}) \mathrm{d}\xi = \sum_{i=0}^{q-1} \omega_i Q^M(\rho, \boldsymbol{\xi}_i, \boldsymbol{u}) \tag{2.19}$$

where $Q^M(\rho, \boldsymbol{\xi}, \boldsymbol{u})$ is once again an M$^{\text{th}}$ order polynomial function, $q-1$ is the number of discrete microscopic velocities[7] $\boldsymbol{\xi}_i$ needed to recover the moments accurately, and ω_i are the corresponding weights which are calculated, for the k$^{\text{th}}$ of the Hermite polynomial function, as follows:

$$\omega_i = \frac{k!(RT)^k}{\left[\mathscr{H}^{(k-1)}(\boldsymbol{\xi}_i)\mathscr{H}'^{(k)}(\boldsymbol{\xi}_i)\right]}. \tag{2.20}$$

Depending on the dimensions d of the problem (1D, 2D, or 3D), the LBM discretization

[6] This method is quite practical in the context of the LBM because the Maxwellian distribution is already a Gaussian function.

[7] The $\boldsymbol{\xi}_i$ are the solutions of the Hermite polynomials $\mathscr{H}^n(\boldsymbol{\xi}_i) = 0$.

is given by a scheme of DdQq and q is the number of discretized vectors used $\boldsymbol{c}_i$. In order to understand the basic idea of this scheme, a D1Q3 is considered[8]. For this 1D case, a particle has 3 choices over a one-time increment. To determine the discretized velocities ξ_i, $\mathscr{H}^{(3)} = 0$ is solved using Eq.(2.16):

$$\mathscr{H}^{(3)} = 0 \rightarrow \xi^3 - 3RT\xi = 0 \rightarrow \xi_i = \begin{cases} \xi_0 = 0 \\ \xi_1 = \sqrt{3RT} \\ \xi_2 = -\sqrt{3RT} \end{cases} . \tag{2.21}$$

These discretized velocities are used to determine the corresponding weights using Eq.(2.20):

$$\begin{aligned} \omega_0 &= \frac{2(RT)^2}{(-3RT)(-RT)} = \frac{2}{3} \\ \omega_1 &= \frac{2(RT)^2}{(2RT)(6RT)} = \frac{1}{6} \\ \omega_2 &= \frac{2(RT)^2}{(2RT)(6RT)} = \frac{1}{6} \end{aligned} \tag{2.22}$$

The vectors $\boldsymbol{\xi}_i$ point to the neighbor nodes, it is therefore practical to consider that the mesh size in the lattice units (lu) is equal to unity ($\Delta x = 1$ lu). Once the space discretization re-scaling is completed, the discretized velocity vectors must also undergo re-scaling as follows:

$$\xi_i = \begin{cases} \xi_0 = 0 \\ \xi_1 = \sqrt{3RT} \\ \xi_2 = -\sqrt{3RT} \end{cases} \Longrightarrow c_i = \xi|_{RT=\frac{1}{3}} \begin{cases} c_0 = 0 \\ c_1 = 1 \\ c_2 = -1 \end{cases} \tag{2.23}$$

Moreover, since the term $\sqrt{3RT}$ consistently appears in Eq. (2.21), supposing $RT = 1/3$ allows us to non-dimensionalize[9] the microscopic velocities ξ_i to become c_i as depicted in Figure (2.4).

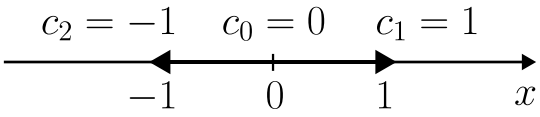

Figure 2.4: Illustration of the D1Q3 scheme.

The same procedure can be employed in 2D and 3D problems, such as in D2Q9, D3Q15, and D3Q19 discretization. The velocity discretization means that the *artificial molecules*[10] live in meshing nodes and are allowed to move only in certain directions. For instance, in the D2Q9 scheme, the molecules are free to move only in 9 directions instead of a continuum range of directions. Same for the D3Q19 scheme in which the particles can only move in the indicated 19 directions in 3D conditions as shown in Figure (2.6).

[8] The same procedure for higher discretization schemes is valid as well, e.g., D2Q9 and D3Q19.

[9] In the D1Q3 scheme example, the $\sqrt{3RT}$ is a common term. It must be pointed out that this is not always the case in all schemes, amongst others, D1Q5, D1Q7, and D3Q39 (Krueger et al., 2016).

[10] This term was used here to indicate that molecules are described using the distribution functions.

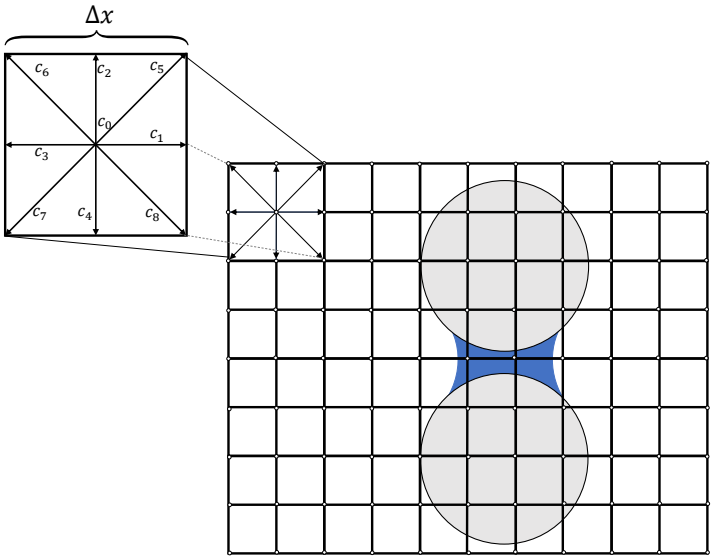

Figure 2.5: Illustration of the D2Q9 scheme.

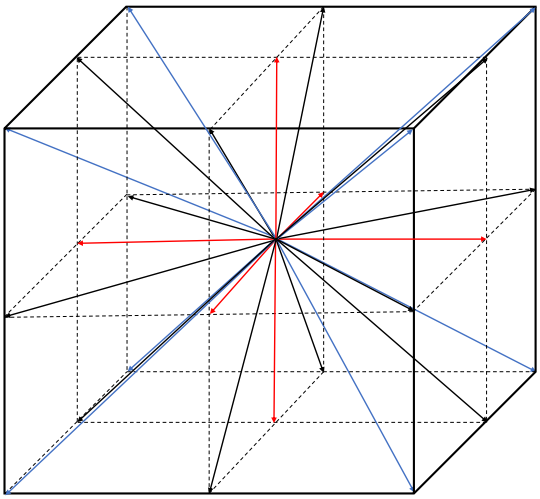

Figure 2.6: Illustration of the D3Q19 scheme for one voxel (cubical mesh in 3D).

A quick recall of thermodynamics reminds us that the isothermal speed of sound, denoted as c_s, is defined as:

$$c_s = \sqrt{\left.\frac{\partial P}{\partial \rho}\right|_T} = \sqrt{RT}. \tag{2.24}$$

In Eq. (2.24) P is the pressure and ρ is the density. Therefore, we deduce that the speed of sound in the lattice units for D2Q9 and D3Q19 is defined $c_s = \frac{1}{\sqrt{3}}$. It must be pointed out that discrete velocities are now expressed in lattice units (lu) which is one of the specificities of the LB method. Particular attention will be given to the conversation between lattice and physical units in Chapter 3, Section 3.6.

The discrete velocities associated with D2Q9 and D3Q19 that will be used in this

Ph.D. work are defined as follows:

$$\text{D2Q9: } \boldsymbol{c}_i \begin{cases} (0,0) & i \in \{0\} \\ (\pm 1,0),(0,\pm 1) & i \in \{1,\ldots,4\} \\ (\pm 1,1),(1,\pm 1) & i \in \{5,\ldots,8\} \end{cases} \tag{2.25}$$

$$\text{D3Q19: } \boldsymbol{c}_i \begin{cases} (0,0,0) & i \in \{0\} \\ (\pm 1,0,0),(0,\pm 1,0),(0,0,\pm 1) & i \in \{1,\ldots,6\} \\ (\pm 1,\pm 1,0),(\pm 1,0,\pm 1)(0,\pm 1,\pm 1) & i \in \{7,\ldots,18\} \end{cases} \tag{2.26}$$

The corresponding weights are $w_0 = 4/9$, $w_{1-4} = 1/9$ and $w_{5-8} = 1/36$ in 2D and $w_0 = 4/9$, $w_{1-4} = 1/9$ and $w_{5-8} = 1/36$ in 3D. The discretized velocities along with the weights have to obey the rotational isotropy condition of the lattice which leads to (Timm et al., 2016)

$$\sum_i \omega_i = 1; \tag{2.27a}$$

$$\sum_i \omega_i c_{i\alpha} = 0; \tag{2.27b}$$

$$\sum_i \omega_i c_{i\alpha} c_{i\beta} = c_s^2 \delta_{\alpha\beta}; \tag{2.27c}$$

$$\sum_i \omega_i c_{i\alpha} c_{i\beta} c_{i\gamma} = 0; \tag{2.27d}$$

$$\sum_i \omega_i c_{i\alpha} c_{i\beta} c_{i\gamma} c_{i\theta} = c_s^4 \left(\delta_{\alpha\beta}\delta_{\gamma\theta} + \delta_{\alpha\gamma}\delta_{\beta\theta} + \delta_{\alpha\theta}\delta_{\beta\gamma}\right); \tag{2.27e}$$

$$\sum_i \omega_i c_{i\alpha} c_{i\beta} c_{i\gamma} c_{i\theta} c_{i\lambda} = 0 \tag{2.27f}$$

where α, β, γ, θ, λ are indices indicating the components of vectors c_i and $\delta_{\alpha\beta}$ is the identity Kronecker delta. Finally, the continuous Maxwellian distribution in Eq. (2.17) is discretized in D2Q9 and D3Q19 to become

$$\begin{aligned} f_i^{\text{eq}} &= \omega_i \rho \left[1 + \frac{\boldsymbol{c}_i.\boldsymbol{u}}{c_s^2} + \frac{1}{2}\frac{(\boldsymbol{c}_i.\boldsymbol{u})^2}{c_s^4} - \frac{1}{2}\frac{\boldsymbol{u}\cdot\boldsymbol{u}}{c_s^2}\right] \\ &= \omega_i \rho \left[1 + 3\,\boldsymbol{c}_i.\boldsymbol{u} + \frac{9}{2}(\boldsymbol{c}_i\cdot\boldsymbol{u})^2 - \frac{3}{2}(\boldsymbol{u}.\boldsymbol{u})\right] \end{aligned} \tag{2.28}$$

The equilibrium function f_i^{eq} must be such that its moments are the same as those of f_i. Finally, after discretizing the velocity space, and according to Eqs. (2.27), (2.11a), and (2.11b), Eqs. (2.4) and (2.5) can be approximated as follows (see Appendix D.1 for more details):

$$\rho \approx \sum_{i=0}^{q-1} f_i = \sum_{i=0}^{q-1} f_i^{\text{eq}} \tag{2.29a}$$

$$\rho \boldsymbol{u} \approx \sum_{i=0}^{q-1} f_i \boldsymbol{c}_i = \sum_{i=0}^{q-1} f_i^{\text{eq}} \boldsymbol{c}_i. \tag{2.29b}$$

2.4.4.3 Discretization of the Boltzmann Equation

As previously seen, two steps are required, collision and streaming. The continuum Boltzmann Equation will be divided into two main steps:

$$\text{Collision: } \tilde{f}_i(\boldsymbol{r},t) = f_i(\boldsymbol{r},t) - \frac{\Delta t}{\tau}\left[f_i(\boldsymbol{r},t) - f_i^{\text{eq}}(\boldsymbol{r},t)\right] \tag{2.30}$$

$$\text{Streaming: } f_i(\boldsymbol{r}+\boldsymbol{c}_i\Delta t, t+\Delta t) = \tilde{f}_i(\boldsymbol{r},t) \tag{2.31}$$

In a nutshell, the LBM algorithm consists of:

- computing the $\tilde{f}_i(\boldsymbol{r},t)$ using Eq. (2.30) on each single node of the grid to represent the shocks and collisions between molecules as presented in Figure 2.9(a)
- spreading the post-collide distribution functions $\tilde{f}_i(\boldsymbol{r},t)$ to the neighboring nodes as can be seen in Figure 2.9(b).

The advantage of the collision step is its locality which makes the LBM amenable to parallelization, especially on Graphical Processing Units (GPUs) which is briefly introduced in Appendix B.

2.4.5 Boundary conditions

Like any other PDE, the Boltzmann Equation should have boundary conditions in order to respect the uniqueness of the solution. LBM possesses its own boundary conditions to handle the edges of the domain. Contrary to macroscopic approaches, the LBM merely works with PDFs $f(\boldsymbol{r},\boldsymbol{\xi},t)$ at the mesoscale. There exist various mesoscale BCs in the literature, amongst them, only two will be elaborated—Periodic and Bounce-Back boundary conditions.

2.4.5.1 Periodic boundary conditions

Technically speaking, it is absolutely impossible to simulate an infinite domain using computers due to their capacity. Thus, an *ad hoc* solution is the *Periodic Boundary Condition*. This latter consists in supposing that any flow leaving a side, will re-enter the other parallel side. The LBM formulation as shown in Figure (2.7) yields to:

$$f_i(\boldsymbol{r}+\boldsymbol{\ell},t) = f_i(\boldsymbol{r},t). \tag{2.32}$$

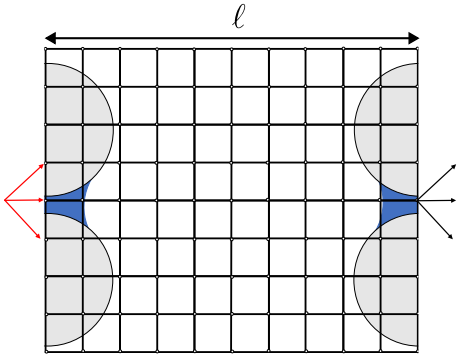

Figure 2.7: Periodic condition applied on the left and the right edges in the x-axis direction.

2.4.5.2 Bounce-Back Boundary Condition

When the fluid is in contact with an obstacle, e.g. walls or sphere solids, the distribution functions $f(\boldsymbol{r_b}, \boldsymbol{\xi}, t)$ of boundary nodes pointing to these obstacles $\boldsymbol{r_s}$ will be reflected back to the node where they came from as shown in Figure (2.8). This is the so-called

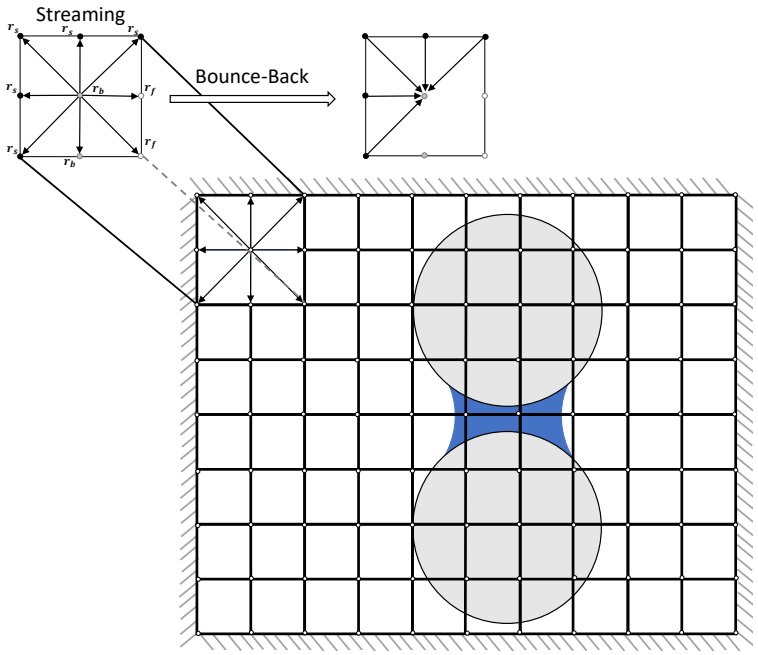

Figure 2.8: Bounce Back boundary condition

non-slip boundary condition applied at all boundary nodes $\boldsymbol{r_b}$. This method guarantees that the macroscopic velocity $\boldsymbol{u}$ at the obstacle is nil. There exist numerous methods for applying the non-slip boundary condition, amongst them, *Half-way Bounce-Back* scheme, used in this thesis, which has a second-order accuracy according to (Zou and He, 1997). The LBM formulation of this approach is:

$$f_{\bar{i}}(\boldsymbol{r}_b, t + \Delta t) = \tilde{f}_i(\boldsymbol{r}_b, t) \tag{2.33}$$

where $\bar{i}$ stands for the opposite direction of i, $\tilde{f}_i$ are the post-collision distribution functions. An illustration of the Bounce-Back scheme can be found in Figure (2.8). Readers may refer to (Timm et al. (2016); Mohamad (2011); Guo and Shu (2013); Sukop (2006)) for more details about LBM boundary conditions.

2.5 Chapman-Enskog expansion

Up to this point, we have provided a brief introduction to kinetic theory and statistical mechanics, presenting how Probability Density Functions (PDFs) are related to the macro-variables, density, and velocity for instance. The Boltzmann equation was next presented as the governing equation that studies the evolution of these PDFs. Additionally, we have offered a concise overview of the discretization of the Boltzmann equation and the velocity space. However, a fundamental question arises: How can we establish a connection between the Boltzmann equation and the governing equations at the macroscopic scale? The solution to this question lies in the application of the Chapman-Enskog expansion. This method, based on a multiscale approach, allows us to systematically derive the macroscale equations that we aim to solve, Navier-Stokes equations for instance.

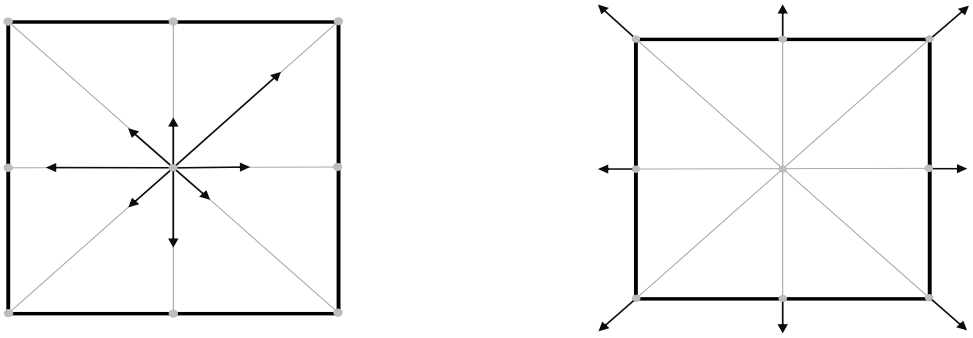

(a) (b)

Figure 2.9: (a) Collision and (b) streaming steps to solve the BE in 2D.

2.5.1 From Boltzmann Equation to Euler Equation

If we suppose that the fluid is at equilibrium at some point, it implies that the PDFs $f(\boldsymbol{r}, \boldsymbol{\xi}, t)$ are equal to f^{eq}. Within the BGK collision model, if we replace $f(\boldsymbol{r}, \boldsymbol{\xi}, t)$ by f^{eq} ($\Omega(f) = 0$) in the BE, cf. Eq. (2.8), it leads to:

$$\frac{\partial f^{\text{eq}}}{\partial t} + \boldsymbol{\xi} \cdot \boldsymbol{\nabla} f^{\text{eq}} = 0. \tag{2.34}$$

By integrating Eq. (2.34) in the microscopic velocity space, the equation becomes:

$$\frac{\partial}{\partial t} \int f^{\text{eq}} \mathrm{d}\xi^3 + \boldsymbol{\nabla} \cdot \int \boldsymbol{\xi} f^{\text{eq}} \mathrm{d}\xi^3 = 0. \tag{2.35}$$

According to Eqs. (2.4) and (2.5), one finds:

$$\frac{\partial \rho}{\partial t} + \boldsymbol{\nabla} \cdot (\rho \boldsymbol{u}) = 0. \tag{2.36}$$

The mass conservation principle is retrieved via BE.
Next, multiplying Eq. (2.34) by $\boldsymbol{\xi}$, the equation becomes:

$$\frac{\partial}{\partial t} \int \boldsymbol{\xi} f^{\text{eq}} \mathrm{d}\xi^3 + \boldsymbol{\nabla} \cdot \int (\boldsymbol{\xi} \otimes \boldsymbol{\xi}) f^{\text{eq}} \mathrm{d}\xi^3 = 0. \tag{2.37}$$

Likewise, Eq. (2.37) becomes

$$\frac{\partial}{\partial t}(\rho \boldsymbol{u}) + \boldsymbol{\nabla} \cdot \boldsymbol{\Pi} = \boldsymbol{0} \tag{2.38}$$

where $\boldsymbol{\Pi}$ is a second-order tensor. By identification, if one considers that $\boldsymbol{\Pi} = p\boldsymbol{I} + \rho \boldsymbol{u} \otimes \boldsymbol{u}$, where $\boldsymbol{I}$ is the identity matrix in $\mathbb{R}^3$, Eq. (2.38) eventually becomes

$$\frac{\partial}{\partial t}(\rho \boldsymbol{u}) + \boldsymbol{\nabla} \cdot (\rho \boldsymbol{u} \otimes \boldsymbol{u}) = -\boldsymbol{\nabla} p. \tag{2.39}$$

that corresponds to the Euler equation for non-viscous fluids while supposing that no collisions are considered between molecules $\Omega(f) = 0$.

In order to retrieve the NSE, one must employ the Chapman-Enskog expansion while supposing a non-equilibrium state $\Omega(f) \neq 0$, which will be explained in the next section.

2.5.2 From BE to Navier-Stokes Equations

After discretizing the LBE equation to the velocity space, a detailed analysis of retrieving the Navier-Stokes will be explained. We have previously proved that the Maxwellian distribution $f_i = f_i^{\text{eq}}$ is capable of retrieving the Euler equation. Knowing a particular solution of the LBE, a more general solution can be deduced using the perturbation method[11]. In the expansions that will come after, the vector $\boldsymbol{c}_i$ is replaced by $c_{i\alpha}$ and $\boldsymbol{r}$ by x_α where α corresponds to the components of vectors, for the sake of simplicity. Indeed, the probability density function $f(\boldsymbol{r}, \boldsymbol{c}, t)$ can be expanded as follows[12] (Timm et al., 2016; Huang et al., 2015)

$$f_i = \underbrace{f_i^{\text{eq}}}_{\text{equilibrium term}} + \overbrace{\varepsilon f_i^{(1)} + \varepsilon^2 f_i^{(2)} + \ldots}^{\text{non-equilibrium term}} = f_i^{\text{eq}} + f^{\text{neq}} \tag{2.40}$$

where ε is a small parameter relation to the Knudsen number Kn. The sum of Eq. (2.40) gives

$$\sum_i f_i = \sum_i f_i^{\text{eq}} + \varepsilon \sum_i f_i^{(1)} + \varepsilon^2 \sum_i f_i^{(2)} + \ldots \tag{2.41}$$

Since $\sum_i f_i = \sum_i f_i^{\text{eq}} = \rho$, Eq. (2.41) becomes:

$$\varepsilon \sum_i f_i^{(1)} + \varepsilon^2 \sum_i f_i^{(2)} + \cdots = 0 \tag{2.42}$$

Similarly, Eq. (2.40) is multiplied by $c_{i\alpha}$ and then summed, yields:

$$\sum_i f_i c_{i\alpha} = \sum_i f_i^{\text{eq}} c_{i\alpha} + \varepsilon \sum_i f_i^{(1)} c_{i\alpha} + \varepsilon^2 \sum_i f_i^{(2)} c_{i\alpha} + \ldots \tag{2.43}$$

with $\alpha \in \{x, y, z\}$. Furthermore, since $\sum_i f_i c_{i\alpha} = \sum_i f_i^{\text{eq}} c_{i\alpha} = \rho u_\alpha$, Eq. (2.43) yields to:

$$\varepsilon \sum_i f_i^{(1)} c_{i\alpha} + \varepsilon^2 \sum_i f_i^{(2)} c_{i\alpha} + \cdots = 0 \tag{2.44}$$

Therefore, after an identification with respect to ε for both Eqs. (2.42) and (2.44), it can be deduced that:

$$\sum_i f_i^{(k)} = 0 \qquad \& \qquad \sum_n c_i f_i^{(k)} = 0 \text{ for } k \geq 1 \tag{2.45}$$

The two relations in Eq. (2.45) are tremendously important for the rest of the Chapman-Enskog analysis.

It is worth mentioning that the Navier-Stokes equation possesses advection as well as diffusion terms which evolve on different time scales. It is, therefore, useful to decompose

[11] This technique is based on finding a solution E_λ of an equation E if a particular solution E_0 is known (when $\lambda = 0$).

[12] We could have used $f_i^{(0)}$ instead of f_i^{eq}. And, by identification we would find $f_i^{(0)} = f_i^{eq}$.

the derivative with respect to time into two-time scales in order to retrieve the Navier-Stokes equation. Basically, the diffusion process is slower than the advection, thus one can consider that:

$$\frac{\partial}{\partial t} = \underbrace{\varepsilon \frac{\partial}{\partial t_1}}_{\text{Advection}} + \overbrace{\varepsilon^2 \frac{\partial}{\partial t_2}}^{\text{Diffusion}} . \tag{2.46}$$

Regarding the gradient, only one space scale is sufficient to retrieve NSE:

$$\frac{\partial}{\partial x_\alpha} = \varepsilon \frac{\partial}{\partial x_{\alpha_1}}. \tag{2.47}$$

The Navier-Stokes equations will be recovered by identification of the terms of the expansion used in Eq. (2.40). The first step consists in using the discretized LBE derived from Eq. (2.30):

$$f_i(\boldsymbol{r} + \boldsymbol{c}_i \Delta t, t + \Delta t) - f_i(\boldsymbol{r}, t) = -\frac{\Delta t}{\tau} \left[f_i(\boldsymbol{r}, t) - f_i^{\text{eq}}(\boldsymbol{r}, t) \right]. \tag{2.48}$$

Next, a Taylor expansion of the previous equation to the second order $\mathcal{O}(\Delta t^2)$ is carried out:

$$\begin{aligned} \Delta t \left(\frac{\partial}{\partial t} + c_{i\alpha} \frac{\partial}{\partial x_\alpha} \right) f_i + \frac{\Delta t^2}{2} \left(\frac{\partial}{\partial t} + c_{i\alpha} \frac{\partial}{\partial x_\alpha} \right)^2 f_i \\ + \mathcal{O}(\Delta t^3) = -\frac{\Delta t}{\tau} f_i^{\text{neq}}. \end{aligned} \tag{2.49}$$

Then, multiplying Eq. (2.49) by $\frac{\Delta t}{2} \left(\frac{\partial}{\partial t} + c_{i\alpha} \frac{\partial}{\partial x_\alpha} \right)$ we find:

$$\begin{aligned} \frac{\Delta t^2}{2} \left(\frac{\partial}{\partial t} + c_{i\alpha} \frac{\partial}{\partial x_\alpha} \right)^2 f_i + \overbrace{\frac{\Delta t^3}{4} \left(\frac{\partial}{\partial t} + c_{i\alpha} \frac{\partial}{\partial x_\alpha} \right)^3 f_i}^{\text{Neglected to } \mathcal{O}(\Delta t^2)} \\ = -\frac{\Delta t}{2\tau} f_i^{\text{neq}} \left(\frac{\partial}{\partial t} + c_{i\alpha} \frac{\partial}{\partial x_\alpha} \right) \end{aligned} \tag{2.50}$$

The second term of the R.H.S of Eq. (2.50) can be neglected since we are only interested in terms of the second order $\mathcal{O}(\Delta t^2)$. Then, by subtracting Eq. (2.50) from Eq. (2.49), one obtains:

$$\boxed{\Delta t \left(\frac{\partial}{\partial t} + c_{i\alpha} \frac{\partial}{\partial x_\alpha} \right) f_i = -\frac{\Delta t}{\tau} f_i^{\text{neq}} + \frac{\Delta t^2}{2\tau} \left(\frac{\partial}{\partial t} + c_{i\alpha} \frac{\partial}{\partial x_\alpha} \right) f_i^{\text{neq}}.} \tag{2.51}$$

Replacing Eqs. (2.46) and (2.47) into (2.51), and using Eq. (2.40) yields to:

$$\begin{aligned} \Delta t \left(\varepsilon \frac{\partial}{\partial t_1} + \varepsilon^2 \frac{\partial}{\partial t_2} + \varepsilon c_{i\alpha} \frac{\partial}{\partial x_{\alpha 1}} \right) (f_i^{\text{eq}} + \varepsilon f_i^{(1)} + \varepsilon^2 f_i^{(2)} + ...) \\ = -\frac{\Delta t}{\tau} (\varepsilon f_i^{(1)} + \varepsilon^2 f_i^{(2)} + ...) + \\ \frac{\Delta t^2}{2\tau} \left(\varepsilon \frac{\partial}{\partial t_1} + \varepsilon^2 \frac{\partial}{\partial t_2} + \varepsilon c_{i\alpha} \frac{\partial}{\partial x_{\alpha 1}} \right) (\varepsilon f_i^{(1)} + \varepsilon^2 f_i^{(2)} + ...). \end{aligned} \tag{2.52}$$

An identification of the terms in ε and ε^2 in Eq.(2.52)

$$\mathcal{O}(\varepsilon^1) : \left(\frac{\partial}{\partial t_1} + c_{i\alpha}\frac{\partial}{\partial x_{\alpha 1}}\right) f_i^{\mathrm{eq}} = -\frac{1}{\tau} f_i^{(1)} \tag{2.53a}$$

$$\mathcal{O}(\varepsilon^2) : \frac{\partial f_i^{\mathrm{eq}}}{\partial t_2} + \left(\frac{\partial}{\partial t_1} + c_{i\alpha}\frac{\partial}{\partial x_{\alpha 1}}\right)\left(1 - \frac{\Delta t}{2\tau}\right) f_i^{(1)} = -\frac{1}{\tau} f_i^{(2)} \tag{2.53b}$$

In order to retrieve the NSE, the sum of Eq. (2.53b) and the sum of Eq. (2.53b) multiplied by $c_{i\beta}$ are calculated

$$\frac{\partial \rho}{\partial t_2} = -\frac{1}{\tau}\sum f_i^{(2)} = 0 \tag{2.54a}$$

$$\frac{\partial \rho u_\alpha}{\partial t_2} + \frac{\partial}{\partial x_{\beta_1}}\left(1 - \frac{\Delta t}{2\tau}\right)\Pi_{\alpha\beta}^{(1)} = -\frac{1}{\tau}\sum c_{i\beta} f_i^{(2)} = 0 \tag{2.54b}$$

according to Eq. (2.45). In Eq. (2.54b) the term $\Pi_{\alpha\beta}^{(1)}$ is an unknown for now. In the same way, the sum of Eq. (2.53a) gives:

$$\frac{\partial \rho}{\partial t_1} + \frac{\partial(\rho u_\alpha)}{\partial x_{\alpha 1}} = -\frac{1}{\tau}\sum f_i^{(1)} = 0. \tag{2.55}$$

according to Eq. (2.45) as well. To determine the term $\Pi_{\alpha\beta}^{(1)}$, Eq. (2.53a) is multiplied by $c_{i\beta}c_{i\gamma}$, and summed over i to get

$$\frac{\partial(\Pi_{\alpha\beta}^{\mathrm{eq}})}{\partial t_1} + \frac{\partial(\Pi_{\alpha\beta\gamma}^{\mathrm{eq}})}{\partial x_{\gamma_1}} = -\frac{1}{\tau}\Pi_{\alpha\beta}^{(1)} \tag{2.56}$$

Then, $\Pi_{\alpha\beta}^{\mathrm{eq}}$ and $\Pi_{\alpha\beta\gamma}^{\mathrm{eq}}$ are determined *via* both Eqs. (2.27) and (2.28):

$$\Pi_{\alpha\beta}^{\mathrm{eq}} = \sum_i c_{i\alpha}c_{i\beta}f_i^{\mathrm{eq}} = \rho u_\alpha u_\beta + \rho c_s^2 \delta_{\alpha\beta} \tag{2.57a}$$

$$\Pi_{\alpha\beta\gamma}^{\mathrm{eq}} = \sum_i c_{i\alpha}c_{i\beta}c_{i\gamma}f_i^{\mathrm{eq}} = \rho c_s^2(u_\alpha\delta_{\beta\gamma} + u_\beta\delta_{\alpha\gamma} + u_\gamma\delta_{\alpha\beta}) \tag{2.57b}$$

Using Eqs. (2.57a) and (2.57b) and conducting some mathematical manipulations, the expression for $\Pi_{\alpha\beta}^{(1)}$ eventually becomes:

$$\Pi_{\alpha\beta}^{(1)} = \sum_i c_{i\alpha}c_{i\beta}f_i^{(1)} = \underbrace{-\rho c_s^2\tau\left(\frac{\partial u_\alpha}{\partial x_{\beta_1}} + \frac{\partial u_\beta}{\partial x_{\alpha_1}}\right)}_{\text{viscous stress tensor}} + \underbrace{\tau\frac{\partial}{\partial x_{\gamma 1}}(\rho u_\alpha u_\beta u_\gamma)}_{\text{Error term}}. \tag{2.58}$$

The last step is to assemble the different time and space scales in such a way that we recover Navier-Stokes Equations. To do so, the following steps must be considered:

- Eq. (2.55) is multiplied by ε and summed with Eq. (2.54a) multiplied by ε^2 gives Eq. (2.59a) and
- Eq. (2.55) is multiplied by ε and summed with Eq. (2.54b) multiplied by ε^2 gives Eq. (2.59b)

$$\underbrace{\left(\varepsilon\frac{\partial}{\partial t_1}+\varepsilon^2\frac{\partial}{\partial t_2}\right)}_{\frac{\partial}{\partial t}}\rho+\overbrace{\varepsilon\frac{\partial}{\partial x_{\alpha_1}}}^{\frac{\partial}{\partial x_\alpha}}(\rho u_\alpha)=0 \tag{2.59a}$$

$$\underbrace{\left(\varepsilon\frac{\partial}{\partial t_1}+\varepsilon^2\frac{\partial}{\partial t_2}\right)}_{\frac{\partial}{\partial t}}(\rho u_\alpha)+\varepsilon\frac{\partial}{\partial x_{\beta_1}}\Pi^{\mathrm{eq}}_{\alpha\beta}=-\varepsilon^2\frac{\partial}{\partial x_{\beta_1}}\left(1-\frac{\Delta t}{2\tau}\right)\Pi^{(1)}_{\alpha\beta} \tag{2.59b}$$

After substituting each term with its appropriate expression, Eqs. (2.59a) and (2.59b) ultimately become

$$\begin{aligned}\frac{\partial(\rho u_\alpha)}{\partial t}+\overbrace{\varepsilon\frac{\partial}{\partial x_{\beta_1}}}^{\frac{\partial}{\partial x_\beta}}(\rho u_\alpha u_\beta)+\overbrace{\varepsilon\frac{\partial}{\partial x_{\beta_1}}}^{\frac{\partial}{\partial x_\beta}}(\rho c_s^2\delta_{\alpha\beta})=-\overbrace{\varepsilon\frac{\partial}{\partial x_{\beta_1}}}^{\frac{\partial}{\partial x_\beta}}\left(1-\frac{\Delta t}{2\tau}\right)\\ \left[-\rho c_s^2\tau\underbrace{\varepsilon\frac{\partial}{\partial x_{\beta_1}}}_{\frac{\partial}{\partial x_\beta}}(u_\alpha)+\tau\underbrace{\varepsilon\frac{\partial}{\partial x_{\gamma_1}}}_{\frac{\partial}{\partial x_\gamma}}(\rho u_\alpha u_\beta u_\gamma)\right]\end{aligned} \tag{2.60}$$

To retrieve the Navier-Stokes equations by identification:

$$\text{Pressure: } p=\rho c_s^2 \tag{2.61a}$$

$$\text{Kinematic viscosity: } \nu=c_s^2\left(\tau-\frac{\Delta t}{2}\right) \tag{2.61b}$$

$$\frac{\partial\rho}{\partial t}+\frac{\partial\rho u_\alpha}{\partial x_\alpha}=0 \tag{2.62a}$$

$$\begin{aligned}\frac{\partial(\rho u_\alpha)}{\partial t}+\frac{\partial(\rho u_\alpha u_\beta)}{\partial x_\beta}&=-\frac{\partial p}{\partial x_\alpha}\\ &+\frac{\partial}{\partial x_\beta}\left[\mu\left(\frac{\partial u_\beta}{\partial x_\alpha}+\frac{\partial u_\alpha}{\partial x_\beta}+\underbrace{\tau\varepsilon\frac{\partial}{\partial x_{\gamma_1}}(\rho u_\alpha u_\beta u_\gamma)}_{\text{Error}}\right)\right]\end{aligned} \tag{2.62b}$$

The main key of this section is that through the identification of pressure p and the dynamic viscosity μ, the Boltzmann Equation converges towards the Navier-Stokes equations using the Chapman-Enskog expansion. It is important to highlight that this convergence holds true under the conditions that (1) the relaxation time τ is greater than $\Delta t/2$ which is equivalent to $1/2$ due to the non-dimensionalization of both space and time (2) the negligible error term, which holds when ε is low. This implies that the Knudsen number is low meaning that the macroscopic fluid velocity is not high which is related to the Mach number Ma. In the numerical framework, in most cases, the LBM does not diverge if the Ma < 0.3 (Timm et al., 2016). For higher velocities, other precautions must be taken into consideration, such as the truncation of the equilibrium function to a higher order of macroscopic velocity than 2 $\mathcal{O}(\boldsymbol{u}^2)$.

As will be seen later in Chapter 4, in the context of capillary bridges at a quasi-static state, not only the error term will be negligible, but even the viscous term itself will tend to zero.

2.6 Conclusion

In this chapter, a concise introduction to the Lattice Boltzmann Method (LBM) for single-phase flow was provided. It is a multiscale numerical method that fills the gap between micro and macro scales through statistical mechanics and using probability density functions. The evolution of these latter is described using the Boltzmann Equation and its velocity discretization. Using the Chapman-Enskog expansion, which is based on the perturbation theory, the Navier-Stokes equations can be retrieved from the Boltzmann Equation. Some classical boundary conditions were briefly presented namely the periodic condition and the non-slip boundary condition also known as the bounce-back condition. In the context of capillary bridges, an air-water system has to be considered. Therefore, the concepts presented in this chapter will be extended to multi-phase flow modeling.

Chapter 3

Lattice Boltzmann Method for multi-phase fluids

3.1 Introduction

In Chapter 2, the single-phase LBM model to solve the NSE has been covered. It has been demonstrated that the BE converges to the NSE using the Chapman-Enskog expansion based on the perturbation theory through the identification of pressure p and dynamic viscosity μ. However, in the context of water-air capillary interfaces, the need for a multi-phase model is indispensable. Therefore, the multi-phase LBM model will be covered hereafter.

One of the most widely used and most popular models in LBM for multi-phase flows is the Single Component Multi-Phase (SCMP) Shan-Chen (SC) family due to its simplicity and its efficiency compared to other models (Shan and Chen, 1993, 1994; Shan and Doolen, 1995). The fundamental idea of this model is based upon using pseudo-potentials accounting for interactions between molecules at the mesoscopic level. These interactions are characterized by a force F^{SC} that separates a single component fluid into two phases. The LB model of SCMP solves the Navier-Stokes equations and also requires an Equation Of State (EOS) to simulate two fluids. One of the most important points about multi-phase modeling is the density ratio. As previously mentioned, this approach was widely used in the literature for treating unsaturated media (Richefeu et al., 2006a; Delenne et al., 2015; Benseghier et al., 2021). It is worth mentioning that in the SCMP model, multiple drawbacks were reported in the literature, such as:

- the density ratio is directly connected to the EOS, and the maximum one reached so far is $\mathcal{O}(100)$ (Huang et al., 2015) which is not sufficiently large to model air-water interface;
- spurious velocities and densities are observed in the neighborhood of obstacles (Benseghier et al., 2021); and
- large values of pressure and temperature states in order to guarantee numerical stability which do not correspond to reasonable experimental conditions (Benseghier et al., 2021).

Having presented these disadvantages, obviously, the SCMP is not a suitable candidate to comprehensively tackle partially saturated media because of its inaccuracy in this precise domain.

Diffuse interface approaches become widely used in sophisticated physical applications thanks to the fact that they are capable of modeling large density ratios $\mathcal{O}(1000)$ (Sun and Beckermann, 2007; Chiu and Lin, 2011a) and dealing with complex geometries. Contrary to sharp interfaces, diffuse ones possess a width W as seen in Figure (3.1a) in which the density, viscosity, and pressure are characterized in a regularized evolution. Furthermore, diffuse interface models are linked to thermodynamic equilibrium which requires a minimization of the free-energy mixing functional $\mathscr{F}(\phi, \boldsymbol{\nabla}\phi)$ (Penrose and Fife, 1990) defined as

$$\mathscr{F}(\phi, \boldsymbol{\nabla}\phi) = \int_{\Omega} \left[\psi(\phi) + \frac{k}{2} |\boldsymbol{\nabla}\phi|^2 \right] \mathrm{d}V + \int_{\partial\Omega} \psi_s(\phi) \mathrm{d}s \tag{3.1}$$

where $\psi(\phi)$ is the free-energy density defined as follows

$$\psi(\phi) = \beta\phi^2(\phi - 1)^2 \tag{3.2}$$

The physical domain occupied by the matter is Ω, whereas $\partial\Omega$ is the contour of the domain, and $\psi_s(\phi)$ represents the free-energy density on the solid-fluid boundary (Jacqmin,

1999; Lee and Kim, 2012; Liang et al., 2019). The parameters k and β are connected to the surface tension γ and the interface thickness W through the following relationships, which will be demonstrated later in Sections (3.2) and (3.3):

$$\begin{aligned} k &= \frac{3}{2}\gamma W \\ \beta &= \frac{12\gamma}{W}. \end{aligned} \tag{3.3}$$

Among the diffuse interface techniques, we find the phase-field-based model which is used for solving Cahn-Hilliard (CHE) or Allen-Cahn (ACE) to track the interface, along with the NSE to calculate velocity fields and pressure fields within the domain (Fakhari and Rahimian, 2010; Fakhari and Lee, 2013; Fakhari et al., 2017a,b; Wang et al., 2016; Timm et al., 2016; Zheng et al., 2015; He et al., 2019; Wang et al., 2019). The CHE and ACE describe the evolution of the phase field $\phi(\boldsymbol{r}, t)$ defined in all the domains which is equal to ϕ_1 and ϕ_2 in the bulk fluids, and $\phi \in]\phi_1; \phi_2[$ in the interface. From now on, the values of the phase field bulk fluids are $\phi_1 = 0$ and $\phi_2 = 1$. The most advantageous asset of this method is that we do not need to manually track the interface, instead, it will be naturally tracked by solving the aforementioned equations. These methods are tremendously suitable for problems in which the interface motion depends on external conditions, among others, the wetting condition.

Although the Cahn-Hilliard equation conserves the mass, it contains a fourth-order term, making it difficult to solve and even more time-consuming Chiu and Lin (2011b). However, the ACE is both a mass-conserved and an easy-to-solve equation as already reported in Liang et al. (2018, 2019). Therefore, in this chapter, and to capture the air-water interface, the Allen-Cahn equation is coupled with the two-phase Navier-Stokes equation through a surface tension term.

3.2 Allen-Cahn Equation

As previously mentioned, the motion of the interface separating water from air is captured using ACE due to its good mass conservation (Chiu and Lin, 2011a; Sun and Beckermann, 2007)

$$\frac{\partial \phi}{\partial_t} + \boldsymbol{\nabla} \cdot (\phi \boldsymbol{u}) = \boldsymbol{\nabla} \cdot [M(\boldsymbol{\nabla}\phi - \lambda \boldsymbol{n})] \tag{3.4}$$

where $\phi(\boldsymbol{r}, t)$ is the phase-field parameter used to identify the regions occupied by the two fluids. This parameter takes the value 1 in the liquid phase, 0 in the gas phase, and between 0 and 1 in the interface as indicated in Figure (3.1b). Once $\phi(\boldsymbol{r}, t)$ is determined, the fluid density ρ is computed as follows

$$\rho = \phi(\rho_l - \rho_g) + \rho_g \tag{3.5}$$

where ρ_l and ρ_g are liquid and gas densities far from the interface, assumed to be constant. In Eq. (3.4), M represents the mobility and $\boldsymbol{n}$ is the unit normal vector to the interface as illustrated in Figure (3.1a). Its mathematical expression can be written as follows:

$$\boldsymbol{n} = \frac{\boldsymbol{\nabla}\phi}{||\boldsymbol{\nabla}\phi||}. \tag{3.6}$$

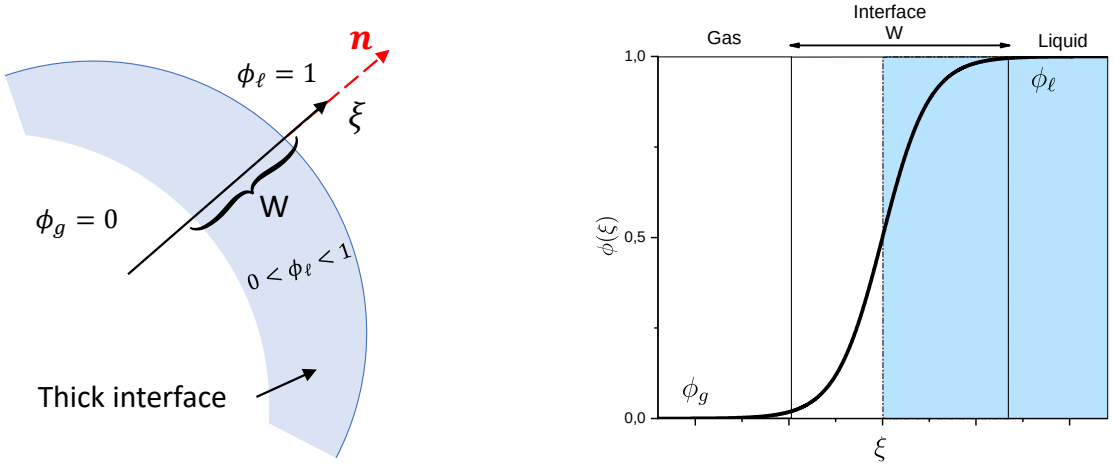

(a) Scheme describing the interface.

(b) Evolution of ϕ through the interface.

Figure 3.1: Presentation of concepts and phenomena related to the interface.

In the bulk fluid, only the first term of the R.H.S of Eq. (3.1) is considered. Furthermore, the chemical potential μ_ϕ is defined as the minimum of the mixing energy $\mathscr{F}(\phi, \boldsymbol{\nabla}\phi)$ and satisfies:

$$\begin{aligned}\mu_\phi = \frac{\delta \mathscr{F}}{\delta \phi} &= \frac{\partial \mathscr{F}}{\partial \phi} - \boldsymbol{\nabla} \cdot \left(\frac{\partial \mathscr{F}}{\partial \boldsymbol{\nabla}\phi} \right) = \frac{\partial \psi}{\partial \phi} - k\boldsymbol{\nabla}^2\phi \\ &= 4\beta\phi(\phi - 1)\left(\phi - \frac{1}{2}\right) - k\boldsymbol{\nabla}^2\phi. \end{aligned} \tag{3.7}$$

The regularized interface evolution ϕ^{eq} is defined at thermodynamic equilibrium when the μ_ϕ is nil. If we express ϕ^{eq} in terms of the interface normal local system ξ as indicated in Figure (3.1a), $\boldsymbol{\nabla}^2\phi$ becomes then[1] $\phi''(\xi)$. Consequently, after substitutions, and at the thermodynamic equilibrium, Eq. (3.7) yields:

$$\mu_\phi = 4\beta\phi_{\text{eq}}(\xi)\left[\phi_{\text{eq}}(\xi) - 1\right]\left[\phi_{\text{eq}}(\xi) - \frac{1}{2}\right] - k\phi''_{\text{eq}}(\xi) = 0. \tag{3.8}$$

After solving the above differential equation, ϕ^{eq} can be expressed as:

$$\phi^{\text{eq}}(\xi) = \frac{1}{2} + \frac{1}{2}\tanh\left(\sqrt{\frac{\beta}{2k}}\,\xi\right). \tag{3.9}$$

It is now the time to introduce the interface thickness W in Eq. (3.9) as follows:

$$\phi^{\text{eq}}(\xi) = \frac{1}{2} + \frac{1}{2}\tanh\left(\frac{2\xi}{W}\right) \tag{3.10a}$$

$$W = \sqrt{\frac{8k}{\beta}} \tag{3.10b}$$

Therefore, the regularized interface is simply defined as a hyperbolic tangent function as depicted in Figure (3.1b). Moreover, the parameter λ, from the R.H.S of Allen-Cahn

[1] $\phi(x, y, z)$ becomes a local single-component variable ξ, which makes the Laplacien a second-order derivative.

equation (3.4), is the norm of gradient vector of ϕ^{eq} at equilibrium which can be expressed as:

$$\lambda = ||\boldsymbol{\nabla}\phi^{\text{eq}}|| = \frac{4\phi(1-\phi)}{W}. \tag{3.11}$$

3.3 Modified Navier-Stokes Equation

For incompressible two-phase flows, the modified Navier-Stokes equations may be written as

$$\rho\left(\frac{\partial \boldsymbol{u}}{\partial_t} + \boldsymbol{u}\cdot\boldsymbol{\nabla}\boldsymbol{u}\right) = -\boldsymbol{\nabla}p + \boldsymbol{\nabla}\cdot\left[\rho\nu\left(\boldsymbol{\nabla}\boldsymbol{u} + \boldsymbol{\nabla}\boldsymbol{u}^T\right)\right] + \boldsymbol{F}_s + \boldsymbol{B} \tag{3.12a}$$

$$\boldsymbol{\nabla}\cdot\boldsymbol{u} = 0 \tag{3.12b}$$

which corresponds to Eq. (2.2) where $\boldsymbol{F}_s$ is the surface tension force accounting for the interface separating the two phases, e.g. air and water. In Eq. (3.12), the coupling with Allen-Cahn equation is included in the definition of the surface tension term $\boldsymbol{F}_s$ as in Liang et al. (2018); Li et al. (2019); Fakhari and Bolster (2017); Younes et al. (2023a, 2022):

$$\begin{aligned} \boldsymbol{F}_s &= \mu_\phi\boldsymbol{\nabla}\phi \\ \mu_\phi &= 4\phi(\phi-1)\left(\phi - \frac{1}{2}\right) - k\boldsymbol{\nabla}^2\phi. \end{aligned} \tag{3.13}$$

It is worth mentioning that the coupling is also done via the fluid density ρ which depends on ϕ as already seen in Eq. (3.5).

To begin, let us prove that Eq. (3.13) of $\boldsymbol{F}_s$ takes the following equivalent form at equilibrium

$$\boldsymbol{F}_s = -\gamma\kappa\boldsymbol{n}\delta_s \tag{3.14}$$

where γ designates the liquid-gas surface tension, κ denotes the trace[2] of the curvature operator, $\boldsymbol{n} = \dfrac{\boldsymbol{\nabla}\phi}{||\boldsymbol{\nabla}\phi||}$ is the unit normal vector to the interface, and δ_s is a smooth Dirac function defined, on the interface, as $\delta_s = \alpha||\boldsymbol{\nabla}\phi^{\text{eq}}||^2$ which satisfies:

$$\int_{-\infty}^{+\infty}\delta_s \mathrm{d}\xi = 1. \tag{3.15}$$

The value of i may be determined using Eq. (3.10a) of ϕ^{eq}. At equilibrium, and along the thickness of the diffuse interface, $||\boldsymbol{\nabla}\phi^{\text{eq}}||$ is given by Eq. (3.11). Therefore, condition (3.15) reduces to

$$\alpha\int_{-\infty}^{+\infty}\frac{2\beta}{k}(\phi-1)^2\phi^2\mathrm{d}\xi = 1 \tag{3.16}$$

leading to

$$\alpha = 6\sqrt{\frac{k}{2\beta}} \tag{3.17}$$

and so that

$$\delta_s = 6\sqrt{\frac{k}{2\beta}}||\boldsymbol{\nabla}\phi||^2 \tag{3.18}$$

[2] $\mathrm{Tr}(A) = \sum_i A_{ii}$ for a matrix (A_{ij}).

On the other hand, the interface curvature κ is given as $\kappa = \boldsymbol{\nabla} \cdot \boldsymbol{n}$. Using the definition (3.6) of $\boldsymbol{n}$, we have:

$$\kappa = \frac{1}{||\boldsymbol{\nabla}\phi||}\left[\boldsymbol{\nabla}^2\phi - \frac{\boldsymbol{\nabla}\phi \cdot \boldsymbol{\nabla}(||\boldsymbol{\nabla}\phi||)}{||\boldsymbol{\nabla}\phi||}\right]. \tag{3.19}$$

Using (3.6) and (3.10a), the latter term can be developed at equilibrium as follows:

$$\frac{\boldsymbol{\nabla}\phi \cdot \boldsymbol{\nabla}(||\boldsymbol{\nabla}\phi||)}{||\boldsymbol{\nabla}\phi||} = \frac{\mathrm{d}^2\phi^{\mathrm{eq}}}{\mathrm{d}\xi^2} = \frac{4\beta}{k}\phi(\phi-1)\left(\phi - \frac{1}{2}\right). \tag{3.20}$$

Substitution of Eq. (3.20) into Eq. (3.19) yields:

$$\kappa = \frac{1}{||\boldsymbol{\nabla}\phi||}\left[\boldsymbol{\nabla}^2\phi - \phi\frac{4\beta}{k}(\phi-1)\left(\phi - \frac{1}{2}\right)\right]. \tag{3.21}$$

Using Eqs. (3.18), (3.21) and (3.6), we get:

$$-\gamma\kappa\boldsymbol{n}\delta_s = -6\gamma\sqrt{\frac{k}{2\beta}}\left[\boldsymbol{\nabla}^2\phi - \frac{4\beta}{k}(\phi-1)\phi\left(\phi - \frac{1}{2}\right)\right]\left(\frac{\boldsymbol{\nabla}\phi}{||\boldsymbol{\nabla}\phi||}\right)||\boldsymbol{\nabla}\phi||. \tag{3.22}$$

Obviously, for Eq. (3.22) to be consistent, γ must be expressed as

$$\gamma = \frac{1}{6}\sqrt{2k\beta} \tag{3.23}$$

and therefore we get:

$$-\gamma\kappa\boldsymbol{n}\delta_s = \left[-k\boldsymbol{\nabla}^2\phi + 4\beta(\phi-1)\phi(\phi-\frac{1}{2})\right]\boldsymbol{\nabla}\phi = \mu_\phi.\boldsymbol{\nabla}\phi \tag{3.24}$$

This proves that, at equilibrium, $\boldsymbol{F}_s$ can be directly expressed as in Eq. (3.14). It is also worth noting that Eq. (3.14) was also added to NSE in Scardovelli and Zaleski (1999) in order to take into account the discontinuity at the interface separating two fluids.

It is extremely important to know that the combination of Eqs. (3.23) and (3.10b) will retrieve the relations between k, β, and γ as introduced in Eq. (3.3).

3.4 LBM models for Multi-phase simulations

The LB models for solving the conservative ACE (3.4) and NSE (3.12) rely on two families of particle distribution functions. For ACE, $g_i(\boldsymbol{r}, t)$ are used, whereas, $f_i(\boldsymbol{r}, t)$ are related for NSE.

3.4.1 Discretization of Allen-Cahn Equation with Liang model

3.4.1.1 Numerical scheme

The spatio-temporal evolution of $g_i(\boldsymbol{r}, t)$ described using the Bhatnagar-Gross-Krook (BGK) collision operator based on the discretization method proposed in Liang et al. (2018, 2019); Younes et al. (2023a, 2022) is defined as

$$g_i(\boldsymbol{r} + \boldsymbol{c}_i\Delta t, t + \Delta t) = g_i(\boldsymbol{r}, t) - \frac{\Delta t}{\tau_g}\left[g_i(\boldsymbol{r}, t) - g_i^{\mathrm{eq}}(\boldsymbol{r}, t)\right] + \Delta t G_i(\boldsymbol{r}, t) \tag{3.25}$$

in which τ_g is the non-dimensional relaxation time for $g(\boldsymbol{r},t)$ probability density function, $G_i(\boldsymbol{r},t)$ is the source term, and $g_i^{\text{eq}}(\boldsymbol{r},t)$ is the equilibrium distribution function given by

$$g_i^{\text{eq}}(\boldsymbol{r},t) = \omega_i \phi \left(1 + \frac{\boldsymbol{c}_i \cdot \boldsymbol{u}}{c_s^2}\right) \tag{3.26}$$

where $\boldsymbol{u} = \boldsymbol{u}(\boldsymbol{r},t)$ is the fluid velocity which will be calculated from NSE as elaborated later on in Section 3.4.2 and $\phi \in [0;1]$ is the phase-field variable.

The parameter ϕ is computed from the distribution function g_i as:

$$\phi = \sum_i g_i. \tag{3.27}$$

In Eq. (3.26), $c_s = c/\sqrt{3}$ is the lattice speed of sound for D2Q9, D3Q15, and D3Q19 for discretization schemes. For D3Q7, we have $c_s = c/\sqrt{4}$. The characteristic velocity c is defined classically as $c = \Delta x/\Delta t$, where Δx and Δt denote the lattice size and time step (which are equal to one in lattice units). Furthermore, $\boldsymbol{c}_i$ are the discrete velocities, which depend on the discretization scheme. In lattice units, the discrete velocities for the D3Q19 scheme are

$$\boldsymbol{c}_i = \begin{cases} (0,0,0) & i = 0 \\ (\pm 1,0,0),(0,\pm 1,0),(0,0,\pm 1), & i = 1,2,...,6 \\ (\pm 1,\pm 1,0),(\pm 1,0,\pm 1),(0,\pm 1,\pm 1) & i = 7,8,...,18 \end{cases} \tag{3.28}$$

with the corresponding weights $w_0 = 1/3$, $w_{1-6} = 1/18$ and $w_{7-18} = 1/36$. Indeed, the rotational isotropy conditions, introduced in Eqs. (2.27), are also valid here.

The source term G_i in Eq. (3.25) is defined as in Liang et al. (2018) by

$$G_i = \left(1 - \frac{\Delta t}{2\tau_g}\right) \frac{\omega_i \boldsymbol{c}_i \cdot [\partial_t(\phi \boldsymbol{u}) + c_s^2 \lambda \boldsymbol{n}]}{c_s^2} \tag{3.29}$$

where $\partial_t = \dfrac{\partial}{\partial_t}$. The mobility M in the ACE is related to the relaxation time τ_g as it will be proven in Section 3.4.1.2 deduced from Chapman-Enskog expansion:

$$M = c_s^2 \left(\tau_g - \frac{\Delta t}{2}\right). \tag{3.30}$$

Finally, an explicit Euler scheme is used to compute the temporal derivative in Eq. (3.38):

$$\partial_t(\phi \boldsymbol{u}) = \frac{\phi(t)\boldsymbol{u}(t) - \phi(t-\Delta t)\boldsymbol{u}(t-\Delta t)}{\Delta t} \tag{3.31}$$

The second-order isotropic central schemes are applied for the evaluation of gradient and Laplacian operators involved in the calculation of $\boldsymbol{n}$, λ, and μ_ϕ (Liang et al., 2018; Younes et al., 2022, 2023d):

$$\boldsymbol{\nabla}\phi(\boldsymbol{r}) = \sum_{i \neq 0} \frac{\omega_i \boldsymbol{c}_i \phi(\boldsymbol{r} + \boldsymbol{c}_i \Delta t)}{c_s^2 \Delta t} \tag{3.32a}$$

$$\boldsymbol{\nabla}^2\phi(\boldsymbol{r}) = \sum_{i \neq 0} \frac{2\omega_i \left[\phi(\boldsymbol{r} + \boldsymbol{c}_i \Delta t) - \phi(\boldsymbol{r})\right]}{c_s^2 \Delta t^2}. \tag{3.32b}$$

3.4.1.2 Chapman-Enskog expansion for Liang model

As previously done in Section 2.5.2, a perturbation of the distribution functions is applied

$$g_i = g_i^{(0)} + \varepsilon g_i^{(1)} + \varepsilon^2 g_i^{(2)} + ... \tag{3.33}$$

where ε is a small parameter related to the Knudsen number Kn. Then, the time and the space derivatives can be written as follows in the same way[3] as in Chapter 2:

$$\partial_t = \varepsilon \partial_{t_1} + \varepsilon^2 \partial_{t_2} \tag{3.34}$$

$$\boldsymbol{\nabla} = \varepsilon \boldsymbol{\nabla}_1 \tag{3.35}$$

Having all of these tools, we will proceed to the recovery of the Allen-Cahn Equation. As G_i contains a derivative with respect to time and a gradient, it is convenient to decompose it as follows:

$$\begin{aligned} G_i = &\left(1 - \frac{\Delta t}{2\tau_g}\right) \left\{ \varepsilon \frac{\omega_i \boldsymbol{c}_i}{c_s^2} \cdot \left[\partial_{t_1}(\phi \boldsymbol{u}) + c_s^2 \lambda \frac{\boldsymbol{\nabla}_1 \phi}{||\boldsymbol{\nabla}_1 \phi||} \right] \right. \\ &\left. + \varepsilon^2 \frac{\omega_i \boldsymbol{c}_i}{c_s^2} \cdot \partial_{t_2} (\phi \boldsymbol{u}) \right\} \end{aligned} \tag{3.36}$$

$$= \left(1 - \frac{\Delta t}{2\tau_g}\right) \left[\varepsilon H_i^{(1)} + \varepsilon^2 H_i^{(2)} \right] \tag{3.37}$$

where $H_i^{(1)}$ and $H_i^{(2)}$ are defined as follows:

$$H_i^{(1)} = \frac{\omega_i \boldsymbol{c}_i}{c_s^2} \cdot \left[\partial_{t_1}(\phi \boldsymbol{u}) + c_s^2 \lambda \frac{\boldsymbol{\nabla}_1 \phi}{||\boldsymbol{\nabla}_1 \phi||} \right] \tag{3.38a}$$

$$H_i^{(2)} = \frac{\omega_i \boldsymbol{c}_i}{c_s^2} \cdot \partial_{t_2} (\phi \boldsymbol{u}) \,. \tag{3.38b}$$

The first step consists of using the Taylor development of Eq. (3.25) in the second order:

$$\begin{aligned} &\Delta t \left(\partial_t + \boldsymbol{c}_i \cdot \boldsymbol{\nabla}\right) g_i + \frac{\Delta t^2}{2} \left(\partial_t + \boldsymbol{c}_i \cdot \boldsymbol{\nabla}\right)^2 g_i + \mathcal{O}\left(\Delta t^3\right) \\ &\qquad = -\frac{\Delta t}{\tau_g} \left[g_i - g_i^{\mathrm{eq}} \right] + \Delta t G_i. \end{aligned} \tag{3.39}$$

We then simplify by Δt in Eq. (3.39), and we expand g_i, ∂_t, G_i, and $\boldsymbol{\nabla}_1$ using Eqs.(3.33)-(3.35), and (3.38)

$$\begin{aligned} &\left(\varepsilon \partial_{t_1} + \varepsilon^2 \partial_{t_2} + \varepsilon \boldsymbol{c}_i \cdot \boldsymbol{\nabla}_1\right) \left[g_i^{(0)} + \varepsilon g_i^{(1)} + \varepsilon^2 g_i^{(2)} \right] \\ &+ \left(\varepsilon \partial_{t_1} + \varepsilon^2 \partial_{t_2} + \varepsilon \boldsymbol{c}_i \cdot \boldsymbol{\nabla}_1\right)^2 \left[g_i^{(0)} + \varepsilon g_i^{(1)} + \varepsilon^2 g_i^{(2)} \right] \frac{\Delta t}{2} \\ &= -\frac{\Delta t}{\tau_g} \left[g_i^{(0)} + \varepsilon g_i^{(1)} + \varepsilon^2 g_i^{(2)} - g_i^{\mathrm{eq}} \right] + \left(1 - \frac{\Delta t}{2\tau_g}\right) \left[\varepsilon H_i^{(1)} + \varepsilon^2 H_i^{(2)} \right] \end{aligned} \tag{3.40}$$

[3] Although the notations here have been changed a little bit, the reasoning is the same as in Chapter 2, Section 2.5.2.

By identification of order of ε^p with $p \in \mathbb{N}$, we have:

$$\mathcal{O}(\varepsilon^0) : g_i^{(0)} = g_i^{\text{eq}} \tag{3.41a}$$

$$\mathcal{O}(\varepsilon^1) : (\partial_{t_1} + \boldsymbol{c}_i \cdot \boldsymbol{\nabla}_1)\, g_i^{(0)} = -\frac{1}{\tau_g} g_i^{(1)} + \left(1 - \frac{\Delta t}{2\tau_g}\right) H_i^{(1)} \tag{3.41b}$$

$$\begin{aligned}\mathcal{O}(\varepsilon^2) &: \partial_{t_2} g_i^{(0)} + (\partial_{t_1} + \boldsymbol{c}_i \cdot \boldsymbol{\nabla}_1)\, g_i^{(1)} + (\partial_{t_1} + \boldsymbol{c}_i \cdot \boldsymbol{\nabla}_1)^2\, g_i^{(0)} \frac{\Delta t}{2} \\ &= -\frac{1}{\tau_g} g_i^{(2)} + \left(1 - \frac{\Delta t}{2\tau_g}\right) H_i^{(2)}\end{aligned} \tag{3.41c}$$

Based on Eq. (3.41a), $g_i^{(0)} = g_i^{\text{eq}}$. Therefore, from now on, $g_i^{(0)}$ will be replaced by g_i^{eq}. The conservation of mass must be respected, therefore, the zeroth moment of the PDFs $\Omega(g)$, from Eq. (2.11a), is conserved which means:

$$\sum_i g_i^{\text{eq}} = \sum_i g_i = \phi. \tag{3.42}$$

As for the first moment (momentum), it should not be conserved. This is the distinguishing characteristic between the Chapman-Enskog expansion of ACE and the NSE for single-phase flow seen in Chapter 2. In fact, using Eq. (3.26) and based on the same approach used in Appendix D.1, we know that:

$$\sum_i g_i^{\text{eq}} \boldsymbol{c}_i = \phi \boldsymbol{u}. \tag{3.43}$$

However, it must be noted that the velocity $\boldsymbol{u}$ is determined through the Navier-Stokes equation using the PDFs f_i, which will be detailed later in this chapter. Therefore, to avoid incompatibility between f_i and g_i, the imposition of the conservation of the first moment of $\Omega(g_i)$ is no longer required. In other words:

$$\sum_i g_i^{\text{eq}} \boldsymbol{c}_i = \phi \boldsymbol{u} \neq \sum_i g_i \boldsymbol{c}_i. \tag{3.44}$$

Now, based on Eq. (3.33), the zeroth and the first moments of g_i are determined as follows:

$$\sum_i g_i = \sum_i g_i^{\text{eq}} + \varepsilon \sum_i g_i^{(1)} + \varepsilon^2 \sum_i g_i^{(2)} \tag{3.45a}$$

$$\sum_i g_i \boldsymbol{c}_i = \sum_i g_i^{\text{eq}} \boldsymbol{c}_i + \varepsilon \sum_i g_i^{(1)} \boldsymbol{c}_i + \varepsilon^2 \sum_i g_i^{(2)} \boldsymbol{c}_i. \tag{3.45b}$$

Therefore, from Eqs. (3.44), (3.45a), and (3.42), the solvability functions satisfy:

$$\sum_i g_i^{(n)} = 0 \qquad \& \qquad \sum_i \boldsymbol{c}_i g_i^{(n)} \neq \boldsymbol{0} \quad \text{for } n \geq 1. \tag{3.46}$$

The sum of Eq. (3.41b) over i, using Eqs. (3.42) and (3.44) yields

$$\partial_{t_1} \phi + \boldsymbol{\nabla}_1 \cdot (\phi \boldsymbol{u}) = 0. \tag{3.47}$$

Then Eq. (3.41b) is multiplied by $(\partial_{t_1} + \boldsymbol{c}_i \cdot \boldsymbol{\nabla}_1)$ yields to:

$$\begin{aligned}(\partial_{t_1} + \boldsymbol{c}_i \cdot \boldsymbol{\nabla}_1)^2 g_i^{\text{eq}} = -\frac{1}{\tau_g}(\partial_{t_1} + \boldsymbol{c}_i \cdot \boldsymbol{\nabla}_1) g_i^{(1)} \\ + \left(1 - \frac{\Delta t}{2\tau_g}\right)(\partial_{t_1} + \boldsymbol{c}_i \cdot \boldsymbol{\nabla}_1) H_i^{(1)}\end{aligned} \tag{3.48}$$

Next, Eq. (3.48) is substituted in Eq. (3.41c) to give:

$$\begin{aligned}\partial_{t_2} g_i^{\text{eq}} + (\partial_{t_1} + \boldsymbol{c}_i \cdot \boldsymbol{\nabla}_1) g_i^{(1)} - \frac{\Delta t}{2\tau_g}(\partial_{t_1} + \boldsymbol{c}_i \cdot \boldsymbol{\nabla}_1) g_i^{(1)} \\ + \left(1 - \frac{\Delta t}{2\tau_g}\right)(\partial_{t_1} + \boldsymbol{c}_i \cdot \boldsymbol{\nabla}_1) H_i^{(1)} \frac{\Delta t}{2} = -\frac{1}{\tau_g} g_i^{(2)} + \left(1 - \frac{\Delta t}{2\tau_g}\right) H_i^{(2)}\end{aligned} \tag{3.49}$$

Eq. (3.49) readily leads to:

$$\begin{aligned}\partial_{t_2} g_i^{\text{eq}} + \left(1 - \frac{\Delta t}{2\tau_g}\right)(\partial_{t_1} + \boldsymbol{c}_i \cdot \boldsymbol{\nabla}_1)\left[g_i^{(1)} + \frac{\Delta t}{2} H_i^{(1)}\right] \\ = -\frac{1}{\tau_g} g_i^{(2)} + \left(1 - \frac{\Delta t}{2\tau_g}\right) H_i^{(2)}\end{aligned} \tag{3.50}$$

Then, Eq. (3.50) is summed[4] over i:

$$\begin{aligned}\partial_{t_2}\phi + \left(1 - \frac{\Delta t}{2\tau_g}\right)\left[\boldsymbol{\nabla}_1 \cdot \sum_i \boldsymbol{c}_i g_i^{(1)} + \frac{\Delta t}{2}\boldsymbol{\nabla}_1 \cdot \sum_i \boldsymbol{c}_i H_i^{(1)}\right] = 0 \\ \partial_{t_2}\phi + \left(1 - \frac{\Delta t}{2\tau_g}\right)\boldsymbol{\nabla}_1 \cdot \left[\sum_i \boldsymbol{c}_i g_i^{(1)} + \frac{\Delta t}{2}\sum_i \boldsymbol{c}_i H_i^{(1)}\right] = 0\end{aligned} \tag{3.51}$$

Note that the terms $\sum_i H_i^{(1)} = 0$ and $\sum_i H_i^{(2)} = 0$ because of Eq. (2.27b). Indeed, we have:

$$\sum_i H_i^{(2)} = \sum_i \frac{1}{c_s^2}\omega_i \boldsymbol{c}_i \cdot \partial_{t_2}(\phi \boldsymbol{u}) = \frac{1}{c_s^2}\partial_{t_2}(\phi \boldsymbol{u}) \cdot \underbrace{\sum_i \omega_i \boldsymbol{c}_i}_{=0}. \tag{3.52}$$

The same reasoning is applied for $\sum_i H_i^{(1)}$. However, the computation of $\sum_i \boldsymbol{c}_i H_i^{(1)}$ is not straightforward. We have

$$\sum_i \boldsymbol{c}_i H_i^{(1)} = \sum_i \boldsymbol{c}_i \left\{\frac{\omega_i \boldsymbol{c}_i}{c_s^2} \cdot \left[\partial_{t_1}(\phi \boldsymbol{u}) + c_s^2 \lambda \frac{\boldsymbol{\nabla}_1 \phi}{||\boldsymbol{\nabla}_1 \phi||}\right]\right\} \tag{3.53}$$

$$= \sum_i \omega_i \frac{\boldsymbol{c}_i \otimes \boldsymbol{c}_i}{c_s^2} \cdot \left[\partial_{t_1}(\phi \boldsymbol{u}) + c_s^2 \lambda \frac{\boldsymbol{\nabla}_1 \phi}{||\boldsymbol{\nabla}_1 \phi||}\right] \tag{3.54}$$

where the dot $\cdot$ denotes the contraction of the tensor of order two $\boldsymbol{c}_i \otimes \boldsymbol{c}_i$ with a vector $\boldsymbol{u}$ such as $(\boldsymbol{c}_i \otimes \boldsymbol{c}_i) \cdot \boldsymbol{u} = \boldsymbol{c}_i(\boldsymbol{c}_i \cdot \boldsymbol{u})$. Using Eq. (2.27c), $\sum_i \frac{\omega_i \boldsymbol{c}_i \otimes \boldsymbol{c}_i}{c_s^2} = \boldsymbol{I}$ which is the identity

[4] Based on Eq. (3.46), $\sum_i g_i^{(k)} = 0$ with $k \geq 1$.

matrix in $\mathbb{R}^3$, and therefore, $\sum_i \boldsymbol{c}_i H_i^{(1)}$ becomes eventually:

$$\sum_i \boldsymbol{c}_i H_i^{(1)} = \partial_{t_1}(\phi \boldsymbol{u}) + \lambda c_s^2 \frac{\boldsymbol{\nabla}_1 \phi}{||\boldsymbol{\nabla}_1 \phi||}. \tag{3.55}$$

The term $\sum_i \boldsymbol{c}_i g_i^{(1)}$ in Eq. (3.51) is an unknown. To determine it, we multiply Eq. (3.41b) by $\boldsymbol{c}_i$ and sum it over i, we obtain, using Eq. (3.42), (3.43), and Eq. (3.55, after some basic calculations:

$$\begin{aligned}\sum_i \boldsymbol{c}_i g_i^{(1)} = \tau_g \left(1 - \frac{\Delta t}{2\tau_g}\right) \left[\partial_{t_1}(\phi \boldsymbol{u}) + c_s^2 \lambda \frac{\boldsymbol{\nabla}_1 \phi}{||\boldsymbol{\nabla}_1 \phi||}\right] \\ -\tau_g \left[\partial_{t_1}(\phi \boldsymbol{u}) - c_s^2 \boldsymbol{\nabla}_1 \phi\right].\end{aligned} \tag{3.56}$$

See Appendix D.1.2 for the calculation of $\sum_i (\boldsymbol{c}_i \cdot \boldsymbol{\nabla}_1 g_i^{\text{eq}}) \boldsymbol{c}_i$. After performing some manipulations, we get:

$$\sum_i \boldsymbol{c}_i g_i^{(1)} = \left(\tau_g - \frac{\Delta t}{2}\right) c_s^2 \lambda \frac{\boldsymbol{\nabla}_1 \phi}{||\boldsymbol{\nabla}_1 \phi||} - \frac{\Delta t}{2} \partial_{t_1}(\phi \boldsymbol{u}) - \tau_g c_s^2 \boldsymbol{\nabla}_1 \phi \tag{3.57}$$

By substituting Eq. (3.57) in Eq. (3.51), we get:

$$\begin{aligned}\partial_{t_2}\phi + \left(1 - \frac{\Delta t}{2\tau_g}\right) \boldsymbol{\nabla}_1 \cdot \left[-\frac{\Delta t}{2} \partial_{t_1}(\phi \boldsymbol{u}) - \tau_g c_s^2 \boldsymbol{\nabla}_1 \phi\right. \\ \left. + \tau_g c_s^2 \lambda \frac{\boldsymbol{\nabla}_1 \phi}{||\boldsymbol{\nabla}_1 \phi||} - \frac{\Delta t}{2} c_s^2 \lambda \frac{\boldsymbol{\nabla}_1 \phi}{||\boldsymbol{\nabla}_1 \phi||} + \frac{\Delta t}{2} \partial_{t_1}(\phi \boldsymbol{u}) + \frac{\Delta t}{2} c_s^2 \lambda \frac{\boldsymbol{\nabla}_1 \phi}{||\boldsymbol{\nabla}_1 \phi||}\right] = 0.\end{aligned} \tag{3.58}$$

By simplification, Eq. (3.58) reduces to

$$\partial_{t_2}\phi + \left(1 - \frac{\Delta t}{2\tau_g}\right) \boldsymbol{\nabla}_1 \cdot \left(-\tau_g c_s^2 \boldsymbol{\nabla}_1 \phi + \tau_g c_s^2 \lambda \frac{\boldsymbol{\nabla}_1 \phi}{||\boldsymbol{\nabla}_1 \phi||}\right) = 0 \tag{3.59}$$

or equivalently:

$$\partial_{t_2}\phi - c_s^2 \left(\tau_g - \frac{\Delta t}{2}\right) \boldsymbol{\nabla}_1 \cdot \left(\boldsymbol{\nabla}_1 \phi - \lambda \frac{\boldsymbol{\nabla}_1 \phi}{||\boldsymbol{\nabla}_1 \phi||}\right) = 0. \tag{3.60}$$

Finally, in order to retrieve the Allen-Cahn equation, we multiply Eq. (3.47) by ε and sum it with ε^2 multiplied by Eq. (3.60) to get:

$$\begin{aligned}&\overbrace{(\varepsilon\partial_{t_1} + \varepsilon^2 \partial_{t_2})}^{\partial_t} \phi + \underbrace{\varepsilon \boldsymbol{\nabla}_1}_{\nabla} \cdot (\phi \boldsymbol{u}) = \\ &\overbrace{\varepsilon \boldsymbol{\nabla}_1}^{\nabla} \cdot \left\{ \underbrace{c_s^2 \left(\tau_g - \frac{\Delta t}{2}\right)}_{M} \left[\underbrace{\varepsilon \boldsymbol{\nabla}_1}_{\nabla} \phi - \lambda \frac{\overbrace{\varepsilon \boldsymbol{\nabla}_1}^{\nabla} \phi}{||\boldsymbol{\nabla}_1 \phi||} \right] \right\}\end{aligned} \tag{3.61}$$

It is possible to recover the Allen-Cahn equation (3.4) through the definition of the interface unit vector $\boldsymbol{n}$, seen in Eq. (3.6), and the following identification:

$$M = c_s^2 \left(\tau_g - \frac{\Delta t}{2} \right). \tag{3.62}$$

With the reverse change of variable using Eqs. (3.34) and (3.35), we eventually obtain:

$$\frac{\partial \phi}{\partial t} + \boldsymbol{\nabla}\phi \cdot (\phi \boldsymbol{u}) = \boldsymbol{\nabla} \cdot \left[M \left(\boldsymbol{\nabla} - \lambda \frac{\boldsymbol{\nabla}\phi}{||\boldsymbol{\nabla}\phi||} \right) \right] \tag{3.63}$$

which proves that the discretization used in Eqs. (3.25), (3.26), and (3.38) converges to the Allen-Cahn equation.

3.4.2 Discretization of Navier-Stokes Equations for two-phase flow

We present hereafter the discretization of NSE for the two-phase flow that will be used in this work. The procedure used here is the same as in Section 2.5.2 with a different expression of f_i^{eq} and with supplementary terms to take into account the air-water interface. We will eventually prove that through identification, the discretized Boltzmann Equation converges to the two-phase flow Navier-Stokes equations.

3.4.2.1 LBM model for two-phase flow

The spatio-temporal evolution of $f_i(\boldsymbol{r}, t)$ described using the Bhatnagar-Gross-Krook (BGK) collision operator based on the discretization method proposed in Liang et al. (2018, 2019); Younes et al. (2023a, 2022) is defined as

$$f_i(\boldsymbol{r} + \boldsymbol{c}_i \Delta t, t + \Delta t) = f_i(\boldsymbol{r}, t) - \frac{\Delta t}{\tau_f} \left[f_i(\boldsymbol{r}, t) - f_i^{\text{eq}}(\boldsymbol{r}, t) \right] + \Delta t F_i(\boldsymbol{r}, t) \tag{3.64}$$

where τ_f is the non-dimensional relaxation time for $f(\boldsymbol{r}, t)$ probability density function and $F_i(\boldsymbol{r}, t)$ is the source term. The equilibrium distribution function $f_i^{\text{eq}}(\boldsymbol{r}, t)$ is given by:

$$f_i^{\text{eq}} = \begin{cases} \dfrac{p}{c_s^2}(\omega_i - 1) + \rho s_i(\boldsymbol{u}) & i = 0 \\ \dfrac{p}{c_s^2}\omega_i + \rho s_i(\boldsymbol{u}) & i \neq 0 \end{cases} \tag{3.65}$$

with

$$s_i(\boldsymbol{u}) = \omega_i \left[\frac{\boldsymbol{c}_i \cdot \boldsymbol{u}}{c_s^2} + \frac{(\boldsymbol{c}_i \cdot \boldsymbol{u})^2}{2c_s^4} - \frac{\boldsymbol{u} \cdot \boldsymbol{u}}{2c_s^2} \right] \tag{3.66}$$

where $\boldsymbol{u} = \boldsymbol{u}(\boldsymbol{r}, t)$ is the fluid velocity, ρ is the density, and p is the macroscopic pressure.

The macroscopic quantities $\boldsymbol{u}$ and p can be calculated as follows (Liang et al., 2018, 2019, 2014; Younes et al., 2022)

$$\rho \boldsymbol{u} = \sum_i f_i \boldsymbol{c}_i + \frac{\Delta t}{2} \boldsymbol{F} \tag{3.67}$$

$$p = \frac{c_s^2}{(1 - \omega_0)} \left[\sum_{i \neq 0} f_i + \frac{\Delta t}{2} (\rho_l - \rho_g) \, \boldsymbol{u} \cdot \boldsymbol{\nabla}\phi + \rho s_0(\boldsymbol{u}) \right]. \tag{3.68}$$

where ρ_l is the liquid density, ρ_g gas density, and $\boldsymbol{F}$ is defined as the total force, including body forces $\boldsymbol{B}$:

$$\begin{aligned} \boldsymbol{F} &= \boldsymbol{F}_s + \boldsymbol{B} \\ \boldsymbol{F} &= \mu_\phi \boldsymbol{\nabla}\phi + \boldsymbol{B}. \end{aligned} \tag{3.69}$$

according to the definition of $\boldsymbol{F}_s$ (3.13).

The source term F_i in Eq. (3.64) is defined as in Liang et al. (2018) by[5]:

$$F_i = \left(1 - \frac{\Delta t}{2\tau_f}\right) \omega_i \left(\frac{\boldsymbol{c}_i \cdot \boldsymbol{F}}{c_s^2} + \frac{\boldsymbol{u} \otimes \boldsymbol{\nabla}\rho : \boldsymbol{c}_i \otimes \boldsymbol{c}_i}{c_s^2}\right) \tag{3.70}$$

The kinematic viscosity ν is linked to the relaxation time τ_f as

$$\nu = c_s^2 \left(\tau_f - \frac{\Delta t}{2}\right) \tag{3.71}$$

in the same manner as for the single-flow model.

3.4.2.2 Chapman-Enskog expansion

As previously done, a perturbation of the distribution functions is applied

$$f_i = f_i^{(0)} + \varepsilon f_i^{(1)} + \varepsilon^2 f_i^{(2)} + ... \tag{3.72}$$

Using Eq. (3.35), we can rewrite Eq. (3.70) in the following manner:

$$\begin{aligned} F_i &= \left(1 - \frac{\Delta t}{2\tau_f}\right) \omega_i \left(\frac{\boldsymbol{c}_i \cdot \mu_\phi \boldsymbol{\nabla}\phi}{c_s^2} + \frac{\boldsymbol{u} \otimes \boldsymbol{\nabla}\rho : \boldsymbol{c}_i \otimes \boldsymbol{c}_i}{c_s^2}\right) \\ &= \varepsilon \left(1 - \frac{\Delta t}{2\tau_f}\right) \omega_i \left(\frac{\boldsymbol{c}_i \cdot \mu_\phi \boldsymbol{\nabla}_1\phi}{c_s^2} + \frac{\boldsymbol{u} \otimes \boldsymbol{\nabla}_1\rho : \boldsymbol{c}_i \otimes \boldsymbol{c}_i}{c_s^2}\right) \\ &= \varepsilon \left(1 - \frac{\Delta t}{2\tau_f}\right) L_i^{(1)} \end{aligned} \tag{3.73}$$

where have set:

$$L_i^{(1)} = \omega_i \left(\frac{\boldsymbol{c}_i \cdot \mu_\phi \boldsymbol{\nabla}_1\phi}{c_s^2} + \frac{\boldsymbol{u} \otimes \boldsymbol{\nabla}_1\rho : \boldsymbol{c}_i \otimes \boldsymbol{c}_i}{c_s^2}\right). \tag{3.74}$$

Let us now perform a Taylor's expansion of Eq. (3.64) up to the second order:

$$\begin{aligned} &\Delta t \left(\partial_t + \boldsymbol{c}_i \cdot \boldsymbol{\nabla}\right) f_i + \frac{\Delta t^2}{2} \left(\partial_t + \boldsymbol{c}_i \cdot \boldsymbol{\nabla}\right)^2 f_i + \mathcal{O}\left(\Delta t^3\right) \\ &\qquad = -\frac{\Delta t}{\tau_g} \left[f_i - f_i^{\mathrm{eq}}\right] + \Delta t F_i. \end{aligned} \tag{3.75}$$

Using Eqs. (3.35), (3.34), (3.72), and (3.73), we obtain:

$$\begin{aligned} &\left(\varepsilon\partial_{t_1} + \varepsilon^2\partial_{t_2} + \varepsilon \boldsymbol{c}_i \cdot \boldsymbol{\nabla}_1\right) \left[f_i^{(0)} + \varepsilon f_i^{(1)} + \varepsilon^2 f_i^{(2)}\right] \\ &+ \left(\varepsilon\partial_{t_1} + \varepsilon^2\partial_{t_2} + \varepsilon \boldsymbol{c}_i \cdot \boldsymbol{\nabla}_1\right)^2 \left[f_i^{(0)} + \varepsilon f_i^{(1)} + \varepsilon^2 f_i^{(2)}\right] \frac{\Delta t}{2} + \mathcal{O}(\Delta t^3) \\ &\qquad = -\frac{\Delta t}{\tau_f} \left[f_i^{(0)} + \varepsilon f_i^{(1)} + \varepsilon^2 f_i^{(2)} - f_i^{\mathrm{eq}}\right] + \left(1 - \frac{\Delta t}{2\tau_f}\right) \varepsilon L_i^{(1)}. \end{aligned} \tag{3.76}$$

[5]We recall that ": " denotes the double dot product of two tensors of order two.

By identification of order of ε^p with $p \in \mathbb{N}$, we have:

$$\mathcal{O}(\varepsilon^0) : f_i^{(0)} = f_i^{\text{eq}} \tag{3.77a}$$

$$\mathcal{O}(\varepsilon^1) : (\partial_{t_1} + \boldsymbol{c}_i \cdot \boldsymbol{\nabla}_1) f_i^{(0)} = -\frac{1}{\tau_f} f_i^{(1)} + \left(1 - \frac{\Delta t}{2\tau_f}\right) L_i^{(1)} \tag{3.77b}$$

$$\begin{aligned}\mathcal{O}(\varepsilon^2) : &\partial_{t_2} f^{(0)} + (\partial_{t_1} + \boldsymbol{c}_i \cdot \boldsymbol{\nabla}_1) f_i^{(1)} + \frac{\Delta t}{2} (\partial_{t_1} + \boldsymbol{c}_i \cdot \boldsymbol{\nabla}_1)^2 f_i^{(0)} \\ &= -\frac{1}{\tau_f} f_i^{(2)}\end{aligned} \tag{3.77c}$$

Based on Eq. (3.77a), $f_i^{(0)} = f_i^{\text{eq}}$. Therefore, from now on, $f_i^{(0)}$ will be replaced by f_i^{eq}. Note that since $\boldsymbol{c}_i$ is a constant vector, we have $\boldsymbol{c}_i \cdot \boldsymbol{\nabla}_1 f_i^{\text{eq}} = \boldsymbol{\nabla}_1 \cdot \boldsymbol{c}_i f_i^{\text{eq}}$. Therefore, the sum over i of Eq. (3.77b) leads to

$$\partial_{t_1} \left(\sum_i f_i^{\text{eq}} \right) + \boldsymbol{\nabla}_1 \cdot \left(\sum \boldsymbol{c}_i \cdot f_i^{\text{eq}} \right) = -\frac{1}{\tau_f} \sum_i f_i^{(1)} + \left(1 - \frac{\Delta t}{2\tau_f}\right) \sum_i L_i^{(1)} \tag{3.78}$$

Following the same procedure as in Appendix D.1.1, we can readily calculate the following terms in Eq. (3.80):

$$\begin{aligned}\sum_i f_i^{\text{eq}} &= 0 \\ \sum_i f_i^{\text{eq}} \boldsymbol{c}_i &= \rho \boldsymbol{u}\end{aligned} \tag{3.79}$$

The calculation of the term $\sum_i L_i^{(1)}$ is detailed in Appendix D.1.3 in Eq. (D.7). We have $\sum_i L_i^{(1)} = \boldsymbol{u} \cdot \boldsymbol{\nabla}_1 \rho$. Therefore, Eq. (3.78) becomes:

$$\boldsymbol{\nabla}_1 \cdot (\rho \boldsymbol{u}) = -\frac{1}{\tau_f} \sum_i f_i^{(1)} + \left(1 - \frac{\Delta t}{2\tau_f}\right) (\boldsymbol{u} \cdot \boldsymbol{\nabla}_1 \rho) \tag{3.80}$$

To guarantee the incompressibility condition of the fluid flow, the term $\sum_i f_i^{(1)}$ in Eq. (3.80) must satisfy the following equality[6]:

$$\sum_i f_i^{(1)} = -\frac{\Delta t}{2} \boldsymbol{u} \cdot \boldsymbol{\nabla}_1 \rho. \tag{3.81}$$

Substituting Eq. (3.81) into Eq. (3.80) eventually leads to

$$\boldsymbol{\nabla}_1 \cdot (\rho \boldsymbol{u}) - \boldsymbol{u} \cdot \boldsymbol{\nabla}_1 \rho = 0 \tag{3.82}$$

or equivalently

$$\boldsymbol{\nabla}_1 \cdot \boldsymbol{u} = 0 \tag{3.83}$$

as $\rho \neq 0$. Therefore, using the reverse change of variables (3.35), we obtain the following equation

$$\boldsymbol{\nabla} \cdot \boldsymbol{u} = \operatorname{div} \boldsymbol{u} = 0. \tag{3.84}$$

[6] We will see that this is a necessary condition for satisfying $\boldsymbol{\nabla}.\boldsymbol{u} = 0$ in the NSE.

which represents the incompressibility condition of the fluid.

Returning to Eq. (3.72), the zeroth-order moment of $f_i(\boldsymbol{r},t)$ writes:

$$\sum_i f_i = \sum_i f_i^{\text{eq}} + \varepsilon \sum_i f_i^{(1)} + \varepsilon^2 \sum_i f_i^{(2)}. \tag{3.85}$$

According to Eq. (3.79), $\sum_i f_i^{\text{eq}} = 0$, and thus Eq.(3.85) leads to:

$$\sum_i f_i = \varepsilon \sum_i f_i^{(1)} + \varepsilon^2 \sum_i f_i^{(2)} \tag{3.86}$$

Due to the incompressibility condition (3.81), returning to the change of variables (3.35), we deduce the compatibility condition on the solvability functions $f_i^{(k)}$:

$$\sum_i f_i = -\frac{\Delta t}{2} \boldsymbol{u} \cdot \boldsymbol{\nabla} \rho \tag{3.87}$$

$$\sum_i f_i^{(1)} = -\frac{\Delta t}{2} \boldsymbol{u} \cdot \boldsymbol{\nabla}_1 \rho \qquad \& \qquad \sum_i f_i^{(k)} = 0 \text{ for } k \geq 2 \tag{3.88}$$

Using Eq. (3.67), the momentum of $f_i(\boldsymbol{r},t)$ is defined[7] as:

$$\sum_i f_i \boldsymbol{c}_i = \rho \boldsymbol{u} - \frac{\Delta t}{2} \boldsymbol{F}_s = \rho \boldsymbol{u} - \frac{\Delta t}{2} \mu_\phi \varepsilon \boldsymbol{\nabla}_1. \tag{3.89}$$

From Eq. (3.72), the first-order moments of f_i write:

$$\sum_i f_i \boldsymbol{c}_i = \sum_i f_i^{\text{eq}} \boldsymbol{c}_i + \varepsilon \sum_i f_i^{(1)} \boldsymbol{c}_i + \varepsilon^2 \sum_i f_i^{(2)} \boldsymbol{c}_i. \tag{3.90}$$

Furthermore, based on Eq. (3.79) and Eq. (3.89), Eq. (3.90) then becomes:

$$-\varepsilon \frac{\Delta t}{2} \mu_\phi \boldsymbol{\nabla}_1 \phi = \varepsilon \sum_i f_i^{(1)} \boldsymbol{c}_i + \varepsilon^2 \sum_i \boldsymbol{c}_i f_i^{(2)} \tag{3.91}$$

Consequently, the first-order moments of the solvability functions must satisfy the following compatibility conditions:

$$\sum_i f_i^{(1)} \boldsymbol{c}_i = -\frac{\Delta t}{2} \mu_\phi \boldsymbol{\nabla}_1 \phi \qquad \& \qquad \sum_i f_i^{(k)} \boldsymbol{c}_i = \boldsymbol{0} \text{ for } k \geq 2. \tag{3.92}$$

Let us now continue the recovery of the modified NSE. The sum of Eq. (3.77b) over i multiplied by $\boldsymbol{c}_i$ leads to:

$$\sum_i \left(\partial_{t_1} + \boldsymbol{c}_i \cdot \boldsymbol{\nabla}_1\right) f_i^{\text{eq}} \boldsymbol{c}_i = -\frac{1}{\tau_f} \sum_i f_i^{(1)} \boldsymbol{c}_i + \left(1 - \frac{\Delta t}{2\tau}\right) \sum_i L_i^{(1)} \boldsymbol{c}_i \tag{3.93}$$

Firstly, the second term can be calculated as follows:

$$\begin{aligned} \sum_i \boldsymbol{c}_i \cdot \boldsymbol{\nabla}_1 f_i^{\text{eq}} \boldsymbol{c}_i &= \boldsymbol{\nabla}_1 \cdot \sum_i f_i^{\text{eq}} \boldsymbol{c}_i \otimes \boldsymbol{c}_i \\ &= \boldsymbol{\nabla}_1 \cdot \left[\rho(\boldsymbol{u} \otimes \boldsymbol{u}) + p\boldsymbol{I}\right] \end{aligned} \tag{3.94}$$

[7] We suppose that there is no body force $\boldsymbol{B} = \boldsymbol{0}$.

(see Appendix D.1.3 for more details).

Secondly, the term $\sum_i L_i^{(1)} \boldsymbol{c}_i$ is given by (D.11) in Appendix (D.1.3):

$$\sum_i L_i^{(1)} \boldsymbol{c}_i = F_s^{(1)} = \mu_\phi \boldsymbol{\nabla}_1 \phi. \tag{3.95}$$

Additionally, we know that: $\sum_i f_i^{(1)} \boldsymbol{c}_i = -\frac{\Delta t}{2} \mu_\phi \boldsymbol{\nabla}_1 \phi = -\frac{\Delta t}{2} F_s^{(1)}$ given (3.92).

Therefore, using again (3.79), Eq. (3.93) leads to

$$\partial_{t_1}(\rho \boldsymbol{u}) + \boldsymbol{\nabla}_1 \cdot \left[\rho \left(\boldsymbol{u} \otimes \boldsymbol{u}\right) + p \boldsymbol{I}\right] = F_s^{(1)} \tag{3.96}$$

or equivalently:

$$\partial_{t_1}(\rho \boldsymbol{u}) + \boldsymbol{\nabla}_1 \cdot \rho \left(\boldsymbol{u} \otimes \boldsymbol{u}\right) = -\boldsymbol{\nabla}_1 p + F_s^{(1)} \tag{3.97}$$

On the other hand, Eq. (3.77b) is multiplied by $(\partial_{t_1} + \boldsymbol{c}_i \cdot \boldsymbol{\nabla}_1)$ to give:

$$\begin{aligned} \left(\partial_{t_1} + \boldsymbol{c}_i \cdot \boldsymbol{\nabla}_1\right)^2 f_i^{\mathrm{eq}} = -\frac{1}{\tau_f} \left(\partial_{t_1} + \boldsymbol{c}_i \cdot \boldsymbol{\nabla}_1\right) f_i^{(1)} \\ + \left(1 - \frac{\Delta t}{2\tau_f}\right) \left(\partial_{t_1} + \boldsymbol{c}_i \cdot \boldsymbol{\nabla}_1\right) L_i^{(1)} \end{aligned} \tag{3.98}$$

Substituting Eq. (3.98) into Eq. (3.77c) yields to:

$$\begin{aligned} \partial_{t_2} f_i^{\mathrm{eq}} + \left(\partial_{t_1} + \boldsymbol{c}_i \cdot \boldsymbol{\nabla}_1\right) f_i^{(1)} - \frac{\Delta t}{2\tau_f} \left(\partial_{t_1} + \boldsymbol{c}_i \cdot \boldsymbol{\nabla}_1\right) f_i^{(1)} \\ + \frac{\Delta t}{2} \left(1 - \frac{\Delta t}{2\tau_f}\right) \left(\partial_{t_1} + \boldsymbol{c}_i \cdot \boldsymbol{\nabla}_1\right) L_i^{(1)} = -\frac{1}{\tau_f} f_i^{(2)} \end{aligned} \tag{3.99}$$

After regrouping some terms of Eq. (3.99), it becomes:

$$\partial_{t_2} f_i^{\mathrm{eq}} + \left(1 - \frac{\Delta t}{2\tau_f}\right) \left(\partial_{t_1} + \boldsymbol{c}_i \cdot \boldsymbol{\nabla}_1\right) \left[f_i^{(1)} + \frac{\Delta t}{2} L_i^{(1)}\right] = -\frac{1}{\tau_f} f_i^{(2)} \tag{3.100}$$

After multiplying Eq. (3.100) with $\boldsymbol{c}_i$ and summing it over i, and after performing some manipulations, using in particular (3.92) and (D.12), it becomes[8]:

$$\partial_{t_2}(\rho \boldsymbol{u}) + \left(1 - \frac{\Delta t}{2\tau_f}\right) \boldsymbol{\nabla}_1 \cdot \left[\sum_i f_i^{(1)} \boldsymbol{c}_i \otimes \boldsymbol{c}_i + \frac{\Delta t}{2} \sum_i L_i^{(1)} \boldsymbol{c}_i \otimes \boldsymbol{c}_i\right] = \boldsymbol{0} \tag{3.101}$$

After replacing each term by its expression, Eq. (3.101) gives (see Appendix D.1.3 for the detailed calculations):

$$\begin{aligned} \partial_{t_2}(\rho \boldsymbol{u}) + \left(1 - \frac{\Delta t}{2\tau_f}\right) \boldsymbol{\nabla}_1 \cdot \left[\rho c_s^2 \left(\boldsymbol{\nabla}_1 \boldsymbol{u} + \boldsymbol{\nabla}_1 \boldsymbol{u}^T\right) - \rho c_s^2 \boldsymbol{\nabla}_1 \cdot \boldsymbol{u} \boldsymbol{I}\right. \\ \left. - \partial_{t_1}(\rho \boldsymbol{u} \otimes \boldsymbol{u} + p \boldsymbol{I})\right] = \boldsymbol{0} \end{aligned} \tag{3.102}$$

[8] The terms multiplied by ∂_{t_1} in Eq. (3.100) cancel each other because $\sum_i \boldsymbol{c}_i f_i^{(1)} = -\frac{\Delta t}{2} \mu_\phi \boldsymbol{\nabla}_1 \phi$ according to Eq. (3.92) and $\frac{\Delta t}{2} \sum_i \boldsymbol{c}_i L_i^{(1)} = \frac{\Delta t}{2} \mu_\phi \boldsymbol{\nabla}_1 \phi$ according to (D.12)

Now, Eq. (3.97) is multiplied by ε and summed with Eq. (3.102) multiplied by ε^2 gives:

$$\begin{aligned}\overbrace{\left(\varepsilon\partial_{t_1}+\varepsilon^2\partial_{t_2}\right)}^{\partial_t}(\rho\boldsymbol{u})+\overbrace{\varepsilon\boldsymbol{\nabla}_1}^{\nabla}\cdot\left[\rho(\boldsymbol{u}\otimes\boldsymbol{u})\right]=-\overbrace{\varepsilon\boldsymbol{\nabla}_1}^{\nabla}p+\overbrace{\varepsilon F_s^{(1)}}^{F_s}+\\ \underbrace{\varepsilon\boldsymbol{\nabla}_1}_{\nabla}\cdot\left[\rho c_s^2\left(\tau_f-\frac{\Delta t}{2}\right)\left(\underbrace{\varepsilon\boldsymbol{\nabla}_1}_{\nabla}\boldsymbol{u}+\underbrace{\varepsilon\boldsymbol{\nabla}_1}_{\nabla}\boldsymbol{u}^T\right)\right.\\ \left.+\rho c_s^2\underbrace{\varepsilon\boldsymbol{\nabla}_1}_{\nabla}\cdot\boldsymbol{u}\boldsymbol{I}+\underbrace{\varepsilon\partial_{t_1}(\rho\boldsymbol{u}\otimes\boldsymbol{u}+p\boldsymbol{I})}_{\text{Error}}\right].\end{aligned}\tag{3.103}$$

In addition, it can be seen that the error term contains ε which has been defined as being related to the Knudsen number Kn ($\varepsilon\sim$ Kn). As previously highlighted in Chapter 2, in this Ph.D. work the Knudsen number is low $\varepsilon\ll 1$, hence the error term can be neglected.

While the incompressibility condition was already recovered in (3.84), it is now possible to recover the modified Navier-Stokes equations (3.12a) through the following identification:

$$\nu=c_s^2\left(\tau_f-\frac{\Delta t}{2}\right).\tag{3.104}$$

Applying the reverse change of variables (3.34) and (3.35) on Eq. (3.103) ultimately leads to the modified Navier-Stokes equations:

$$\begin{aligned}\rho\left(\frac{\partial\boldsymbol{u}}{\partial_t}+\boldsymbol{u}\cdot\boldsymbol{\nabla}\boldsymbol{u}\right)&=-\boldsymbol{\nabla}p+\boldsymbol{\nabla}\cdot\left[\rho\nu\left(\boldsymbol{\nabla}\boldsymbol{u}+\boldsymbol{\nabla}\boldsymbol{u}^T\right)\right]+\boldsymbol{F}_s\\ \boldsymbol{\nabla}\cdot\boldsymbol{u}&=0.\end{aligned}\tag{3.105}$$

3.5 Wetting condition

We recall that wettability is defined as the ability of a liquid to keep in contact with a solid surface. When a liquid droplet comes into contact with a solid surface, a thermodynamic equilibrium is established between the three phases (liquid, gas, and solid).

3.5.1 Theoretical description

We recall the free-energy mixing functional $\mathscr{F}(\phi,\boldsymbol{\nabla}\phi)$ used to model the wetting is:

$$\mathscr{F}(\phi,\boldsymbol{\nabla}\phi)=\int_\Omega\left[\psi(\phi)+\frac{k}{2}|\boldsymbol{\nabla}\phi|^2\right]\mathrm{d}V+\int_{\partial\Omega}\psi_s(\phi)\mathrm{d}s.\tag{3.106}$$

The second term of the R.H.S of Eq. (3.106) will not be nil if one is interested in the boundary separating the solid from the fluid. The variation of this free energy can be written as:

$$\delta\mathscr{F}(\phi,\boldsymbol{\nabla}\phi)=\int_\Omega\left[\frac{\partial\psi(\phi)}{\partial\phi}\delta\phi+k\boldsymbol{\nabla}\phi\cdot\delta(\boldsymbol{\nabla}\phi)\right]\mathrm{d}V+\int_{\partial\Omega}\frac{\partial\psi_s(\phi)}{\partial\phi}\delta\phi\mathrm{d}s\tag{3.107}$$

We recall from vector calculus the following relation

$$\int_\Omega\boldsymbol{\nabla}\cdot(v\boldsymbol{\nabla}u)\,\mathrm{d}V=\int_\Omega v\boldsymbol{\nabla}^2u\,\mathrm{d}V+\int_\Omega\boldsymbol{\nabla}v\cdot\boldsymbol{\nabla}u\,\mathrm{d}V\tag{3.108}$$

where v and u are scalar fields, and $\boldsymbol{\nabla}$ is the gradient defined in $\mathbb{R}^3$. We also recall the Stokes theorem

$$\int_\Omega \boldsymbol{\nabla}\cdot\boldsymbol{\omega}\,\mathrm{d}V = -\int_{\partial\Omega}\boldsymbol{\omega}\cdot\boldsymbol{n}_w\,\mathrm{d}s \tag{3.109}$$

where $\boldsymbol{w}$ is a vector field, $\partial\Omega$ the boundary of Ω, and $\boldsymbol{n}_w$ is the unit inward-normal vector to $\partial\Omega$.

Using Eq. (3.108) with $v=\delta\phi$ and $u=\phi$, we have:

$$\int_\Omega \boldsymbol{\nabla}(\delta\phi)\cdot\boldsymbol{\nabla}\phi\,\mathrm{d}V = \int_\Omega \boldsymbol{\nabla}\cdot(\delta\phi\boldsymbol{\nabla}\phi)\,\mathrm{d}V - \int_\Omega \delta\phi\boldsymbol{\nabla}^2\phi\,\mathrm{d}V. \tag{3.110}$$

By applying the Stokes theorem on the first term of the R.H.S of Eq. (3.110), we obtain:

$$\int_\Omega \boldsymbol{\nabla}(\delta\phi)\cdot\boldsymbol{\nabla}\phi\,\mathrm{d}V = -\int_{\partial\Omega}\delta\phi\boldsymbol{\nabla}\phi\cdot\boldsymbol{n}_w\mathrm{d}S - \int_\Omega \delta\phi\boldsymbol{\nabla}^2\phi\,\mathrm{d}V. \tag{3.111}$$

Considering Eq. (3.111) with Eq. (3.107) and using the fact that $\delta(\boldsymbol{\nabla}\phi)=\boldsymbol{\nabla}(\delta\phi)$, we obtain:

$$\begin{aligned}\delta\mathscr{F}(\phi,\boldsymbol{\nabla}\phi) = &\int_\Omega\left(\frac{\partial\psi(\phi)}{\partial\phi} - k\boldsymbol{\nabla}^2\phi\right)\delta\phi\mathrm{d}V\\ &+\int_{\partial\Omega}\left(-k\boldsymbol{n}_w\cdot\boldsymbol{\nabla}\phi + \frac{\partial\psi_s(\phi)}{\partial\phi}\right)\delta\phi\mathrm{d}s.\end{aligned} \tag{3.112}$$

At equilibrium, the mixing free energy is minimized which corresponds to $\delta\mathscr{F}(\phi,\boldsymbol{\nabla}\phi)=0$. From Eq.(3.112) which must be verified $\forall\delta\phi$, one obtains the general conditions:

$$\frac{\partial\psi(\phi)}{\partial\phi} = k\boldsymbol{\nabla}^2\phi \text{ in } \Omega \tag{3.113}$$

$$\frac{\partial\psi_s(\phi)}{\partial\phi} = k\boldsymbol{n}_w\cdot\boldsymbol{\nabla}\phi \text{ on } \partial\Omega \tag{3.114}$$

In this Ph.D. work, we will use the cubic[9] wetting condition proposed by Liang et al. (2019) which is defined as

$$\psi_s(\phi) = \frac{a_1}{2}\phi^2 - \frac{a_1}{3}\phi^3 \tag{3.115}$$

where a_1 is a parameter containing the wetting angle θ. Moreover, we consider that the surface tensions γ_{sg} and γ_{sl} are given by the values of ψ_s for $\phi=0$ and $\phi=1$, respectively. Therefore, we have:

$$\gamma_{sg} = \psi_s(\phi=0) = 0 \tag{3.116a}$$

$$\gamma_{sl} = \psi_s(\phi=1) = \frac{a_1}{6}. \tag{3.116b}$$

Thomas Young has linked the three surface tensions (liquid-gas, solid-gas, solid-liquid) with the wetting contact angle θ by this formula:

$$\cos\theta = \frac{\gamma_{sg}-\gamma_{sl}}{\gamma_{lg}}. \tag{3.117}$$

[9] A linear wall potential was commonly used in the literature, particularly by Briant (2002); Lee and Liu (2008). However, it has been found that a linear form leads to numerical problems, and high-order potentials can help resolve the spurious film problem.

Based on Eqs. (3.116a), (3.116b), and (3.23), one finds that:

$$\cos\theta = -\frac{a_1}{\sqrt{2k\beta}}. \tag{3.118}$$

Finally, by replacing a_1 deduced from Eq. (3.118) in Eq.(3.114), the wetting condition can be ultimately written as follows:

$$\boldsymbol{n_w}\cdot\boldsymbol{\nabla}\phi|_{x_w} = -\sqrt{\frac{2\beta}{k}}\cos\theta\left(\phi_w - \phi_w^2\right) \tag{3.119}$$

3.5.2 Numerical discretization

In this section, Eq. (3.119) will be discretized for spherical particles in order to be used in capillary bridge applications. It is first worth mentioning that $\boldsymbol{n_w}\cdot\nabla\phi|_{x_w}$ corresponds to the derivative of ϕ along direction $\boldsymbol{n_w}$. Consequently, Eq. (3.119) is discretized using a central difference scheme. For a boundary solid node (i,j,k) we have

$$\boldsymbol{n_w}\cdot\boldsymbol{\nabla}\phi|_{x_w} = \frac{\phi_p - \phi_{(i,j,k)}}{2h} \tag{3.120}$$

where h is the distance from the solid node (i,j,k) to the solid surface and ϕ_p is the interpolated value of ϕ at the fluid node located at a distance h from the solid surface (see Figure 3.2). ϕ_p is determined using a trilinear interpolation between the adjacent nodes in a cubic lattice 3D conditions. See Appendix D.2.1 for more details about the trilinear interpolation. The value of ϕ_w on the solid interface is then approximated as:

$$\phi_w = \frac{\phi_{(i,j,k)} + \phi_p}{2}. \tag{3.121}$$

Combining Eqs. (3.119), (3.120) and (3.121) lead to (see Appendix D.2.2)

$$\begin{cases} \phi_{(i,j,k)} = \dfrac{1}{a}\left(1 + a \pm \sqrt{(1+a)^2 - 4a\phi_p}\right) - \phi_p, & \left(\theta \neq \dfrac{\pi}{2}\right) \\ \phi_{(i,j,k)} = \phi_p & \left(\theta = \dfrac{\pi}{2}\right) \end{cases} \tag{3.122}$$

with $a = -h\sqrt{\dfrac{2\beta}{k}}\cos\theta$. In practice, h is usually approximated to half $h = \dfrac{1}{2}$ in lattice units. Note that for $\theta \neq \dfrac{\pi}{2}$, there are two solutions, but only the one that ranges between 0 and 1 is selected.

3.6 Units conversion

In LBM simulations, the mesh size and the time step are supposed to be equal to 1, i.e. $\Delta x_{\text{LBM}} = 1$ lattice unit (lu) and $\Delta t_{\text{LBM}} = 1$ lattice unit (lu) which are absolutely different from Δx_{Phy} and Δt_{Phy}. Therefore, a rescaling between physical and lattice units must be performed in order to make the simulations consistent with the physics at hand, because all the LBM parameters are given in lu.

For sake of simplicity, the following convention will be used: the subscripts 'LBM' and 'Phy' will be replaced by $\widetilde{\square}$ and nothing $\square$ for lattice and physical units, respectively. For instance, $\Delta x_{\text{LBM}} = \widetilde{\Delta x}$ and $\Delta x_{\text{Phy}} = \Delta x$.

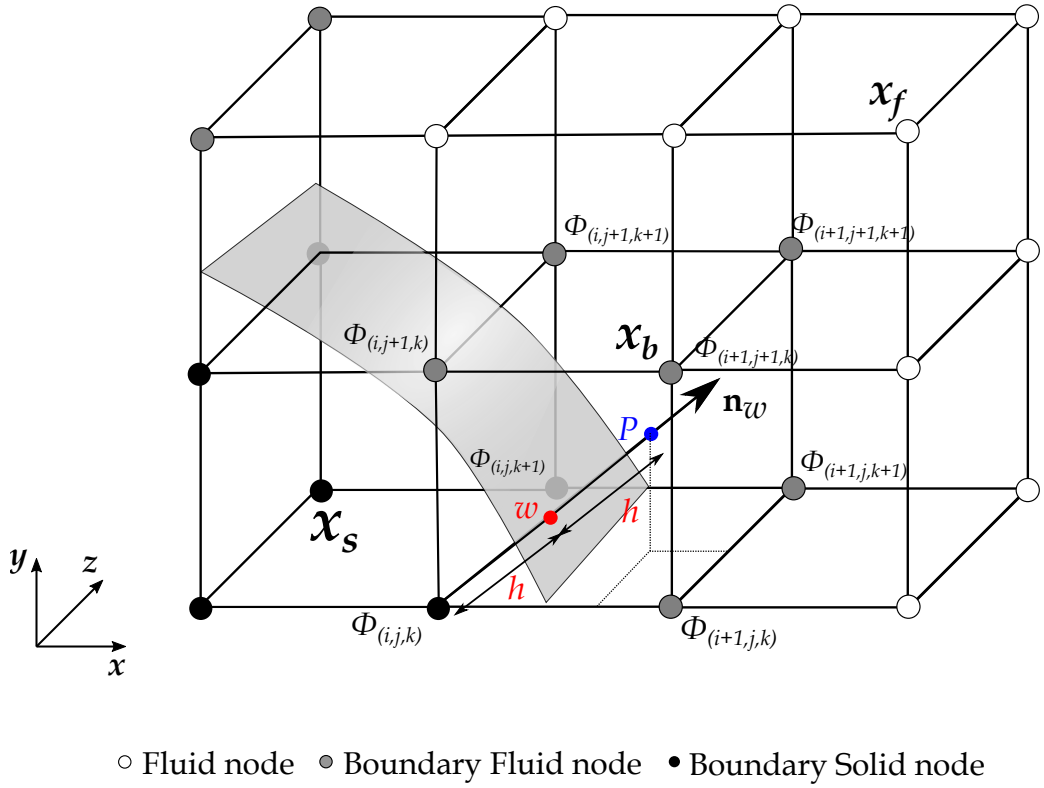

Figure 3.2: Scheme depicting the geometric parameters for applying the wetting condition. $\boldsymbol{n}_w$ is the normal unit vector pointing away from the solid wall to the fluid. A tri-linear interpolation is used to obtain the unknown phase value ϕ_p between the 8 adjacent nodes in a cubic lattice.

The re-scaling of lengths[10], time, and densities are defined as follows

$$\Delta x = C_{\mathrm{L}} \underbrace{\widetilde{\Delta x}}_{=1} \qquad \Delta t = C_t \underbrace{\widetilde{\Delta t}}_{=1} \qquad \rho = C_\rho \widetilde{\rho} \tag{3.123}$$

where the units involved are respectively meters (m), seconds (s), and kg/m^3. Eq. (3.123) gives the so-called canonical conversion factors. As will be seen below, the choice of C_t in the context of capillary bridges is slightly tricky. Let us start with the two easiest ones C_{L} and C_ρ:

- C_{L}: physical and lattice characteristic lengths must be chosen L_{C} and $\widetilde{L}_{\mathrm{C}}$, respectively. For instance, if the physical characteristic length of the domain is $L_{\mathrm{C}} = 1$ cm and the lattice characteristic length domain[11] $\widetilde{L}_{\mathrm{C}} = 200$, thus $C_{\mathrm{L}} = \Delta x = L_{\mathrm{C}}/\widetilde{L}_{\mathrm{C}}$ [cm];

- C_ρ: it is purely and solely a choice of the user. In this study, the canonical density conversion factor is chosen to be $C_\rho = 1$ [kg.m^{-3}]. In other words, $\rho_{\mathrm{water}} = \widetilde{\rho}_{\mathrm{water}} = 1000$ and $\rho_{\mathrm{air}} = \widetilde{\rho}_{\mathrm{air}} = 1$;

The first step to determine the conversion coefficient of any given physical parameter is to link its unit to the canonical aforementioned ones. For instance, the unit of surface

[10] It is supposed that the meshes are equal in all directions, i.e. $\Delta x = \Delta y = \Delta z$.

[11] The lattice characteristic length domain is simply the number of meshes in the domain in a given direction.

tension γ becomes:

$$[\gamma] = \mathrm{N.m^{-1}} = \overbrace{\mathrm{kg.m.s^{-2}}}^{\mathrm{N}}.\mathrm{m^{-1}} = \frac{\mathrm{kg}}{\mathrm{m^3}}.\mathrm{m^3}.\mathrm{s^{-2}} = C_\rho.\frac{C_\mathrm{L}^3}{C_t^2}. \tag{3.124}$$

Thus, the conversion between surface tension γ in lattice and physical units yields:

$$\gamma = \underbrace{C_\rho \frac{C_\mathrm{L}^3}{C_t^2}}_{C_\gamma}\ \widetilde{\gamma}\,[\mathrm{N.m^{-1}}]. \tag{3.125}$$

When the fluid is in motion, obviously, the time step is controlled by the viscosity. In our study, however, we are solely interested in the equilibrium state of the capillary bridge, whereas the transition phase between initialization and equilibrium is not investigated. Therefore, the time step C_t is chosen via γ from Eq. (3.125) as follows:

$$\Delta t = C_t = \sqrt{\frac{\widetilde{\gamma}}{\gamma} C_\rho\ C_\mathrm{L}^3}\ [\mathrm{sec}]. \tag{3.126}$$

Since we are interested in capillary forces, suctions (pressures), and stresses, the conversion coefficients between lattice and physical units are here listed, following the same way as Eq. (3.125):

$$C_\mathrm{F} = C_\rho \frac{C_\mathrm{L}^4}{C_t^2} \Longrightarrow F = C_\mathrm{F}\widetilde{F} \tag{3.127a}$$

$$C_\mathrm{P} = C_\rho \frac{C_\mathrm{L}^2}{C_t^2} \Longrightarrow P = C_\mathrm{P}\widetilde{P}. \tag{3.127b}$$

3.7 Choice of LBM parameters

In order to accurately model real multiphase fluids, one should choose wisely the simulation parameters, especially in LBM models.
First, the interface width is selected, generally $\widetilde{W} = 5-10$ lu to make the interface smooth enough—as shown in Figure (3.3)—to preclude numerical instabilities.

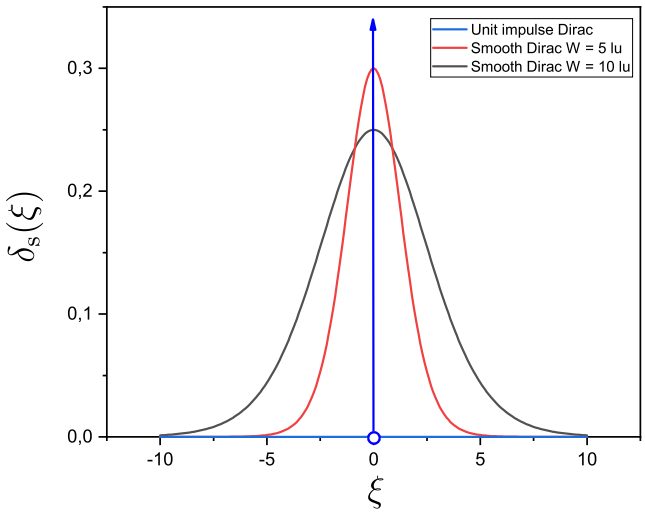

Figure 3.3: Smooth Dirac functions for $\widetilde{W} \in \{5; 10\}$ lu as well as the unit impulse Dirac function.

Next, densities $\widetilde{\rho}_l$ and $\widetilde{\rho}_g$ are calculated using Eq. (3.123). As previously mentioned, C_ρ is usually taken as 1 which is the case in all the simulations in this work. Then, C_L is calculated based on the physical and LBM characteristic lengths L_c and $\widetilde{L}_c$ as follows: $C_\mathrm{L} = \dfrac{L_c}{\widetilde{L}_c}$. Following that, $\widetilde{\gamma}$ is chosen whereby C_t is calculated using Eq. (3.126). Once the C_t is determined, the relaxation times $\tilde{\tau_h}^\ell$ and $\tilde{\tau_h}^g$ are computed based on the scaling of the liquid and gas viscosities:

$$\nu^{\ell,g} = \underbrace{\tilde{c}_s^2 \left(\tilde{\tau}_h^{\ell,g} - \frac{\widetilde{\Delta t}}{2} \right)}_{\widetilde{\nu}^{\ell,g}} \overbrace{\frac{C_\mathrm{L}^2}{C_t}}^{C_\nu} \iff \tilde{\tau}_h^{\ell,g} = \frac{C_t \nu^{\ell,g}}{\tilde{c}_s^2 C_\mathrm{L}^2} + \frac{\widetilde{\Delta t}}{2}. \tag{3.128}$$

According to Timm et al. (2016), numerical instabilities are observed if the values of $\tilde{\tau}_h^{\ell,g}$ are too close of $\dfrac{1}{2}$. Moreover, $\widetilde{\gamma}$ determines C_t whereby relaxation times are calculated.

3.8 Conclusion

In this chapter, the multi-phase LBM model was presented. A phase-field-based model—Allen-Cahn equation—coupled with the Navier-Stokes equation through a surface tension force was elaborated. Next, an improved wetting condition was provided explaining the numerical scheme implementation. Lastly, a unit conversion was given to connect real physical units to lattice ones.

In the next chapter, this model will be validated on several benchmarks, amongst others, Rayleigh-Taylor instability, and water droplets on curved surfaces. Then applications on capillary forces for doublet and triplet will be carried out.

Chapter 4

Numerical Validations

4.1 Introduction

After presenting the method in Chapter 3, it is time to proceed with the validation of the phase-field-based LBM model along with the wetting condition. This validation process is structured as follows:

- LBM Model Validation: We start by conducting the Rayleigh-Taylor instability, which serves as a fundamental benchmark for fluid flow simulations.
- Wetting Angle Evaluation: Following the LBM model validation, we proceed to evaluate the wetting angle across various examples. This includes scenarios such as liquid droplets on spherical grains and planes, allowing us to verify the accuracy of wetting angle predictions.
- Capillary bridge geometry and mean curvature H: We then push the boundaries of the proposed model to assess its ability to accurately represent the geometries of capillary bridges formed between two spherical particles. Furthermore, we investigate the evolution of the mean curvature (H) as we vary the separation distance between these two particles. The results obtained through the LBM simulations are compared with analytical solutions based on the Young-Laplace Equation (YLE).
- A new expression for capillary forces: In the next stage, a new formulation is derived to calculate capillary forces applied to spherical particles. First, its validity is examined in the context of two spherical grains in the pendular regime. Afterward, we extend its application to the funicular regime, considering a three-particle configuration.

This rigorous validation process ensures that the phase-field-based LBM model, along with the wetting condition, is a reliable and accurate tool for subsequent practical applications and research investigations at the REV scale.

4.2 Rayleigh-Taylor Instability

Rayleigh-Taylor instability belongs to the family of hydrodynamics fingering instabilities. This instability is induced by the density stratification and the interface's perturbation, where the heavy fluid ρ_h rests on a lighter one ρ_ℓ in a gravitational field (Sharp, 1983). During this phenomenon, the fluids will keep pushing each other until the inversion takes place. This instability will lead to the creation of spikes, bubbles, and saddles as shown in Figure 4.1).

4.2.1 Choice of the LBM parameters

The simulation will be conducted in the following domain: $N_x \times N_y \times N_z = [0; L] \times [0; 4L] \times [0; L]$ with $L = 128$. In order to validate the Allen-Cahn-based model, a comparison between the present model and other models in the literature will be provided; see He et al. (1999); Zu and He (2013). To do so, the choice of the parameters will be done based on the dimensionless numbers used for the other models, such as, Reynold's number (Re), Capillary number (Ca), and Atwood number (At) which are defined as follows:

$$\mathrm{Re} = \frac{L \times U}{\nu} = 128 \tag{4.1a}$$

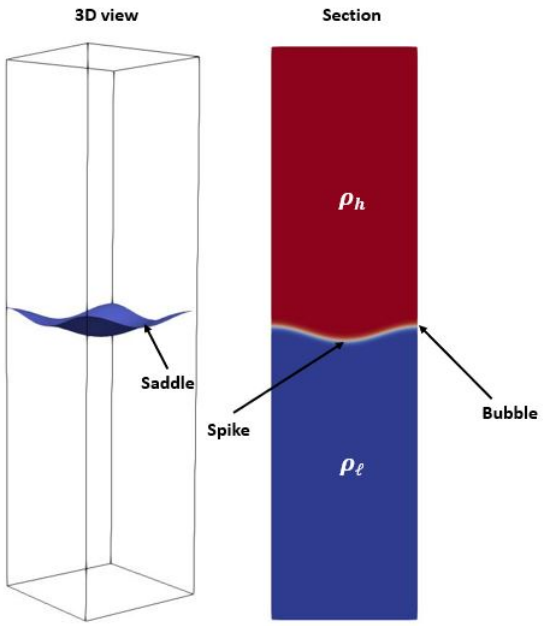

Figure 4.1: Spike, bubble, and saddle in 3D and 2D (section) views. The heavier fluid of density ρ_h is resting on the lighter one of density ρ_l

$$\text{Ca} = \frac{\mu \times U}{\gamma} = 85.71 \tag{4.1b}$$

$$\text{At} = \frac{\rho_h - \rho_\ell}{\rho_h + \rho_\ell} = 0.5. \tag{4.1c}$$

Accordingly, the LB parameters in lattice units are chosen in the following way:

- The lattice velocity is chosen to be $U = 0.02$ in such a way that the Mach number Ma is acceptable in order to respect the incompressibility effect;
- Based on Eq. (4.1a), the kinematic viscosity is computed and has the value of $\nu = 0.02$;
- Based on Eq. (2.61b), we consider $\tau = 0.56$;
- The densities $\rho_h = 0.12$ and $\rho_\ell = 0.04$ chosen are the same as in He et al. (1999); Zu and He (2013);
- Based on Eq. (4.1b), the value of the surface tension is $\gamma = 1.12 \times 10^{-6}$; and
- The gravity in the -y direction[1] $g = -3.125 \times 10^{-6}$, is deduced from the characteristic velocity $U = \sqrt{L \times g}$, the same as in He et al. (1999); Zu and He (2013).

In order to induce the Rayleigh-Taylor instability using LBM simulation, a perturbation at the interface[2] must be made. In this example, a perturbation of 5% is chosen, in other words, the position of the interface at the initialization phase will be as follows:

$$y_{\text{interface}}(x, z) = 2L + 0.05L \left[\cos\left(\frac{2\pi x}{L}\right) + \cos\left(\frac{2\pi z}{L}\right)\right] \tag{4.2}$$

[1]The gravity points downward, hence the negative sign.
[2]The white curved line in the 2D as shown in Figure 4.1

Then, the initialization of the order parameter will be:

$$\phi(x,y,z) = 0.5 + 0.5\tanh\left[2 \times \frac{y - y_{\text{interface}}(x,z)}{W}\right] \tag{4.3}$$

In this simulation, both the hydrodynamic as well as the interface-tracking equations are solved within the D3Q19 scheme. It has been found that both the D3Q7 and D3Q19 produce exactly the same results. Contrarily, the D3Q15 scheme was not numerically stable for this benchmark.

Results in Figure (4.2) show the evolution of the interface for a value of $\phi = 0.5$ for different dimensionless times $t^* = t/\sqrt{L/g}$.

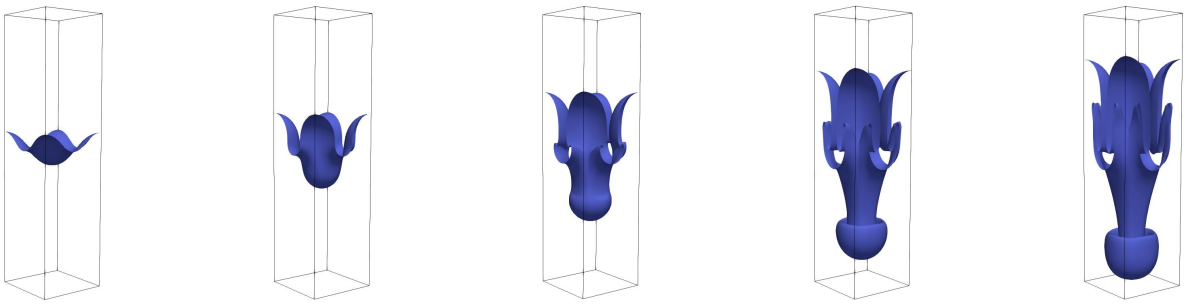

Figure 4.2: Evolution of the interface $\phi = 0.5$ as a function of the dimensionless time $t^* = 1; 2; 3; 4; 4.5$, respectively.

Figure (4.3) depicts the dimensionless position ($y^* = y/L$) of the spike, bubble, and saddle for the present model and others used in the literature. Obviously, the results shown in the figure, prove that the Allen-Cahn-based model is in complete agreement with the other models.

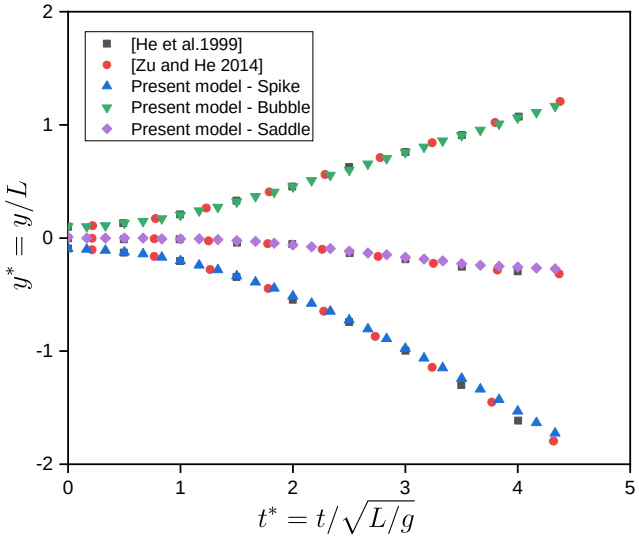

Figure 4.3: Comparison between present LB, He et al. (1999), and Zu and He (2013) models of $y^* = y/L$ in function of $t^* = t/\sqrt{L/g}$

4.3 Wetting condition Benchmark

As already indicated, one of the most important parameters in capillary bridges is the contact angle θ. Before getting into the details of capillary bridges, the wetting

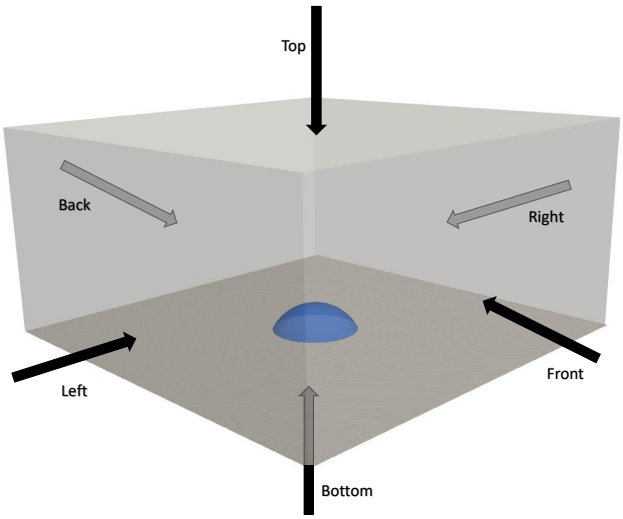

Figure 4.4: Sketch showing different directions.

condition—previously explained in Section 3.5—must be validated in two benchmarks: water droplets on flat and curved surfaces.

4.3.1 Water droplet on flat surfaces

In order to validate the wetting condition, a 3D drop on a plane is simulated with a density ratio $\rho_{\text{water}}/\rho_{\text{air}} = 1000$. The initial radius of the drop is $R_0 = 20$ lu, and the domain size is $N_x \times N_y \times N_z = [0; 2L] \times [0; L] \times [0; 2L]$ with $L = 128$. The parameters used for this simulation are $\gamma = 0.2$, $W = 5$, and $M = 0.1$. The initialization of the parameter order ϕ is

$$\phi(x, y, z) = \frac{1}{2} + \frac{1}{2} \tanh\left[2 \times \frac{R_0 - \sqrt{(x - x_0)^2 + (y - y_0)^2 + (z - z_0)^2}}{W}\right] \tag{4.4}$$

with $x_0 = N_x/2$, $y_0 = 1$, and $z_0 = N_z/2$.

Periodic Boundary Conditions (PBCs) are applied on the left, right, front, and back of the domain as shown in Figure (4.4). Regarding the top and the bottom, the wetting and the bounce-back conditions are applied.

In the absence of gravity, the shape of the drop must take a spherical shape at equilibrium. For that reason, in order to verify if the contact angle is respected at the equilibrium, it must be geometrically computed. Two cases will be found, which are:

$$\theta = \begin{cases} 2\tan^{-1}\left(2\dfrac{h}{b}\right) & \text{For} \quad \theta \leq \frac{\pi}{2} \\ \arcsin\left[\dfrac{h - r}{r}\right] + \dfrac{\pi}{2} & \text{For} \quad \theta > \frac{\pi}{2} \end{cases} \tag{4.5}$$

where h, r, and b are geometric parameters described in Figure (4.5).

Figure (4.6) depicts the shapes of the water droplets at equilibrium on a plane for different contact angles, $\theta \in \{30; 60; 90; 120\}^\circ$. All the angles are calculated and summarized in Table 4.1. Given that the absolute errors are small enough, the wetting condition on plane surfaces is quite reliable.

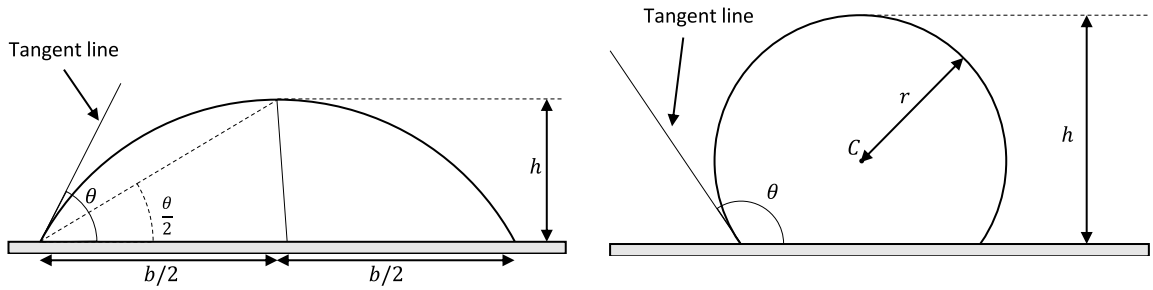

Figure 4.5: Geometrical methods to determine the contact angle θ at of a droplet on a plane at equilibrium. (a) $\theta \leq \frac{\pi}{2}$ and (b) $\theta > \frac{\pi}{2}$.

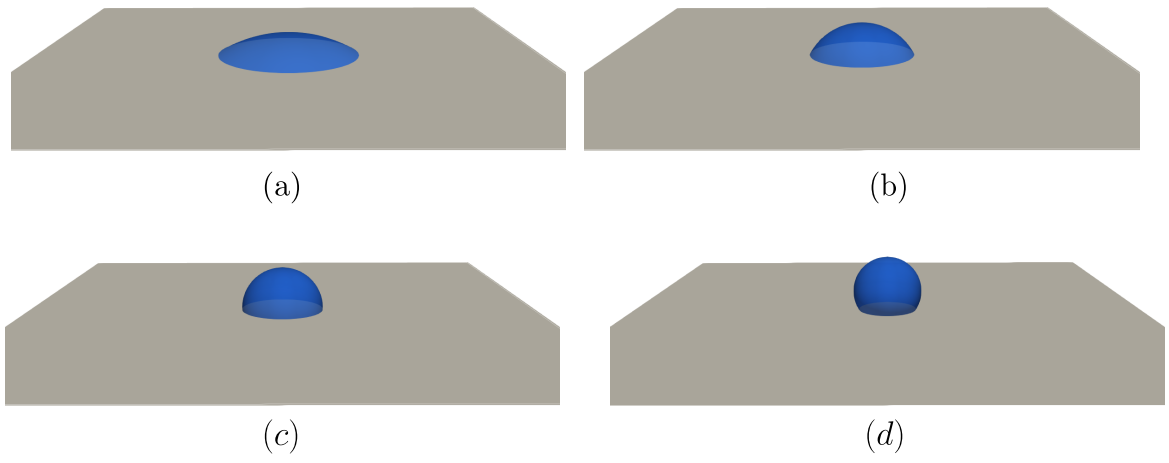

Figure 4.6: The shape of water droplets at equilibrium on a plane. (a) $\theta = 30°$, (b) $\theta = 60°$, (c) $\theta = 90°$, and (d) $\theta = 120°$.

Imposed contact angle (°)	Measured contact angle (°)	Absolute error (°)
30	30.33	0.33
60	61.11	1.11
90	91.38	1.38
120	117.20	2.8

Table 4.1: Comparison between measured and imposed contact angles of water drops on a plane.

4.3.2 Water droplet on curved surfaces (spherical particle)

Given that we will be treating capillary bridges between spherical particles, it is wise to study the reliability of the wetting condition of water droplets on spherical grains. A water droplet with a radius $r_0 = 20$ lu is placed at the top of the particle with a radius $R = 60$ lu. The mesh size is $(256 \times 256 \times 256)$. The simulation parameters are $\gamma = 0.2$ lu, $W = 5$ lu, $\rho_l = 1000$ lu, and $\rho_g = 1$ lu. Periodic BCs are applied in all directions. For the solid boundary nodes, we apply the wetting boundary condition Eq. (3.122).

Figure (4.7) shows the shapes of the droplet at equilibrium for different imposed contact angles. To measure the effective contact angle, the generalized Pythagorean theorem is used, i.e.

$$\varphi = \arccos\left(\frac{R^2 + r^2 - d^2}{2rR}\right) \tag{4.6}$$

where r is the drop radius at equilibrium[3], R is the particle radius, and d is the distance between the center of the drop and the particle as shown in Figure (4.8).

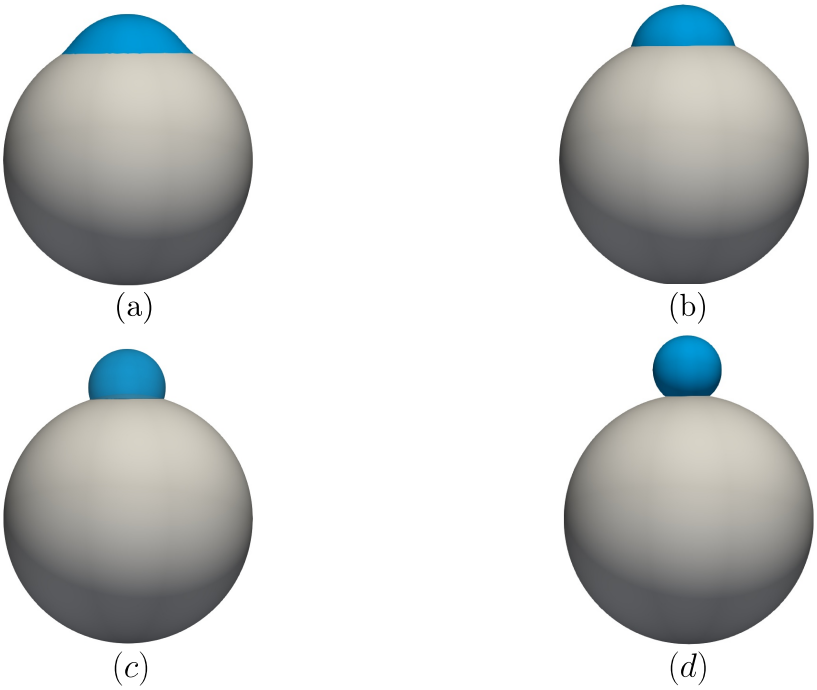

Figure 4.7: Shapes of water droplets on spherical grains at equilibrium. (a) $\theta = 30°$, (b) $\theta = 60°$, (c) $\theta = 90°$, and (d) $\theta = 120°$.

[3]The water droplet at equilibrium is considered to be a spherical cap.

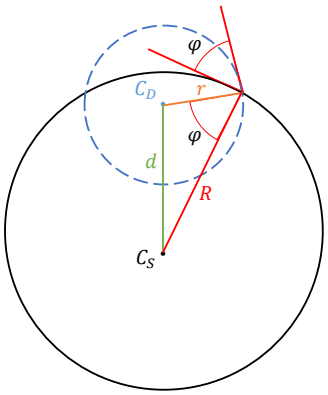

Figure 4.8: Illustration of the effective contact angle φ. C_S and C_D are the centers of the solid particle sphere and water droplet, respectively.

The geometrical parameters d and r are determined using an in-house image processing *Matlab* code (Younes et al., 2023a; Nguyen et al., 2019b,c, 2020a).

Figure (4.9) compares the measured φ and imposed contact θ angles and shows that φ and θ coincide, which validates the wetting condition in Eq. (3.119).

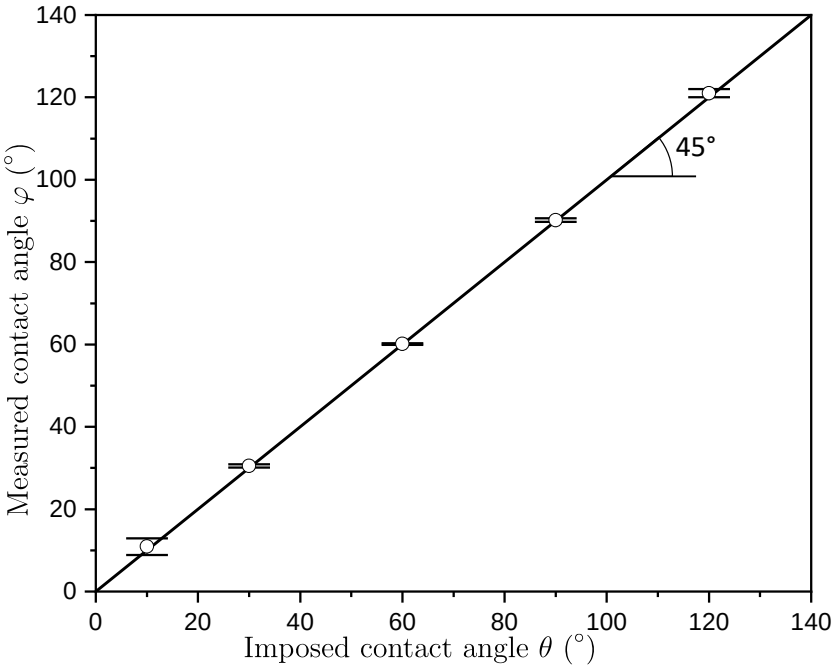

Figure 4.9: Measured (φ) versus imposed contact angles (θ) for a water droplet on a spherical particle. The solid line represents $\varphi = f(\theta) = \theta$.

Imposed θ (°)	R	r	d	Measured φ (°)	Absolute error (°)
30	318.58	180.89	188.0589	30.33	0.33
60	466.57	184.13	407.0714	60.01	0.01
90	462.21	144.97	486.7614	90.98	0.98
120	571.47	158.34	670.72	122.86	2.86

Table 4.2: Comparison between measured and imposed contact angles of water drops on spherical grains (cf. Figure 4.8 for a complete description of the geometrical parameters R, r, and d).

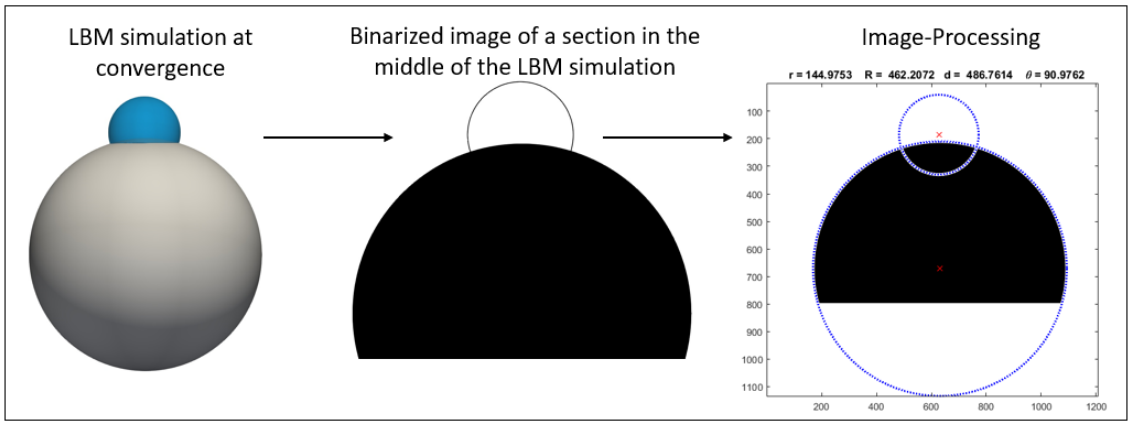

Figure 4.10: Procedure adopted to determine the geometrical parameters d and r to measure the wetting angle from Eq. (4.6).

Results in Table 4.2 show that the wetting condition is highly reliable when dealing with spherical grains.

4.4 Capillary rise - Jurin's Law

The capillary rise benchmark is performed to validate the model. This benchmark consists of a tube with a radius r, which is placed vertically in a reservoir filled with a liquid subjected to gravity. Due to capillary effect in the tube, the liquid will rise to a certain height h as seen in Figure (4.11). In the numerical setup, periodic BCs are applied

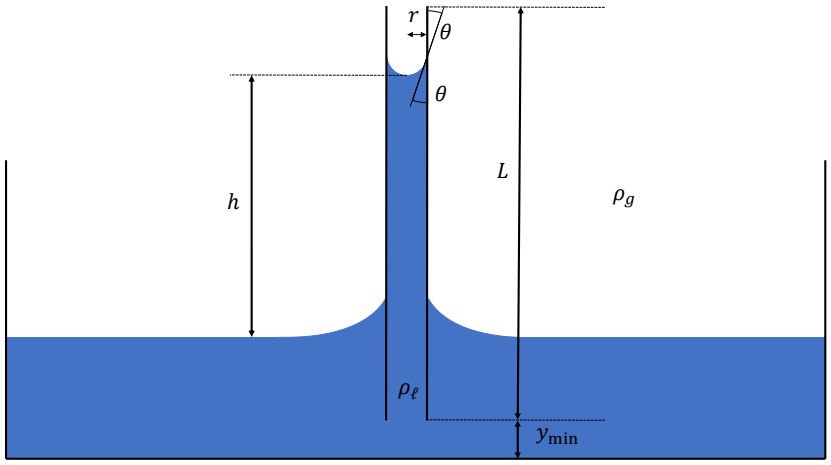

Figure 4.11: Side view schematic describing the capillary rise benchmark.

on the left, right, front, and back boundaries. In both cases, bounce-back and wetting conditions are applied on the tube wall as well as on the top and bottom of the domain. The domain size is $N_x \times N_y \times N_z = 192 \times 224 \times 192$. The domain is initialized with the liquid film below $y = 80$ lu, both inside and outside of the tube. This latter has a thickness of 3 lu, and a radius $r = 12$ lu. The minimum position of the tube is at $y_{min} = 15$ lu with a length $L = 185$ lu as shown in Figure (4.11).

Jurin's law can be applied to find the height h of capillary rise at hydrostatic equilib-

rium

$$h = \frac{2\gamma \cos\theta}{\Delta\rho g r} \tag{4.7}$$

where $\Delta\rho = \rho_\ell - \rho_g$, r is the tube radius, γ is the surface tension, g is the gravity, and θ is the contact angle.

For a contact angle $\theta = 0°$, h yields:

$$h = \frac{2\gamma}{\Delta\rho g r}. \tag{4.8}$$

The parameters for the real system and the simulation are shown in Table 4.3. According to Eq. (4.8), the expected capillary rise is $h = 9.8 \times 10^{-3}$ m with $r = 1.5$ mm.

To simulate the capillary rise, conversion of units must be carried out to link physical to lattice units. In the presence of gravity, the conversion between gravity in lattice and physical units is given as:

$$g = \widetilde{g}\,\frac{C_\ell}{C_t^2}. \tag{4.9}$$

After calculating C_t from (3.125), the gravity in lattice units can be deduced from (4.9) as:

$$\widetilde{g} = g\,\frac{C_\mathrm{t}^2}{C_\ell}. \tag{4.10}$$

The measured equilibrium height (as defined in Figure 4.12) is $h^{lu} = 10.06$ mm (80 lu) which is in good agreement with the expected value of 9.8 mm (78 lu) with error of 2.65 %.

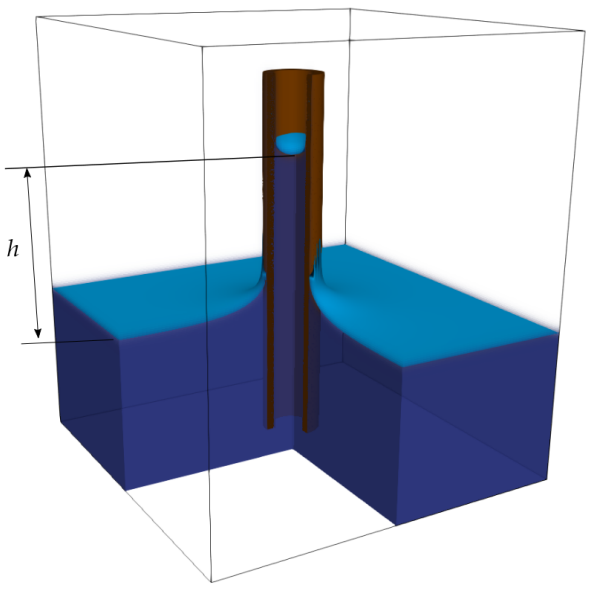

Figure 4.12: Capillary rise at equilibrium.

Quantities	Physical parameters	Value in SI units	Lattice parameters	Values in lattice units
Liquid density (water)	ρ_ℓ	1000 kg/m^3	ρ_ℓ^{lu}	1000
Gas density (air)	ρ_g	1 kg/m^3	ρ_g^{lu}	1
Characteristic length	r	1.5 mm	r^{lu}	12
Surface tension	γ	0.07213 N/m	γ^{lu}	0.2
Contact angle	θ	0°	θ	0°
Gravity	g	9.81 m/s^2	g^{lu}	4.25×10^{-7}
Expected capillary rise	h	9.82 mm	h^{lu}	78.56
Measured capillary rise	h	10.06 mm	h^{lu}	80.5

Table 4.3: Capillary rise parameters in physical and lattice units.

4.5 Capillary bridge profiles

The most important equation that describes precisely capillary bridge profiles is the Young-Laplace Equation (YLE). It is here emphasized that all the simulations of capillary bridges are performed at zero-gravity conditions, which corresponds to the experiments of Mielniczuk et al. (2018) for small volumes of water and small separation distances, when the Bond number is small and when the effect of gravity can be neglected. Thus, horizontal or vertical capillary bridges are exactly the same, as shown in Figures. (1.11) and (4.13), respectively.

4.5.1 Young-Laplace Equation

We recall the expression of Young-Laplace Equation (YLE) that describes the capillary bridge's profile between two solid particles. In the absence of gravity, YLE in the particular case of axisymmetric capillary bridges of revolution around x-axis is classically written as (Gagneux and Millet, 2014)

$$\frac{y''(x)}{(1+y'^2(x))^{3/2}} - \frac{1}{y(x)\sqrt{1+y'^2(x)}} = -\frac{\Delta p}{\gamma} = H \tag{4.11}$$

where $H = -\frac{\Delta p}{\gamma}$ is the mean curvature, $\Delta p = p_{in} - p_{out}$ is the pressure difference between inside and outside of the capillary bridge, γ is the surface tension of the fluid-gas system, and $y(x)$ is the meridian profile shown in Figure (1.11).

Moreover, only capillary bridges with nodoid and unduloid shapes are investigated as they are the most stable cases observed experimentally. The present study is limited to a concave capillary bridge with a convex upper meridian, where the condition $y^* \leq r \sin\delta$ is satisfied.

The main objective of the section is to provide a demonstration that—by solving ACE as well as NSE coupled with the wetting condition—a spherical liquid drop between two solid grains will take the shape of a capillary bridge at equilibrium as shown in Figure (4.13).

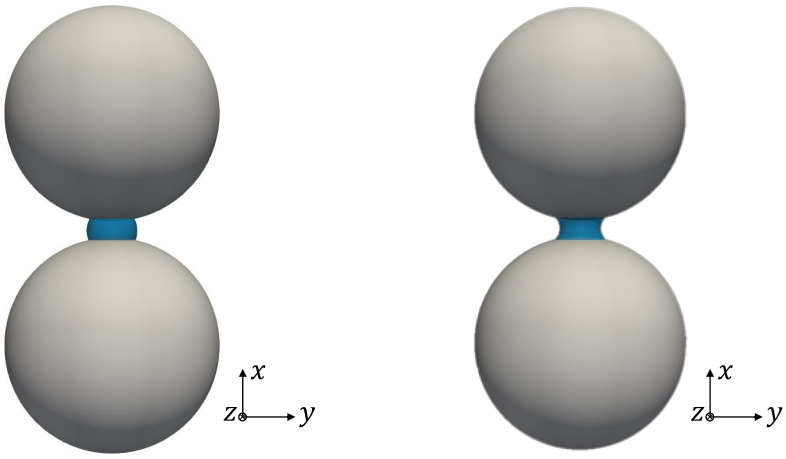

(a) (b)

Figure 4.13: From: (a) the initialization of a water droplet at mid-distance to the convergence, and (b) of the capillary bridge for water volume of $V = 10\,\mu\text{L}$, for $\theta = 20°$.

4.5.2 Numerical simulations and comparison with the solution of Young-Laplace equation

We now simulate the formation of a capillary bridge between two spherical particles of the same size with the LBM code for multi-phase flow developed and validated on several benchmarks and examples. Then, we use an in-house image processing code developed in *Matlab* to solve the Young-Laplace equation as an inverse problem when the R.H.S involving the capillary pressure is unknown, but when we can access the half-filling angle δ, the wetting angle θ and the neck radius y^*, as depicted in Figure 1.11 (Gagneux et al., 2016; Nguyen et al., 2019a; Mielniczuk et al., 2018; Nguyen et al., 2019c,d). The values of y^*, δ, and θ will be deduced from image processing performed on the results of LBM simulations.

Once the geometrical parameters y^*, δ, and θ are determined, the criterion for determining the shape of capillary bridges, given in Appendix D.3, is checked and then the Young-Laplace equation is numerically solved as an inverse problem based on integration of the parametric equations (D.45)-(D.46) or (D.53)-(D.54).

Concerning the LBM simulations, they were performed by considering a domain size of $Nx \times Ny \times Nz = 160 \times 250 \times 160$. The domain length in the x-direction in the physical unit is $L_x = 0.015$ m; thus, the lattice length is $\Delta x \approx 7.5 \times 10^{-5}$ m. The particle radii are fixed at $R = 4$ mm, the water volume of 10 μL, and different separation distances $D \in \{0.5, 1, 1.5, 2, 2.25\}$ mm.

After the convergence of the LBM simulation[4], the main steps are the following (they are summarized in Figure 4.14):

1. A section is made in the middle of the bridge at $(Nz/2)$, then

2. an isoline of the value of $\phi = 0.5$ is drawn[5] using *Paraview*, then

3. the image is binarized using the open-source image processing software *ImageJ*, and

[4]The simulation converges when the evolution of water volume is stabilized in time.
[5]Since the interface has a thickness W, a value of $\phi = 0.5$ corresponds to the middle of the interface.

4. the binarized image is analyzed using a *Matlab* code which calculates the geometrical parameters y^*, δ, and θ and solves the Young-Laplace equation as an inverse problem using the theory presented in Appendix D.3. Finally, the capillary bridge profile is plotted on the image resulting from the LBM simulation.

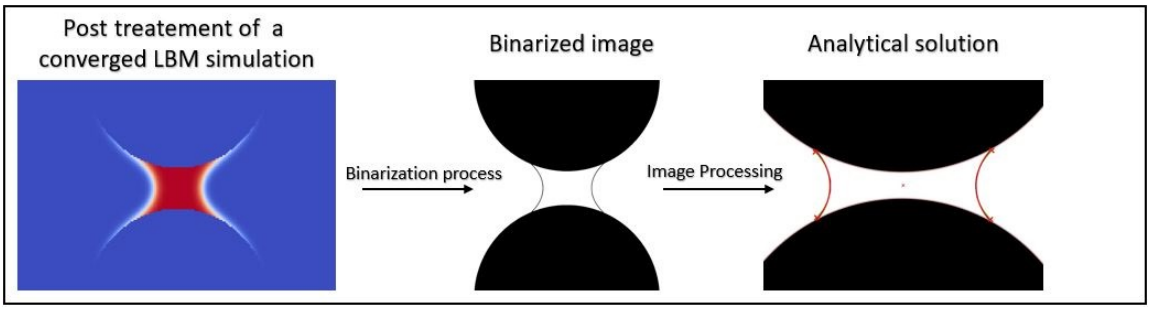

Figure 4.14: Flow chart summarizing the above steps.

More precisely, once the image is binarized, the edges of the capillary bridge and the two particles are detected using the image treatment tool *ImageJ*, and the image is saved in Tiff format (table of 1 for black contours and 0 otherwise) to be treated using the *Matlab* code.

The *Matlab* code will detect the center of the upper and lower spheres and both spheres radii, using the method proposed by Taubin (1991), and the coordinates of the triple points. The half filing angle δ_j for each triple point ($j = 1$ to 4) is calculated, then the resulting half-filling angle δ is averaged of all δ_j.

The contact angle θ_j is calculated using the tangent vectors to the particle and to the profile of the capillary bridge approximated by a sixth-degree polynomial at the triple point. Then, the resulting contact angle θ is averaged for all θ_j. More details of the image treatment procedure can be found in (Gagneux et al., 2016).

Once the geometrical parameters (y^*, δ, θ) are determined, the criterion for determining the shape of capillary bridges (nodoid and unduloid) is checked. After that, the corresponding parameters a and b^2 are calculated. Then, the resulting curves (a portion of nodoid or unduloid) are plotted on the same image of the capillary bridge profile as shown in Figure (4.15).

4.5.3 Comparison between theoretical, experimental, and numerical results

In this section, we present a comparison between experimental, theoretical, and numerical results of the mean curvature H for different separation distances between particles. For the present study, H is deduced in two ways: using the image processing tool based on the theory of Section D.3, using Eqs. (D.52) or (D.60), or directly from the LBM simulation using the definition of $H = -\Delta P/\gamma$.

In Figure (4.16), we plot the non-dimensional $H^* = H \times R$ value, where R is given in lattice units. The values obtained are compared with the experimental data of (Mielniczuk et al., 2018). We observe that for small separation distance, e.g., $D \in \{0.5; 0.1\}$ mm, the shape of the capillary bridge is a portion of nodoid ($H > 0$). For larger separation distances, however, for instance, $D \in \{1.5; 2; 2.25\}$ mm, the capillary bridge profile switches to a portion of unduloid ($H < 0$). The inversion of the sign of H, from positive (nodoid) to negative (unduloid), can be easily observed with the increasing of separation

distance between spherical grains. Therefore, we recover—via LBM simulations, with a rather accurate precision— the experimental data of Mielniczuk et al. (2018).

4.5.4 Discussion of results

Based on the aforementioned results of Figures (4.15) and (4.16), the shapes of the capillary bridges correspond exactly to the ones found by YLE. It is therefore obvious that the two-phase NSE converges somehow to YLE at equilibrium when the fluid velocity $\boldsymbol{u}$ tends toward zero. Indeed, in the absence of gravity and at equilibrium, NSE (3.12) reduces to

$$-\boldsymbol{\nabla} \boldsymbol{p} + \boldsymbol{F}_s = 0 \tag{4.12}$$

with:

$$\boldsymbol{F}_s = -\gamma \kappa \boldsymbol{n} \delta_s. \tag{4.13}$$

From (4.12), we obtain in the normal direction to the interface

$$-\boldsymbol{n} \cdot \boldsymbol{\nabla} \boldsymbol{p} = \gamma \kappa \delta_s \tag{4.14}$$

where the dot denotes the scalar product of $\mathbb{R}^3$. Note that δ_s is equal to zero outside the diffuse interface and so that the surface tension force $\boldsymbol{F}_s$ vanishes and the pressure is constant. By integrating (4.14) along ξ across the diffuse interface, as seen in Figure (3.1a), we get[6]

$$-\int_{-\infty}^{+\infty} \boldsymbol{n} \cdot \boldsymbol{\nabla} p \mathrm{d}\xi = \gamma \kappa \int_{-\infty}^{+\infty} \delta_s \mathrm{d}\xi = \gamma \kappa \tag{4.15}$$

as κ is constant with respect to ξ and the surface tension γ is assumed to be constant also.

Moreover, we have $-\int_{-\infty}^{+\infty} \boldsymbol{n} \cdot \boldsymbol{\nabla} p \mathrm{d}\xi = p_{\text{in}} - p_{\text{out}}$, as p is constant outside the interface. Therefore, we recover the classical Young-Laplace equation:

$$\Delta p = \gamma \kappa. \tag{4.16}$$

For axisymmetric capillary bridges of revolution, Eq. (4.16) is equivalent to (4.11). This result proves that the modified Navier-Stokes equation (3.12) for two-phase flow converges at equilibrium to the Young-Laplace equation. It explains why the LBM simulations performed enable us to recover very accurately the capillary bridge profiles, and solutions of the Young-Laplace equation.

4.6 Computation of capillary forces

After validating the model as well as the wetting condition through benchmarks, the problem of evaluating the capillary forces can be next tackled. In this section, we will see that classical stress expression in a Newtonian fluid is not sufficient for computing capillary forces. It is then necessary to include a supplementary adhesion term—due to Fisher (1926)—in order to retrieve the experimental data. In this section, a numerical method is presented to compute this supplementary term.

[6] By definition of the Dirac interface δ_s, we have $\int_{-\infty}^{+\infty} \delta_s \mathrm{d}\xi$.

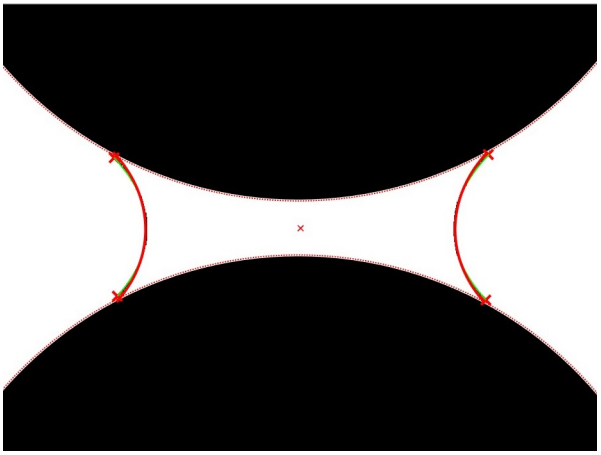

(a) Portion of nodoid, D =0.5mm, y^*=1.577mm, δ_1=27.84°, δ_2=28.8°, θ_1=19.06°, θ_2=21.15°.

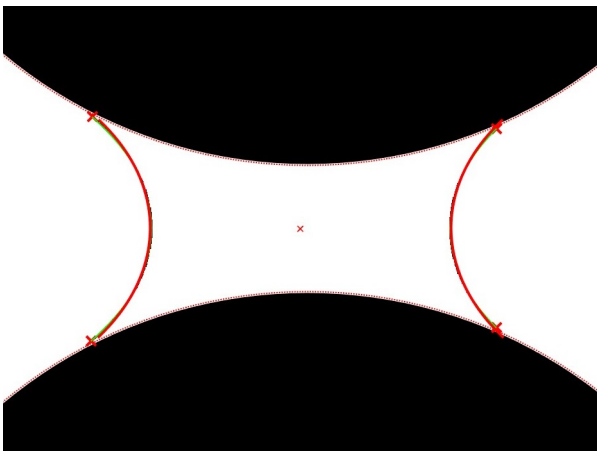

(b) Portion of nodoid, D = 1mm, y^*=1.265mm, δ_1=26.75°, δ_2=23.32°, θ_1=18.52°, θ_2=18.6°.

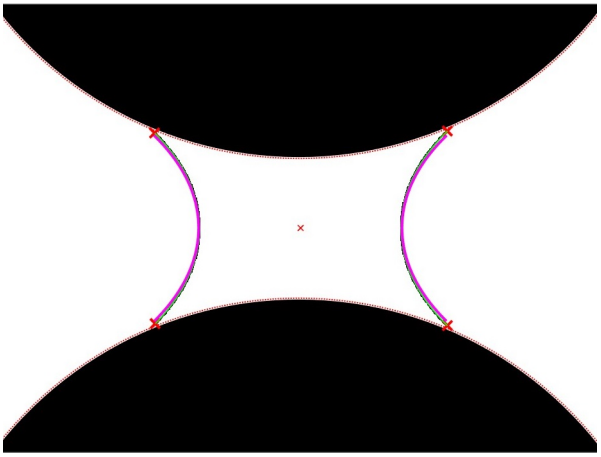

(c) Portion of unduloid, D = 1.5mm, y^*=1.062mm, δ_1=21.91°, δ_2=22.13°, θ_1=22.13°, θ_2=22.88°.

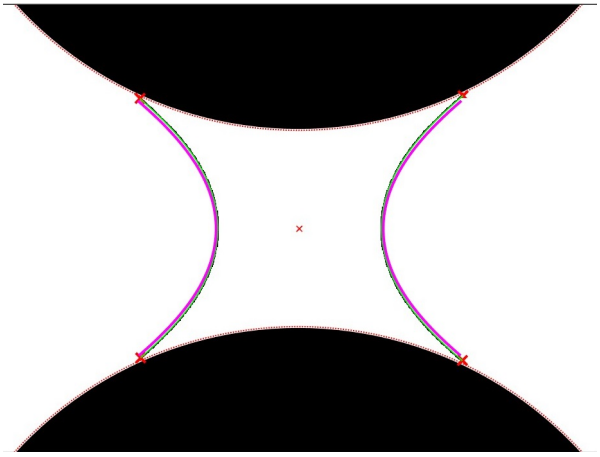

(d) Portion of unduloid, D = 2mm, y^*=0.8713mm, δ_1=24.25°, δ_2=25.3°, θ_1=16.06°, θ_2=16.23°.

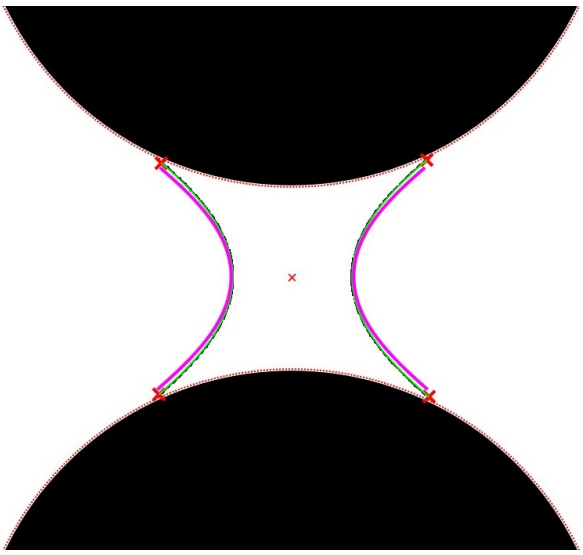

(e) Portion of unduloid, D = 2.25mm, y^*=0.767mm, δ_1=23.7°, δ_2=24.77°, θ_1=16.29°, θ_2=16.35°.

Figure 4.15: Superposition between theoretical and numerical shapes of capillary bridge profiles.

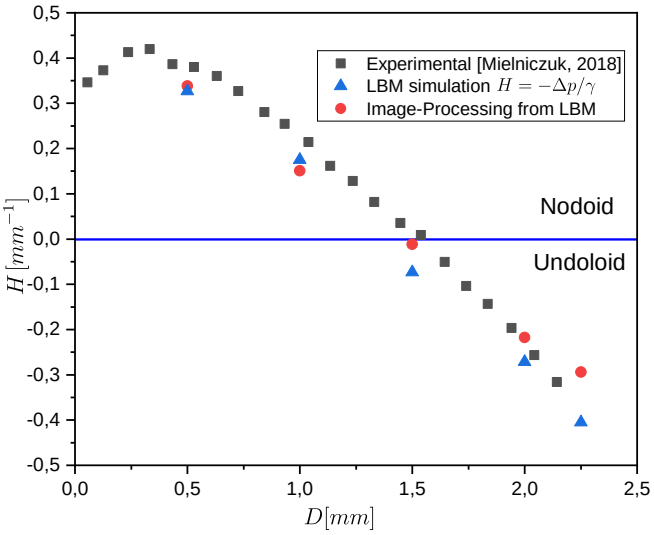

Figure 4.16: Mean curvature H [mm^{-1}] of capillary bridge versus separation distances D [mm]. $H > 0$ and $H < 0$ correspond to nodoid and unduloid shapes, respectively.

4.6.1 Forces exerted by the fluid on a solid

4.6.1.1 Classical case without interface

In a classical way, the force exerted by a fluid on a solid can be calculated based on the integration of the fluid stress tensor $\boldsymbol{\sigma}_f$ on a given surface Ω close to the particle as shown in Figure (4.17). Thus,

$$\boldsymbol{F}_f = \int_{\Omega} \boldsymbol{\sigma}_f \cdot \boldsymbol{n}_{\Omega} \mathrm{d}S \tag{4.17}$$

where $\boldsymbol{n}_{\Omega}$ is the outer unit normal vector to the surface Ω and $\mathrm{d}S$ is an elementary area element. The stress tensor $\boldsymbol{\sigma}_f$ for a Newtonian fluid is classically given by

$$\boldsymbol{\sigma}_f = -p\boldsymbol{I} + \boldsymbol{\tau} \tag{4.18}$$

where p is the fluid pressure, $\boldsymbol{I}$ is the identity matrix in $\mathbb{R}^3$.
The viscous stress tensor $\boldsymbol{\tau}$ is defined as

$$\boldsymbol{\tau} = 2\mu(\boldsymbol{\nabla}\boldsymbol{u} + \boldsymbol{\nabla}\boldsymbol{u}^T) \tag{4.19}$$

where μ is the dynamic fluid viscosity ($\mu = \rho\nu$) and $\boldsymbol{u}$ the fluid velocity. Eq. (4.17) is valid when no discontinuity surfaces are intercepted by Ω. Let us calculate the contribution (4.17) over the domain Ω surrounding the solid S—Figure (4.17). The domain Ω can be split into Ω_g and Ω_l ($\Omega = \Omega_g \cup \Omega_l$), where Ω_g and Ω_ℓ are the gas and liquid domains[7], respectively. From Eq. (4.17), we have

$$\boldsymbol{F}_f = \int_{\Omega_g} \boldsymbol{\sigma}_f \cdot \boldsymbol{n}_{\Omega} \mathrm{d}S + \int_{\Omega_l} \boldsymbol{\sigma}_f \cdot \boldsymbol{n}_{\Omega} \mathrm{d}S \tag{4.20}$$

and considering only the pressure term at equilibrium[8] we get:

$$\boldsymbol{F}_f = \int_{\Omega_g} -p_g \boldsymbol{n}_{\Omega} \mathrm{d}S + \int_{\Omega_l} -p_l \boldsymbol{n}_{\Omega} \mathrm{d}S. \tag{4.21}$$

[7]The interface is defined at the isosurface $\phi = 0.5$. Above that value, we enter in the liquid domain Ω_ℓ. And below $\phi = 0.5$, we enter in the gas domain Ω_g as shown in Figure (3.1b).

[8]Because the macroscopic velocity $\boldsymbol{u}$ will tend to 0 at equilibrium $\boldsymbol{u} \to \boldsymbol{0}$, as shown in Figure (4.20).

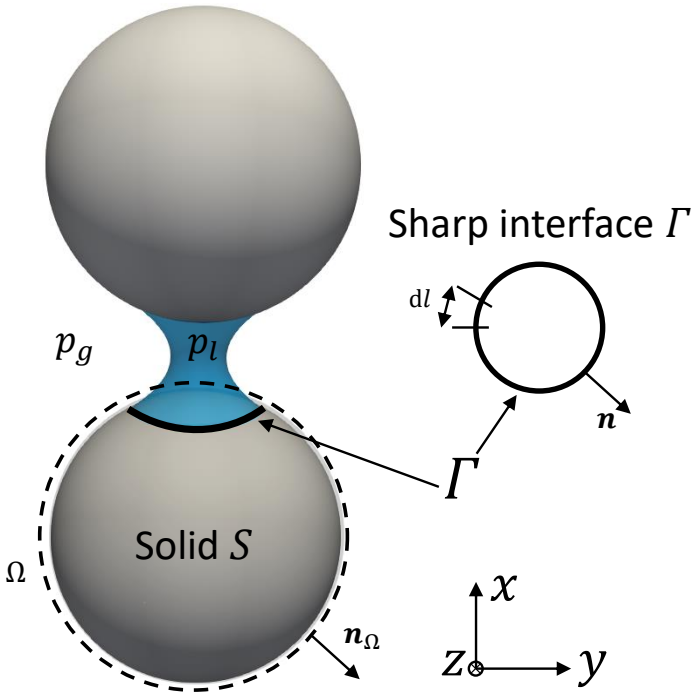

Figure 4.17: Capillary bridge and integration domain within a sharp interface.

If we assume that p_g is constant, we can then write

$$\boldsymbol{F}_f = -\int_{\Omega_l}(p_l - p_g)\boldsymbol{n}_\Omega \mathrm{d}S - \int_{\Omega} p_g \boldsymbol{n}_\Omega \mathrm{d}S = -\int_{\Omega_l} \Delta p\, \boldsymbol{n}_\Omega \mathrm{d}S \tag{4.22}$$

where Δp is the pressure difference between air and water[9]. For negative values of Δp or positive value of the mean curvature H, that is the general case of stable nodoid configurations (Gagneux and Millet, 2014), we have an attractive capillary force. However, Eq. (4.22) involves only the Laplace pressure contribution leading to the first term F_p in Eqs. (1.13), (1.14) or (1.15) for the capillary force. A supplementary term must therefore be added to account for the adhesion term.

4.6.1.2 Capillary interface surface stress-like tensor

In the case of a sharp interface, the stress is not continuous in the fluid phase across the capillary interface and a supplementary term must be added to Eq. (4.18) of the fluid stress to account for the adhesion term involved in Eq. (1.13). Therefore, we have to consider that

$$\hat{\boldsymbol{\sigma}}_f = \begin{cases} \gamma \boldsymbol{I}_{Tw} & \text{on the interface} \\ \boldsymbol{\sigma}_f & \text{otherwise} \end{cases} \tag{4.23}$$

where I_{Tw} denotes the identity of the tangent plane of the capillary interface (see Figure 4.18). It is worth noting that $\hat{\boldsymbol{\sigma}}_f$ is a 2D object on the interface and a 3D object in the bulk fluids. A similar stress-like tensor term has been added for describing the contribution of capillary interfaces in stress calculation in partially saturated media (Duriez

[9]We have used the property that $\int_{\Omega} p_g \boldsymbol{n}_\Omega \mathrm{d}S = 0$ for constant p_g and where Ω is a closed surface.

and Wan, 2017; Popinet, 2018; Scardovelli and Zaleski, 1999).

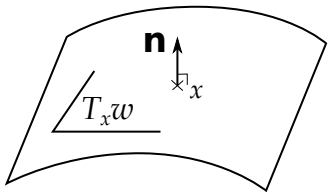

Figure 4.18: Sketch of an identity of the tangent plane.

The capillary force is therefore now expressed as

$$\hat{\boldsymbol{F}}_f = \int_\Omega \boldsymbol{\sigma}_f \boldsymbol{n}_\Omega \mathrm{d}S + \int_\Gamma \gamma \boldsymbol{I}_{Tw} \cdot \boldsymbol{n}_\Omega \mathrm{d}l \tag{4.24}$$

where Γ is the intersection of Ω with the capillary interface as shown in Figure 4.17. Using the fact that $\boldsymbol{I}_{Tw} \cdot \boldsymbol{n}_\Omega$ is independent of ξ, and denoting $\boldsymbol{m} = (\boldsymbol{n} \times \boldsymbol{n}_\Omega) \times \boldsymbol{n}$, Eq. (4.24) yields to:

$$\hat{\boldsymbol{F}}_f = \int_\Omega \boldsymbol{\sigma}_f \boldsymbol{n}_\Omega \mathrm{d}S + \gamma \int_\Gamma \boldsymbol{m} \mathrm{d}l. \tag{4.25}$$

We have used the classical formula $\boldsymbol{I}_{Tw} \cdot \boldsymbol{n}_\Omega = \boldsymbol{n}_\Omega - (\boldsymbol{n}_\Omega \cdot \boldsymbol{n}) \cdot \boldsymbol{n} = (\boldsymbol{n} \times \boldsymbol{n}_\Omega) \times \boldsymbol{n}$, where $\boldsymbol{n}$ denotes the normal to the interface as shown in Figure 4.17. It is worth noting that the second term of $\hat{\boldsymbol{F}}_f$ in Eq. (4.25) corresponds to that mentioned in Connington et al. (2015); Zhang et al. (2020). It is general and valid for a sharp interface. It is also worth mentioning that $\boldsymbol{m}$ represents the unit tangent vector to the interface as illustrated in Figure (4.21).

In the phase-field LBM model, however, the interface is defined with a thickness W as already seen in Figure (3.1a). In that particular case, the interface becomes a surface[10] case as depicted in Figure (4.19), instead of a contour in $\Omega \cap \Gamma$ as seen in Figure (4.17). Therefore Eq. (4.25) must be rewritten as follows

$$\hat{\boldsymbol{F}}_f = \int_\Omega \boldsymbol{\sigma}_f \boldsymbol{n}_\Omega \mathrm{d}S + \gamma \int_\Omega \boldsymbol{m} \delta_\mathrm{s}(\xi) \mathrm{d}S \tag{4.26}$$

where $\delta_\mathrm{s}(\xi)$ is the regularized Dirac function of the capillary interface defined along the thickness direction ξ as seen in Figure (3.3):

$$\delta_s(\xi) = \frac{24}{W} \phi(\xi)^2 \left[\phi(\xi) - 1\right]^2. \tag{4.27}$$

Eq. (4.27) satisfies the following condition:

$$\int_{-\infty}^{+\infty} \delta_s(\xi) \mathrm{d}\xi = 1. \tag{4.28}$$

It is worth noting that the second term of the R.H.S of Eq.(4.26) would exactly be the same as the second term of Eq.(4.25) if one supposed that the interface was sharp (zero thickness). In the case of a sharp interface, the Dirac function would be the unit

[10] The surface becomes a set of multiple contours Γ_i. In other words, the interface becomes $= \bigcup_i \Gamma_i$

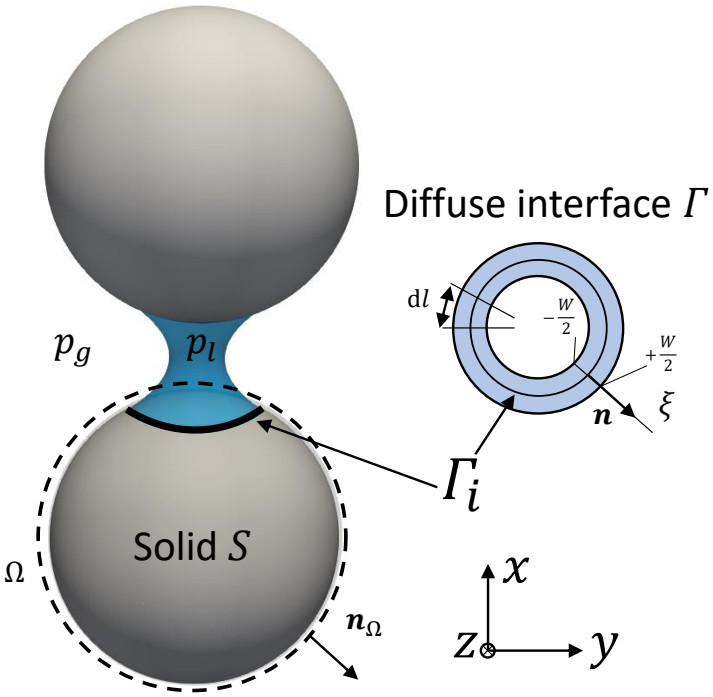

Figure 4.19: Capillary bridge and integration domain within a thick interface.

impulse Dirac as depicted in Figure (3.3). In fact, the unit impulse Dirac function δ_s will transform the domain Ω into a contour Γ.

Obviously, the larger the width W is, the smoother δ_s is, as illustrated in Figure (3.3). For all of the simulations in this chapter, the value of the width $W = 5$ lu is chosen, which is suitable to make the Dirac function smooth enough to avoid numerical instabilities. As a consequence, the contribution of the second term of the R.H.S of (4.26) leads to:

$$\boldsymbol{F}_\gamma = \gamma \left[\sum_i \int_{\Gamma_i} \left[\int_{-\infty}^{+\infty} \delta_s(\xi) d\xi \right] \boldsymbol{m}_i \mathrm{d}l \right]. \tag{4.29}$$

Using Eq. (4.27), as $\boldsymbol{m}$ does not depend on ξ, the adhesion force $\boldsymbol{F}_\gamma$ acting on Γ_i can be written as:

$$\boldsymbol{F}_\gamma = \frac{24\gamma}{W} \sum_i \left[\int_{\Gamma_i} \int_{-\infty}^{+\infty} \phi^2(\xi) \left[\phi(\xi) - 1\right]^2 \boldsymbol{m}_i \mathrm{d}\xi \right]. \tag{4.30}$$

The integral can be appropriately expressed with respect to the phase function ϕ. For this purpose, we take advantage of the inverse of Eq. (3.10a) to express ξ as a function of ϕ:

$$\xi = \frac{W}{4} \ln\left(\frac{\phi}{1-\phi}\right), \quad \phi \in [0;1]. \tag{4.31}$$

Next, $\mathrm{d}\xi$ can be explicitly transformed into $\mathrm{d}\phi$ as:

$$\mathrm{d}\xi = \frac{W}{4\phi(1-\phi)} \mathrm{d}\phi. \tag{4.32}$$

Then, by substituting Eq. (4.32) into (4.30), the expression of the adhesion force for diffuse

interface can be derived:

$$\boldsymbol{F}_{\gamma} = -6\gamma \sum_{i} \left[\int_{\Gamma_i} \int_{0}^{1} \phi(\phi - 1) \boldsymbol{m}_i \mathrm{d}\phi \mathrm{d}l \right]. \tag{4.33}$$

4.6.2 Numerical LBM-based implementation

To evaluate numerically the force given in Eq. (4.26), a discrete form in terms of pressure contribution is required, i.e.:

$$\boldsymbol{F}_{p} = \sum_{\boldsymbol{x}_S} \boldsymbol{\sigma}_f \cdot \boldsymbol{n}_{\Omega} \, \Delta S. \tag{4.34}$$

Note that the sum runs over all lattice points $\boldsymbol{x}_S$ located on the voxelated surface Ω, and the area element ΔS is equal 1 in lattice units. We define F_{τ} as the viscous force, resulting from the viscous stress tensor $\boldsymbol{\tau}$, as follows:

$$\boldsymbol{F}_{\tau} = \int_{\Omega} \boldsymbol{\tau} \cdot \boldsymbol{n}_{\Omega} \mathrm{d}S \tag{4.35}$$

Once the capillary bridge is established, the macroscopic velocity $\boldsymbol{u}$ will tend to zero. Consequently, according to Eq. (4.35), viscous forces $\boldsymbol{F}_{\tau}$ will also be nil. The x-component of viscous force F_x^{τ} is depicted in Figure 4.20. It shows that the x-component will tend to zero at the equilibrium of the simulation[11]. Accordingly, viscous forces are therefore not taken into consideration in the computation of capillary forces.

Technically speaking, in order to compute the viscous stress tensor $\boldsymbol{\tau}$, each node of LBM simulations in 3D conditions should contain 6 components[12] $\{\tau_{\alpha\beta}\}$, where $\alpha, \beta \in \{x; y; z\}$.

In fact, when using 16 GBs—which is the total amount of memory in the graphics card Quadro RTX 5000 used in this study—the declaration of these 6 variables for each node would cost roughly 2 GBs. Thus, from a technical point of view, it is advantageous to neglect the viscous force for memory optimization to provide maximum performance.

[11] Since the capillary bridge is oriented along x-axis, as illustrated in Figure 4.13, the y and z components of the viscous force F_{τ}^{y} and F_{τ}^{z} will automatically be zero from the beginning to the end of the simulation due to symmetry.

[12] Thanks to the symmetry of the tensor.

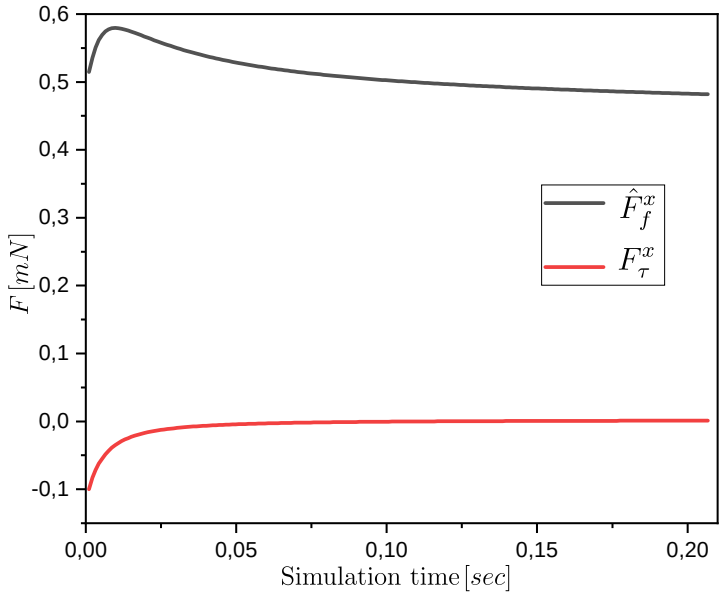

Figure 4.20: The x-component viscous force F_x^τ tends gradually to 0 when reaching equilibrium.

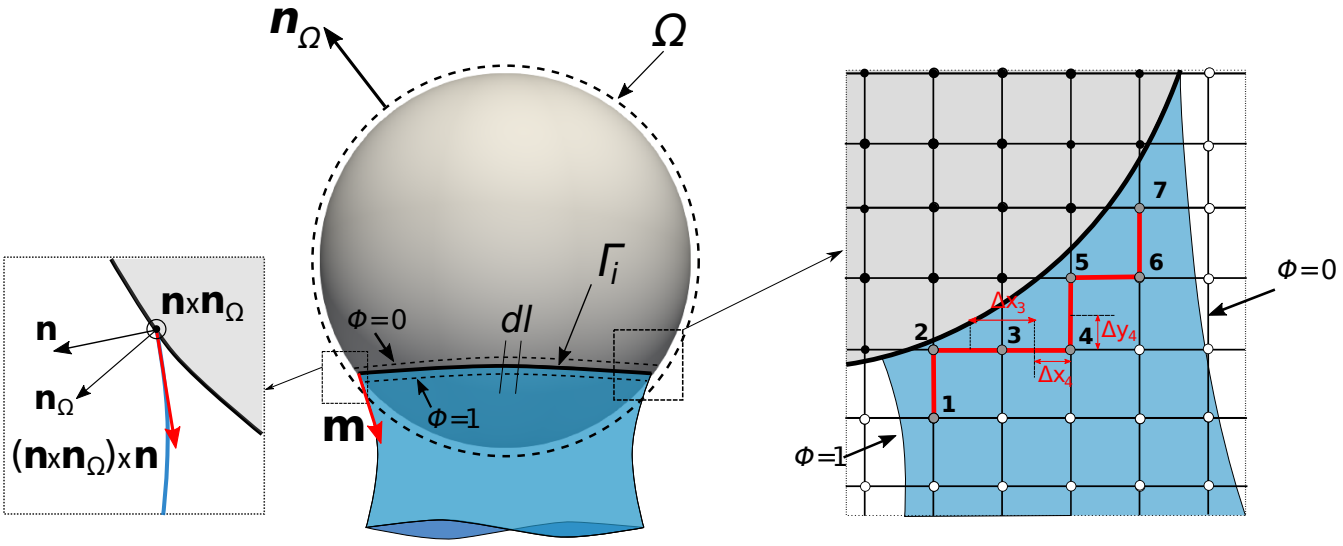

Figure 4.21: Schematic view of the contact line Γ_i on a spherical particle. dl is a line element on the contact line and $\boldsymbol{m}$ represents the unit vector directed along the local capillary force. In the zoom, the live nodes (grey circles numbered from 1 to 7) used to calculate the capillary force along the width direction of a diffuse interface around a curved solid boundary. The white and black circles represent the fluid and solid nodes, respectively.

The expression (4.33) leads to the discrete form of the elementary adhesion force $\boldsymbol{f}_\gamma$ along an element dl of Γ_i (with d$l = 1$ lu)

$$\boldsymbol{f}_\gamma \approx -6\gamma \sum_j \phi_j(\phi_j - 1)\boldsymbol{m}_j\,|\Delta\phi_j| \tag{4.36}$$

with

$$|\Delta\phi_j| = \left|\frac{\partial\phi}{\partial x}\bigg|_j\right| \Delta x_j + \left|\frac{\partial\phi}{\partial y}\bigg|_j\right| \Delta y_j + \left|\frac{\partial\phi}{\partial z}\bigg|_j\right| \Delta z_j \tag{4.37}$$

We have noted $\left.\frac{\partial\phi}{\partial x}\right|_j$, $\left.\frac{\partial\phi}{\partial y}\right|_j$ and $\left.\frac{\partial\phi}{\partial z}\right|_j$ the local partial derivatives at the live node j, and Δx_j, Δy_j, and Δz_j the local coordinate increments in the x, y, and z directions, respectively. They can be computed as

$$\begin{cases} \Delta x_j = & \sum_{k=1}^{2} 0.5\Psi(\boldsymbol{x}_j + \boldsymbol{\varepsilon}_k^x) \\ \Delta y_j = & \sum_{k=1}^{2} 0.5\Psi(\boldsymbol{x}_j + \boldsymbol{\varepsilon}_k^y) \\ \Delta z_j = & \sum_{k=1}^{2} 0.5\Psi(\boldsymbol{x}_j + \boldsymbol{\varepsilon}_k^z) \end{cases} \tag{4.38}$$

with the notations

$$\begin{gathered} \boldsymbol{\varepsilon}^x = [\boldsymbol{\varepsilon}_1^x, \boldsymbol{\varepsilon}_2^x] = \begin{bmatrix} 1 & -1 \\ 0 & 0 \\ 0 & 0 \end{bmatrix}, \quad \boldsymbol{\varepsilon}^y = [\boldsymbol{\varepsilon}_1^y, \boldsymbol{\varepsilon}_2^y] = \begin{bmatrix} 0 & 0 \\ 1 & -1 \\ 0 & 0 \end{bmatrix}, \\ \boldsymbol{\varepsilon}^z = [\boldsymbol{\varepsilon}_1^z, \boldsymbol{\varepsilon}_2^z] = \begin{bmatrix} 0 & 0 \\ 0 & 0 \\ 1 & -1 \end{bmatrix} \end{gathered} \tag{4.39}$$

and

$$\Psi(\boldsymbol{x}) = \begin{cases} 0, & \text{if } \boldsymbol{x} \text{ is not a live node} \\ 1, & \text{if } \boldsymbol{x} \text{ is a live node } [13] \end{cases} \tag{4.40}$$

Note that Eqs. (4.38)-(4.40) are compact notations that simplify the numerical implementation. Finally, the total surface tension force exerted on a particle can be obtained by

$$\boldsymbol{F}_\gamma = \sum_i \boldsymbol{f}_\gamma \approx -6\gamma \sum_i \sum_j \phi_j(\phi_j - 1)\boldsymbol{m}_j \left|\Delta\phi_j\right| \Delta l_i \tag{4.41}$$

where the first sum runs over all the discrete line elements $\Delta l_i = 1$ lu, while the second one runs over all live nodes in the i^{th} line element. Finally, the complete capillary force $\hat{\boldsymbol{F}}_f = \boldsymbol{F}_p + \boldsymbol{F}_\gamma$ may be calculated as follows using (4.34) and (4.41):

$$\hat{\boldsymbol{F}}_f \approx \sum_{\boldsymbol{x}_S} \boldsymbol{\sigma}_f \cdot \boldsymbol{n}_\Omega \Delta S - 6\gamma \sum_i \sum_j \phi_j(\phi_j - 1)\boldsymbol{m}_j \left|\Delta\phi_j\right| \Delta l_i. \tag{4.42}$$

4.7 Numerical examples

In this section, capillary forces will be computed for two and three spherical particle grains and compared to experimental and numerical data from Mielniczuk et al. (2018) and Miot et al. (2021), respectively. It is worth mentioning that all the simulations of capillary bridges—whether for doublets or triplets—are carried out in zero-gravity condition.

[13] Gray or the numbered nodes in Figure (4.21) are the so-called live nodes.

4.7.1 Capillary bridge between two spherical particles

A capillary bridge between two spherical particles is simulated to validate the calculation of the associated capillary forces presented in the previous section. The simulations are carried out with a domain size of $N_x \times N_y \times N_z = 160 \times 250 \times 160$, with the particles having a radius of $R = 4$ mm. The characteristic length is $L_c = 12$ mm in x-direction, therefore the mesh size is $\Delta x = 0.012/(N_x - 1) \approx 7.5 \times 10^{-5}$ m. A drop of water with a spherical shape is created at mid-distance between the two particles as illustrated in Figure (4.13a); two different initialization setups are used with water volumes of 4 and 10 µL. Also, different separation distances $D \in \{0.5, 1, 1.5, 2, 2.25\}$ mm are considered. The contact angle $\theta = 20°$ is imposed through the wetting condition (3.120).

Figure (4.22) shows the simulation results of the capillary forces F^{cap} for different separation distances D and for two distinct volumes: 4 and 10 μL. At the convergence of the LBM simulation[14] as shown in Figure (4.13b), the capillary forces are calculated at the contact line (CL) using Eq. (4.42). The experimental and numerical data of Mielniczuk et al. (2018) and Miot et al. (2021), respectively, are added for comparison. It can be seen that the simulation results are in a very good agreement with experimental as well as numerical data of Mielniczuk et al. (2018) and Miot et al. (2021), which validates the proposed approach, while also proving that Eq. (4.33) coincides with the adhesion term at contact line given by Eq. (1.14).

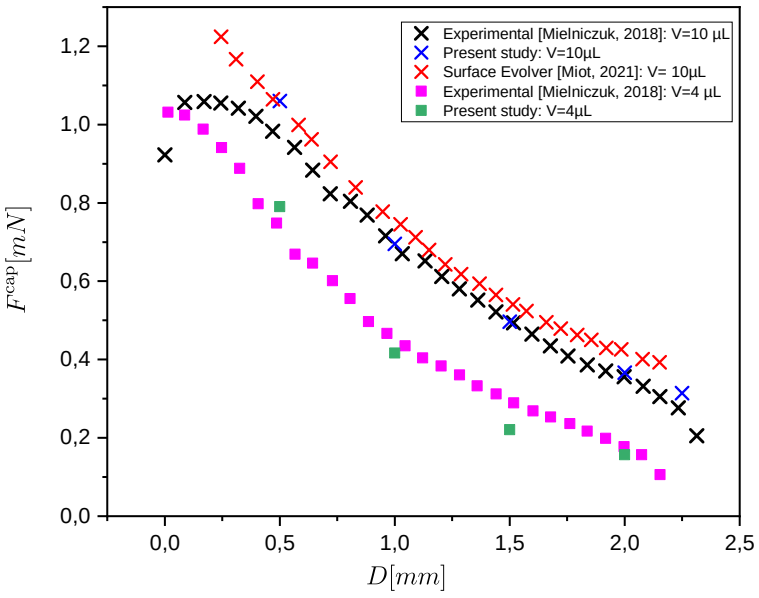

Figure 4.22: Capillary forces F^{cap} [mN] versus separation distances D [mm] for water volumes of 10 and 4 µL.

[14]The selected capillary force value compared to experimental data is taken at the end of the simulation—around 0.22 sec in Figure (4.20)—when F_f^x reaches a plateau, which corresponds to the equilibrium of the capillary bridge.

4.7.2 Capillary bridges between three spherical particles (coalescence)

Given that the numerical approach was validated with the case of a capillary doublet between two spherical particles, the challenge is to next explore the capillary forces of three solid grains and, in particular, at coalescence (merging) of the two menisci. The configuration used in Miot et al. (2021) is used to provide a comparison between LBM and energy minimization results altogether.

The triplet configuration is defined as follows: the centers of the two bottom particles are separated by a distance $D_2 = 8.3$ mm. The upper particle is placed at a distance $D_1 = 8.7$ mm from the centers of the bottom particles as presented in Figure (4.23a). Note that the particles are in the same plane in z-direction. The particles are of the same radius $R = 4$ mm.

All the simulations are performed with the domain size of $N_x \times N_y \times N_z = 320 \times 320 \times 320$ nodes. The characteristic length considered is $L_c = 24$ mm in x-direction. Therefore, the mesh size chosen is $\Delta x = 0.024/(N_x - 1) \approx 7.5 \times 10^{-5}$ m. Two spherical water drops are initialized in the mid-segment between the top and the right bottom particle, and between the top and the left bottom particle as seen in Figure (4.23a). In this latter, where there is no contact between capillary bridges at any moment of the simulation, each capillary bridge will converge separately to its own equilibrium as shown in Figure (4.23b). However, when the water volume is sufficiently large as illustrated in Figure (4.24a), a contact between capillary bridges may probably take place at some point in the simulation[15] producing a merging (coalescence) between both capillary bridges as shown in Figure (4.24b). Once capillary bridges coalesce, they will be treated as a single merged capillary bridge and will not converge until the imposed contact angle θ is respected, as seen in Figure (4.24c).

A parametric study is performed by varying the initial water volume V and contact angle θ. The vertical capillary force exerted onto the upper particle is also computed from Eq. (4.42). Figure (4.25) depicts the capillary force for different liquid volumes (from 1

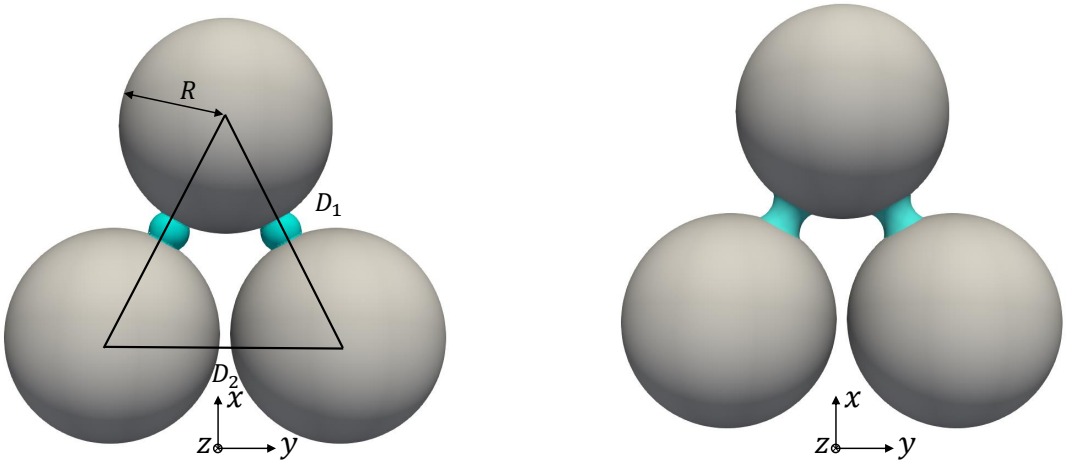

(a) Initialization of water droplets

(b) Equilibrium of separate bridges

Figure 4.23: From initialization of two water droplets to the equilibrium of capillary bridges for a total water volume of $V = 3.5\,\mu$L for $\theta = 20°$.

[15] When every single capillary bridge is converging to its own equilibrium until satisfying the imposed contact angle θ, contact lines of the both capillary bridges may touch.

to 33 μL) and different contact angles $\theta \in \{20°, 40°, 50°\}$. The LBM simulations are performed without gravity so as to compare with those of Miot et al. (2021) carried out under the same conditions.

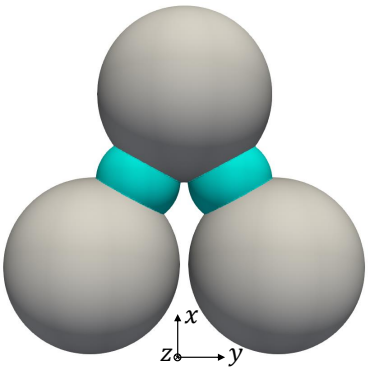

(a) Initialization of water drops

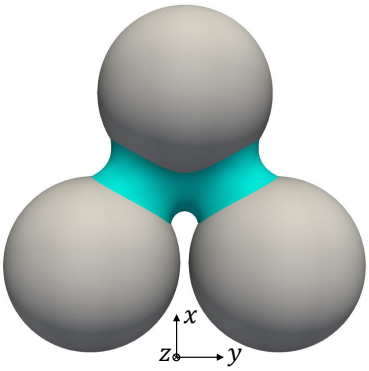

(b) Merging capillary bridges phase

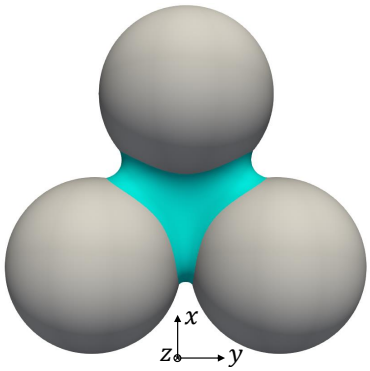

(c) Equilibrium coalesced bridges

Figure 4.24: From initialization of two water drops to the equilibrium of coalesced capillary bridges for a total water volume of $V = 31.5\,\mu$L for $\theta = 20°$.

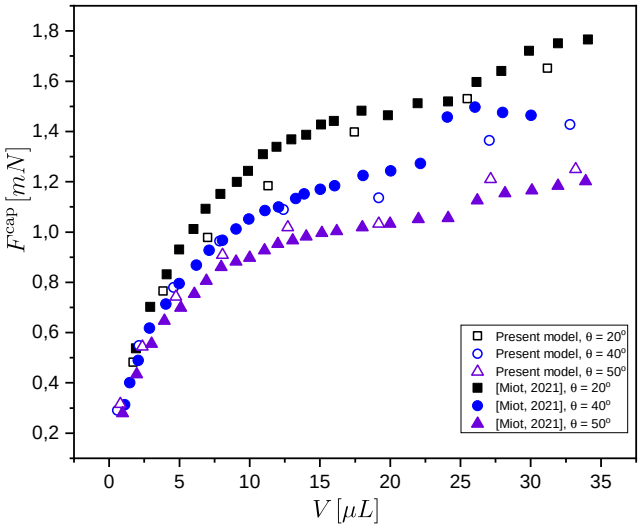

Figure 4.25: Comparison of the capillary forces F^{cap}, computed on the upper particle, between the present model (LBM simulations) and Surface Evolver used in Miot et al. (2021) for different volumes V [μL] and contact angles θ.

A rather good agreement can be noted between the results. Most importantly, the advantage of the present method is that the forces (adhesion, pressure, and viscous forces) are accessible at any time step, while in Miot et al. (2021) the total forces are calculated only at equilibrium using the Virtual Work Principle. Moreover, the most precious asset of the present model is that it can easily handle the dynamics of capillary bridges without needing to choose whether the bridges are coalesced or not in the first place (funicular or pendular regimes), which makes this model extremely powerful and promising for treating partially saturated granular assemblies. In addition to these features, the new geometric algorithm for computing capillary forces using Eq. (4.42) is proved to be applied to all types of capillary bridges regardless of their regime (coalesced or isolated capillary bridges).

4.8 Conclusion

In this chapter, the phase-field LBM-based model as well as the wetting condition have been validated on several benchmarks. Next, the formation of capillary bridges between two spherical grains was simulated, analyzed, and then compared to experimental as well as theoretical data reported in the literature. Excellent results were found using the present model when comparing the mean curvature H with its experimental and theoretical counterparts, especially in capturing the inversion of the sign of H from a portion of nodoid ($H > 0$) to a portion of an undoloid ($H < 0$) when increasing the separation distance between particles. Moreover, associated capillary forces are in very good agreement with published experimental and numerical results. The study was next extended to three particles. The present model has proved once again of its capability to handle the transition of capillary bridges when they merge—transition from pendular to funicular regimes. Capillary forces match the numerical data well in the same configuration.

Chapter 5

DEM-LBM coupling for REV scale simulations: Mechanical response of unsaturated granular assemblies

5.1 Introduction

In Chapter 4, the shapes of capillary bridges and their associated forces have been well validated using the Lattice Boltzmann phase-field-based model. These benchmarks were carried out with fixed particles in both *pendular* and *funicular* regimes. It is important, however, to consider the dynamics and motion of particles especially if one desires to investigate the mechanical behavior of unsaturated soils at the scale of the Representative Elementary Volume (REV). The Discrete Element Method (DEM) is widely recognized as one of the most valuable approaches for considering particle motion and contact forces at this small scale. Therefore, this chapter introduces a coupling between DEM and LBM, referred to as DEM-LBM for simplicity. We extensively reviewed the state-of-the-art aspects of the LBM method for unsaturated conditions in Chapter 3. In this chapter, we provide a quick review of the DEM.
The aim of this chapter is to validate this devised coupling model by focusing on the analysis of the Soil-Water Characteristic Curve (SWCC) and the estimation of the capillary stress for a large range of saturation levels. It must be pointed out that all simulations are conducted under zero gravity conditions.

5.2 Discrete Element Method (DEM)

Dr. Peter Cundall and Professor Otto Strack are commonly recognized as the pioneering developers of the Discrete Element Method (DEM), also referred to as the Distinct Element Method (Cundall and Strack, 1979). In DEM, solid grains are represented as rigid, spherical, polydispersed particles that can overlap and interact through contact laws[1]. The significant advantage of DEM, in the simulation of the mechanical behavior of granular materials, lies in its ability to work at a scale where continuum descriptions of granular materials do not apply. However, when enough grains are simulated, both discrete and continuum descriptions can be applied simultaneously. This merging scale is known as the Representative Elementary Volume (REV), introduced by Hill in 1963 (Hill, 1963). When describing the grains in the DEM, it is important to note that some hypothetical assumptions are made, which include neglecting surface asperities and assuming that the contact area between particles is relatively small compared to the dimensions of the grains. Two different DEM families exist:

- Non-smooth contact dynamics model which relies on an implicit integration scheme (Moreau, 1988; Jean, 1999; Radjai and Richefeu, 2009; Perales et al., 2010; Radjai et al., 1996, 1998; Nouguier-Lehon et al., 2003; Renouf et al., 2004; Fortin et al., 2003, 2005; de Saxcé et al., 2004);

- Smooth contact dynamics model which relies on an explicit integration scheme (Younes et al., 2023d; Wautier et al., 2019; Duriez and Wan, 2016; Duriez et al., 2017; Scholtes et al., 2009).

Like all methods, they both have advantages and disadvantages. For instance, the smooth contact model must respect the CFL (Courant-Friedrichs-Lewy) time step condition, whereas the non-smooth does not. However, the latter is slower than the smooth contact model. A comprehensive review comparison was conducted in Dubois et al. (2018) for more details about non-smooth and smooth contact dynamics models.

[1] Although DEM can model very complicated grain shapes, it is completely out of the scope of this study.

In this Ph.D. work the open-source software YADE (Yet Another Dynamic Engine) has been used, which was originally developed by 3SR laboratory in Grenoble, France, and uses the smooth contact dynamics model (Šmilauer et al., 2021). YADE is implemented in C++ and offers a user-friendly interface written in Python. This software has gained popularity among researchers due to its ease of use and user-friendly interface, making it straightforward to operate. It employs the smooth contact dynamic code, allowing particles to inter-penetrate during simulations.
DEM is based on the time-discretization of Newton's second law of motion for rigid bodies, following the Lagrangian approach. Its mathematical representation is defined as follows

$$m_p \frac{\mathrm{d}^2 \boldsymbol{x}_p}{\mathrm{d}t^2} = \sum_c \boldsymbol{f}_c \tag{5.1}$$

where m_p corresponds to the particle mass, $\boldsymbol{x}_p$ mass center position of the particle, and $\boldsymbol{f}_c$ is the external contact forces[2].
Contact forces are computed when particles overlap. In addition to geometrical characteristics, e.g. grain radius, each grain possesses multiple material parameters that are used to define contact laws, for instance, stiffness E, stiffness ratio ν, and inter-particle friction angle φ. There exist many contact laws between particles in the literature, but the most common one is the elasto-frictional contact law which is briefly presented hereafter. Two types of contact forces are generated upon overlapping: normal $\boldsymbol{f}_n^{(i)}$ and tangential $\boldsymbol{f}_t^{(i)}$ contact forces applied on the i^{th} particle, as illustrated in Figure (5.1). The former one,

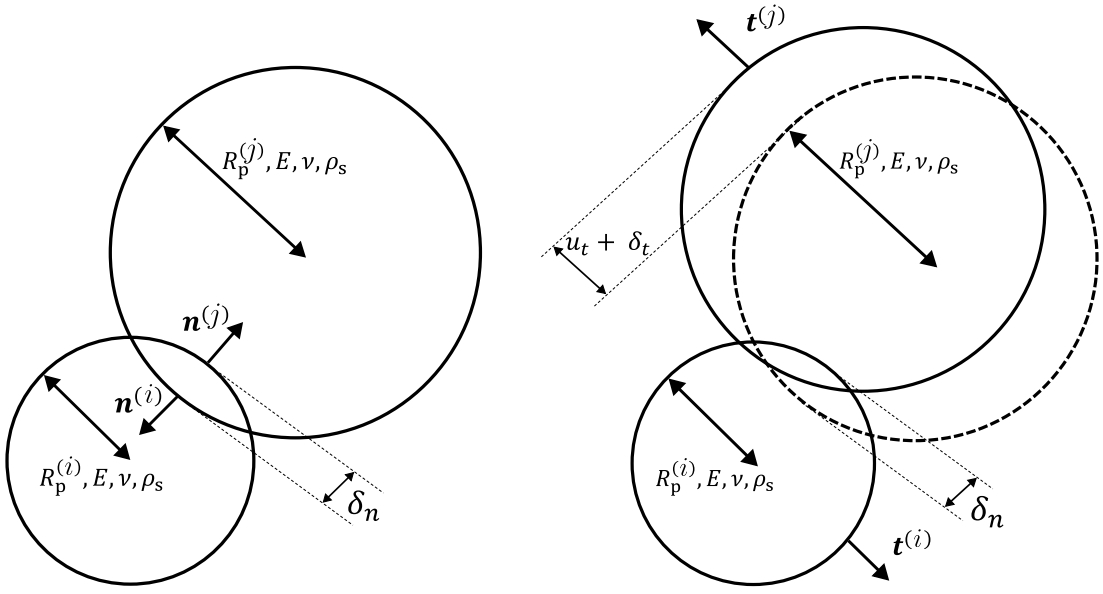

Figure 5.1: (a) Overlapping of two spherical particles and (b) tangential displacement between particles.

which is *repulsive* and whose direction is parallel to the direction joining the centers of two overlapped grains, is defined as follows

$$||\boldsymbol{f}_n^{(i)}|| = k_n \delta_n \tag{5.2}$$

[2]Later in this chapter, it will be shown that $\boldsymbol{f}_c$ will be replaced by the contact forces as well as the capillary forces due to the presence of capillary bridges.

where δ_n is the normal overlapping distance, k_n is the normal stiffness defined as the harmonic average of the two particles' radii $R_\mathrm{p}^{(i)}$ and $R_\mathrm{p}^{(j)}$ and proportional to the stiffness E:

$$k_n = 2E\frac{R_\mathrm{p}^{(i)}R_\mathrm{p}^{(j)}}{R_\mathrm{p}^{(i)}+R_\mathrm{p}^{(j)}}. \tag{5.3}$$

It should be noted that the normal contact force $\boldsymbol{f}_n^i$ is pointed outward in the direction of the vector joining the centers of the grains in contact, i.e., vector $\boldsymbol{n}^{(i)}$ as shown in Figure (5.1a).
Regarding the tangential contact force $\boldsymbol{f}_t^{(i)}$ applied on the i^{th} particle, it is defined as follows:

$$||\boldsymbol{f}_t^{(i)}|| = \begin{cases} k_t\delta_t\,, & \text{if } ||\boldsymbol{f}_t^{(i)}|| < ||\boldsymbol{f}_n^{(i)}||\tan(\varphi) \\ ||\boldsymbol{f}_n^{(i)}||\tan(\varphi) & \text{otherwise} \end{cases} \tag{5.4}$$

$\boldsymbol{f}_t^{(i)}$ is pointed in the direction of the tangential unit vector $\boldsymbol{t}^{(i)}$, whose direction is opposed to the relative motion between the grains, as seen in Figure (5.1b), and k_t is the tangential stiffness simply proportional to the normal stiffness k_t:

$$k_t = \nu k_n. \tag{5.5}$$

The computation of $\boldsymbol{f}_t^{(i)}$ is not as straightforward as the normal component, because it depends on the history of the shear displacement. As indicated in Eq. (5.4), the tangential component is bounded by a $||\boldsymbol{f}_n^{(i)}||\tan(\varphi)$, a limit defined by the Coulomb friction model criteria that takes into account the internal friction angle φ as shown in both Eq. (5.4) and Figure (5.2). The polydispersed grain parameters of the REV are summarized in

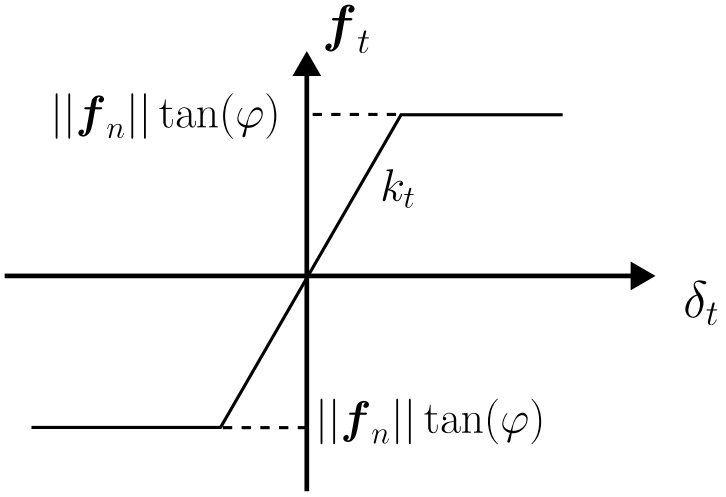

Figure 5.2: (a) Overlapping of two spherical particles and (b) tangential displacement between particles.

Table 5.1.

5.3 Numerical Procedures

The DEM-LBM computations rely on an explicit coupling algorithm whereby the fluid and solid mechanics simulation modules run sequentially at a frequency that is expressed

Parameters	Values	Units
Density ρ_s	2,600	$kg.m^{-3}$
Stiffness E	110	MPa
Stiffness ratio (α)	0.3	–
Inter-particle friction angle	30	°
$\{D_{min}; D_{max}\}$	{80; 108}	µm
Number of particles	3,750	–

Table 5.1: YADE mechanical parameters for the grains used in Section 5.4. The same mechanical parameters are used later in Chapter 6, Sections 6.4.2 and 6.4.3.

as a function of the time scales of the DEM and LBM simulations. Details of the algorithm will be discussed in a later sub-section.

We use the in-house LBM master code developed in CUDA C/C++ language for GPU computations presented in Chapter 3, whereas the DEM code, YADE, is launched using a C++ command. The GPU-based code is found to largely alleviate the computational efforts. A 16GB GPU memory has been used and has been found to be just adequate for the size of the model herein presented.

5.3.1 Initialization of the grain packing - YADE

The initialization of the spherical grains is done in YADE. First, the creation of a cloud of grains as well as the walls on the six sides of a cubical sample is completed as shown in Figure (5.3a). Then, an isotropic confining pressure step is carried out with σ^{conf} = 100 kPa by moving the bounding walls to compress isotropically the granular assembly. Then, the walls move backward until σ^{conf} reaches 0 kPa as illustrated in Figure (5.3b).

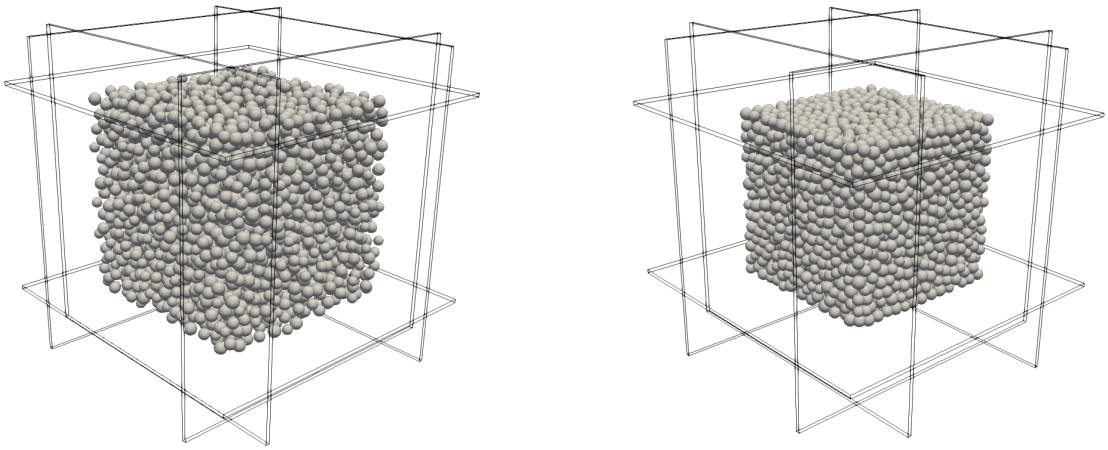

(a) (b)

Figure 5.3: The sequence of steps for generating a polydispersed sample.

5.3.2 Initialization of capillary bridges in LBM

Capillary bridges are initialized in the form of equally-sized water droplets between each pair of grains (i, j) for which their separation distance D_{ij} is less than a user-defined specific value ε as depicted in Figure (5.4a). Next, after running several LBM iterations with fixed grains, the spherical drops evolve to form capillary bridges of realistic geometries involving more than a pair of grains; see as seen in Figure (5.4b). It is worth mentioning

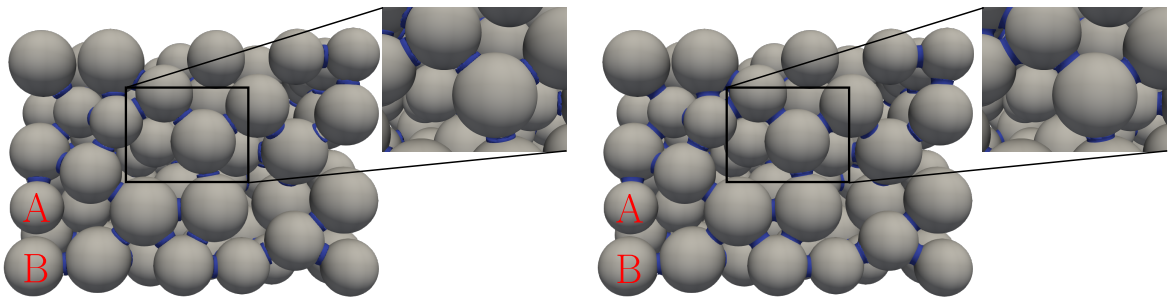

(a) (b)

Figure 5.4: (a) Initialization spherical drops at mid-distance between pair of grains. (b) Converged capillary bridges after several LBM iterations. In (a) the separation distance between particles A and B was larger than the allowed distance ε, therefore, no capillary bridge was initialized between these two grains.

that the number of LBM iterations to converge to a final liquid geometry depends on several parameters, e.g. the droplet volume created at mid-distance between two spherical grains and the value of the surface tension $\tilde{\gamma}$ in lattice units. Based on the selected parameters, 500 LBM iterations are enough to reach the initial equilibrium of capillary bridges. Readers are invited to consult Appendix E for more details.

5.3.3 DEM-LBM coupling scheme

There are two points to be considered in this multi-physics coupling: first, the time scales involved in the processes are different, and second, the discretization scheme to solve each piece of physics leads to different time steps. To achieve both accurate physics and numerical stability, the latter requires frequent synchronization. However, this synchronization should be carefully balanced to avoid excessive computational costs.
For numerical stability, the time step Δt_{DEM} in DEM simulations should be smaller than the critical time step:

$$\Delta t_{\mathrm{crit}} = \min_i \left(R^{(i)} \sqrt{\frac{\rho_{\mathrm{s}}}{E}} \right). \tag{5.6}$$

Regarding the LBM time step, it is usually taken as 1 in lattice units. Using conversion coefficients as elaborated in Section 3.6, it can be expressed as:

$$\Delta t_{\mathrm{LBM}} = \sqrt{C_\rho \frac{\tilde{\gamma}}{\gamma} C_{\mathrm{L}}^3}. \tag{5.7}$$

From Eq. (5.7), it can be seen that once C_{L} and C_ρ are selected, the only parameter that controls the Δt_{LBM} is the LBM surface tension $\tilde{\gamma}$ in lattice units. Ideally, it is more convenient to maximize Δt_{LBM} for numerical efficiency while also guaranteeing numerical stability. The pros and cons of large values $\tilde{\gamma}$ are discussed in the following.

On one hand, the advantages are:

- Faster simulations:
  Based on Eq. (3.67), when $\tilde{\gamma}$ increases, the interface velocity rises.

- Reasonable relaxation times:
  Based on Eq. (3.128), when $\tilde{\gamma}$ increases, C_{t} increases, which makes the relaxation times $\tilde{\tau}_h^{\ell,g}$ larger than $\widetilde{\Delta t}/2 = 0.5$ which is crucial for numerical stability (Timm et al., 2016).

On the other hand, the disadvantages of large values of $\tilde{\gamma}$ are:

- Reasonable LBM velocities:
  According to Timm et al. (2016), the lattice Mach number should be low (Ma $\ll 1$). Moreover, LBM fluid velocities are related to $\tilde{\gamma}$. Consequently, the larger the LBM surface tension $\tilde{\gamma}$, the larger the velocities, making the Ma larger which is repugnant when using LBM.

One has to consider the above-mentioned points when setting up the value of $\tilde{\gamma}$ to achieve the best computational performance of the coupling while respecting the numerical stability of both LBM and DEM time step restrictions.

Next, to ease the synchronization between these two time steps, the ratio between them must be such that:

$$\frac{m}{n} = \frac{\Delta t_{\mathrm{LBM}}}{\Delta t_{\mathrm{DEM}}} \Rightarrow n\Delta t_{\mathrm{LBM}} = m\Delta t_{\mathrm{DEM}} \tag{5.8}$$

where n and m are integers. Figure (5.5) highlights at which iteration the exchange of data between LBM and DEM takes place. Note that the DEM and LBM algorithms run sequentially, hence, during the LBM cycle, the grains are fixed. However, another issue can arise regarding the coupling for two main reasons:

- Convergence of spherical droplets to capillary bridges:
  The capillary bridge is initialized as a spherical drop, and since we focus on the steady state, only the converged capillary bridges are considered[3]. Thus, 1 single LBM iteration will not be sufficient for the convergence of capillary bridges.

- Computational time performance:
  Data exchange between LBM and YADE is a time-consuming procedure. Therefore, making information exchange for every single LBM iteration will drastically reduce the efficiency of the coupling.

To overcome this issue, it is convenient to multiply both iteration numbers (n and m) by a coefficient n_{ratio}, in order: (1) to make the capillary bridge converge to its equilibrium state between two synchronization points, and (2) to avoid huge computation time in exchanging data between LBM and YADE. Therefore, DEM and LBM numbers of iterations needed for the simulations are:

$$\begin{aligned} N_{\mathrm{LBM}} &= n_{\mathrm{ratio}} \times n \\ N_{\mathrm{DEM}} &= n_{\mathrm{ratio}} \times m. \end{aligned} \tag{5.9}$$

[3]The viscous effect is not taken into account in this study. Readers are invited to consult Younes et al. (2022) for more details.

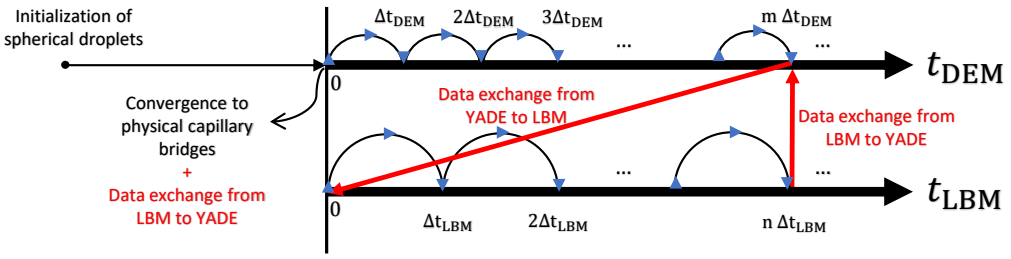

Figure 5.5: Timelines of both LBM and DEM simulations and information exchange procedure between LBM code and YADE

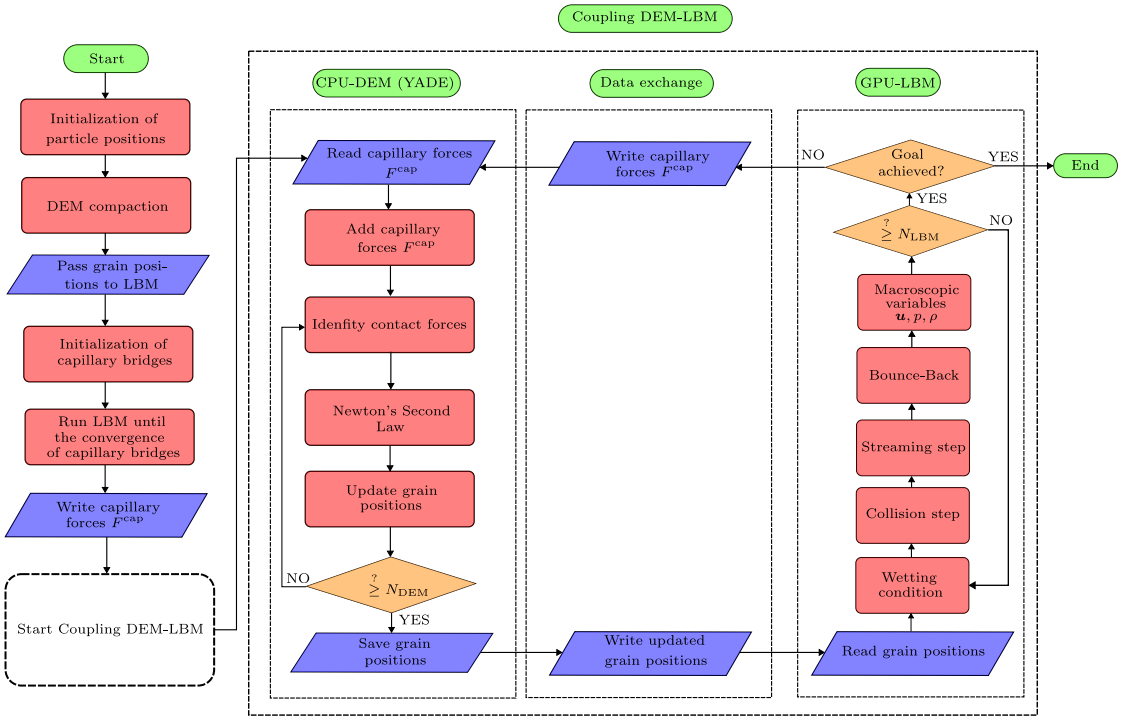

Figure 5.6: Flowchart showing the coupling between LB and DE methods

Figure (5.6) presents the flowchart of the coupling between LBM and DEM. The first steps correspond to the initialization of a cloud of particles in YADE to be then passed to LBM in order to initialize spherical drops at the mid-distance of the grains. Next, multiple LBM iterations will be run until the convergence of all capillary bridges. Capillary forces are then computed and used in YADE to couple the DEM-LBM calculations.

The main steps of the DEM are herein summarized: (a) contact forces are determined, (b) Newton's Second Law is applied for each grain to update the velocities of the grains, and (c) particle positions are updated. Then, if the DEM iteration is less than N_{DEM}, the DEM algorithm will return back to step (a). Otherwise, the new positions of particles are saved.

Finally, the updated grain positions are used to start the LBM algorithm. The main steps in the LBM algorithm include: (1) wetting condition, (2) collision, (3) streaming, (4) Bounce-Back boundary condition, and (5) determination of macroscopic variables. Then, the synchronization condition is verified. If the number of iterations is less than N_{LBM}, the cycle will return to step (1). Otherwise, capillary forces F^{cap} are computed for each

grain. Next, capillary forces are read in YADE and applied to grains and back and forth iteratively.

In what follows in the chapter, we will be conducting an 'indirect' validation of the coupling aspect by investigating the capillary stress versus water saturation relationship in an assembly of wetted particles. The numerical results show a departure from Bishop's relationship, which is validated by available data in the literature.

5.4 Application to capillary water in a granular assembly

In this section, we apply the DEM-LBM coupling model to simulate the mechanical behavior of a granular assembly composed of 3,750 spherical grains following a uniform grain size distribution such that $D_{\max}/D_{\min} = 1.35$ with $D_{\max} = 108\,\mu\text{m}$, and $D_{\min} = 80\,\mu\text{m}$. The DEM parameters were summarized in Table 5.1.

One may ask whether the number of grains (3,750) is sufficient to justify the requirements of a Representative Elementary Volume (REV). It turns out that for such a narrow grain size distribution where the grain diameters are limited, the chosen number of grains is deemed large enough for an REV at least in the dry/saturated and low saturation conditions. When the water cluster dimensions approach the sample dimension the concept of REV becomes more questionable, but this question is far beyond the scope of this study.

The LBM domain size is $N_x \times N_y \times N_z = 350 \times 350 \times 350$, with a mesh size of $\Delta x = 5 \times 10^{-6}$ m, and an imposed contact angle of $\theta = 25°$. The capillary interfaces are modeled with the air-water surface tension $\gamma = 0.072\ \text{N.m}^{-1}$. The critical time step based on Eq. (5.6) is $\Delta t_{\text{crit}} = 1.944 \times 10^{-7}$ s. The selected value of LBM surface tension is $\tilde{\gamma} = 10$. Using Eq. (5.7), the LBM time step is $\Delta t_{\text{LBM}} = 1.3176 \times 10^{-7}$ s. Therefore, the DEM time step Δt_{DEM} is chosen equal to LBM time step ($n = m = 1$ from Section 5.3.3) along with $n_{\text{ratio}} = 50$, and the ratio between DEM time step and the critical one is $\Delta t_{\text{DEM}}/\Delta t_{\text{crit}} = 0.6774$ which is reasonably high for not slowing down DEM simulations significantly. Accordingly, the relaxation times of water and air are $\tilde{\tau}_h^{\ell} = 0.5158$ and $\tilde{\tau}_h^{g} = 0.7846$, respectively[4] (in lattice units). Both relaxation times are larger than 0.5, which ensures numerical stability (Timm et al., 2016).

From a mechanical point of view, and according to Scholtès et al. (2009); Scholtes et al. (2009); Duriez and Wan (2016, 2017); Duriez et al. (2017), the total stress tensor $\boldsymbol{\sigma}^{\text{tot}}$ can be decomposed into the sum of the so-called contact stress tensor $\boldsymbol{\sigma}^{\text{cont}}$ that accounts for grain-to-grain interactions and the capillary stress tensor $\boldsymbol{\sigma}^{\text{cap}}$ to take into account the effect of capillary bridges:

$$\boldsymbol{\sigma}^{\text{tot}} = \boldsymbol{\sigma}^{\text{cap}} + \boldsymbol{\sigma}^{\text{cont}} \tag{5.10}$$

In the framework of micro-mechanics, the contact stress tensor is calculated via the Love-Weber stress tensor formula $\boldsymbol{\sigma}^{\text{LW}}$ expressed as follows (Love, 2013; Weber, 1966; Nicot et al., 2013; Duriez and Wan, 2016, 2017; Duriez et al., 2017)

$$\boldsymbol{\sigma}^{\text{cont}} = \boldsymbol{\sigma}^{\text{LW}} = \frac{1}{V} \sum_{c} \boldsymbol{f}_{ij}^{c} \otimes \boldsymbol{\ell}_{ij}^{c} \tag{5.11}$$

where $\boldsymbol{f}_{ij}^{c}$ is the contact force between pair of grains (i and j) and $\boldsymbol{\ell}_{ij}^{c}$ is the branch vector from the center of i to that of j, and $\otimes$ refers to dyadic product.

[4] Water and air viscosities are $\nu^{\text{water}} = 10^{-6}\,\text{m}^2.\text{s}^{-1}$ and $\nu^{\text{air}} = 1.8 \times 10^{-5}\,\text{m}^2.\text{s}^{-1}$, respectively, at a temperature of $T = 20°\text{C}$.

Previously, in Scholtès et al. (2009); Scholtes et al. (2009); Duriez and Wan (2016, 2017); Duriez et al. (2017) the capillary stress $\boldsymbol{\sigma}^{cap}$ has been computed directly based on capillary forces using a Love-Weber-like expression. However, this relation between capillary forces and capillary stresses applies exclusively to the *pendular* regime where isolated capillary bridges only exist between pairs of particles.

In this work, the involved degree of saturation range extends the *pendular* regime into the *funicular* and the *capillary* ones as the isolated liquid bridges coalesce, making it complicated to calculate the capillary stress using the virial of force theorem[5]. Instead, we herein compute capillary stresses $\boldsymbol{\sigma}^{\text{cap}}$ indirectly using Eq. (5.10), i.e.

$$\boldsymbol{\sigma}^{\text{cap}} = \boldsymbol{\sigma}^{\text{tot}} - \boldsymbol{\sigma}^{\text{cont}} \tag{5.12}$$

As a matter of fact, it is possible to compute the capillary stress tensor as reconstructed from the topology of the liquid phase in the pores, including the distribution of wetted grain surfaces and air-water, air, solid-water interfaces as derived in Duriez et al. (2017); but this is outside the scope of this work.

5.4.1 Dry sample

Firstly, the sample is initialized as shown in Figure (5.7a), and the lateral walls are then removed. As there is no capillary water within the sample, the latter readily collapses to form a pile of grains after a few seconds as illustrated in Figure (5.7b). The angle of repose of the pile approaches the macroscopic friction angle of the sample (Al-Hashemi and Al-Amoudi, 2018).

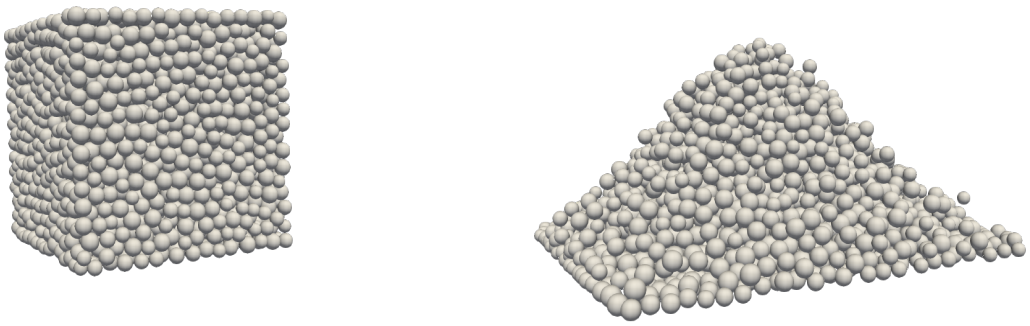

(a) (b)

Figure 5.7: (a) Initial configuration of the dry sample confined within a box of 6 walls. (b) Collapse of the dry sample when lateral walls are removed.

As the sample is dry, the capillary stress is necessarily zero. Moreover, the computed mean contact stress[6] also gives an extremely low value of approximately -0.46 Pa (here negative means compression), corresponding to self-weight of the pile. Therefore, based on Eq. (5.10), the total stress tensor is also approximately zero.

5.4.2 Wet sample

Next, the same sample as in Figure (5.7a) is considered, but under unsaturated conditions. Contrary to Figure (5.7b), Figure (5.8b) shows that despite removing the lateral

[5]This theorem consists in replacing contact forces in Eq. (5.11) by capillary forces.

[6]Mean contact stress is defined as $\frac{1}{3}\text{Tr}(\boldsymbol{\sigma}^{\text{cont}})$.

walls, the partially saturated specimen ($S_r \approx 54\%$) does not collapse, thanks to capillary forces just like in the case of a self-standing wet sandcastle at the beach. Figure (5.8b)

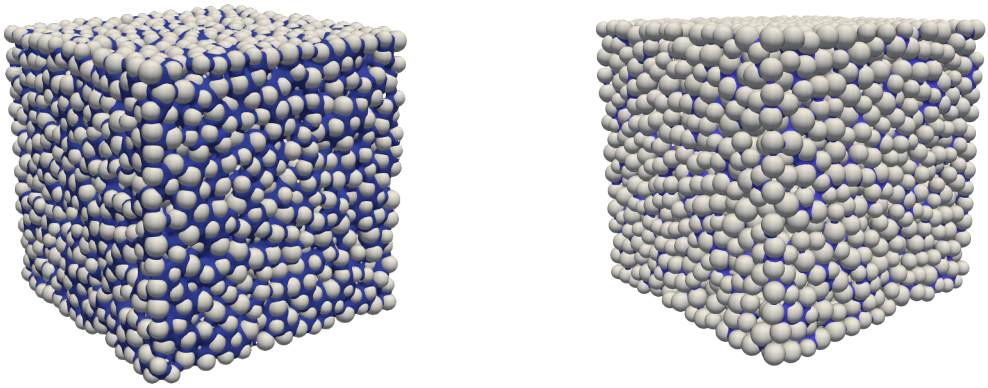

(a) (b)

Figure 5.8: (a) Initial configuration of a wet cubical sample confined within six walls. (b) Stable wet sample even after removing the lateral walls. The degree of saturation in this example is $S_r \approx 54\,\%$.

readily demonstrates the capillary effects at hand.

5.4.2.1 Initial degree of saturation setup

It is certainly of interest to numerically investigate the effects of capillarity at different degrees of saturation. In our numerical experiment, we initialize the granular assembly starting with a known volume of water as per the procedure outlined in Section 5.3.2, and let the system reach equilibrium both hydraulically and mechanically under zero external stress through many cycles of coupled DEM-LBM computations.

A total number of 10,877 spherical droplets are initialized between particles at a cutoff distance of $\varepsilon = 5\,\mu\text{m}$ which corresponds to approximately 10% of the maximum particle radius in the assembly. It is worth noting that several simulations were carried out for different values of ε, and it has been found that the results are not influenced by ε. Also, by growing or reducing the size of the initialized spherical droplet radius we thereby control the increase or decrease of the degree of saturation in our numerical exercise.

Finally, a variety of interesting results will next be explored to establish how both matric suction s and the capillary stress tensor evolve as a function of the degree of saturation.

5.4.2.2 Matric suction and Soil Water Characteristic Curve

For a given initial volume of water in the granular sample, we can readily calculate the degree of saturation as well as the volumetric water content, knowing the porosity. On the other hand, determining the suction operating at the sample level is more complicated, but can be estimated as the average of all local suctions s^i at capillary menisci weighted by their respective volumes as in Delenne et al. (2015), i.e.

$$s = \frac{1}{V_w} \sum_{i=1}^{\mathrm{N^{cap}}} \overbrace{(u_a - u_w^i)}^{s^i} V_w^i \tag{5.13}$$

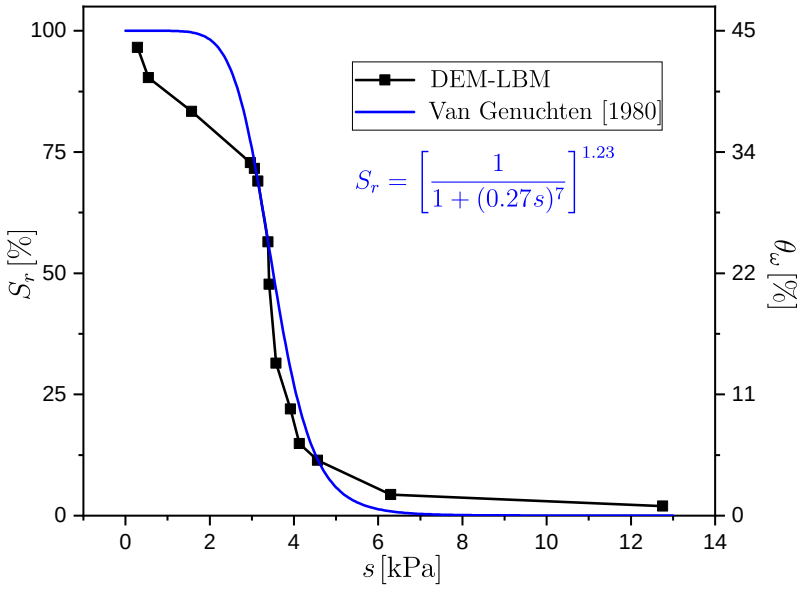

Figure 5.9: Degree of saturation and volumetric water content evolution in terms of the matric suction s of the present model. Van Genuchten (1980) model has been plotted for comparison.

where V_w is the total water volume, $\mathrm{N}^{\mathrm{cap}}$ is the number of capillary bridges, u_w^i is the pore water pressure within the i^{th} capillary bridge, and V_w^i is the volume of the i^{th} capillary bridge. Here, the air pressure u_a is negligible when compared to the negative water pressure u_w within the capillary bridges so that suction takes on a positive value.

Figure (5.9) shows the evolution of suction s as computed from Eq. (5.13) when the sample is wetted at various degrees of saturation (S_r on the left y-axis) or volumetric water contents (θ_ω on the right y-axis).

For low degrees of saturation which correspond to the *pendular* regime, the suction s is high, roughly equal to 13 kPa. As the degree of saturation increases, the suction drops drastically to reach a limiting value of $s \approx 4$ kPa for $S_r \in [15; 70]$ %. Thereafter, S_r reaches nearly $S_r \approx 70$ % when a change in slope is observed at which point suction will tend to 0 as the level of saturation is being further increased. It is worth mentioning that the suction values (s) obtained from these simulations are lower than typical experimental data. This difference arises due to the difference in conditions used in the laboratory experiments, where suction is imposed. However, these simulations are conducted under saturation-imposed conditions. To illustrate this further, during the experiments, air is blown from the sample initially fully saturated. This results in increased air pressure that causes water to drain into the reservoir beneath the sample (Mitarai and Nori, 2006; Mancuso et al., 2012). This air blowing causes a curvature in water that leads to a high suction value controlled by the smallest contribution sizes (bottle-neck paths for air entry). In contrast, in DEM-LBM simulations, water is more evenly distributed everywhere within the sample. Consequently, the difference in boundary conditions leads to variations in the calculated/measured suctions s.

For comparison purposes, the numerical simulation data has been fitted with the well-known Van Genuchten model given by

$$S_r = \left[\frac{1}{1+(\alpha s)^n}\right]^m \tag{5.14}$$

where n [-] is the parameter responsible for the soil size distribution, m [-] is related to

the symmetry of the retention curve, and α [kPa^{-1}] is the inverse of the suction at the Air Entry Value (AEV) (Matlan et al., 2014b; Oh and Lu, 2014; Matlan et al., 2014a; Fredlund and Xing, 1994).

The van Genuchten fitting parameters are found to be $n = 7$, $m = 1.23$, and $\alpha = 0.27$ with the corresponding best-fitted curve shown in Figure (5.9). Based on the statistical study reported in Matlan et al. (2014a) the values of α range between -0.445 and 1.5020 kPa^{-1} and those of n between 1.472 and 9.731 [-] for sandy soils. Interestingly, the van Genuchten parameters that fit our numerical SWCC fall within the range of sandy soils as a check for its consistency.

Recently, Hosseini et al. (2021) have studied the effect of porosity on the SWCC. According to their findings, as the porosity increases, m increases as well. For porosities within the range of 0.4 and 0.5, the corresponding m values fall between 0.75 and 1.66. Therefore, the value of $m = 1.23$ obtained in our numerical simulations is also in agreement with the numerical sample porosity being equal to 0.44. It must be noted that for a saturation degree larger than 70%, our numerical findings deviate from the van Genuchten model. This non-smoothness behavior is probably related to the way the air invades the water phase in the pores, thus creating large changes in the water menisci topology. As a consequence, significant changes occur in the topology of water menisci. This observation aligns with the experimental results of Matlan et al. (2014b) regarding sandy soils which is indeed our case here with $D_{\min} = 80\,\mu\text{m} > 50\,\mu\text{m}$ (Das, 2019).

The findings of this numerical experiment indicate that the proposed DEM-LBM model is capable of capturing one of the main features in unsaturated soils, i.e., the development of matric suction s and its variation with water saturation. In order to further evaluate the DEM-LBM model, the distinctive properties of the capillary stress tensor $\boldsymbol{\sigma}^{\text{cap}}$ will be next investigated.

5.4.2.3 Capillary stress tensor $\boldsymbol{\sigma}^{\text{cap}}$

In the absence of the lateral walls, the total stress tensor $\boldsymbol{\sigma}^{\text{tot}}$ is negligible. The capillary stress still subsists following Eq. (5.10), as

$$\boldsymbol{\sigma}^{\text{cap}} = -\boldsymbol{\sigma}^{\text{cont}}. \tag{5.15}$$

For contact angles below 90°, capillary forces are attractive in nature, they will tend to bring the particles closer to interpenetrate further, which will induce repulsive contact forces. The particles then move such that an equilibrium state is finally reached when repulsive forces and attractive capillary forces are equal. Thus, the liquid bridge being in tension by virtue of surface tension forces, the effect of capillarity is tensile. Therefore, the contact stress $\boldsymbol{\sigma}^{\text{cont}}$ is in compression, whereas the capillary stress $\boldsymbol{\sigma}^{\text{cap}}$ is tensile.
The following analyses will be based on the mean capillary stress $\boldsymbol{\sigma}^{\text{cap}}$ defined as:

$$p^{\text{cap}} = \frac{1}{3}\text{Tr}(\boldsymbol{\sigma}^{\text{cap}}). \tag{5.16}$$

The computations in the DEM code YADE follow the continuum mechanics convention where compression is negative and tension is positive. Accordingly, a positive p^{cap} corresponds to the traction that confers the sample with an *apparent cohesion* under unconfined conditions. The choice of a mean capillary stress can be justified based on Figure (5.10). In the latter figure, each component of the computed capillary stress tensor $\boldsymbol{\sigma}^{\text{cap}}$ is plotted for a degree of saturation $S_r = 11.41\%$. Although not necessarily true in the most general cases (Duriez and Wan, 2016; Farahnak et al., 2021), the computed capillary stress

tensor $\boldsymbol{\sigma}^{\text{cap}}$ turned out to be nearly spherical (with $\sigma_{xx} \approx \sigma_{yy} \approx \sigma_{zz} \approx 1.12$ kPa and $\sigma_{xy} \approx \sigma_{yz} \approx \sigma_{xz} \approx 7.21 \times 10^{-4}$ kPa) due to the initial arrangement of the solid particles and liquid bridges.

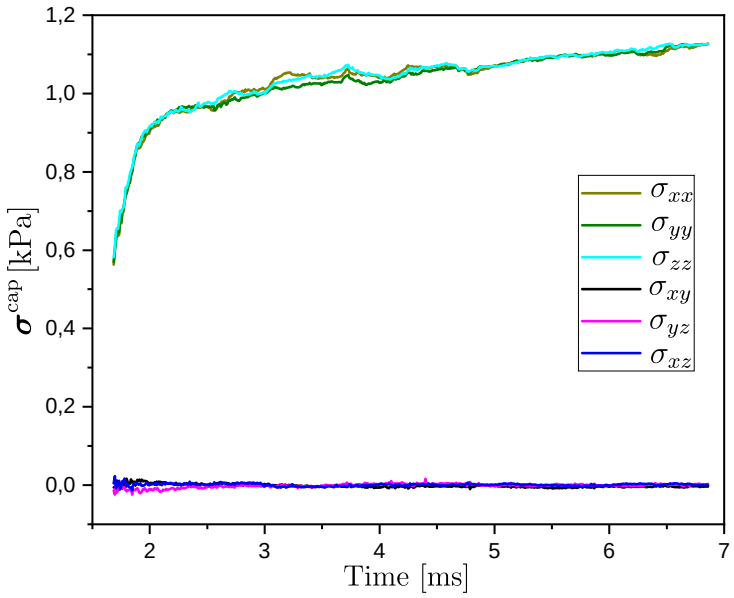

Figure 5.10: Capillary stress tensor components ($\sigma_{xx}, \sigma_{yy}, \sigma_{zz}, \sigma_{xy}, \sigma_{yz}, \sigma_{xz}$) evolution in time for $S_r = 11.41\%$.

Figure (5.11a) shows the evolution of the mean capillary stress with time until equilibrium is reached for different degrees of saturation. The search for an equilibrium state, both mechanically and hydraulically, eventually leads to the plateau shown in Figure (5.11a). The coupling between DEM-LBM calculations was described in detail in Section 5.3.3.

Generally speaking, the higher the degree of saturation with more liquid bridges pulling the grains together, the higher p^{cap} as well as the plateau. Figure (5.11a) depicts the temporal evolution of p^{cap}, demonstrating a gradual increase in mean capillary stress over time for a given degree of saturation S_r. This increase is attributed to the evolving microstructural particle topology until an equilibrium state is attained. Remarkably, the same figure highlights an intriguing observation: the mean capillary stress at the equilibrium state increases with the degree of saturation, leading to a peak at $S_r = 67.47\%$, before experiencing a drop at $S_r = 72.77\%$. This indicates the existence of a maximum value of p^{cap} within the range of S_r between 11.41% and 72.77%.

As a comparative note, the phenomenon of increased capillary stress can also be observed within a small granular assembly composed of three grains (Gagneux and Millet, 2016). Under such conditions, it was found that the capillary force will increase significantly (about 30%) when capillary bridges merge to become one cluster, whereas there were three isolated capillary bridges before. These results are shown in the next chapter after introducing the wetting and drying processes.

We next explore the evolution of p^{cap} as well as that of s in terms of the degree of saturation and volumetric water content θ_ω as plotted on the same Figure (5.12). To explain the evolution of p^{cap} and s, a *topology* analysis of capillary bridges and air bubbles is necessary. To avoid ambiguities, the displayed numbering of labeled[7] air bubbles and

[7]The Flood-Fill algorithm is used to detect capillary bridges as well as air bubbles. Every air bubble

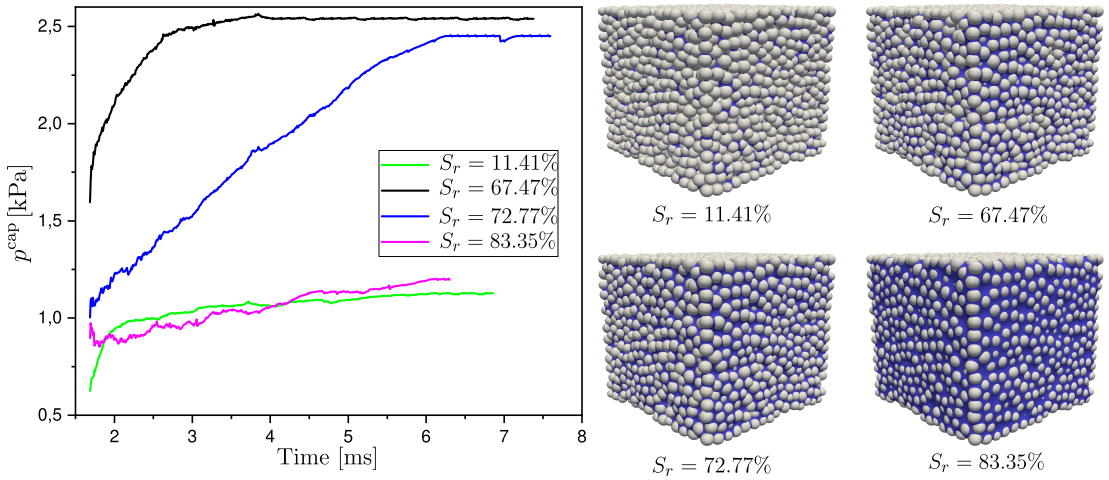

Figure 5.11: (a) The evolution of mean capillary stress p^{cap} [kPa] over time in DEM-LBM coupled simulations for selected values of degrees of saturation are shown, (b) Snapshots of the partially saturated samples at equilibrium for different values of $S_r \in \{11.41; 67.47; 72.77; 83.35\}$ %.

capillary bridges, as shown in Figures (5.13) and (5.14), respectively, is explained next. For example, for a degree of saturation $S_r = 11.41\%$, the total number of capillary bridges is 2,088 and it would be impossible to display them all labeled with distinct colors. We, therefore, show only the first 6 labeled IDs as cut-off values so that capillary bridge IDs higher up to 2,088 are represented by the same color (orange). The same labeling and coloring scheme is applied to air bubbles in Figure (5.13).

Turning to point (1) which corresponds to $S_r = 11.41$ %, it can be seen that the wet granular assembly contains an extensive network of air clusters together with a large number of capillary bridges as illustrated in Figures (5.13) and (5.14), respectively.

As the degree of saturation increases and reaches point (2) which corresponds to the peak of p^{cap} ($S_r \approx 68$ %), the isolated capillary bridges develop into one big cluster, with plenty of trapped air bubbles within the capillary bridge cluster. This particular point corresponds to the maximum curvature in the SWCC where the suction s starts to decrease, as seen in Figure (5.12).

and capillary bridge is labeled and given an ID as indicated in Figures (5.13) and (5.14)for air bubbles and capillary bridges, respectively.

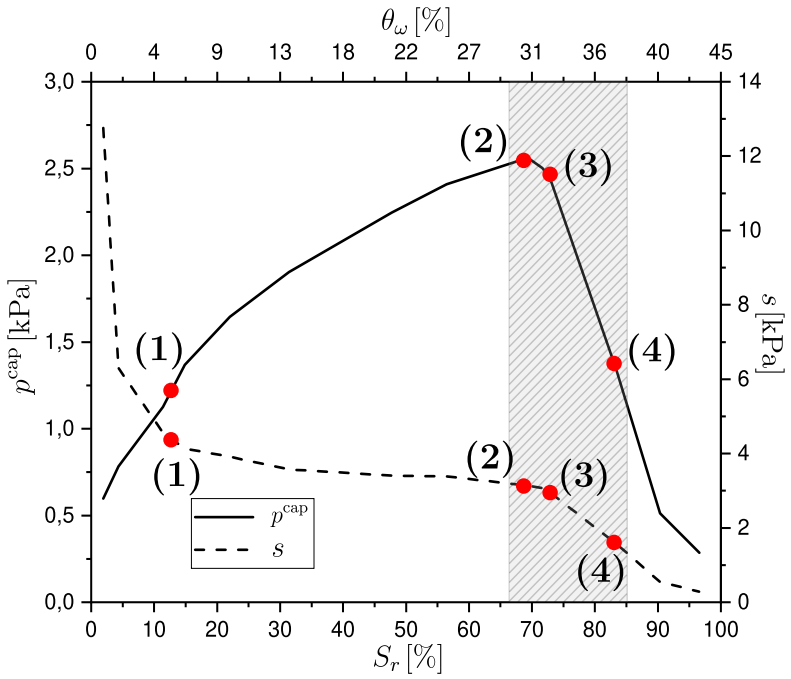

Figure 5.12: Mean capillary stress p^{cap} [kPa] based on Eq. (5.15) and suction s [kPa] in terms of degrees of saturation S_r [%] and volumetric water content θ_ω [%] at the bottom and top x-axis, respectively.

It is important to note that the granular system has only one large cluster of capillary bridges from step (2) onward. For higher degrees of saturation at (3) and (4), the continuous air phase dwindles with ubiquitous trapped air bubbles, thus resulting in concurrent drops in suction and mean capillary stress.

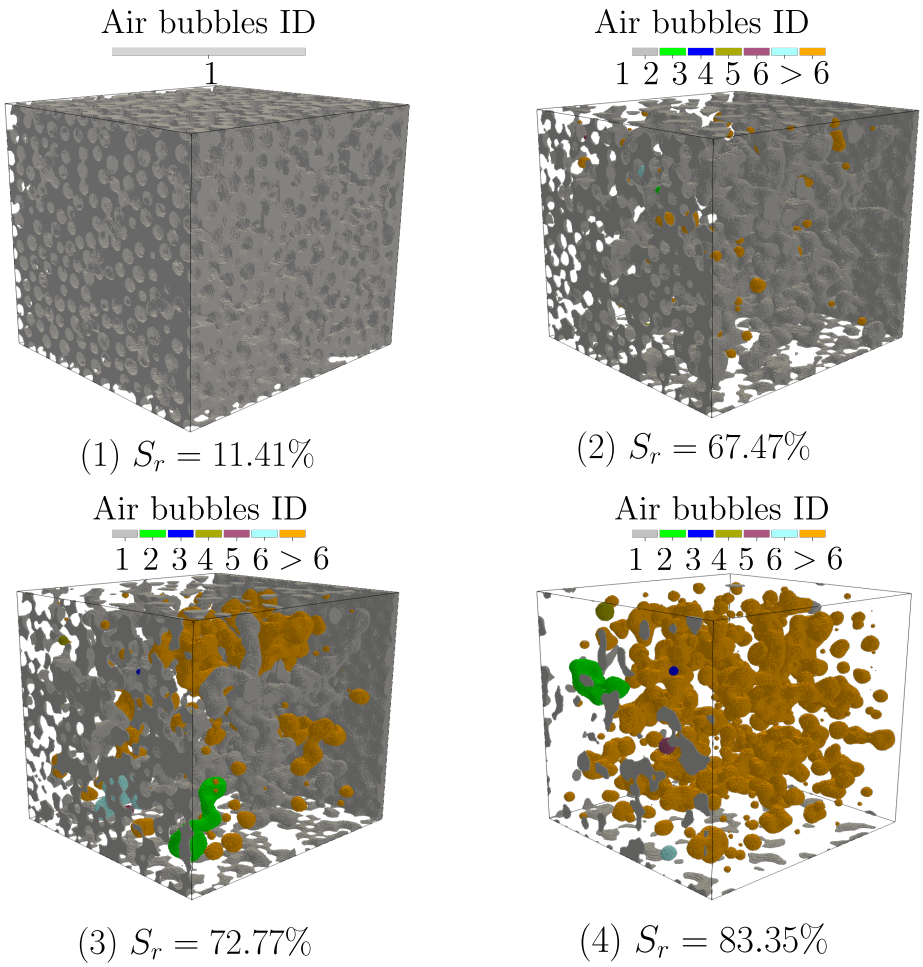

Figure 5.13: Snapshots of the distribution of air bubbles within the domain as the system is wetted for 4 different degrees of saturation $S_r \in \{11.41; 67.47; 72.77; 83.35\}$ %.

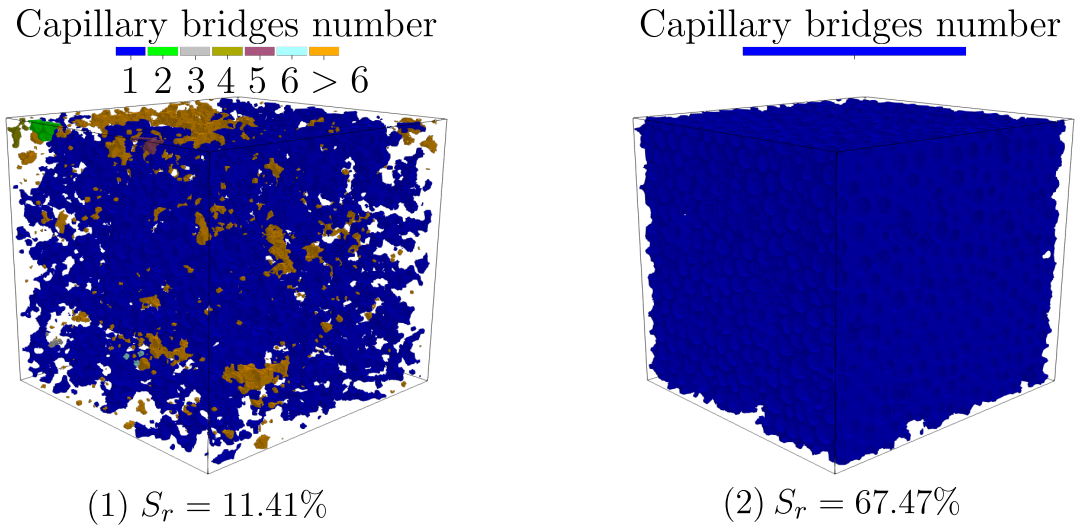

Figure 5.14: Snapshots of capillary bridges within the granular media for 2 different degrees of saturation $S_r \in \{11.41; 67.47\}$ %.

These two aforementioned steps (3 & 4), in fact, correspond to the stage of AEV in SWCC for a path starting from a high saturation. The AEV stage occurs when the

air starts filling the voids of the granular system. In order to provide a clearer picture, Figure (5.15) shows snapshots of a section taken in the middle of the specimen at various levels of saturation similar to those shown in Figure (5.14).

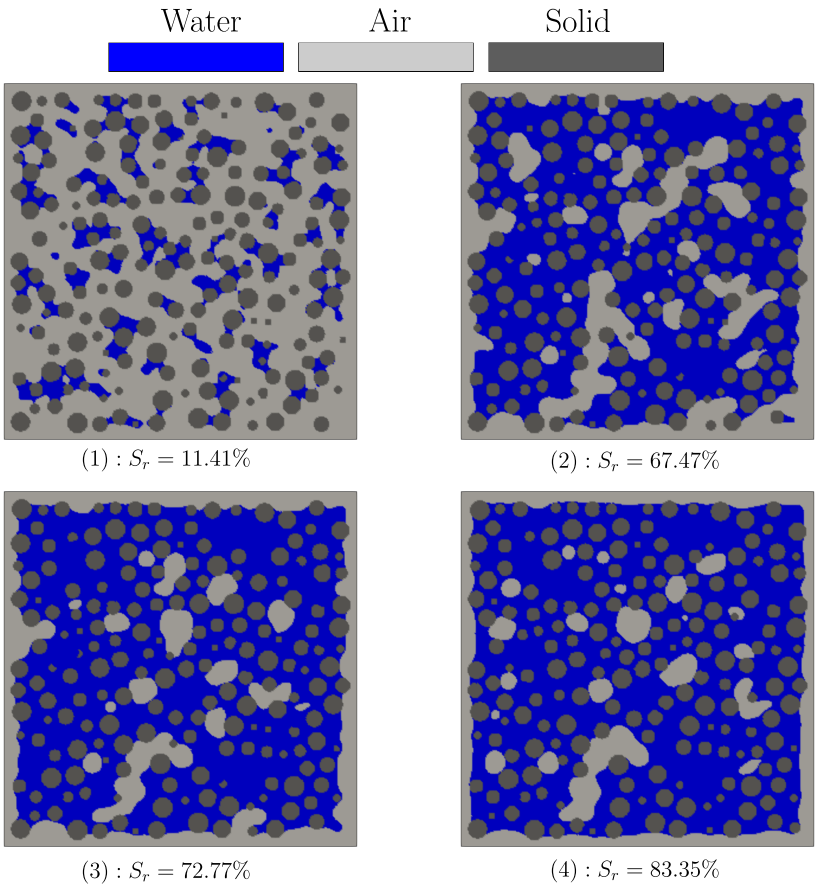

Figure 5.15: Snapshots of a section made in the middle of the sample at various degrees of saturation. Blue, gray, and dark gray colors correspond to water, air, and solid grains, respectively.

As can be seen, for high degrees of saturation, the sample contains one extensively large interconnected water cluster engulfing isolated trapped air bubbles which correspond to the *capillary*[8] regime, as shown in (4) at $S_r = 83.35\%$. As the degree of saturation decreases, the air starts to infiltrate through the specimen to become partially connected to the external air, as seen in (3) and (2). These two latter configurations represent the *funicular* regime. Lastly, for low degrees of saturation below (1): isolated and coalesced capillary bridges can be found, and the air becomes one big interconnected cluster which corresponds to the end of the *pendular* regime or the beginning of the *funicular* regime.

5.4.2.4 Capillary stress tensor and Bishop's equation

In light of the DEM-LBM simulations, it is tempting to revisit the long-standing debate in unsaturated soil mechanics such as how the stresses are partitioned to reflect the contribution of each phase. The existence of single effective stress that controls both skeleton deformation and failure of unsaturated soils is herein not addressed as it has been thoroughly discussed in Duriez et al. (2018); Nuth and Laloui (2008); Laloui and Nuth

[8]The degree of saturation marking the onset of the capillary regime depends on the water spatial distribution in the sample. In laboratory experiments, air invades the pores from the sample boundaries. In this case, the capillary regime is likely to be observed for a wider range of saturation.

(2009); Scholtes et al. (2009); Vlahinić et al. (2011). However, the capillary stress tensor will be analyzed to elucidate and provide a micro-scale perspective to Bishop's stress equation. As previously seen in Figure (5.10), the capillary stress tensor is spherical, hence, the relation between the capillary stress tensor $\boldsymbol{\sigma}^{\text{cap}}$ and the suction s as a scalar can be simplified as (Duriez et al., 2017):

$$\boldsymbol{\sigma}^{\text{cap}} = sS_r\boldsymbol{I}. \tag{5.17}$$

In fact, Eq. (5.17) represents a simplified version of Bishop's equation previously seen in Eq. (1.36) with the assumption that $\chi = S_r$, which is debatable and subjected to controversy in the literature. In our DEM-LBM computations, the capillary stress tensor is directly deduced by subtracting the contact stress tensor from the total stress one following Eq. (5.15).
Figure (5.16) gives the plot of p^{cap} as calculated from simplified Bishop's equation (Eq. 5.17) and our DEM-LBM simulations (Eq. (5.15)) in terms of degrees of saturation S_r and volumetric water content θ_ω on the bottom and top x-axis of the figure, respectively.

As the granular assembly is being wetted, both mean capillary stresses will increase until a certain threshold ($S_r \approx 68$ %, $\theta_\omega \approx 30$ %) beyond which the specimen starts to lose the effects of capillarity. We can observe that p^{cap} based on Bishop's simplified equation is always less than our computed values.

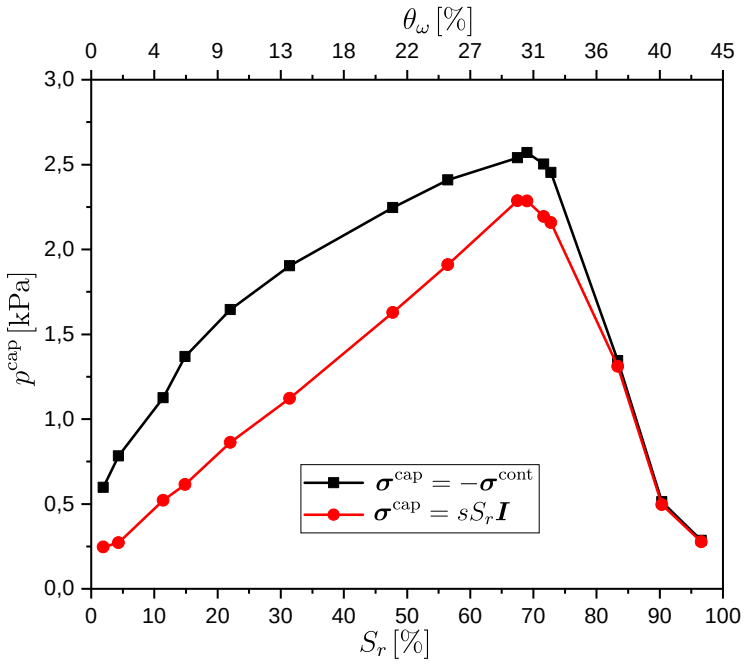

Figure 5.16: Mean capillary stresses p^{cap} [kPa] based on Eqs. (5.15) and (5.17) evolution in terms of degrees of saturation S_r [%] and volumetric water contents θ_ω [%].

Despite the same tendency displayed in both curves, they do not perfectly match, especially before the threshold is reached. The reason for this lies in the assumption: $\chi = S_r$ noted earlier in Bishop's equation.

To investigate whether S_r and χ coincide or not, χ is back-calculated from our DEM-LBM computations for various degrees of saturation and suction values. In the present study, since the specimen is unconfined ($\boldsymbol{\sigma}^{\text{tot}} = \boldsymbol{0}$), the capillary stress coincides with the negative of the contact stress tensor, and thus:

$$\chi = \frac{1}{3}\frac{\mathrm{Tr}(\boldsymbol{\sigma}^{\mathrm{cont}})}{s}. \tag{5.18}$$

Several points should be noted:

- The effective stress parameter χ can be generally defined as a tensor, but since in the present simulations, all the stress tensors are diagonal and isotropic, mean values are considered, *i.e.*, $\frac{1}{3}\mathrm{Tr}(\boldsymbol{\sigma})$;
- Eq. (5.18) is deduced from Eq. (1.36) which is formulated in the Soil Mechanics convention (compression > 0 and tension < 0). The mean contact stress is therefore positive, $\frac{1}{3}\mathrm{Tr}(\boldsymbol{\sigma}^{\mathrm{cont}}) > 0$;
- The air pressure u_a is negligible with respect to the mean capillary stress.

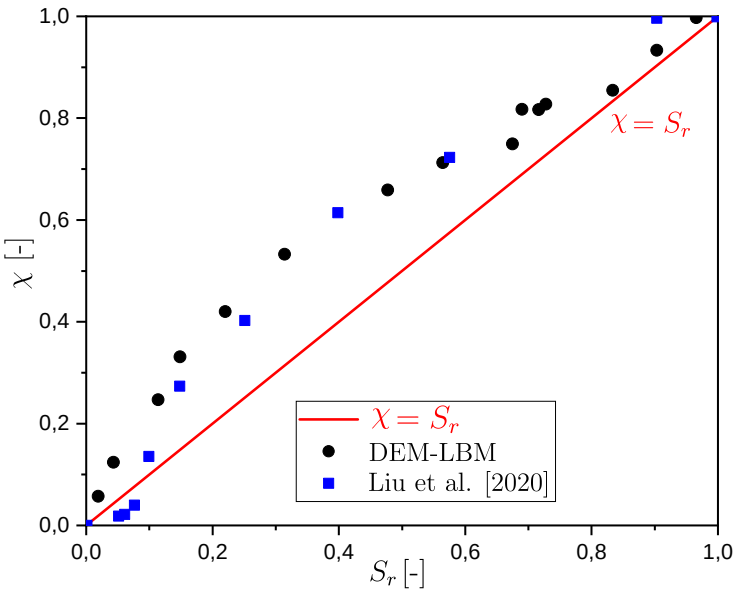

Figure 5.17: The evolution of χ in terms of S_r. Linear relation ($\chi = S_r$) and Liu et al. (2020b) results are plotted for comparison.

The back-calcualted χ is then plotted against S_r as shown in Figure (5.17) where χ and S_r almost never coincide proving why both $\boldsymbol{\sigma}^{\mathrm{cap}}$ are not exactly similar in Figure (5.16). To ensure that our findings are right on course, another numerical data set for χ in terms of S_r (Liu et al., 2020b) has been added to Figure (5.17).

Our findings and the ones determined by Liu et al. (2020b) are generally in good agreement. Clearly, the two numerical results do not line up perfectly, especially for low levels of degrees of saturation $S_r < 10$ %. For this particular range, and contrary to our findings, Liu et al. (2020b) have found that $\chi < S_r$.

The above discrepancy can be attributed to the difference between particle size distributions used in this work and theirs. In fact, the grain size used in Liu et al. (2020b) is roughly four times smaller than the one we have used in this study, which results in

changes not only in porosity but also the attendant capillary effects—the smaller the particles, the greater the capillary effect. Moreover, and according to Bishop and Blight (1963), for clayey soils the effective stress parameter χ is smaller than the S_r not only for low saturation but even up to approximately 50 % (Talybont Clay). In contrast, silty-sandy soils lead to $\chi < S_r$ only for low degrees of saturation $S_r < 20$ %—see Vaich moraine soil in Bishop and Blight (1963). Hence, χ tends to remain greater than S_r as particle size increases, which renders our results reasonable since our particle size is greater than the one used in Liu et al. (2020b).

It is also interesting to fit the findings using a fourth-order polynomial function $\chi = f(S_r) = \sum_{i=0}^{4} a_i S_r^i$ as shown in Figure (5.18). The fitting was determined using *Matlab*. In order to determine the goodness of the fitting model, the R-squared (R^2), also known as the determination coefficient, residual norm, and the Mean Square Error (MSE), are respectively determined as follows

$$\begin{aligned} R^2 &= 1 - \frac{\sum_i (y_i - \hat{y}_i)^2}{\sum_i (y_i - \bar{y})^2} = 0.997; \\ \text{Residual} &= \sum_i (y_i - \hat{y}_i)^2 = 3.77 \times 10^{-3}; \\ \text{MSE} &= \sum_i (y_i - \hat{y}_i) = 2.1 \times 10^{-2} \end{aligned} \tag{5.19}$$

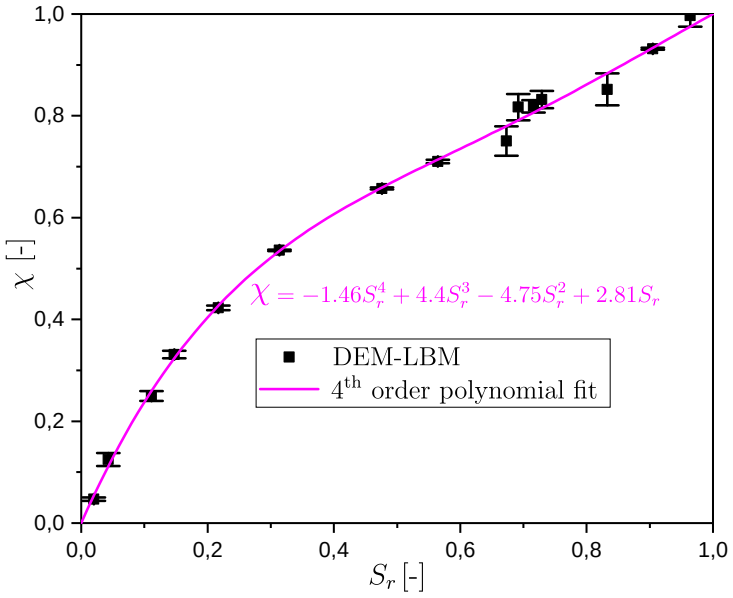

Figure 5.18: The evolution of χ in terms of S_r of DEM-LBM simulations and their fitting function.

where y_i is the numerical data (observed), $\hat{y}_i$ the estimated data, and $\bar{y}$ is the mean value of the numerical data. The aim of this polynomial function is to be used in macroscopic methods, such as FEM or FDM, as a replacement for Bishop's effective stress with the assumption of $\chi = S_r$.

5.5 Conclusion

In this chapter, the DEM-LBM coupling algorithm is developed to investigate the characteristics of partially saturated granular assemblies for different degrees of saturation. The air-water interfaces were handled by the phase-field-based Lattice Boltzmann model (LBM). As such, the proposed LBM approach successfully handled the dynamics of isolated as well as coalesced capillary bridges, and most importantly calculates capillary forces throughout *pendular, funicular* and *capillary* regimes. As for the particle dynamics and contacts between them, they were handled by employing the non-smooth Discrete Element Method (DEM) using the open-source software YADE. The predictive capabilities of the DEM-LBM algorithm are investigated in the modeling of unsaturated granular assemblies. First, the variation of suction in terms of the degree of saturation or volumetric water content has been qualitatively recovered and compared to the van Genuchten model.

Furthermore, when the sample is wetted at various degrees of saturation, we recover the classic result of a self-standing sandcastle under no confinement, whereas an unconfined cubical dry sample readily collapses. Another finding is the elucidation of the mean capillary stress for several degrees of saturation. The obtained results demonstrate that the mean capillary stress only increases with the degree of saturation up to a certain level $\approx 68\%$ after which there is a drop, explainable by the dynamics of water clusters filling the void space. Next, we also have convincingly demonstrated that the so-called Bishop's parameter χ does not coincide with the degree of saturation S_r, but takes a form that can be readily calculated numerically and that coincides with experimental results.

In conclusion, it appears that the DEM-LBM coupling is indeed a valuable numerical tool for investigating partially saturated granular assemblies across various regimes—*pendular*, *funicular*, and *capillary*. This approach allows for an elucidation of the dynamics of the different phases at the pore scale. Further research endeavors should dig deep into the micro-mechanical behavior of partially saturated granular assemblies subjected to wetting (condensation) and drying (evaporation) cycles, with the objective of understanding thoroughly the interaction between capillary bridges and the *hysteresis* phenomenon. This investigation will also assess their impact on suction and mean capillary stress, which will be the focus of the next chapter.

Chapter 6

Condensation and Evaporation Processes: Hysteresis in partially saturated granular assemblies

6.1 Introduction

In this chapter, an investigation of the hysteresis phenomenon in the dynamics of air-water capillary bridges within a small system comprised of three (triplet) and four (quadruplet) particles is carried out. A mathematical transformation has been developed to address the processes of both evaporation and condensation. The proposed approach is validated using two benchmark examples: mono-dispersed triplet and quadruplet of particles in contact and for a wetting angle of $\theta = 50°$ for which capillary forces are examined. The condensation and evaporation processes are next applied to triplets and quadruplets of particles in numerous configurations, e.g., different separation distances with different wetting angles θ.

Next, the condensation and evaporation processes are applied to a larger granular assembly with fixed particles (only LBM) at the REV scale to investigate the hysteresis of suction s between condensation and evaporation for the same wetting angle θ. Moreover, another example at the REV scale subjected to condensation and evaporation is carried out for the same wetting angle, but this time using the DEM-LBM model to study the impact of particle rearrangements within the REV. In this case, both suction s and capillary stress $\boldsymbol{\sigma}^{\text{cap}}$ can be calculated.

Then, the wetting angle hysteresis is enforced within the simulations: during the evaporation process, the wetting angle θ_e is chosen to be lower than θ_c which stands for the wetting angles during the evaporation and condensation processes, respectively.

6.2 Evaporation and condensation processes

Evaporation and condensation processes occur at the interface separating water from air, leading to a change in the interface's position. Hence, in a phase-field model, where the interface corresponds to a threshold value for ϕ, eliminating or adding matter may be achieved by increasing or decreasing the value of ϕ around the equilibrium position of the interface. Formally, this is done by applying a mathematical transformation of the $\phi^{\text{eq}}(\xi)$ to become $\phi^{\text{e}}(\xi)$ or $\phi^{\text{c}}(\xi)$ to simulate evaporation or condensation, respectively; see Figure (6.1).

At the thermodynamic equilibrium, the evolution of the phase-field parameter ϕ through the interface has to fulfill the equilibrium condition: $\phi(\xi) = \phi^{\text{eq}}(\xi)$. Based on Eq. (3.10a), the differentiation of $\phi^{\text{eq}}(\xi)$ yields:

$$\mathrm{d}\phi = \frac{4}{W}\phi(1-\phi)\mathrm{d}\xi \tag{6.1}$$

where $\mathrm{d}\phi$ is the infinitesimal variation of ϕ and $\mathrm{d}\xi$ is the infinitesimal variation of ξ within the capillary bridge interface. Numerically speaking, Eq. (6.1) can be re-written as follows:

$$\Delta\phi = \frac{4}{W}\phi(1-\phi)\Delta\xi \tag{6.2}$$

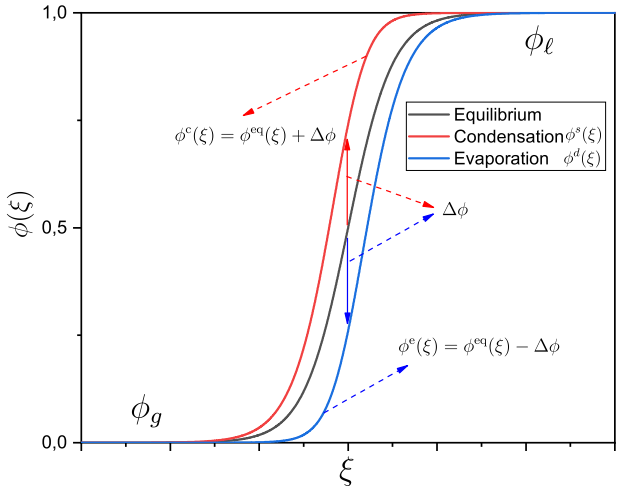

Figure 6.1: Profiles of condensed and evaporated liquid-gas capillary interfaces $\phi^c(\xi)$ $\phi^e(\xi)$, respectively for $\Delta\xi = 1$.

where $d\phi$ is replaced by $\Delta\phi$ and $d\xi$ by $\Delta\xi$. As such, Eq. (6.2) provides the relationship between the change in ϕ and the change in the position of the interface in lattice units.

The proposed numerical technique is such that evaporation or the condensation of fluid can be imposed as follows:

$$\phi^e(\xi) = \phi^{eq}(\xi) - \Delta\phi\,(\Delta\xi) \tag{6.3a}$$

$$\phi^c(\xi) = \phi^{eq}(\xi) + \Delta\phi\,(\Delta\xi) \tag{6.3b}$$

where $\phi^e(\xi)$ and $\phi^e(\xi)$ are the profiles of the phase-field parameters after applying evaporation and condensation processes, respectively.

Figure (6.1) shows the equilibrium $\phi^{eq}(\xi)$ profile (black curve) and the new curves after condensation (red) and evaporation (blue) for an imposed displacement of the interface by 1 lattice unit $\Delta\xi = \pm 1$. As can be seen from Figure (6.1), the variations of ϕ are significant only in the liquid-gas interface, whereas, in the bulk fluids the variation is quasi nil and respect $\phi \in \{0; 1\}$.

6.3 Jumps in capillary forces and hysteresis effects on small grain assemblies

In this section, the condensation/evaporation technique is implemented to capture the hysteresis effects in small clusters composed of three and four spherical grains. For all the triplets and quadruplets applications, only mono-dispersed particles are considered with a radius of $R = 4$ mm, with a size mesh $\Delta x = 7.5 \times 10^{-5}$ m.

6.3.1 Equidistant triplet of grains

The first case study deals with a triplet of particles forming an equilateral triangle with a separation distance $D = 0.1$ mm, as illustrated in Figure (6.2). This separation distance is the minimum distance we can simulate, which corresponds to 1 voxel, to prevent numerical instabilities. The 1 voxel distance (equivalent to $\Delta x = 7.5 \times 10^{-5}$ m) is relatively small compared to the size of the particles and hence they can be assumed to be almost in contact. We also show in the same figure how capillary bridges are initialized

at the mid-distance of each pair of spherical grains. This configuration approximately matches the one used in Gagneux and Millet (2016) and Gras (2011), in which case the particles were all touching.

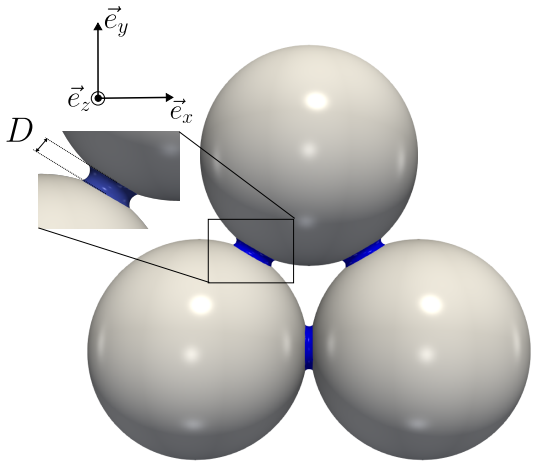

Figure 6.2: Three capillary bridges located at the mid-distance of each pair of particles.

After initializing capillary bridges, the proposed condensation/evaporation process is numerically enforced and the resulting capillary force acting on the top particle is calculated via Eq. (4.26).

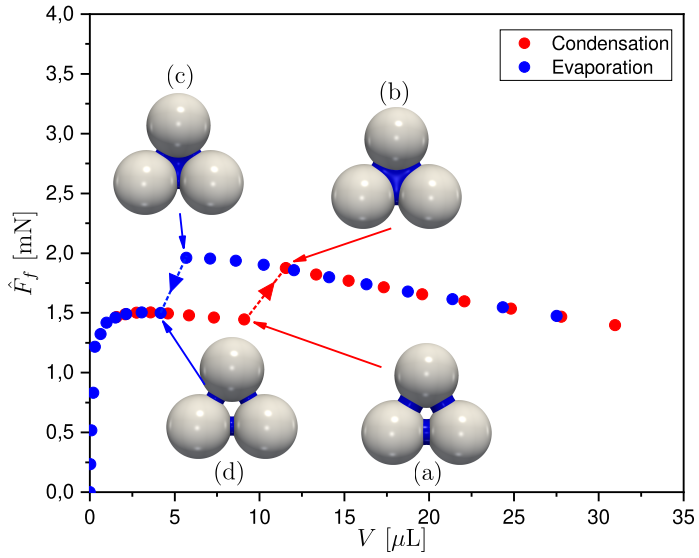

Figure 6.3: Capillary force evolution in terms of the water volume as the system undergoes a cycle of condensation and evaporation with a contact angle of $\theta = 50°$ and for a separation distance of $D = 0.1$ mm. The capillary force is calculated on the top grain in the y-direction, see Figure (6.2).

Figure (6.3) depicts the capillary forces evolution when the granular system is subjected to condensation followed by evaporation. As the volume of water increases, when the triple (three-phase contact) lines of the isolated capillary bridges touch each other, *coalescence* takes place, resulting in the transition of the system from the pendular to the funicular regime. The merging occurs for a volume of $V \approx 10\,\mu$L as seen in Figure (6.3)

from state (a) to (b). It is important to note that at the coalescence, a discontinuity in capillary forces is observed with a relatively sharp increase of 29.9% in capillary forces, which is completely in agreement with the theoretical calculation of 30% reported by Gagneux and Millet (2016) for the same contact angle $\theta = 50°$.

To better understand the physics behind the sharp increase in capillary forces at coalescence, the evolution of *Laplace* F_{p} and surface tension F_γ forces are plotted in Figure (6.4).

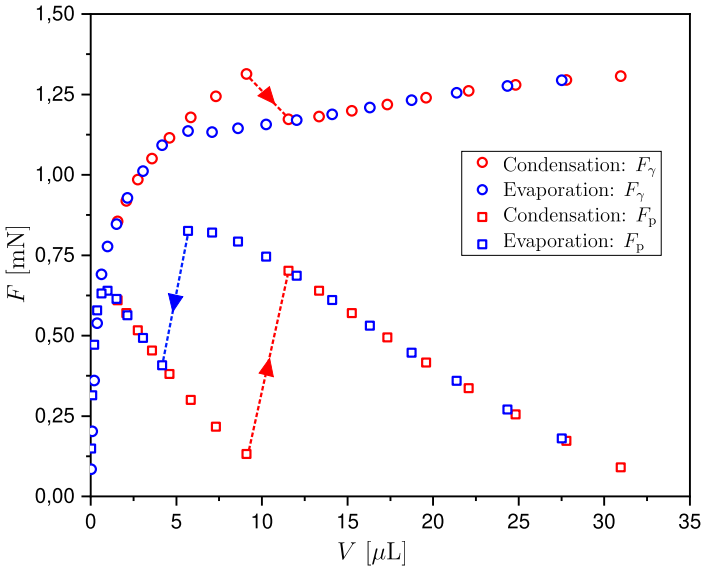

Figure 6.4: The evolution of pressure force F_{p} and surface tension force F_γ of Eq. (4.26) in terms of water volumes while subjected to condensation and evaporation processes.

In the pendular regime and as the water volume increases, it can be observed that F_{p} decreases continuously. By contrast, the surface tension force F_γ term increases because the wetting surface (solid-water interface) expands gradually around the particle. At coalescence, it is observed that the *Laplace* force suffers a significant jump whereby it increases, whereas the surface tension force shows a slight decrease also through a jump. It is the two forces when combined that give an overall increase of $\approx 29.9\,\%$ in capillary force, which coincides with the value reported by Gagneux and Millet (2016).

It is worth noting that the discontinuities in F_{p} and F_γ have two origins. First, based on Eq. (4.26), the surface tension force F_γ will increase in direct proportion with the size of the wet contour Γ. Figure (6.5) depicts how the contours evolve before and after coalescence. It can be observed that the contour before coalescence (blue contour) slides into the middle to fill the air between capillary bridges at coalescence, causing a slight decrease in the wet contour Γ (red contour), hence a decrease in the surface tension force.

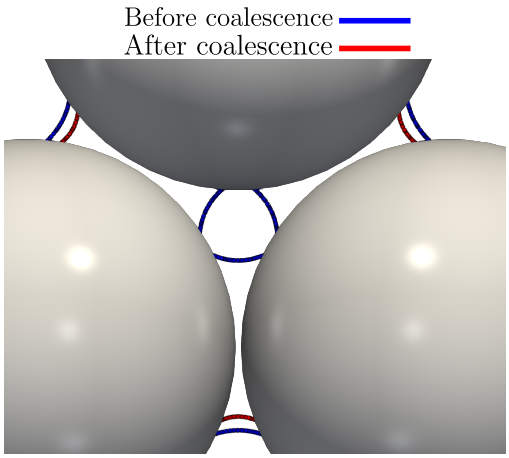

Figure 6.5: Air-water interface contour before and after coalescence for $\theta = 50°$ and $D = 0.1$ mm.

Second, F_p increases drastically despite the volume V changes slightly at *coalescence*. This drastic increase in F_p is due to the change in the suction $s = u_a - u_w$ when the isolated capillary bridges become one big cluster, which is illustrated in Figure (6.6). It is highlighted here that the change in the suction s is caused by the change in curvatures upon the air-water interface after and before coalescence—according to the Young-Laplace equation (Mielniczuk et al., 2018; Hueckel et al., 2020; Younes et al., 2023a).

When the water volume exceeds $V = 30\,\mu\mathrm{L}$, we choose to begin the evaporation process by using Eq. (6.3a). The merged capillary bridge shrinks as evaporation proceeds until the water volume reaches $V \approx 5.2\,\mu\mathrm{L}$ at step (c) in Figure (6.3). At this point, the capillary bridge spontaneously splits up into three smaller capillary bridges of equal size as seen in Figure (6.3) at step (d). This rupture event causes a sharp decrease of 30.88% in the capillary force as also obtained by Gras (2011).

It is important to note that in Figure (6.4), the force acting on the top grain with one single bridge or three distinct bridges is the same during either the condensation or evaporation path, which is in agreement with the fact that the wetting angle remains constant during the simulation. Only the volume at which bridges merge or split is different. The same observation is true for the variation of suction as shown in Figure (6.6).

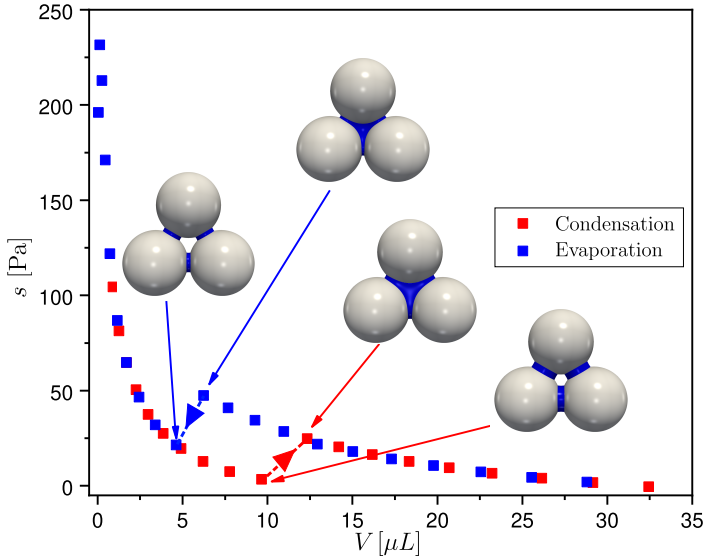

Figure 6.6: Evolution of suction s [Pa] evolution in terms of water volumes V [μL] during condensation and evaporation processes.

To understand the underlying physics of this *hysteresis*, we show the snapshots of the merged capillary bridge as it is being evaporated until the rupture phase—from (a) to (c) of Figure (6.7). As the merged capillary bridge is being evaporated, the thickness z^* of the capillary bridge in the yz plane is being narrowed, as illustrated in Figures (6.7c.1), (c.2), and (6.8). Once z^* reaches zero, the single bridge splits ultimately into 3 separate bridges as precisely illustrated in Figure (6.8). As previously mentioned, coalescence takes place when the triple lines of distinct capillary bridges touch each other. Therefore, during condensation and evaporation processes, the geometrical conditions for the switch from 1 to 3 bridges and *vice-versa* are forcibly different, which explains the hysteresis. In short, the rupture of a capillary bridge involves a thinning mechanism, whereas the merging of capillary bridges involves the meeting of triple lines.

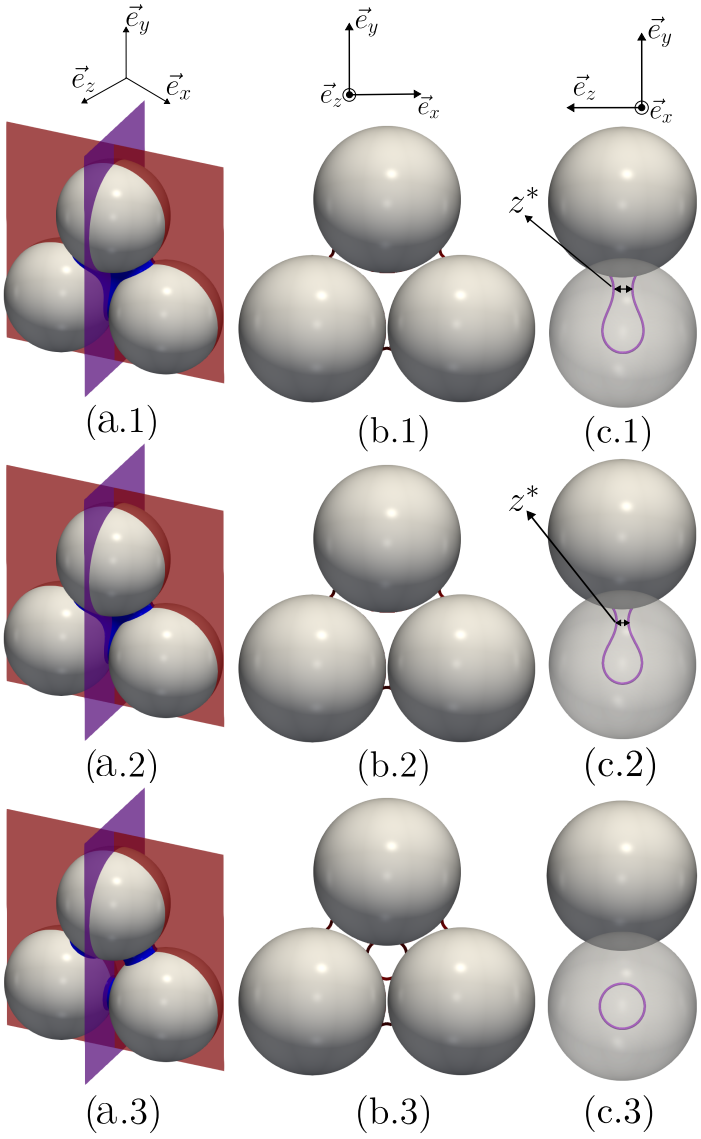

Figure 6.7: Evaporation process steps from 1 to 3 for a contact angle $\theta = 50°$. (a) 3D view, (b) 2D section view in $xy-$plane, (c) 2D section view in $yz-$plane. The bottom particles in (c) are in transparent mode to better visualize the merged capillary bridge.

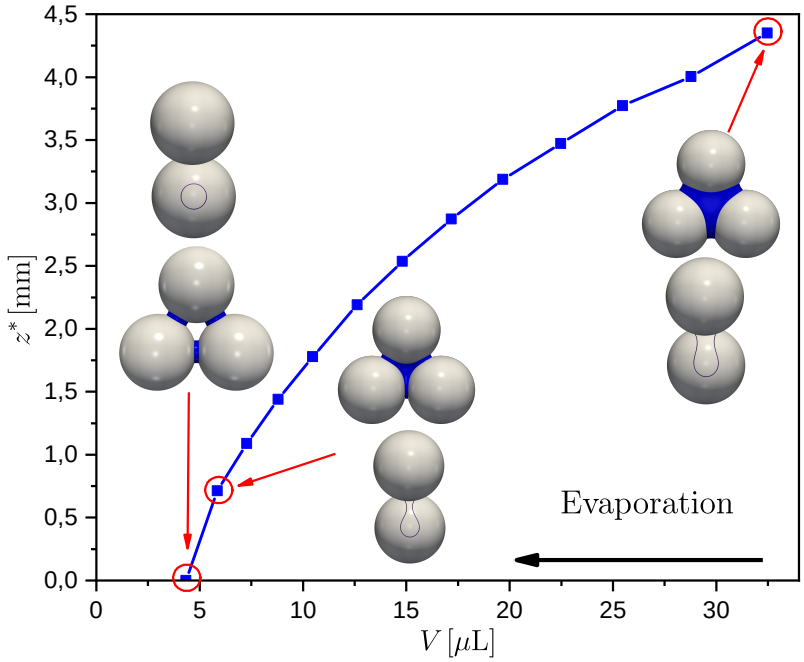

Figure 6.8: Evolution of the capillary bridge thickness in yz-plane (z^*) in terms of total water volume V during the evaporation phase. Figure (6.7c) shows the illustration of z^*.

6.3.2 Influence of separation distances and wetting angle

After recovering experimental results in the previous subsection, the next step is to explore the influence of separation distances and wetting angle on the sharp jump and drop of capillary forces at coalescence and rupture, respectively. This study is essential because capillary forces vary with the contact angle as well as the separation distance Younes et al. (2022); Benseghier et al. (2022); Mielniczuk et al. (2018); Miot et al. (2021). The new configurations are set in such a way that the centers of the spherical particles still form an equilateral triangle, but the separation distance D is varied as in $D \in \{0.2; 0.3\}$ mm with $\theta = 50°$.

Figure (6.9) shows the sharp relative capillary force $|\Delta F|$ [%] in terms of the separation distances during the condensation and evaporation processes, respectively. It can be observed that the farther apart the particles are, the lower the capillary force jumps/drops. These findings are consistent with the fact that when the separation distance increases the suction s decreases as already seen in Figure (4.16). Nevertheless, the *hysteresis* phenomenon is still observed even when increasing D, for the same reasons explained previously.

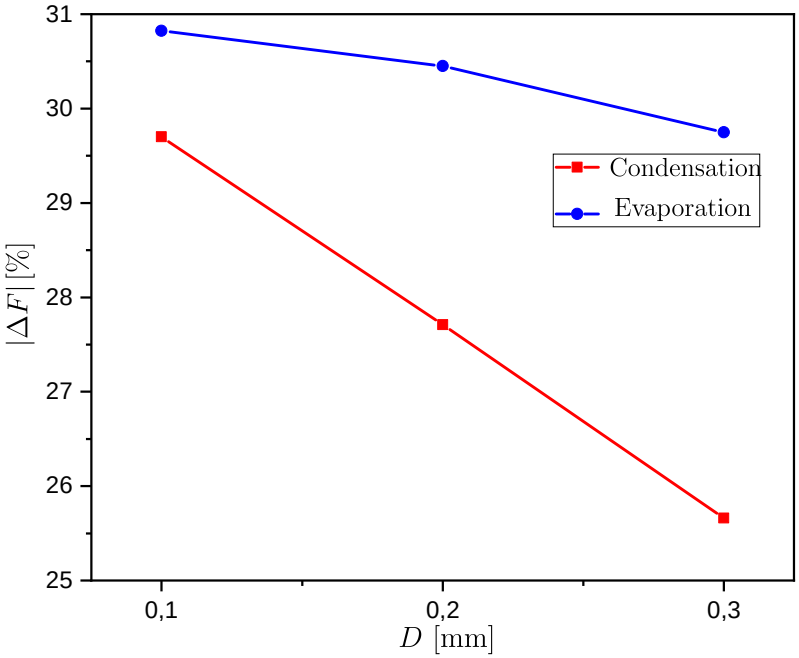

Figure 6.9: The evolution of the relative difference in capillary forces $|\Delta F|$ [%] in terms of separation distance D for both condensation and evaporation processes for $\theta = 50°$.

The effect of the wetting angle θ is next investigated. Multiple simulations are carried out with $\theta \in [10; 70]°$ and for $D \in \{0.1; 0.2; 0.3\}$ mm. Figures (6.10a) and (b) show the absolute difference $|\Delta F|$ [mN] at coalescence and rupture, respectively, for different separation distances D and wetting angles θ. These findings show that increasing the wetting angle decreases the absolute jump/drop of capillary forces either at coalescence or rupture. It is interesting to note that during evaporation for $D = 0.3$ mm and $\theta = 70°$, the merged capillary bridge splits up into two capillary bridges instead of three. Therefore, no discontinuity in capillary force, applied on the top particle, has been observed for this particular point. The reason behind this revolves around the fact that just before the rupture, the bottom triple line interface is above the line joining the centers of the bottom particles as shown in Figure(6.11). This may be due to one of these two reasons: (1) the configuration is theoretically symmetrical. However, the horizontal meshing is different than the oblique one, and (2) the configuration (shape of the merged capillary bridge) in Figure (6.11b) might not be stable[1] but (c) is stable while (z^*) did not reach 0 yet. Therefore, the merged capillary bridge is forced to become two stable capillary bridges. We note that another hysteresis effect has been reported for $\theta = 70°$ between evaporation and condensation processes.

[1]This a hypothetical assumption because there is no criterion indicating whether this configuration is stable or not.

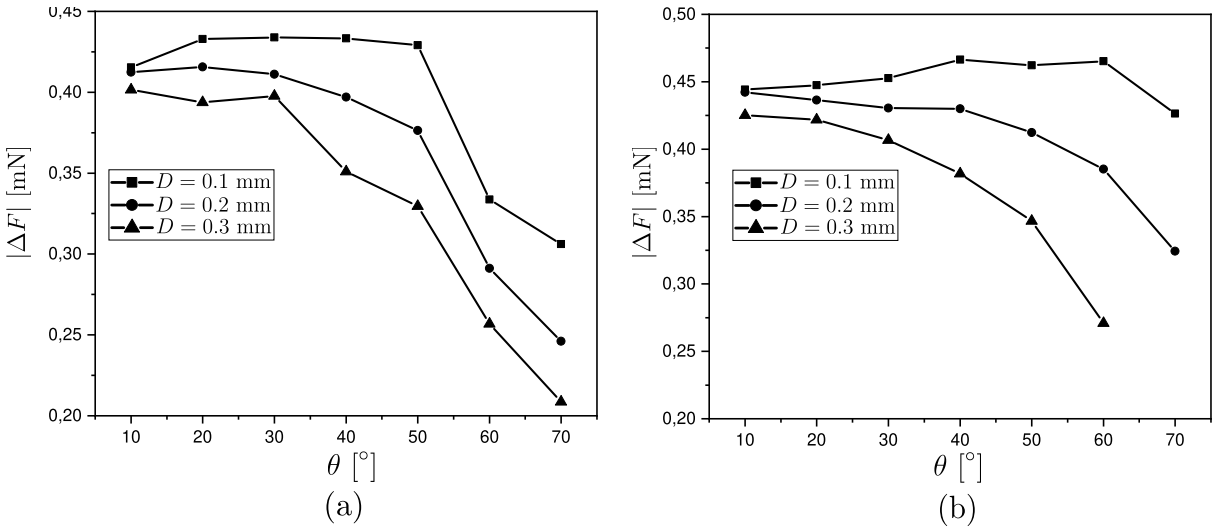

Figure 6.10: The evolution of the absolute difference in capillary forces $|\Delta F|$ [mN] in terms of the wetting angle θ for different separation distances $D \in \{0.1; 0.2; 0.3\}$ mm, during (a) condensation and (b) evaporation processes.

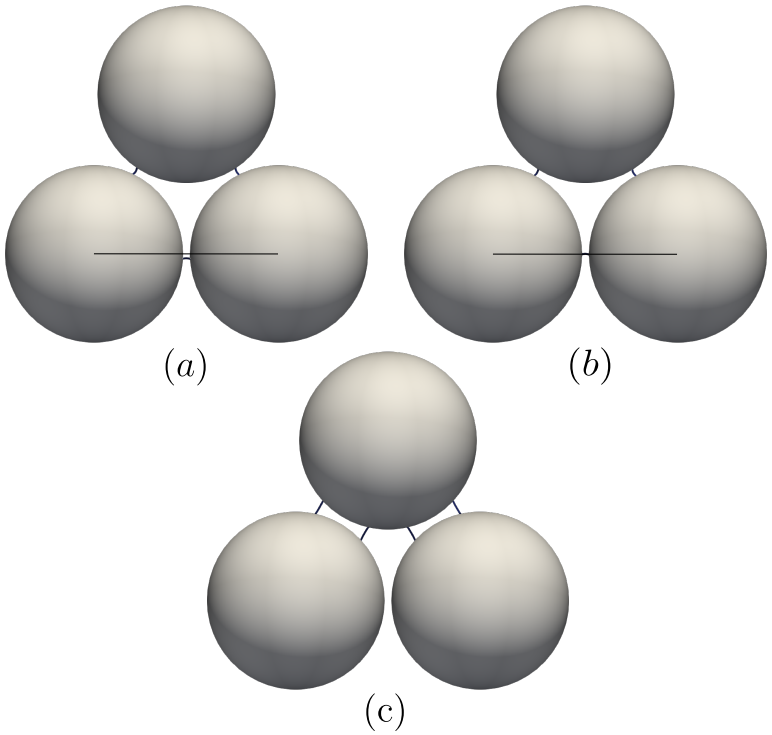

Figure 6.11: Profiles of capillary bridges. (a) Merged capillary bridge. (b) Merged capillary bridge just before the rupture. (c) After the rupture of the capillary bridge. In (b) the bottom air-water interface is at the same level as the horizontal line joining the particles' centers.

6.3.3 Quadruplet of particles - Regular tetrahedron

From the planar configuration of the previous subsections, we now move on to 3D structures of grains. The question is whether the sharp jump and drop in capillary forces remain $\approx 30\%$ even for 4 particles (non-planar systems) for $\theta = 50°$? To answer this question, in this section, we examine a quadruplet of particles forming a regular tetrahedron with different separation distances, *e.g.*, $D \in \{0.1; 0.2; 0.3\}$ mm, along with $\theta = 50°$.

Figure (6.12) illustrates the initialization phase of the capillary bridges created at the mid-distance between particles. Capillary forces are hereafter calculated on the top particle along the z-direction as shown in Figure (6.12).

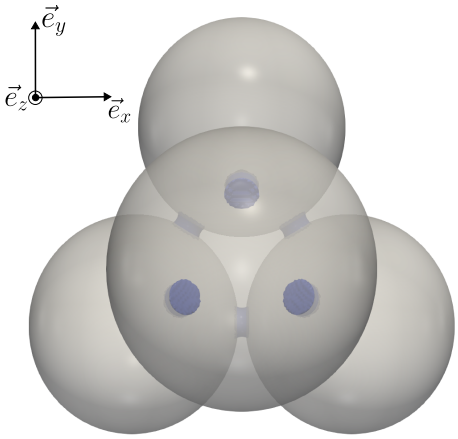

Figure 6.12: Initialization of capillary bridges at the mid-distance of spherical particles for a quadruplet of particles.

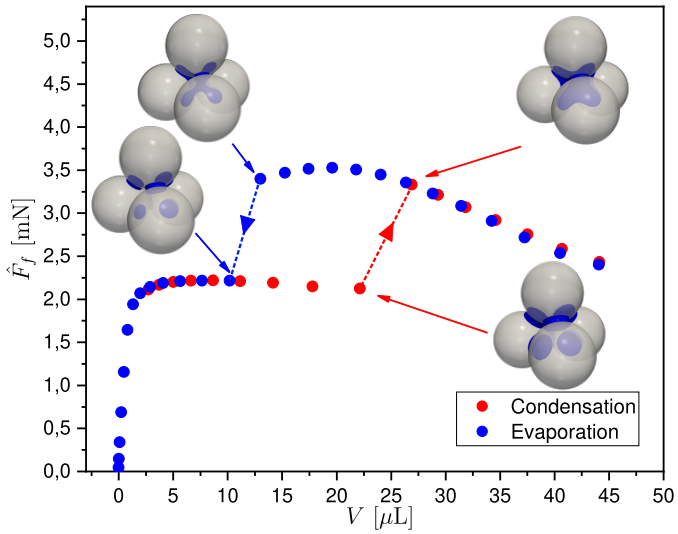

Figure 6.13: Capillary force evolution in terms of water volumes for condensation and evaporation processes for a wetting angle of $\theta = 50°$ and for a separation distance of $D = 0.1$ mm. The capillary force is computed on the top grain in the z-direction

The first considered configuration is similar to Section 6.3.1. The first configuration to be considered is the same as before, i.e., $D = 0.1$ mm and $\theta = 50°$. In the same way as before, the condensation and evaporation processes are imposed successively. Figure (6.13) depicts the capillary force $\hat{F}_f$ evolution in terms of water volumes. It can be observed that the capillary force, in this case, follows roughly the same tendency as the case of a triplet shown earlier in Figure (6.3). Although they have roughly the same tendency, here, capillary force is larger than the triplet case. This is due to the fact that in the four-particle case, 3 capillary bridges are connected to the top spherical particle, with 1 capillary bridge more than the top grain of the three-particle case.
The jump and drop in capillary forces are found to be 58% and 52% for condensation and evaporation, respectively (compared with 30% in Section 6.3.1). The reason why the

jump and drop of capillary forces are considerably higher than in the triplet case is that, in this case, three capillary bridges are attached to the bottom grain instead of one as was the case of the triplet. This forms a larger volume of water that contributes to the capillary force applied on the top grain after coalescence. Once again, as expected, the *hysteresis* phenomenon is observed—coalescence and rupture do not occur for the same volume.

Figure (6.14) depicts the evolution of the relative difference in capillary forces as a function of separation distances during condensation and evaporation processes. These findings are in line with the triplet case in which the relative difference in capillary forces $|\Delta F|$ [%] decreases when the separation distance increases. However, contrary to the triplet case, $|\Delta F|$ [%] is larger than 30% ($\geq$ 40%) for all three separation distances $D \in \{0.1; 0.2; 0.3\}$. This is probably due to two effects: (1) more "dead water" not contributing to the capillary force on the top grain before coalescence, *i.e.*, the horizontal capillary bridges in the triplet case, (2) rupture later because of "3D" effects (the planar bridge gets thinner quicker).

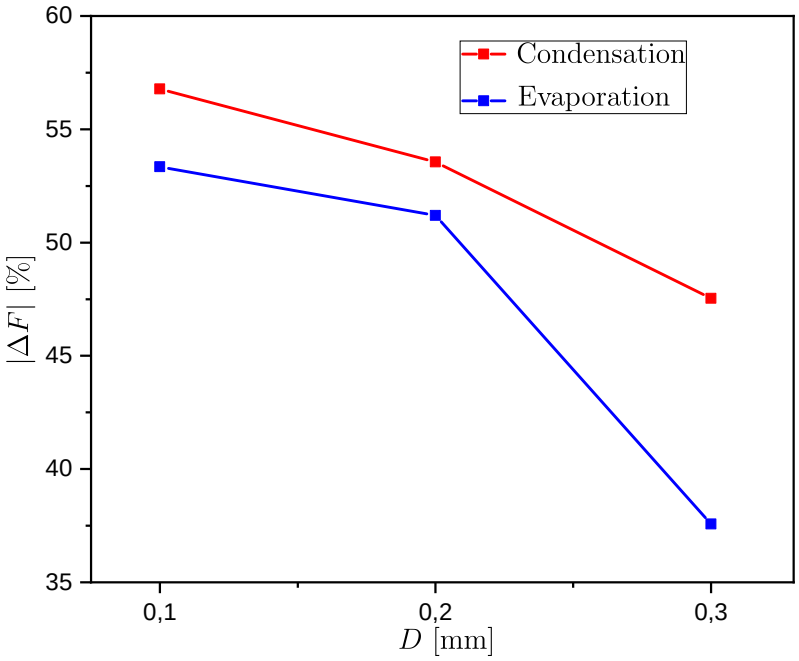

Figure 6.14: Relative difference in capillary forces $|\Delta F|$ [%] in terms of separation distances D [mm] for both coalescence and rupture for a wetting angle of $\theta = 50°$ for the quadruplet case.

6.4 Hysteresis effects at REV scale

Previously, we have examined how the *hysteresis* phenomenon affects the capillary force jumps and drops within small granular assemblies during condensation and evaporation, respectively. In order to come back to the material point scale, we propose to consider much larger systems of grains.

Two cases are considered. The first one, in which 1,000 particles are kept fixed, allows us to separate the hysteresis effect arising from capillary bridge topology from the particle rearrangement. The second one, in which the Particle Size Distribution (PSD) is the same as Chapter 5 with 3,750 particles, is used, but here with a confining pressure of $\sigma^{\text{conf}} = 2$ kPa.

6.4.1 Fixed microstructure: impact of the void space topology

For this example, the PSD is shown in Figure (6.15). Granular assembly characteristics are summarized in Table 6.1.

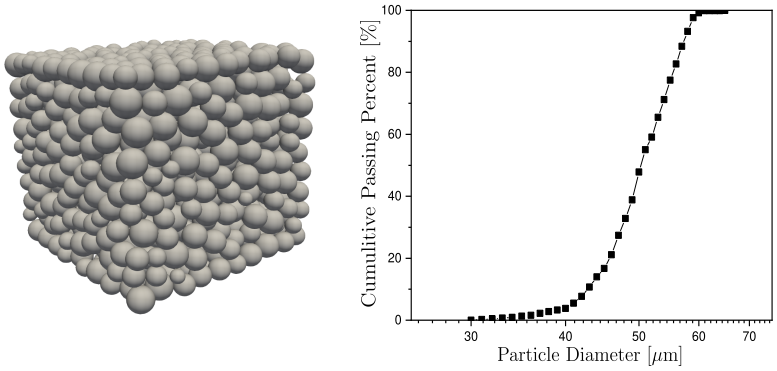

Figure 6.15: (a) An illustration of the granular assembly composed of 1,000 spherical grains. (b) The Particle Size Distribution (PSD) of (a). The largest and the smallest grain diameters are 64.48 µm and 30.45 µm, respectively.

Table 6.1: Granular system statistical characteristics: N_{grains} is the number of grains, D_{max}/D_{min} is the packing polydispersity, D_{50} is the grain diameter at which 50% of cumulative percent is reached, $C_u = D_{60}/D_{10}$ is the uniformity coefficient, and ϕ^p is the granular media porosity.

N_{grains} [-]	D_{max}/D_{min} [-]	D_{50} [µm]	C_u [-]	ϕ^p [-]
1,000	2.11	50.35	1.22	0.4624

The first step consists of initializing equal-sized isolated capillary bridges at the mid-distance of each pair of grains. Only those that are separated by 1.5 µm or 1 voxel in the LBM discretization, capillary bridges are initialized as shown in Figure 6.16. Consequently, 1,458 isolated capillary bridges are created for this case resulting in an initial degree of saturation of $S_r = 4.14\%$ which is defined as the ratio of the water volume to the void volume. From this point, the condensation process begins, leading to the growth of capillary bridges that enable the water to transit from the *pendular* regime to the *funicular*, and eventually to the *capillary* regime.

Figure (6.18) shows the suction evolution during condensation and evaporation processes in terms of degrees of saturation S_r. A sharp decrease is observed from $S_r \in [4; 17]\%$. Afterward, a change of slope is then observed until $S_r \approx 60\%$. Finally, the suction tends to zero as the system enters the capillary regime. The SWCC found in this example is quite similar to the one obtained in Figure (5.9). It must be noted that the values of suctions between this example and one done in Chapter 5 are not the same since the PSD is different.

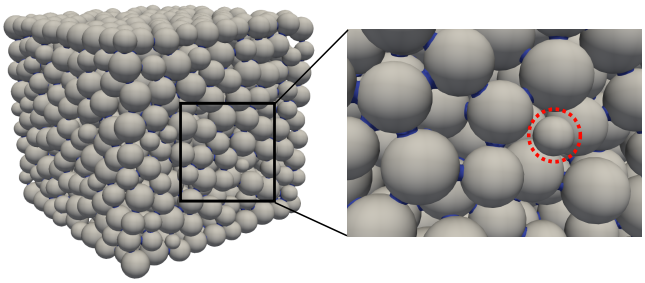

(a) (b)

Figure 6.16: (a) Initialization of the capillary bridges at the mid-distance of spherical grains. (b) A zoomed snapshot of (a). It is important to note that due to the large distance between its neighboring spheres, there is no capillary bridge initialized around the red-dotted-circle particle in (b).

The evaporation process begins once the granular system is saturated—blue curve of Figure 6.18. Approximately the same trend is observed between both curves, but the evaporation curve is shifted upward with respect to the condensation one in both capillary and funicular regimes. In other words, the *hysteresis* phenomenon is also observed within the suction ΔP of the large granular assembly. A thorough analysis of the air bubbles' topology can be carried out using the Flood-Fill algorithm to reveal the physics behind the difference in suctions. Figure 6.17 represents screenshots of the air bubbles distribution within the sample for $S_r \approx 40\%$. It is very important to note that in Figure 6.17 the large air cluster has been omitted for better visualization, and only the trapped air bubbles are displayed. It can be easily seen that in situation (a) air bubbles trapped between capillary bridges (encircled in red) are fewer than in situation (b) which results in a larger curvature for (b) than for (a). This observation is consistent with the Young-Laplace equation stating that the higher the curvature, the higher the suction s.

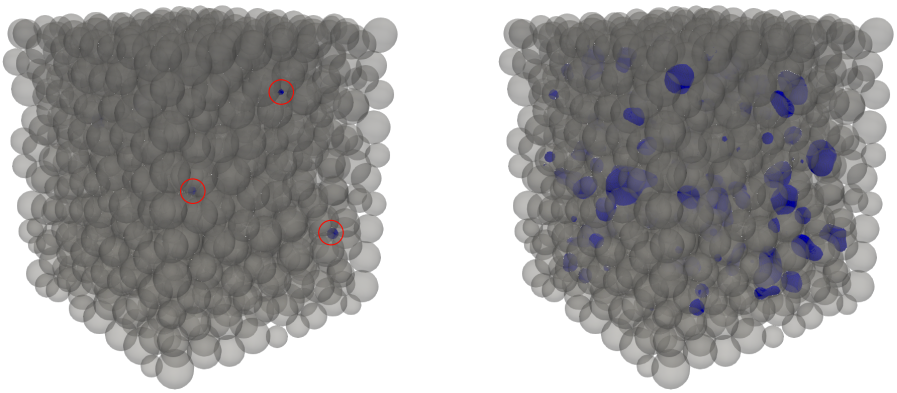

(a) (b)

Figure 6.17: Air bubbles trapped within the granular system are colored in blue with $S_r \approx 40\%$ during (a) condensation and (b) evaporation.

When the first evaporation process is completed, the granular system is condensed and evaporated again, the green and black curves of Figure (6.19), respectively. It is remarkable that the red and green curves do not match, even though they both represent the condensation phase. This is due to the fact that the initial distribution of capillary bridges is not the same, as shown in Figure (6.17). On the contrary, the evaporation curves (blue and black curves) are quite similar because they were in the same condition (capillary

regime) when the evaporation process began—only one geometrical configuration for full saturation $S_r = 1$.

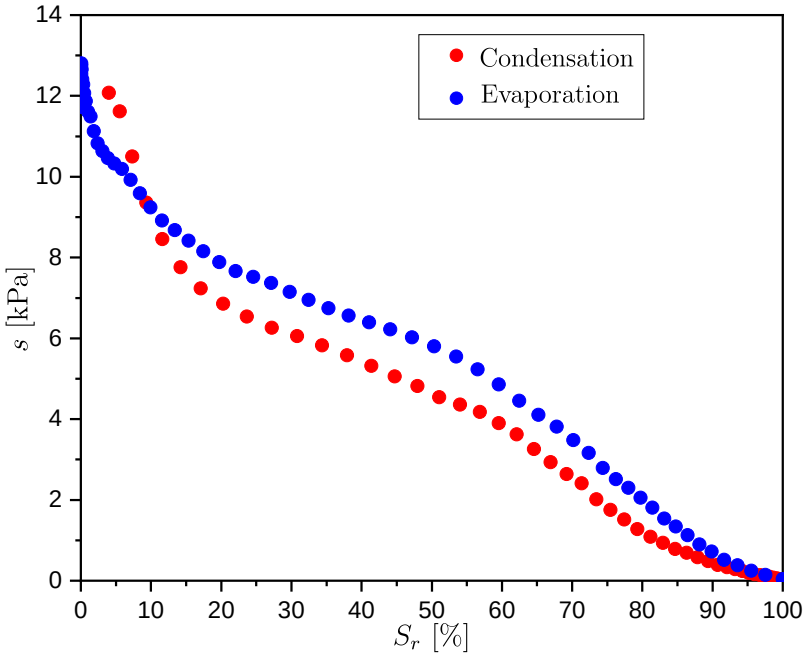

Figure 6.18: Evolution of ΔP in terms of degrees of saturation for condensation and evaporation processes

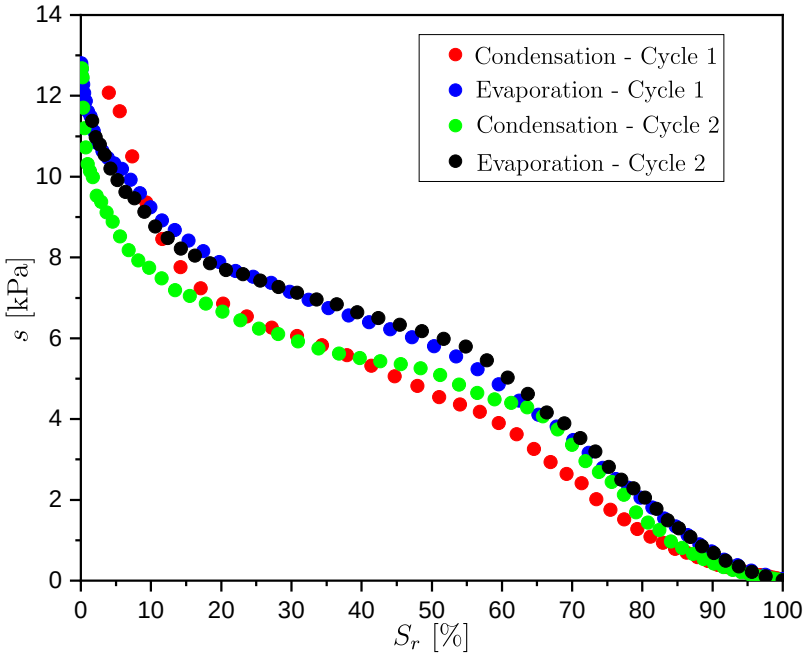

Figure 6.19: Evolution of ΔP in terms of degrees of saturation for condensation and evaporation processes for multiple cycles

6.4.2 Fully coupled problem: adding grain rearrangement effects for a constant wetting angle

In this section, the DEM-LBM approach together with the evaporation condensation techniques introduced earlier are applied to investigate the behavior of granular assemblies under unsaturated conditions. Contrary to the previous case where particles are fixed, here, they move under the action of capillary forces. Consequently, in addition to capillary bridge and air bubble topology hysteresis effects, the rearrangement of grains is taken into account as well. As mentioned earlier, the sample used in Chapter 5 is used here again, but this time with a confining pressure of $\sigma^{\text{conf}} = 2$ kPa.

As seen earlier in Section 6.4.1, the hysteresis of the suction s within unsaturated granular assemblies when subjected to evaporation or condensation depends on the initial configuration of capillary bridges. Therefore, to bypass this dependency on an arbitrary non-physical initial configuration, the initial state of this problem is set in the capillary regime[2] $S_r \approx 95\%$ and the sample is first subjected to evaporation followed by a condensation process. Figure (6.20) depicts the evolution of the suction s in terms of degrees of saturation for a wetting angle $\theta = 25°$ for both cycles. From Figure (6.20), the hysteresis caused by evaporation and condensation processes is well captured. Just as before, although the contact angle is the same for both cycles, the suction is different due to the difference between the capillary bridge and air bubble topology.

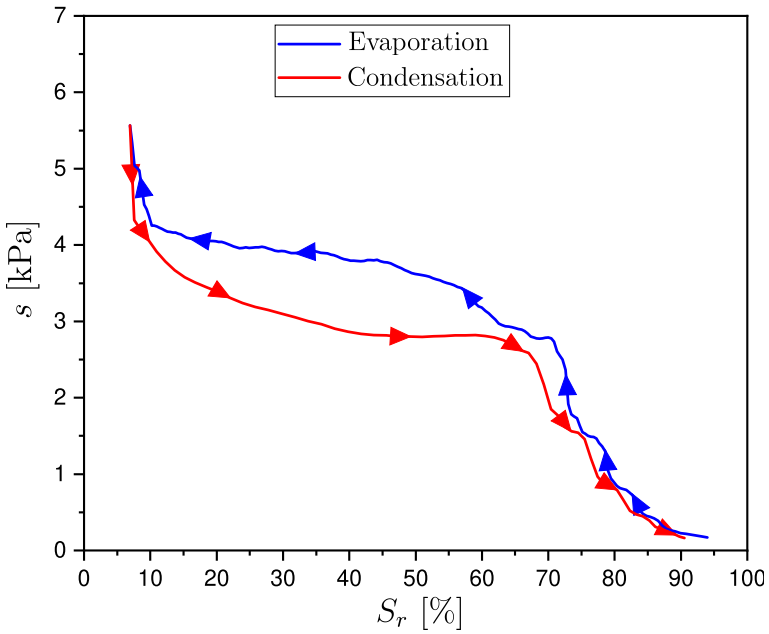

Figure 6.20: The evolution of suction s [kPa] in terms of degrees of saturation S_r during evaporation and condensation processes for a wetting angle of $\theta = 25°$.

Similarly to Chapter 5, capillary stress can be computed indirectly using both Love-Weber and total stress formulae, as depicted in Figure (6.21). While the sample is subjected to evaporation, the mean capillary stress increases up to a threshold $S_r \approx 68\%$ below which it decreases. Also, when the condensation is applied from $S_r \approx 7\%$, the

[2]The choice of $S_r \approx 95\%$, instead of $S_r \approx 100\%$ is taken to ensure that there are some air bubbles present within the sample so that the evaporation does not only occur on the boundaries of the sample but rather to be roughly evenly propagated from the inside.

mean capillary stress increases until it reaches its peak value at $S_r \approx 50\%$ and then decreases toward zero as the system is getting close to full saturation. The peak values of the mean capillary stress p^{cap} are different; with $p^{\text{cap}} = 3.05$ kPa during the evaporation step and $p^{\text{cap}} = 2.37$ kPa during the condensation step. This difference arises from the suction difference between evaporation and condensation processes as seen earlier in Figure (6.20). Moreover, an intriguing result can be also observed in the rate at which the mean capillary stress increases or decreases. Although the maximum value of p^{cap} is indeed reached earlier during condensation, its decrease is smoother than that observed during evaporation. This phenomenon could be attributed to the topological differences in capillary bridges and air bubbles within the sample, which will be explored further herein.
To understand the physics behind this result, the number of capillary bridges and air bubbles are investigated and depicted in Figure (6.22). It can be seen from (a) that the starting point for the evaporation process is in the *capillary* regime with only one large water cluster. As the evaporation continues, a unique capillary bridge is found until it reaches $S_r \approx 68\%$. Then, the number of capillary bridges starts to increase. At this exact stage, the mean capillary stress reaches its maximum value and decreases afterward.

During the evaporation step, the number of air bubbles reaches its maximum value at $S_r \approx 68\%$, which corresponds to the stage when p^{cap} is at its peak. A large number of air bubbles leads to increased curvature, resulting in higher capillary forces. Consequently, the mean capillary stress reaches its highest values. Another interesting result is that the number of air bubbles follows the evolution of the mean capillary stress.

As for the condensation process, the number of capillary bridges increases slightly at low degrees of saturation before decreasing towards 1 at full saturation. The mean capillary stress p^{cap} reaches its maximum value at $S_r \approx 51\%$, but for this degree of saturation, the number of capillary bridges is 138 capillary bridges and not one as is the case of the evaporation process at the maximum value. However, the majority of the water volume, approximately 98%, is contained within a single large cluster capillary bridge. In other words, this suggests that the system can be approximated as having just one dominant cluster capillary bridge. The other capillary bridges may contribute to smoothing the decrease of the mean capillary at larger degrees of saturation. As for the number of air bubbles, it increases slightly as the system is being wetted, but it remains much lower than during the evaporation process. When the saturation level reaches $S_r \approx 80\%$, air bubbles start to completely disappear and the mean capillary stress drops at the same rate as the mean capillary stress for the evaporation process. The larger number of air bubbles may explain why the mean capillary pressure for evaporation is larger than the one for the condensation process.

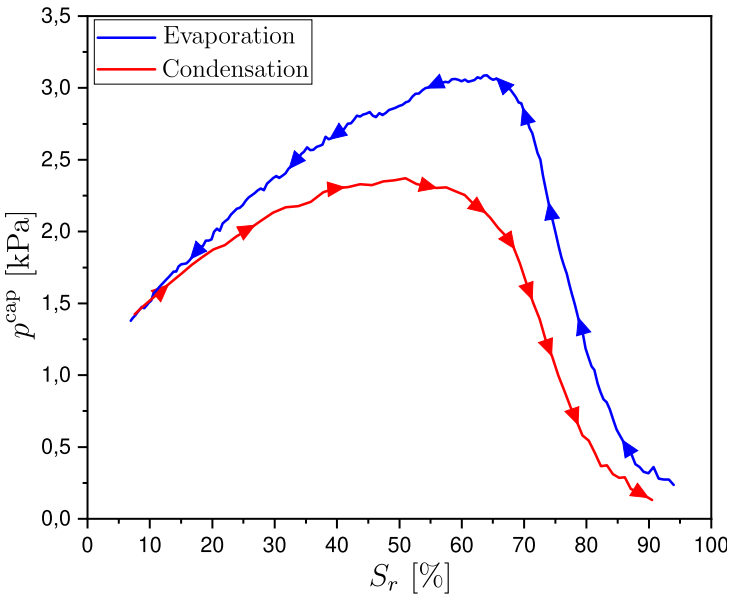

Figure 6.21: The evolution of mean capillary stress p^{cap} [kPa] in terms of degrees of saturation S_r during evaporation and condensation processes for a wetting angle of $\theta = 25°$.

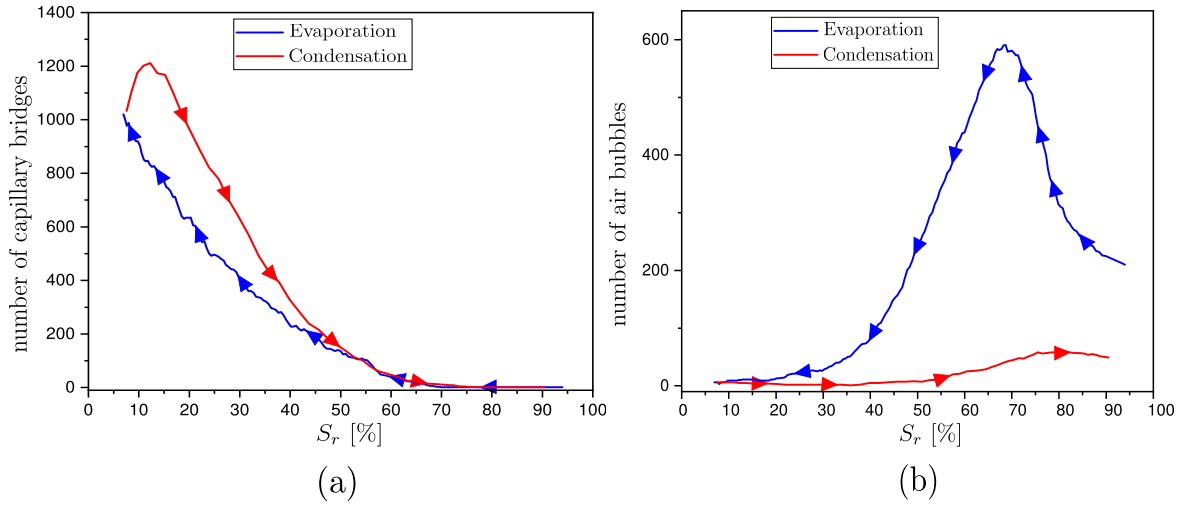

Figure 6.22: The evolution of the number of (a) capillary bridges and (b) air bubbles in terms of degrees of saturation S_r during evaporation and condensation processes for a wetting angle of $\theta = 25°$.

To assess microstructural changes resulting from the evaporation as well as the condensation processes, we can track the change in the porosity of the sample, as shown in Figure (6.23). Based on this figure, the sample displays a contraction behavior throughout the evaporation and condensation cycles. It may be due to the fact that the sample being investigated is loose which is reminescent of the contraction behavior of a loose sample in triaxial tests.

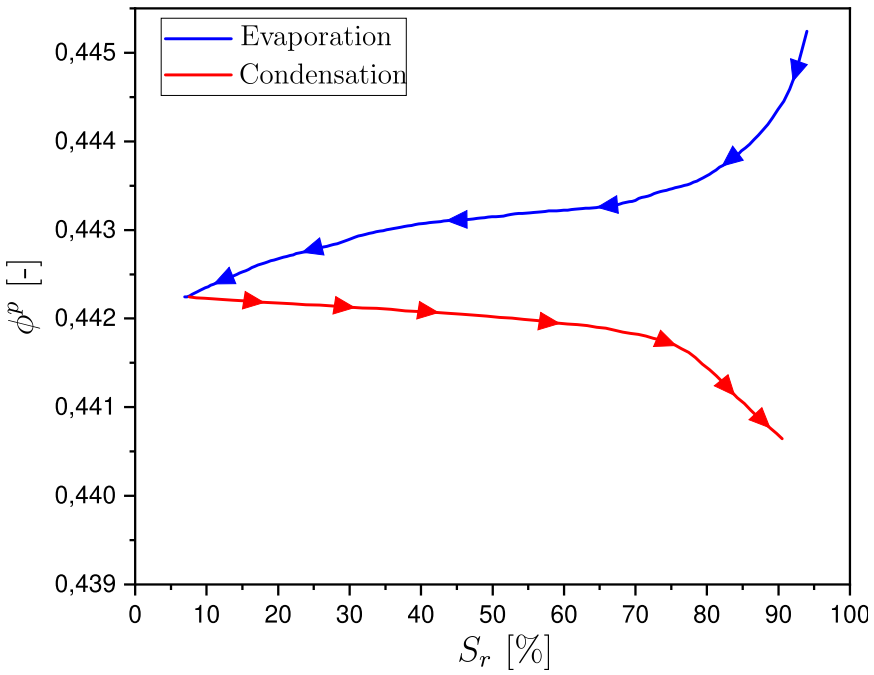

Figure 6.23: The evolution of porosity ϕ^p [-] in terms of degrees of saturation S_r during evaporation and condensation processes for a wetting angle of $\theta = 25°$.

6.4.3 Fully coupled problem: adding grain rearrangement effects for different wetting angles

So far, it has been demonstrated that even when the wetting angle is the same, $\theta = 25°$, unsaturated soils exhibit hysteresis during both condensation and evaporation processes due to the change in the topology of capillary bridges and air bubbles (microstructure rearrangement remains limited in the present case). Another hysteresis phenomenon has been highlighted in Chapter 1, Section 1.2.2.4 called wetting angle hysteresis. Indeed, the wetting angle experiences variation between evaporation and condensation. This difference arises from the behavior of water: during evaporation, water evaporates from wet surfaces, whereas during condensation, it condenses on dry surfaces. This phenomenon results in $\theta_e < \theta_c$. Consequently, a wetting angle hysteresis is examined hereafter.

For the evaporation process, the wetting angle remains the same as before. i.e., $\theta_e = 25°$. Conversely, for the condensation process, larger wetting angles are considered: $\theta_c \in \{25, 40, 50, 60\}°$. Figure (6.24) illustrates the evolution of suctions in terms of saturation levels during both evaporation and condensation processes. This figure highlights that larger values of wetting angles cause the suction to reduce due to the decrease in the curvature, to the point that suctions can even become negative for high contact angles, e.g., $\theta \in \{50; 60\}$. A negative suction reminds us of the undoloid shapes where the water pressure is positive and the mean curvature H is negative as shown in Figures (4.16) and (4.15). It must be noted that while this analogy serves to understand the main idea of the concept, it is not entirely accurate. The so-called undoloid and nodoid shapes are exclusively defined within the *pendular* regime, see Appendix D, Section D.3 for more details.

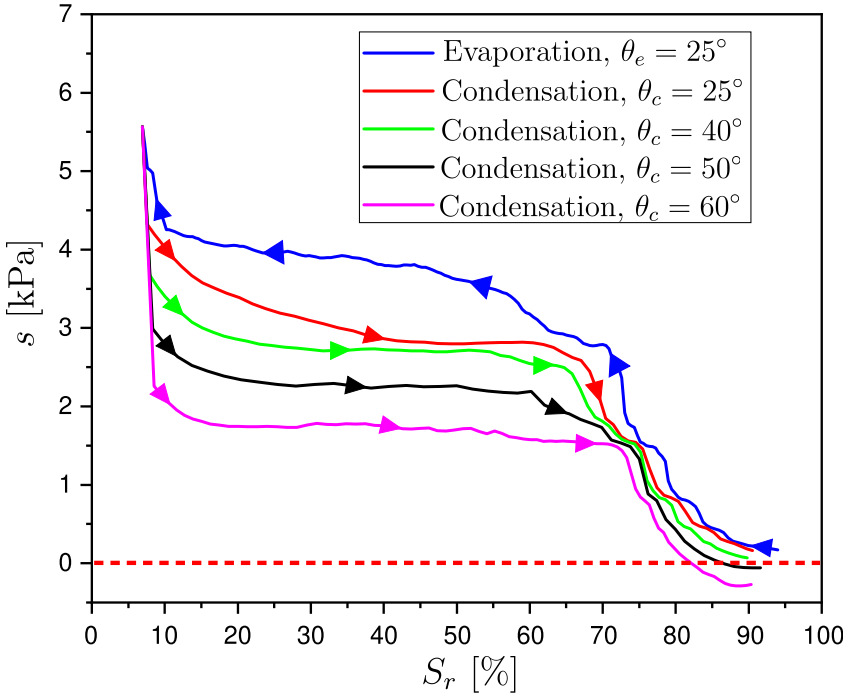

Figure 6.24: The evolution of suction s [kPa] in terms of degrees of saturation S_r during evaporation and condensation processes for wetting angles of $\theta_e = 25°$ and $\theta_c \in \{25; 40; 50; 60\}°$. For a clear visualization, arrows indicating the path directions—evaporation or condensation—are added.

Furthermore, the mean capillary stress p^{cap} has been plotted in terms of degrees of saturation during evaporation and condensation processes for wetting angles of $\theta_e = 25°$ and $\theta_c \in \{25; 40; 50; 60\}°$ in Figure (6.25). Likewise, the mean capillary stress for higher wetting angles is lower than the one for $\theta_c = \theta_e = 25°$.

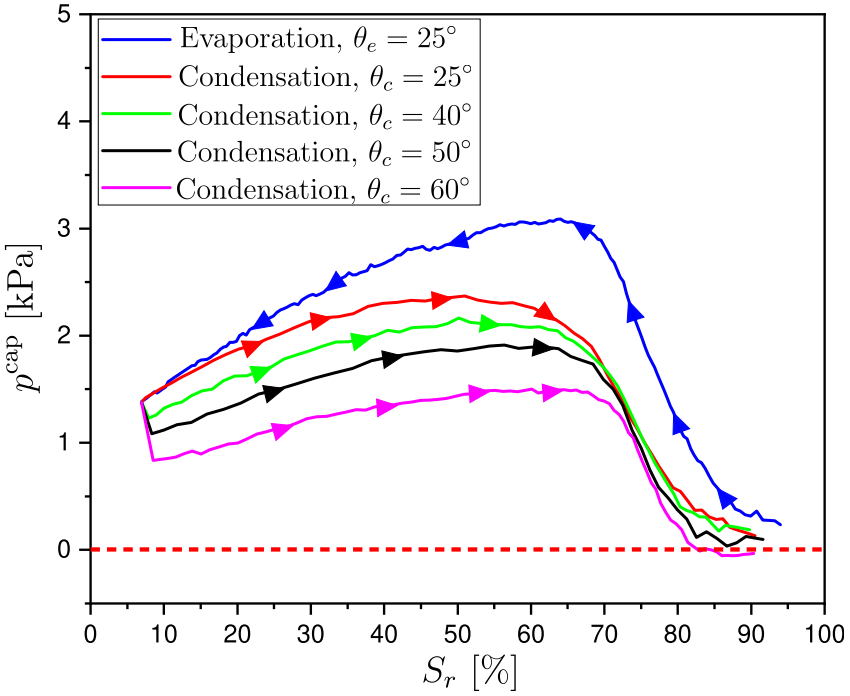

Figure 6.25: The evolution of the mean capillary stress p^{cap} [kPa] in terms of degrees of saturation S_r during evaporation and condensation processes for wetting angles of $\theta_e = 25°$ and $\theta_c \in \{25; 40; 50; 60\}°$. For a clear visualization, arrows indicating the path directions—evaporation or condensation—are added.

As before, the porosity variation is plotted in Figure (6.26) in terms of the saturation degree. Unsurprisingly, the same contraction behavior is observed for the same reason as before: the initial sample is prepared in a loose state.

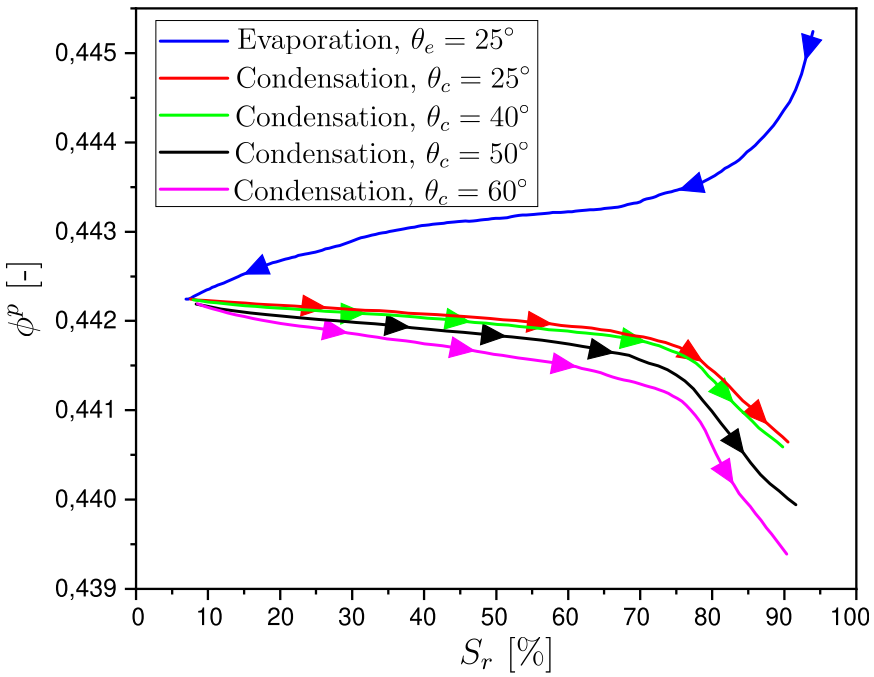

Figure 6.26: The evolution of porosity ϕ^p [-] in terms of degrees of saturation S_r during evaporation and condensation processes for wetting angles of $\theta_e = 25°$ and $\theta_c \in \{25; 40; 50; 60\}°$. For a clear visualization, arrows indicating the path directions—evaporation or condensation—are added.

As mentioned earlier in Chapter 1, Duriez and Wan (2016, 2017, 2018) have derived a theoretical form of the capillary stress, see Eq. (1.48). They only could verify its validity in the *pendular* regime. Using DEM-LBM, however, all the regimes can be investigated, especially funicular and capillary regimes. Figure (6.27) depicts the comparison between the theoretical and numerical mean capillary stress, based on Eq. (1.48) and Eq. (5.12), respectively, in terms of degrees of saturation. A rather good agreement can be observed between the theoretical and DEM-LBM numerical capillary stress.
The theoretical capillary stress possesses 4 terms: the first two are the suction terms and the other half are the surface tension terms. It must be emphasized that the suction terms represent approximately between 80 to 90% of the capillary stress.

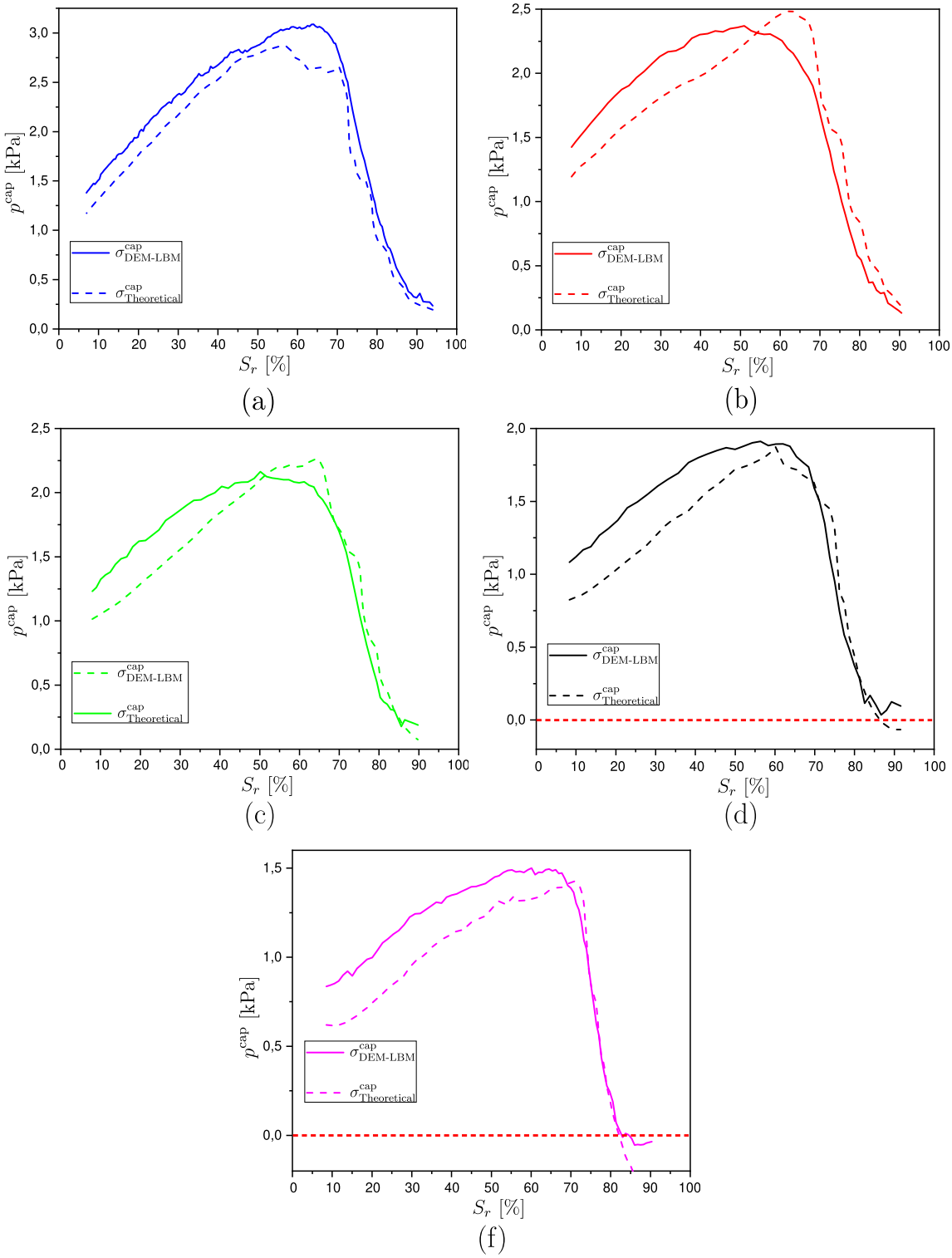

Figure 6.27: The evolution of both theoretical Eq. (1.48) and numerical Eq. (5.12) mean capillary stress p^{cap} [kPa] in terms of degrees of saturation S_r during evaporation and condensation processes for wetting angles of $\theta_e = 25°$ and $\theta_c \in \{25; 40; 50; 60\}°$.

6.5 Conclusion

In this chapter, a new mathematical transformation for simulating condensation and evaporation processes is proposed with the purpose of investigating the hysteresis phe-

nomenon within partially saturated granular assemblies in terms of capillary forces, suction, and mean capillary stress. Multiple crucial conclusions are drawn as follows:

- We have recovered the compelling theoretical and experimental result of the sudden jump of 30% in capillary forces when isolated capillary bridges coalesce during condensation for equilateral triplets of particles for $\theta = 50°$.
- When the same granular assembly is subjected to evaporation, we observe that the steep fall in capillary forces does not occur at the same volume for which the coalescence took place. These jumps in capillary forces upon *coalescence* and *rupture* are known as the *Haines* jumps.
- Regarding the regular quadruplets of particles, we have found that the steep jump and fall range between 35 and 55%. This range depends on the separation distances and whether the system is experiencing a condensation or evaporation process. The same trend as the triplet case has been reported meaning that the relative difference in capillary forces decreases when the separation distance increases.
- The new approach has been extended to a large granular assembly composed of 1000 fixed spherical particles to investigate the hysteresis phenomenon regarding matric suction. The proposed model has proved that the hysteresis phenomenon is reported even with the same wetting angle due to topology variation of the trapped air bubbles between the condensation and evaporation processes.
- The new evaporation and condensation technique has been added to the DEM-LBM coupling accounting for the rearrangement of grains. Despite imposing the same angle during both condensation and evaporation, it has been demonstrated that the suction and mean capillary stress exhibit path-dependent behavior. For both variables, they were higher during evaporation compared to condensation.
- Moreover, the wetting angle for evaporation, denoted as θ_e, has been intentionally set to be different from the wetting angles for condensation, represented as θ_c, with the aim of generating wetting angle hysteresis, where $\theta_c > \theta_e$.
- The same trend has been observed as previously, but this time, it was noted that capillary stresses and suctions decrease as the wetting angle is increased.
- Finally, we have also calculated the capillary stress based on a theoretical formulation and compared it with the one deduced from DEM-LBM for all regimes. Rather good results were reported.

In conclusion, the DEM-LBM model, combined with the novel evaporation and condensation technique, is well-suited for practical applications, including scenarios like dikes exposed to cyclic hydraulic loadings.

Chapter 7

General conclusions and perspectives

The *StabDigue* project is concerned with the stability of maritime dikes under fluctuating hydraulic loads arising from the action of waves and tides, including seasonal precipitation. Potential changes induced by these loading conditions may have far reaching impact on the underlying microstructure of the soil so as to ultimately lead to instabilities, degradations and failure (Wan et al., 2017). In this regard, this Ph.D. work has highlighted the micromechanical behavior of unsaturated soils subjected to wetting and drying cycles with a particular focus on hysteretic behaviors during the cyclic wetting and drying actions in granular materials and their impact on mechanical strength in all possible regimes, e.g., *pendular*, *funicular*, and *capillary* regimes. This will ultimately allow us to evaluate the resilience of civil engineering infrastructure such as dikes under operative and fluctuating climatic scenarios.

To achieve this, one of the main deliverables of this Ph.D. is a numerical code coupling the Discrete Element Method (DEM) and the Lattice Boltzmann Method (LBM). Extensive work has been devoted to the optimization of computational procedures during the coupling of the two methods. Undoubtedly, the developed numerical tool will help improve further the general understanding of the physics of partially saturated materials in the future.

7.1 Main contributions

After three years of dedicated work, this thesis has finally come to fruition, producing important results in partially saturated granular assemblies at both small and large assemblies. These are summarized in the following.

7.1.1 Small granular assemblies: capillary bridge shapes

7.1.1.1 Geometrical aspects of capillary bridges in the pendular regime

The first step is to investigate capillary bridge shapes within a small granular assembly composed of two particles known as a doublet. It has been proven that using the developed phase field LBM model, capillary bridges converge to the solution of the Young-Laplace equation, which is the theoretical description of an axisymmetric capillary bridge between two spherical particles. The developed numerical model has proven its capabilities to capture the change of sign of the mean curvature H, transitioning from a portion of nodoid to a portion of undoloid shape, when increasing the separation distance between these spherical particles (Younes et al., 2023a).

7.1.1.2 Capillary forces of doublets and triplets of spherical particles

The capillary force acting on spherical particles is well-understood in the pendular regime as extensively discussed and investigated in previous works (Gagneux and Millet, 2014; Miot et al., 2021; Pitois et al., 2000). However, the determination of capillary force for three or more particles has remained a longstanding challenge within the context of the funicular regime. One of the most remarkable advantages of the proposed phase-field LBM model lies in its inherent capability to capture the merging of multiple capillary bridges. A novel formulation has been proposed in this work for the accurate calculation

of capillary forces exerted on spherical particles over all the possible regimes (Younes et al., 2022). This groundbreaking result paves the way for the possibility of simulating large partially saturated granular assemblies across a wide range of saturation levels.

7.1.2 Large unsaturated granular assemblies: DEM-LBM coupling

While large granular assemblies have been widely investigated in the past, most of the studies were restricted to the *pendular* regime (Scholtès, 2008; Scholtès et al., 2009; Scholtes et al., 2009; Duriez and Wan, 2016, 2017; Duriez et al., 2017). However, in practice, the funicular regime is probably more dominant than the pendular regime. Therefore, a special algorithm for coupling the DEM with the LBM has been devised to investigate several aspects of partially saturated granular assemblies (Younes et al., 2023d). The key point of the coupling between the two methods lies in the judicious integration of capillary forces computed via LBM into the DEM calculation cycles. Listed below are the main results found this study:

- A qualitative investigation has been conducted to simulate the capillary effect in wet sand whereby a cubical sample can stand up when wet, whereas it would readily collapse when dry.
- The variation of the suction in terms of the degree of water saturation or volumetric water content has been recovered and compared to the well-known van Genuchten equation.
- The mean capillary capillary stress for the entire range of saturation levels and how it evolves depending on the regime at hand has been elucidated. It has been shown that the mean capillary stress p^{cap} increases with the degree of saturation S_r up to a certain threshold beyond which capillary stress drops until complete saturation.
- The Bishop's assumption that $\chi = S_r$ has been disproved through a rigorous analysis using the DEM-LBM model.

7.1.3 Hysteretic aspect of unsaturated granular assemblies

Here, a novel method has been formulated to simulate the condensation and evaporation of capillary bridges within partially saturated granular assemblies. This study is broken down into two cases: small and large granular assemblies which are presented hereafter.

7.1.3.1 Fixed particles

Small granular assemblies: doublets and triplets

The first result of this study is the merging of three isolated capillary bridges within monodispersed triplets of particles whose centers form an equilateral triangle. As capillary bridges are being subjected to a condensation process, their *coalescence* takes place and the capillary force increases suddenly about 30% for a wetting angle of $\theta = 50°$ (Gagneux and Millet, 2016). However, when a large capillary bridge between three particles ruptures and becomes three samller isolated capillary bridges, the capillary force drops roughly about 30% for the same angle (Gras, 2011). These results were both reproduced using the proposed method of condensation and evaporation for the same wetting angle $\theta = 50°$. Furthermore, it has been proven that the coalescence and the rupture of capillary

bridges do not take place the same way for the same volume. Moreover, four particles forming a regular tetrahedron have also been investigated to show the same behavior as the triplet (Younes et al., 2023c).

Hysteresis effects at REV scale

The evaporation and condensation processes were next applied to a large fixed granular assembly to study hysteresis phenomena within the system. It has been shown that, although the wetting angle is the same for both processes, the granular assembly exhibits a hysteretic effect in terms of suctions due to different capillary bridge and air bubble topologies during evaporation and condensation. In addition, it has been found that the suction during evaporation is higher than the suction during condensation which is in accordance with the literature (Younes et al., 2023c).

7.1.3.2 Fully coupled problem

The newly developed evaporation and condensation technique is next incorporated into the DEM-LBM coupling to account for the rearrangement of particles while the system is being evaporated or condensed. Not only the suction has exhibited a hysteretic effect, but the mean capillary stress has been different even for the same wetting angle. It has been shown that the capillary stress during evaporation is larger than the one during condensation. The same result has been found for suction. Furthermore, the wetting angle of evaporation θ_e has been chosen to be different from the ones in condensation θ_c to force the wetting angle hysteresis with $\theta_c > \theta_e$. The same tendency has been found as before, only this time, the capillary stresses and suctions decrease when increasing the wetting angle. Finally, the theoretical capillary stress, which was previously validated solely in the pendular regime according to the literature, has been extended to all possible regimes. It was compared with the one derived from the DEM-LBM coupling, and the results indicated reasonably good agreement (Younes et al., 2023b).

7.2 Future research avenues: A strategic outlook

7.2.1 The existence of an effective stress

The existence of effective stress in unsaturated soils has been a longstanding problem for decades at both the numerical and experimental fronts. In experiments, determining the effective stress is quite challenging, which is why the results are consistently expressed in terms of total stress. However, the calculation of each stress partition is feasible in a numerical framework. Unfortunately, up to this day, the majority of studies have been performed in the pendular regime, where the existence of effective stress has been confirmed (Duriez et al., 2018) at least at the plastic limit condition, i.e., at failure. However, the question remains unanswered in the funicular and capillary regimes. This is when the usefulness of the developed DEM-LBM model comes into play, facilitating the simulation of partially saturated granular assemblies across all possible regimes.

During my Ph.D., some triaxial tests have been conducted but not presented in this manuscript as they fall outside the scope of this work. Figure (7.1) depicts very recent triaxial test results under unsaturated conditions, illustrating different water contents at a confining pressure of $\sigma^{\text{conf}} = 10$ kPa. It can be observed that for $w \in \{7.24; 12.62; 21.33\}\%$, larger deviatoric stress than the dry case can be afforded, thus an increase in strength. In contrast, when the water content increases to $w = 27.32\%$,

the deviatoric stress instead drops and approaches the dry case level. These results are in accordance with our findings on the apparent cohesion due to capillarity seen in Chapters 5 and 6. Pursuing these investigations further within the context of the DEM-LBM coupling under different capillary, stress and strain loading conditions will certainly help toward unravelling the important question of whether an effective stress in unsaturated soils exists or not.

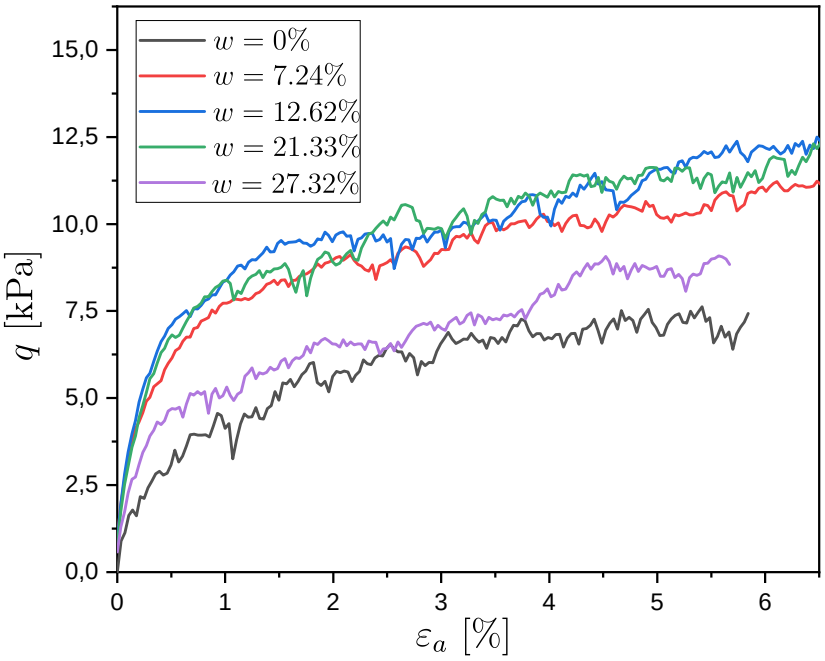

Figure 7.1: The evolution of the deviatoric stress q [kPa] in terms of the axial strain for different water contents $w \in \{0; 7.24; 12.62; 21.33; 27.32\}\%$ at a confining pressure of $\sigma^{\text{conf}} = 10$ kPa.

7.2.2 Instabilities at REV scale

In the framework of the *StabDigue* project, a primary focus lies in the quantitative investigation of the instability of unsaturated granular soils when subjected to wetting and drying cycles. Hence, this constitutive aspect can be investigated through the so-called second-order work criterion (Wan et al., 2017) which describes very well the signature of collapse failure in dry soils. Essentially, the work rate input to the soil cannot be sustained internally anymore under certain conditions with the surplus of energy being dissipated into an outburst of kinetic energy. The extension to wet granular materials can be pursued in the future by using the recently developed analytical expressions of the second-order work criterion in the wet condition (Eghbalian et al., 2023). These will be validated by conducting directional analyses, i.e. probings with controlled stress or strain combined with suction or degree of saturation. The issue of how to account for varying water content in the computation of the second-order work criterion (additional degree of freedom compared with dry or fully saturated materials) should be addressed as a first task.

7.2.3 Coupling with macroscale approaches

Simulating large dikes, which are composed of millions of particles, using the developed DEM-LBM model is practically unfeasible due to large computational time requirements. To overcome this problem, it is possible to integrate the DEM-LBM model with

macro-scale methods such as the Finite Element Method (FEM), Finite Difference Method (FDM), or Material Point Method (MPM). Currently, Raphaël Bouchard's ongoing Ph.D. thesis at La Rochelle University (also part of the *StabDigue* project) revolves around exploring the utilization of the DEM-LBM coupling as a surrogate to an actual constitutive model for simulating large-scale dikes.

To conclude, the DEM-LBM coupling has shown its capabilities in analyzing at the finest levels, the physics of unsaturated granular materials at the microscale, and more importantly the seamless transitions between water saturation regimes. This powerful numerical framework enables us to understand aspects that may otherwise remain unfeasible in laboratory experiments. Indeed, there are numerous untapped avenues for further exploration, offering the potential to uncover insights in the behavior of these complex materials. As we continue to push the boundaries of our understanding of unsaturated soils through the DEM-LBM coupling, we may ultimately propose solutions to current longstanding challenges and contribute to the development of geomechanics at large.

Appendix A

Résumé étendu en français

A.1 Contexte général

Depuis la révolution industrielle, la Terre subit des changements climatiques majeurs, se traduisant par une montée du niveau de la mer, ce qui engendre un risque crucial pour les communautés côtières. Afin d'éviter les catastrophes d'inondation, les êtres humains ont eu une idée de génie de construire ce que l'on appelle aujourd'hui : les digues.

Les digues en remblai sont généralement construites à partir de matériaux granulaires compactés et se trouvent souvent dans des conditions de saturation partielle, ce qui confère à leurs matériaux une certaine cohésion bénéfique pour leur résistance mécanique dite cohésion capillaire. Cependant, lorsque ces matériaux granulaires, situés à la surface de la digue, sont exposés à des cycles de séchage et de mouillage, typiquement provoqués par la variation de pression entre l'amont et l'aval de la digue, ils peuvent devenir vulnérables et risquent de s'effondrer. On peut ainsi considérer l'eau comme une arme à double tranchant : en quantité modérée dans le sol, elle favorise sa cohésion, mais en cas d'absence ou d'excès, la cohésion capillaire disparaît. Ces fluctuations sont généralement engendrées par plusieurs facteurs, tels que des précipitations intenses, des vagues de chaleur, les marées ou encore les tempêtes, des phénomènes malheureusement de plus en plus fréquents dans un contexte de changement climatique. Aujourd'hui, il est admis que les instabilités des digues au niveau macroscopique sont dues à des instabilités microscopiques (Wan et al., 2017). Avant d'étudier ces instabilités microscopiques, il est indispensable de comprendre, dans un premier temps, la physique et la mécanique des milieux partiellement saturés, ainsi que l'impact crucial des fluctuations de la teneur en eau sur la cohésion capillaire de ces sols.

La présente thèse s'inscrit dans le cadre du projet StabDigue, financé pour une durée de cinq ans par la région Nouvelle-Aquitaine, pour l'étude de la stabilité des digues en remblai partiellement saturées. Cette thèse de doctorat est motivée par plusieurs questions clés qui seront abordées :

- Peut-on modéliser et prédire les conséquences sur la stabilité mécanique des sols granulaires dues au changement la teneur en eau ?
- Comment les cycles de mouillage/séchage vont-ils affecter les propriétés hydromécaniques des sols granulaires ?
- Est-il possible d'interpréter ces changements hydromécaniques en terme de microstructure sous-jacente ?

A.2 Les lacunes dans la littérature, motivations de cette étude et objectifs

La problématique centrale réside dans le fait que la physique des sols partiellement saturés se situe à l'échelle des pores et des grains solides, ce qui requiert une étude microstructurale pour analyser les interactions entre les phases solide-liquide-gaz et leur impact sur le comportement global d'un sol partiellement saturé. La grande majorité des

études, qu'elles soient expérimentales, analytiques ou numériques, dans la littérature, se sont focalisées sur les configurations se trouvant dans le régime pendulaire (Scholtès, 2008; Scholtès et al., 2009; Scholtes et al., 2009; Duriez and Wan, 2016, 2017; Duriez et al., 2017; Duriez and Wan, 2018; Mielniczuk et al., 2018). Aujourd'hui, le régime pendulaire est bien compris par les géomécaniciens et les chercheurs. Cependant, ce régime ne représente qu'une petite portion des sols non-saturés. Ces derniers se trouvent généralement dans les régimes funiculaire et capillaire. Hélas, la plupart des études dans la littérature ont été consacrées uniquement au régime pendulaire. Lorsque le régime funiculaire est étudié pour les triplets, les chercheurs se sont contentés d'utiliser des critères géométriques, souvent analytiques, afin de modéliser la coalescence ou la rupture des ponts capillaires (Miot et al., 2021; El Korchi, 2017). Ces critères géométriques, aussi pratiques soient-ils, rendent la modélisation des milliers de particules en régime funiculaire et capillaire quasi-impossible.

Pour s'affranchir de ces approximations et pour modéliser des milieux granulaires partiellement saturés pour tous les régimes possibles, nous proposons un couplage entre la méthode aux éléments discrets dite DEM pour simuler le squelette solide en forme de particules sphériques et la méthode de Boltzmann sur réseau dite LBM afin de modéliser les ponts capillaires eau-air entre les particules solides.

Concernant la LBM, un code maison a été développé sur des cartes GPU (*Graphical Processing Units*) qui est basé sur la résolution des équations Navier-Stokes et Allen-Cahn afin de prendre en compte l'interface eau-air des ponts capillaires. En ce qui concerne la DEM, le logiciel à accès libre YADE a été utilisé (Šmilauer et al., 2021).

A.3 Validation numérique et résultats

Avant de s'attaquer à l'étude du matériau en considérant un volume élémentaire représentatif (VER), plusieurs benchmarks et validations ont été nécessaires pour le modèle LBM, notamment en ce qui concerne la prédiction précise de la forme des ponts capillaires ainsi que les forces associées. A l'équilibre mécanique de la simulation LBM, les formes des ponts capillaires entre deux grains solides sphériques coïncident parfaitement avec la solution théorique de l'équation de Young-Laplace. De plus, les résultats trouvés par la LBM montrent qu'elle est capable de retrouver l'inversion de signe de la courbure moyenne H quand la distance de séparation entre les deux particules augmente. En outre, une nouvelle expression numérique pour le calcul des forces capillaires entre des grains sphériques a été proposée. Cette nouvelle formulation a montré ses capacités à calculer de façon assez précise les forces capillaires résultant des ponts capillaires isolés et coalescents entre deux et trois particules sphériques, en les comparant avec des résultats expérimentaux et numériques dans la littérature. L'avantage de l'approche LBM est sa capacité à modéliser la fusion des ponts capillaires de façon intrinsèques sans avoir besoin de passer par des critères de fusion géométrique. Ainsi, ces résultats montrent que la LBM est capable de modéliser le passage du régime pendulaire au régime funiculaire.

Ensuite, le couplage DEM-LBM est mis en place pour explorer les caractéristiques des assemblages granulaires partiellement saturés pour tous les régimes capillaires. Nous avons pu retrouver la forme classique de la courbe de rétention qui est définie par l'évolution de la succion en fonction du degré de saturation. De plus, l'évolution de la contrainte capillaire moyenne, qui pourrait être considérée comme étant la cohésion apparente, a été tracée en fonction du degré de saturation. Nous observons une augmentation de la contrainte capillaire moyenne avec l'augmentation du degré de saturation jusqu'à un certain seuil au-delà duquel la contrainte capillaire moyenne diminue pour atteindre zéro lorsque

le système devient complètement saturé. Par ailleurs, nous avons également démontré que le paramètre de Bishop pour les contraintes effectives n'est jamais égal au degré de saturation. Ces derniers résultats ont été comparés avec des données numériques déjà existantes dans la littérature.

Nous avons enfin exploité la pleine capacité du couplage DEM-LBM pour simuler des cycles de séchage (évaporation) et de mouillage (condensation) dans les sols non-saturés. Cela a été réalisé à la fois sur de petits assemblages granulaires composés de trois et quatre particules sphériques, ainsi que sur des VER constitués de quelques milliers de grains. Tout d'abord, pour les trois particules sphériques, nous avons réussi à reproduire avec succès les sauts (chutes) des forces capillaires, estimées à 30 % au moment de la coalescence (rupture) des ponts capillaires. Ceci est démontré dans le cas des trois particules sphériques, tel qu'illustré sur la Figure (A.1), et nous avons ensuite comparé ces résultats avec des études expérimentales et théoriques (Gras, 2011; Gagneux and Millet, 2016). Un autre résultat assez remarquable est que nous avons constaté que, pour une même configuration et un même angle de mouillage, le volume auquel les ponts se fusionnent est différent de celui auquel les ponts se rompent, phénomène appelé l'hystérésis. En effet, nous avons observé que lors de la coalescence, la fusion n'aura lieu que si les interfaces capillaires se touchent. En revanche, la rupture des ponts capillaires se produit quand l'épaisseur du pont, dans le plan passant par les centres des particules sphériques, devient nulle.

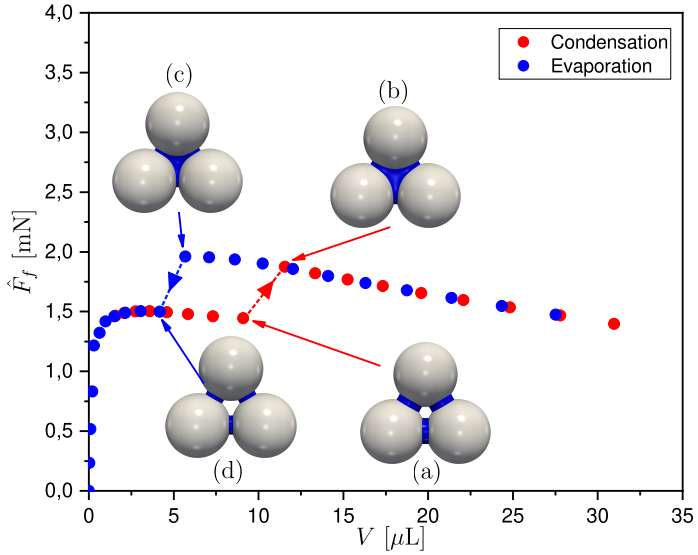

Figure A.1: L'évolution de la force capillaire $\hat{F}_f$ [mN] en fonction du volume d'eau [μL].

A l'échelle du VER, nous avons mis en évidence que la succion et la contrainte moyenne sont plus élevées lors de l'évaporation que celles qui ont été observées lors la condensation pour le même angle de mouillage comme le montre la Figure (A.2). Nous avons également montré que la contrainte capillaire moyenne (cohésion apparente) devient nulle quand le système devient complètement sec ou saturé, comme observé précédemment.

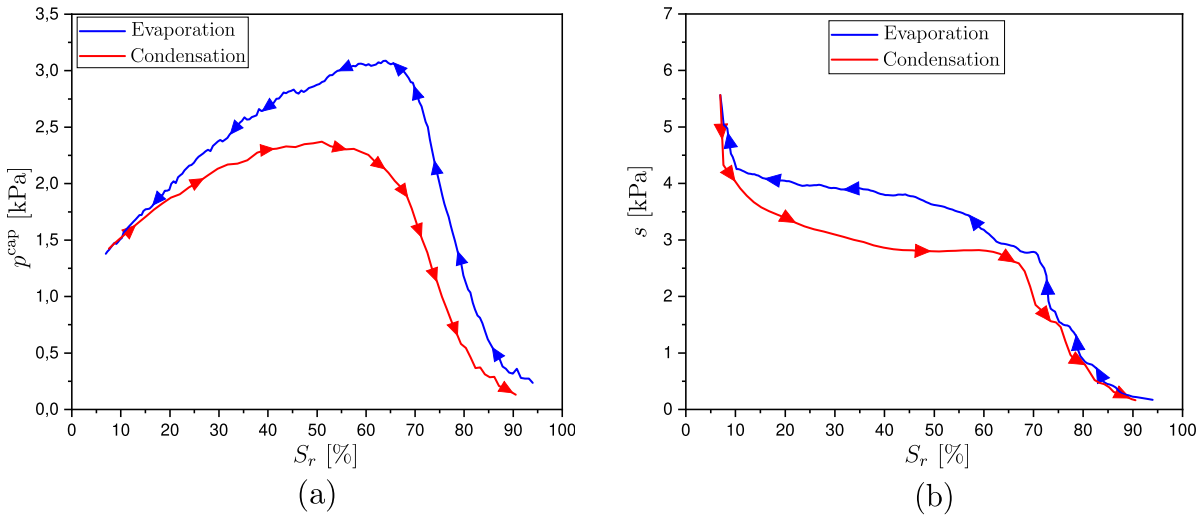

Figure A.2: Les évolutions (a) de la contrainte capillaire moyenne p^{cap} [kPa] et (b) de la succion s [kPa] en fonction du degré de saturation S_r [%].

A.4 Conclusion et perspectives

Pour rappel, l'étude bibliographique effectuée dans ce mémoire a mis en évidence d'importantes lacunes dans la compréhension des milieux granulaires partiellement saturés, notamment le fait que la plupart des études se sont concentrées uniquement sur le régime pendulaire. Par conséquent, l'objectif principal de cette thèse était de développer un modèle numérique capable de simuler les matériaux granulaires partiellement saturés pour tous les régimes possibles : pendulaire, funiculaire et capillaire. Cela a justifié le choix d'utiliser le modèle DEM-LBM, capable de modéliser facilement cette transition entre les régimes, pour étudier et exploiter les milieux granulaires partiellement saturés.

Les perspectives de ces travaux sont nombreuses et peuvent-être résumés en quelques points :

A.4.1 Existence d'une contrainte effective

L'existence de la contrainte effective est depuis longtemps un problème ouvert et majeur pour les géomécaniciens à la fois sur le niveau numérique et expérimental. L'existence de la contrainte effective n'a été justifiée que dans le régime pendulaire lors de la rupture de l'échantillon, c-à-d à la limite plastique. Cependant, la réponse reste malheureusement en suspens pour les régimes funiculaire et capillaire. C'est là où le couplage DEM-LBM entre en jeu afin d'étudier plus en détail cette question dans tous les régimes possibles.

A.4.2 Instabilités à l'échelle du VER

Dans le cadre du projet StabDigue, l'étude la plus cruciale concerne la détermination quantitative des instabilités des sols granulaires partiellement saturés soumis à des cycles de mouillage/séchage. Cet aspect peut être abordé en utilisant le soit-disant critère du travail du second ordre W^2 (Wan et al., 2017), capable de décrire de manière précise l'effondrement des sols granulaires secs. En utilisant le couplage DEM-LBM ainsi que les expressions analytiques récemment dérivées par Eghbalian et al. (2023), nous avons l'opportunité de calculer de façon précise le W^2 pour tous les régimes possibles.

A.4.3 Couplage avec des approches macroscopiques

La modélisation des digues en utilisant le couplage DEM-LBM avec des millions de particules, semble impossible et irréalisable en raison du calcul très intensif. Pour surmonter ce problème, il est envisageable d'intégrer le modèle DEM-LBM avec une méthode macroscopique telle que la méthode des éléments finis (FEM), la méthode des différences finies (FDM) ou la méthode du point matériel (MPM). Actuellement, en parallèle de ma thèse, des chercheurs à l'Université de La Rochelle explorent la possibilité d'utiliser le DEM-LBM comme une loi de comportement pour modéliser, à l'échelle réelle, les digues en remblai.

Pour conclure, le couplage DEM-LBM a montré ses capacités à analyser finement, la physique des matériaux granulaires partiellement saturés à l'échelle macroscopique, et plus particulièrement les transitions fluides entre les régimes capillaires. Ce modèle numérique nous permis de comprendre des aspects qui pourraient sinon rester inaccessibles dans des expériences de laboratoire. Nous pourrons avec ce fameux modèle de repousser les limites de notre compréhension des sols partiellement saturés. Nous pourrons également proposer des solutions aux paradoxes actuelles et contribuer au développement de la géomécanique dans son entièreté.

Appendix B

Graphical Processing Unit - GPU

A brief introduction to GPU computations will be given in this section. Readers can refer to Cheng et al. (2014); Tuomanen (2018) for more technical details.

B.1 Introduction

Unlike the sequential computations of Central Processing Units (CPUs), GPUs perform thousands of parallel computations. Originally developed for computer graphics over two decades ago, GPUs have since been recognized as powerful tools for scientific computation by computer scientists. Nevertheless, applications of GPUs are not only restricted to Graphics rendering or scientific computations but even to:

- **Machine Learning and AI:** GPUs have become indispensable tools in training and deploying deep neural networks. The parallel processing capabilities of GPUs expedite the training process, enabling the development of sophisticated AI models for image recognition, natural language processing, and more.
- **High-Performance Computing:** In the realm of high-performance computing (HPC), GPUs contribute to solving complex problems efficiently. Their parallel architecture allows for substantial speed-ups in tasks such as cryptography, financial modeling, and optimization.

To avoid a very common confusion, it is essential to note that while a CPU is an absolute necessity hardware for a computer's functionality, a GPU is not indispensable. So far, only two companies manufacture GPUs: Nvidia and AMD. However, this brief presentation will exclusively focus on Nvidia.

B.2 Basic GPU coding

There exist several languages to make the graphical cards work, such as CUDA, OpenCL, and others. Our main focus is going to be on CUDA. CUDA, which stands for Compute Unified Device Architecture, is a parallel computing platform and programming model that launches codes in NVIDIA GPUs. CUDA has several programming interfaces, namely C, C++, Python, and more. In this Ph.D. work, CUDA-C was used.
As mentioned earlier, the presence of a CPU is indispensable for GPU computations because it handles all the features a computer needs, even the GPU. In fact, in the computer science realm, the CPU is called the *host* and the GPU is known as the *device* as though the CPU is hosting a new hardware.
To better understand the main differences as well as similarities between C/C++ and CUDA-C programs, a quick and simple example of summing arrays composed of 1024 elements will be given. A name of a project must be given, for instance: SumArrays.cu. In CUDA, the extension of the source code is " .cu ", whereas in C++ the extension is " .cpp ". This example was taken from and slightly modified from Cheng et al. (2014).

```
#include <stdio.h>
#include "cuda_runtime.h"
#include "device_launch_parameters.h"
#include <iostream>

// Declaring function and kernel names //

// ================== Kernels ================== //
__global__ void sumArrayOnDevice(float *a, float *b, float *c);
// ============================================================ //

// ================== Functions ================== //
void sumArrayOnHost(float *a, float *b, float *c, const int N);

void initialData(float *ip, int size);
// ============================================================ //

int main(int argc, char* argv[])
{
    int nElement = 1024;
    size_t nBytes = nElement * sizeof(float);
    bool test = true;

    // Declaration of variables and memory
    // allocation of CPU variables in host
    float *h_a = (float *) malloc(nBytes);
    float *h_b = (float *) malloc(nBytes);
    float *h_c = (float *) malloc(nBytes);
    float *ref_c = (float *) malloc(nBytes);

    // Initialization of an array of nElement in the host
    initialData(h_a, nElement);
    initialData(h_b, nElement);

    // Declaration of GPU variables in the device
    float *d_a, *d_b, *d_c;

    // Memory allocation in the device
    cudaMalloc((float **) &d_a, nBytes);
    cudaMalloc((float **) &d_b, nBytes);
    cudaMalloc((float **) &d_c, nBytes);

    // Copying data from the host to the
    // device variables. Keyword: cudaMemcpyHostToDevice
    cudaMemcpy(d_a, h_a, nBytes, cudaMemcpyHostToDevice);
    cudaMemcpy(d_b, h_b, nBytes, cudaMemcpyHostToDevice);

    // Executing the kernel to add the elements
    // of the d_a array to d_b and storing the result in d_c.
    sumArrayOnDevice <<<1, nElement>>>(d_a, d_b, d_c);
```

```
    // Transferring the results of the device computation
    // to the host variable for comparison, using
    // the keyword cudaMemcpyDeviceToHost.
    cudaMemcpy(ref_c, d_c, nBytes, cudaMemcpyDeviceToHost);

    // Executing the function to add the elements
    // of the h_a array to h_b and storing
    // the result in h_c.
    sumArrayOnHost(h_a, h_b, h_c, nElement);

    // Comparing results between device
    // and host results ref_c and h_c
    for(int i = 0; i < nElement; i++)
        if(ref_c[i] != h_c[i])
        {
            test = false;
            break;
        }

    if (test)
        std::cout << "GPU AND CPU PROVIDED THE SAME RESULTS" << std::endl;
    else
        std::cout << "GPU AND CPU DID NOT PROVIDE THE SAME RESULTS" << std::endl
            ;

    // Free host variables
    free(h_a);
    free(h_b);
    free(h_c);
    free(ref_c);

    // Free device variables
    cudaFree(d_a);
    cudaFree(d_b);
    cudaFree(d_c);

    // Reset the current device resources
    cudaDeviceReset();
    return 0;
}

// Defining functions and Kernels

void sumArrayOnHost(float *a, float *b, float *c, const int N)
{
    for(int i=0; i < N; i++)
        c[i] = a[i] + b[i];
}

// Generating random numbers
void initialData(float *ip, int size)
```

```
{
    time_t t;
    srand((unsigned int) time(&t));

    for(int i=0; i < size; i++)
    {
        ip[i] = (float) ( rand() & 0xFF ) / 10.0f;
    }
}

__global__ void sumArrayOnDevice(float *a, float *b, float *c)
{
    int idx = threadIdx.x;
    c[idx] = a[idx] + b[idx];
}
```

The project must be saved, built using nvcc command, and compiled as follows:

```
nvcc SumArrays.cu -o SumArrays
./SumArrays
```

and the outcome will be:

```
GPU AND CPU PROVIDED THE SAME RESULTS
```

When writing a CUDA-C program, it is common and recommended to differentiate host from device variables by adding as prefix: "h_" for host variables and "d_" for device variables. Let us summarize the previous example:

- Declaration and allocation of host variables using malloc() function;
- Initialization of host variables using initialData() function;
- Declaration of device variables, and then allocate memory in the device;
- Transfering or copying host variables to the device variables;
- Execution of the kernel of summing using the device: sumArrayOnDevice;
- Copying back the results provided by the device;
- Execution of the function of summing using the host: sumArrayOnHost();
- Comparison between host and device results;
- Free the device and host memories.

Coding with CUDA-C has another paradigm compared to the CPU languages because, in the GPU, the user has to code as if there is only one element The first difference between GPU and CPU codes is the keyword[1] __global__. That is how the Host (CPU) knows that this is a GPU kernel and not a CPU function. The third difference is that when the kernel is called, it must be called in the following way:

[1]There are also other keywords, such as __device__ and __host__.

```
Kernel_name <<< the number of blocks, the number of threads per block >>>
```

The configuration must be provided in a way that informs the device about the number of threads for which parallel computations are to be executed.
The second difference is, in the host, the computation is synchronized, the integer variable " i " in sumArrayOnHost() function will not become 5 before it goes through 1 to 4. However, the integer variable " idx " in the sumArrayOnDevice() kernel can be 5 and 1 at the same time in different threads.

Certainly, this example is straightforward for a 1D array application, yet it offers the reader a comprehensive overview of the distinctions between CPU and GPU computations and their respective operational methods.

B.3 GPU Architecture

Modern GPUs are organized into units known as Streaming Multiprocessors (SMs) or compute units. Each SM contains a cluster of CUDA cores, the fundamental processing units responsible for executing instructions. These cores work in harmony, tackling diverse tasks in parallel, and can handle tasks such as arithmetic operations, memory management, and control flow (Cheng et al., 2014).
An efficient memory hierarchy is essential for managing the data processed by GPU cores. Three types of memory exist in GPUs: global, shared, and local memories. The global memory is the larger but the slowest one. It can be accessed by any thread at any time from kernels. The shared memory is faster than the global, but it's smaller and it is only accessed by the threads of the same block. Finally, the local memory is the faster but the smallest one, and it is solely accessed by the thread itself. The user should possess a strong knowledge of memory hierarchy management to ensure optimal efficiency of the code. Several models can be found on the market, including Fermi, Pascal, and Tesla, amongst others.

Appendix C

Hermite Polynomials

C.1 One-dimensional space Hermite polynomials

The Hermite differential equation $f(y'', y', y, x) = 0$ is defined as follows:

$$y'' - 2xy' + 2yk = 0 \tag{C.1}$$

The solutions of Eq. (C.1) for $k \geq 0$ are defined as follows

$$H^{(k)}(x) = \frac{(-1)^k}{\omega(x)} \frac{\mathrm{d}^k \omega(x)}{\mathrm{d}x^k} \tag{C.2}$$

where k denotes the highest order of the polynomial, and $\omega(x)$ is defined as:

$$\omega(x) = \frac{1}{\sqrt{2\pi}} \exp\left(-\frac{x^2}{2}\right). \tag{C.3}$$

Here is some first polynomials deduced from Eq. (C.2).

$$\begin{aligned} H_0(x) &= 1 \\ H_1(x) &= 2x \\ H_2(x) &= 4x^2 - 2 \\ H_3(x) &= 8x^3 - 12x \\ &\vdots \end{aligned} \tag{C.4}$$

The polynomials in Eq.(C.4) are depicted in Fig. (C.1)

C.2 d-dimensional space Hermite polynomials

One of the most important point in discretizing the velocity space $\boldsymbol{\xi}$ is the Hermite decomposition. Therefore, we define the Hermite polynomials $\mathscr{H}^{(k)}(\boldsymbol{r})$ as

$$\mathscr{H}^{(k)}(\boldsymbol{r}) = \frac{(-1)^k}{\omega(\boldsymbol{r})} \boldsymbol{\nabla}^k \omega(\boldsymbol{r}) \tag{C.5}$$

where $\omega(\boldsymbol{r})$ is the weight function

$$\omega(\boldsymbol{r}) = \left[\frac{1}{\sqrt{2\pi}}\right]^d \exp\left(-\frac{\boldsymbol{r}^2}{2}\right) \tag{C.6}$$

If a given function $g(\boldsymbol{r})$ is written as follows

$$g(\boldsymbol{r}) = \omega(\boldsymbol{r}) g_T(\boldsymbol{r}) \tag{C.7}$$

then, $g(\boldsymbol{r})$ can be decomposed into the Hermite polynomials as follows

$$\boldsymbol{g}(\boldsymbol{r}) = \omega(\boldsymbol{r}) \sum_{k=0}^{\infty} \frac{1}{k!} \boldsymbol{b}^k : \mathscr{H}^{(n)}(\boldsymbol{r}) \tag{C.8}$$

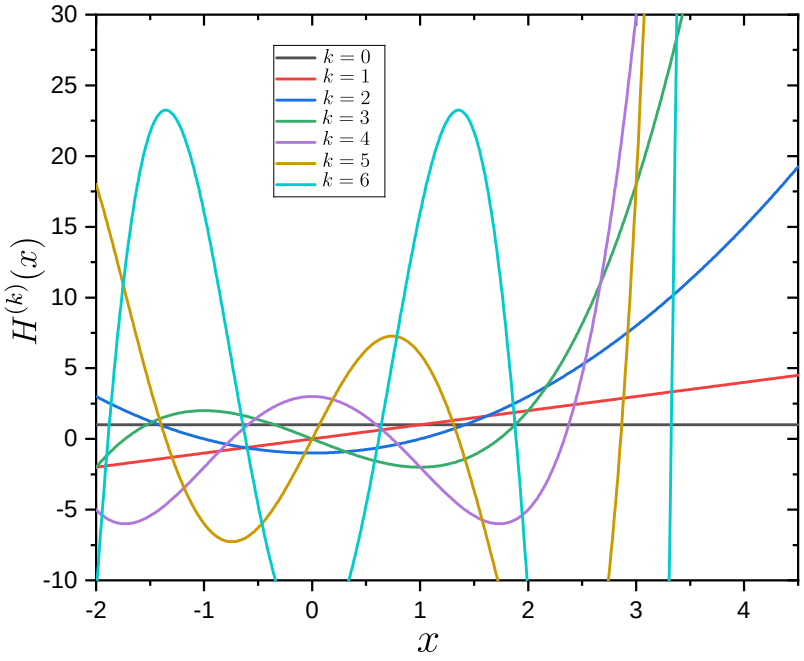

Figure C.1: Curves of Hermite polynomials for $k \in \{0; 1; 2; 3; 4; 5; 6\}$

where ":" is the double dot product, and $\boldsymbol{b}^k$ are k$^{\text{th}}$-order tensor of coefficients which are defined as follows:

$$\boldsymbol{b}^k = \int_{\mathbb{R}^3} g(\boldsymbol{r}) \mathscr{H}^{(k)}(\boldsymbol{r}) \mathrm{d}r. \tag{C.9}$$

The Hermite polynomial series will be used in order to approximate the Maxwellian distribution function.

Appendix D

Theoretical proofs

D.1 Chapman-Enskog - Theoretical proofs:

D.1.1 Chapman-Enskog: single-phase LBM model

Based on Eqs. (2.27), the term $\sum_i f_i^{\text{eq}}$ is calculated as follows:

$$\begin{aligned}\sum_i f_i^{\text{eq}} &= \omega_i \rho \left[1 + \frac{\boldsymbol{u}\cdot\boldsymbol{c}_i}{c_s^2} + \frac{(\boldsymbol{u}.\boldsymbol{c}_i)}{2c_s^4} - \frac{\boldsymbol{u}\cdot\boldsymbol{u}}{2c_s^2}\right] \\ &= \rho\left[\overbrace{\sum_i \omega_i}^{=1} + \sum_i \frac{\boldsymbol{u}\cdot\overbrace{(\omega_i\boldsymbol{c}_i)}^{=0}}{c_s^2} + \sum_i \omega_i \frac{(\boldsymbol{c}_i\cdot\boldsymbol{u})^2}{2c_s^4} - \frac{\boldsymbol{u}\cdot\boldsymbol{u}}{2c_s^2}\overbrace{\sum_i \omega_i}^{=1}\right].\end{aligned} \tag{D.1}$$

However, we have

$$\begin{aligned}\sum_i \omega_i \frac{(\boldsymbol{c}_i\cdot\boldsymbol{u})^2}{2c_s^4} &= \frac{1}{2c_s^4}\sum_i \left[\omega_i(\boldsymbol{c}_i\otimes\boldsymbol{c}_i)\cdot\boldsymbol{u}\right]\cdot\boldsymbol{u} \\ &= \frac{1}{2c_s^2}\left[\underbrace{\sum_i \frac{\omega_i\boldsymbol{c}_i\otimes\boldsymbol{c}_i}{c_s^2}}_{\boldsymbol{I}}\cdot\boldsymbol{u}\right]\cdot\boldsymbol{u} \\ &= \frac{\boldsymbol{u}\cdot\boldsymbol{u}}{2c_s^2}\end{aligned} \tag{D.2}$$

according to (2.27c) where we recall hat $\boldsymbol{I}$ is the identity tensor in $\mathbb{R}^3$. We inject Eq.(D.2) in (D.1) to finally obtain:

$$\sum_i f_i^{\text{eq}} = \rho. \tag{D.3}$$

Following the same procedure as above, using Eqs. (2.27), we calculate the term $\sum_i \boldsymbol{c}_i f_i^{\text{eq}}$:

$$\begin{aligned}\sum_i \boldsymbol{c}_i f_i^{\text{eq}} &= \rho\left[\overbrace{\sum_i \omega_i\boldsymbol{c}_i}^{=0} + \sum_i \frac{\omega_i(\boldsymbol{u}\cdot\boldsymbol{c}_i)}{c_s^2}\boldsymbol{c}_i + \sum_i \omega_i\frac{(\boldsymbol{u}\cdot\boldsymbol{c}_i)^2}{2c_s^4}\boldsymbol{c}_i - \frac{\boldsymbol{u}\cdot\boldsymbol{u}}{2c_s^2}\overbrace{\sum_i \omega_i\boldsymbol{c}_i}^{=0}\right] \\ &= \rho\left\{\overbrace{\sum_i \frac{\omega_i(\boldsymbol{c}_i\otimes\boldsymbol{c}_i)\cdot\boldsymbol{u}}{c_s^2}}^{\boldsymbol{I}} + \left[\frac{1}{2c_s^4}\overbrace{\sum_i \omega_i(\boldsymbol{c}_i\otimes\boldsymbol{c}_i\otimes\boldsymbol{c}_i)}^{=0}\cdot\boldsymbol{u}\right]\cdot\boldsymbol{u}\right\} \\ &= \rho\boldsymbol{u}.\end{aligned} \tag{D.4}$$

D.1.2 Chapman-Enskog: Allen-Cahn multiphase LBM model

Let us calculate the following term:

$$\begin{aligned}\sum_i (\boldsymbol{c}_i \cdot \boldsymbol{\nabla}_1 g_i^{\mathrm{eq}})\boldsymbol{c}_i &= \sum_i (\boldsymbol{c}_i \otimes \boldsymbol{c}_i) \cdot \boldsymbol{\nabla}_1 g_i^{\mathrm{eq}} \\ &= \boldsymbol{\nabla}_1 \cdot \sum_i (\boldsymbol{c}_i \otimes \boldsymbol{c}_i g_i^{\mathrm{eq}})\end{aligned} \tag{D.5}$$

According to the definition of g_i^{eq} in Eq. (3.26), we have

$$\begin{aligned}\sum_i (\boldsymbol{c}_i \cdot \boldsymbol{\nabla}_1)\boldsymbol{c}_i &= \boldsymbol{\nabla}_1 \cdot \left(\sum_i \omega_i \boldsymbol{c}_i \otimes \boldsymbol{c}_i \phi + \sum_i \omega_i \boldsymbol{c}_i \otimes \boldsymbol{c}_i \frac{\boldsymbol{c}_i \cdot \boldsymbol{u}}{c_s^2} \phi \right) \\ &= \boldsymbol{\nabla}_1 \cdot \left[c_s^2 \phi \boldsymbol{I} + \sum_i (\omega_i \boldsymbol{c}_i \otimes \boldsymbol{c}_i \otimes \boldsymbol{c}_i) \cdot \frac{\boldsymbol{u}}{c_s^2} \phi \right] \\ &= c_s^2 \boldsymbol{\nabla}_1 \cdot (\phi \boldsymbol{I}) \\ &= c_s^2 \boldsymbol{\nabla}_1 \phi\end{aligned} \tag{D.6}$$

with $\mathrm{div}(\alpha \boldsymbol{I}) = \mathrm{grad}(\alpha)$.

D.1.3 Chapman-Enskog: Navier-Stokes multiphase LBM model

It is possible to calculate the expression $\sum_i L_i^{(1)}$ introduced in Eq. (3.74) using properties given in (2.27). We have:

$$\begin{aligned}\sum L_i^{(1)} &= \frac{1}{c_s^2} \overbrace{\sum_i \omega_i \boldsymbol{c}_i}^{=0} \cdot \mu_\phi \boldsymbol{\nabla}_1 + \boldsymbol{u} \otimes \boldsymbol{\nabla}_1 \rho \colon \overbrace{\sum_i \frac{\omega_i \boldsymbol{c}_i \otimes \boldsymbol{c}_i}{c_s^2}}^{\boldsymbol{I}} \\ &= (\boldsymbol{u} \otimes \boldsymbol{\nabla}_1 \rho) \colon \boldsymbol{I} \\ &= \mathrm{Tr}\,(\boldsymbol{u} \otimes \boldsymbol{\nabla}_1 \rho) \\ &= \boldsymbol{u} \cdot \boldsymbol{\nabla}_1 \rho\end{aligned} \tag{D.7}$$

Let us now calculate Based $\sum_i L_i^{(1)} \boldsymbol{c}_i$:

$$\begin{aligned}\sum_i L_i^{(1)} \boldsymbol{c}_i &= \sum_i \frac{\omega_i \boldsymbol{c}_i \left(\boldsymbol{c}_i \cdot \mu_\phi \boldsymbol{\nabla}_1 \phi\right)}{c_s^2} + \frac{1}{c_s^2} \sum_i \omega_i \left(\boldsymbol{u} \otimes \boldsymbol{\nabla}_1 \rho \colon \boldsymbol{c}_i \otimes \boldsymbol{c}_i\right) \boldsymbol{c}_i \\ &= \overbrace{\sum_i \frac{(\omega_i \boldsymbol{c}_i \otimes \boldsymbol{c}_i)}{c_s^2}}^{\boldsymbol{I}} \cdot \mu_\phi \boldsymbol{\nabla}_1 \phi \\ &= \mu_\phi \boldsymbol{\nabla}_1 \phi + \frac{1}{c_s^2} \sum_i \omega_i \underbrace{\left(\underbrace{\boldsymbol{u} \otimes \boldsymbol{\nabla}_1 \rho}_{\boldsymbol{A}} \colon \underbrace{\boldsymbol{c}_i \otimes \boldsymbol{c}_i}_{\boldsymbol{B}} \right) \boldsymbol{c}_i}_{\boldsymbol{X}}\end{aligned} \tag{D.8}$$

For the sake of simplicity, we consider $\boldsymbol{A} = \boldsymbol{u} \otimes \boldsymbol{\nabla}_1 \rho$, $\boldsymbol{B} = \boldsymbol{c}_i \otimes \boldsymbol{c}_i$, and $\boldsymbol{X} = (\boldsymbol{A} \colon \boldsymbol{B})\, \boldsymbol{c}_i$. We have:

$$\begin{aligned} \boldsymbol{X} &= (\boldsymbol{A} \colon \boldsymbol{B})\, \boldsymbol{c}_i \\ &= (\boldsymbol{B} \otimes \boldsymbol{c}_i) : \boldsymbol{A}. \end{aligned} \tag{D.9}$$

Therefore, we have

$$\boldsymbol{X} = (\boldsymbol{c}_i \otimes \boldsymbol{c}_i \otimes \boldsymbol{c}_i) : (\boldsymbol{u} \otimes \boldsymbol{\nabla}_1 \rho) \tag{D.10}$$

where we have noted ": " the double contraction between a tensor of order three and a tensor of order two. Using Eqs. (D.9) and (2.27d), Eq. (D.8) eventually becomes:

$$\begin{aligned} \sum_i L_i^{(1)} \boldsymbol{c}_i &= \mu_\phi \boldsymbol{\nabla}_1 \phi + \frac{1}{c_s^2} \underbrace{\sum_i \omega_i \, (\boldsymbol{c}_i \otimes \boldsymbol{c}_i \otimes \boldsymbol{c}_i) \colon \boldsymbol{u} \otimes \boldsymbol{\nabla}_1 \rho}_{=\boldsymbol{0}} \\ &= \mu_\phi \boldsymbol{\nabla}_1 \phi. \end{aligned} \tag{D.11}$$

To summarize:

$$\begin{aligned} \sum_i L_i^{(1)} &= \boldsymbol{u} \cdot \boldsymbol{\nabla}_1 \rho \\ \sum_i L_i^{(1)} \boldsymbol{c}_i &= \mu_\phi \boldsymbol{\nabla}_1 \phi. \end{aligned} \tag{D.12}$$

Following the same procedure as before and using properties (2.27), we calculate the expression $\sum_i f_i^{\mathrm{eq}} \boldsymbol{c}_i \otimes \boldsymbol{c}_i$. We first recall f_i^{eq}:

$$f_i^{\mathrm{eq}} = \begin{cases} \dfrac{p}{c_s^2}(\omega_i - 1) + \rho s_i(\boldsymbol{u}) & i = 0 \\ \dfrac{p}{c_s^2}\omega_i + \rho s_i(\boldsymbol{u}) & i \neq 0 \end{cases} \tag{D.13}$$

with

$$s_i(\boldsymbol{u}) = \omega_i \left[\frac{\boldsymbol{c}_i \cdot \boldsymbol{u}}{c_s^2} + \frac{(\boldsymbol{c}_i \cdot \boldsymbol{u})^2}{2c_s^4} - \frac{\boldsymbol{u} \cdot \boldsymbol{u}}{2c_s^2} \right] \tag{D.14}$$

Let us start first with $\sum_i s_i(\boldsymbol{u}) \boldsymbol{c}_i \boldsymbol{c}_i$:

$$\begin{aligned} \sum_i s_i(\boldsymbol{u})(\boldsymbol{c}_i \otimes \boldsymbol{c}_i) &= \sum_i \omega_i \frac{\boldsymbol{c}_i \otimes \boldsymbol{c}_i}{c_s^2} (\boldsymbol{c}_i \cdot \boldsymbol{u}) + \sum_i \omega_i \boldsymbol{c}_i \otimes \boldsymbol{c}_i \frac{(\boldsymbol{c}_i \cdot \boldsymbol{u})^2}{2c_s^4} - \overbrace{\sum_i \omega_i \frac{\boldsymbol{c}_i \otimes \boldsymbol{c}_i}{c_s^2}}^{\boldsymbol{I}} \frac{\boldsymbol{u} \cdot \boldsymbol{u}}{2} \\ &= \overbrace{\left(\sum_i \omega_i \boldsymbol{c}_i \otimes \boldsymbol{c}_i \otimes \boldsymbol{c}_i \right)}^{=\boldsymbol{0}} \cdot \boldsymbol{u} \\ &\quad + \frac{1}{2} \underbrace{\overbrace{\sum_i \omega_i \frac{(\boldsymbol{c}_i \otimes \boldsymbol{c}_i \otimes \boldsymbol{c}_i \otimes \boldsymbol{c}_i)}{c_s^4} : (\boldsymbol{u} \otimes \boldsymbol{u})}^{A_{\alpha\beta\gamma\mu} u_\gamma u_\mu}}_{A_{\alpha\beta\gamma\mu}} - \frac{||\boldsymbol{u}||^2}{2} \boldsymbol{I}. \end{aligned} \tag{D.15}$$

where $A_{\alpha\beta\gamma\mu}u_\gamma u_\mu = \left[\sum_i \omega_i \frac{(\boldsymbol{c}_i \otimes \boldsymbol{c}_i \otimes \boldsymbol{c}_i \otimes \boldsymbol{c}_i)}{c_s^4} : (\boldsymbol{u}\otimes\boldsymbol{u})\right]_{\alpha\beta}$ for the sake of simplicity. We then use Eq. (2.27e):

$$\begin{aligned}(A_{\alpha\beta\gamma\mu}u_\gamma u_\mu)_{\alpha\beta} &= \left(\delta_{\alpha\beta}\delta_{\gamma\mu} + \delta_{\alpha\gamma}\delta_{\beta\mu} + \delta_{\alpha\mu}\delta_{\beta\gamma}\right) u_\gamma u_\mu \\ &= \delta_{\alpha\beta}\delta_{\gamma\mu}u_\gamma u_\mu + \delta_{\alpha\gamma}\delta_{\beta\mu}u_\gamma u_\mu + \delta_{\alpha\mu}\delta_{\beta\gamma}u_\gamma u_\mu \\ &= \delta_{\alpha\beta}u_\nu u_\nu + u_\alpha u_\beta + u_\alpha u_\beta \end{aligned} \tag{D.16}$$

hence,

$$\boldsymbol{A} : (\boldsymbol{u}\otimes\boldsymbol{u}) = ||\boldsymbol{u}||^2 + 2\boldsymbol{u}\otimes\boldsymbol{u}. \tag{D.17}$$

Injecting (D.17) in (D.15), we finally obtain:

$$\sum_i s_i(\boldsymbol{u})(\boldsymbol{c}_i \otimes \boldsymbol{c}_i) = \boldsymbol{u}\otimes\boldsymbol{u}. \tag{D.18}$$

The remaining term of $\sum_i f_i^{\text{eq}}\boldsymbol{c}_i \otimes \boldsymbol{c}_i$ is the pressure. Indeed, we have:

$$\sum_i f_i^{\text{eq}}\boldsymbol{c}_i \otimes \boldsymbol{c}_i = p\overbrace{\sum_{i=1}^{q-1}\frac{\boldsymbol{c}_i\otimes\boldsymbol{c}_i}{c_s^2}}^{\boldsymbol{I}} + \rho\sum_i s_i(\boldsymbol{u})\boldsymbol{c}_i\otimes\boldsymbol{c}_i \tag{D.19}$$

as $\boldsymbol{c}_0 = \boldsymbol{0}$, $\sum_{i=1}^{q-1}\frac{\boldsymbol{c}_i\otimes\boldsymbol{c}_i}{c_s^2} = \sum_{i=0}^{q-1}\frac{\boldsymbol{c}_i\otimes\boldsymbol{c}_i}{c_s^2}$. Therefore, we obtain:

$$\sum_i f_i^{\text{eq}}\boldsymbol{c}_i \otimes \boldsymbol{c}_i = p\boldsymbol{I} + \rho\boldsymbol{u}\otimes\boldsymbol{u}. \tag{D.20}$$

Let us recall Eq. (3.101)

$$\partial_{t_2}(\rho\boldsymbol{u}) + \left(1 - \frac{\Delta t}{2\tau_f}\right)\boldsymbol{\nabla}_1 \cdot \left[\underbrace{\sum_i f_i^{(1)}\boldsymbol{c}_i\otimes\boldsymbol{c}_i}_{\boldsymbol{A}} + \frac{\Delta t}{2}\underbrace{\sum_i L_i^{(1)}\boldsymbol{c}_i\otimes\boldsymbol{c}_i}_{\boldsymbol{B}}\right] = 0 \tag{D.21}$$

Eq. (3.77b) can be rewritten as follows:

$$f_i^{(1)} + \frac{\Delta t}{2}L_i^{(1)} = \tau_f\left[L_i^{(1)} - (\partial_{t_1} + \boldsymbol{c}_i\cdot\boldsymbol{\nabla}_1)f_i^{\text{eq}}\right]. \tag{D.22}$$

Then, we multiply Eq. (D.22) with $\boldsymbol{c}_i\otimes\boldsymbol{c}_i$ and sum it over i to obtain:

$$\begin{aligned}&\sum_i f_i^{(1)}(\boldsymbol{c}_i\otimes\boldsymbol{c}_i) + \frac{\Delta t}{2}\sum_i L_i^{(1)}(\boldsymbol{c}_i\otimes\boldsymbol{c}_i) = \\ &\tau_f\left[\sum_i L_i^{(1)}(\boldsymbol{c}_i\otimes\boldsymbol{c}_i) - \sum_i(\partial_{t_1} + \boldsymbol{c}_i\cdot\boldsymbol{\nabla}_1)f_i^{\text{eq}}(\boldsymbol{c}_i\otimes\boldsymbol{c}_i)\right]\end{aligned} \tag{D.23}$$

Thus, injecting (D.23) in (D.21), Eq. (D.21) becomes:

$$\begin{aligned}\partial_{t_2}(\rho\boldsymbol{u}) + \tau_f\left(1-\frac{\Delta t}{2\tau_f}\right)\boldsymbol{\nabla}_1\cdot\Bigg[&\sum_i L_i^{(1)}(\boldsymbol{c}_i\otimes\boldsymbol{c}_i)\\ &-\sum_i(\partial_{t_1}+\boldsymbol{c}_i\cdot\boldsymbol{\nabla}_1)f_i^{\mathrm{eq}}(\boldsymbol{c}_i\otimes\boldsymbol{c}_i)\Bigg]=0\end{aligned} \tag{D.24}$$

Therefore, the terms $\sum_i(\partial_{t_1}+\boldsymbol{c}_i\cdot\boldsymbol{\nabla}_1)f_i^{\mathrm{eq}}(\boldsymbol{c}_i\otimes\boldsymbol{c}_i)$ and $\sum_i L_i^{(1)}(\boldsymbol{c}_i\otimes\boldsymbol{c}_i)$ need te be calculated. Let us start with the latter:

$$\sum_i L_i^{(1)}(\boldsymbol{c}_i\otimes\boldsymbol{c}_i)=\left[\overbrace{\sum_i\omega_i\frac{\boldsymbol{c}_i\cdot\mu_\phi\boldsymbol{\nabla}_1\phi}{c_s^2}(\boldsymbol{c}_i\otimes\boldsymbol{c}_i)}^{\boldsymbol{C}}+\overbrace{\sum_i\frac{\boldsymbol{u}\otimes\boldsymbol{\nabla}_1\rho\colon\boldsymbol{c}_i\otimes\boldsymbol{c}_i}{c_s^2}(\boldsymbol{c}_i\otimes\boldsymbol{c}_i)}^{\boldsymbol{D}}\right]. \tag{D.25}$$

We now calculate $\boldsymbol{C}$ and $\boldsymbol{D}$:

$$\begin{aligned}\boldsymbol{C}&=\overbrace{\sum_i\frac{\omega_i\boldsymbol{c}_i\otimes\boldsymbol{c}_i\otimes\boldsymbol{c}_i}{c_s^2}}^{=\mathbf{0}}\cdot\mu_\phi\boldsymbol{\nabla}_1\phi\\ \boldsymbol{C}&=\mathbf{0}.\end{aligned} \tag{D.26}$$

$$\begin{aligned}\boldsymbol{D}&=\sum_i\frac{\omega_i}{c_s^2}(\boldsymbol{u}\otimes\boldsymbol{\nabla}_1\rho\colon\boldsymbol{c}_i\otimes\boldsymbol{c}_i)(\boldsymbol{c}_i\otimes\boldsymbol{c}_i)\\ &=\frac{1}{c_s^2}\overbrace{\sum_i\omega_i(\boldsymbol{c}_i\otimes\boldsymbol{c}_i\otimes\boldsymbol{c}_i\otimes\boldsymbol{c}_i)}^{c_s^4N_{\alpha\beta\gamma\mu}}\colon\boldsymbol{u}\otimes\overbrace{\boldsymbol{\nabla}_1\rho}^{\boldsymbol{v}}\\ &=c_s^2N_{\alpha\beta\gamma\mu}u_\gamma v_\mu\\ &=c_s^2(\delta_{\alpha\beta}\delta_{\gamma\mu}u_\gamma v_\mu+\delta_{\alpha\gamma}\delta_{\beta\mu}u_\gamma v_\mu+\delta_{\alpha\mu}\delta_{\beta\gamma}u_\gamma v_\mu)\\ \boldsymbol{D}&=c_s^2\left(\boldsymbol{u}\cdot\boldsymbol{\nabla}_1\rho\boldsymbol{I}+\boldsymbol{u}\otimes\boldsymbol{\nabla}_1\rho+\boldsymbol{\nabla}_1\rho\otimes\boldsymbol{u}\right).\end{aligned} \tag{D.27}$$

Therefore, expression (D.25) $\sum_i L_i^{(1)}(\boldsymbol{c}_i\otimes\boldsymbol{c}_i)$ becomes:

$$\sum_i L_i^{(1)}(\boldsymbol{c}_i\otimes\boldsymbol{c}_i)=c_s^2\left(\boldsymbol{u}\cdot\boldsymbol{\nabla}_1\rho\boldsymbol{I}+\boldsymbol{u}\otimes\boldsymbol{\nabla}_1\rho+\boldsymbol{\nabla}_1\rho\otimes\boldsymbol{u}\right) \tag{D.28}$$

Using (D.20), the term $\partial_{t_1}\sum_i f_i^{\mathrm{eq}}(\boldsymbol{c}_i\otimes\boldsymbol{c}_i)$ expresses:

$$\partial_{t_1}\sum_i f_i^{\mathrm{eq}}(\boldsymbol{c}_i\otimes\boldsymbol{c}_i)=\partial_{t_1}\left[p\boldsymbol{I}+\rho(\boldsymbol{u}\otimes\boldsymbol{u})\right]. \tag{D.29}$$

In addition, since the vectors $\boldsymbol{c}_i$ are constant, $\sum_i f_i^{\mathrm{eq}}(\boldsymbol{c}_i \cdot \boldsymbol{\nabla}_1)(\boldsymbol{c}_i \otimes \boldsymbol{c}_i)$ is equivalent to $\boldsymbol{\nabla}_1 \cdot \sum_i f_i^{\mathrm{eq}}(\boldsymbol{c}_i \otimes \boldsymbol{c}_i \otimes \boldsymbol{c}_i)$. To calculate the latter term, we start with $\sum_i s_i(\boldsymbol{u})(\boldsymbol{c}_i \otimes \boldsymbol{c}_i \otimes \boldsymbol{c}_i)$:

$$\begin{aligned}
\sum_i s_i(\boldsymbol{u})(\boldsymbol{c}_i \otimes \boldsymbol{c}_i \otimes \boldsymbol{c}_i) &= \sum_i \omega_i \frac{\boldsymbol{c}_i \cdot \boldsymbol{u}}{c_s^2}(\boldsymbol{c}_i \otimes \boldsymbol{c}_i \otimes \boldsymbol{c}_i) + \sum_i \omega_i \frac{(\boldsymbol{c}_i \cdot \boldsymbol{u})^2}{2c_s^4}(\boldsymbol{c}_i \otimes \boldsymbol{c}_i \otimes \boldsymbol{c}_i) \\
&\quad - \overbrace{\sum_i \omega_i \frac{\boldsymbol{c}_i \otimes \boldsymbol{c}_i \otimes \boldsymbol{c}_i}{c_s^2}}^{\mathbf{0}} \frac{\boldsymbol{u} \cdot \boldsymbol{u}}{2} \\
&= \overbrace{\sum_i \omega_i \frac{\boldsymbol{c}_i \otimes \boldsymbol{c}_i \otimes \boldsymbol{c}_i \otimes \boldsymbol{c}_i}{c_s^2}}^{c_s^2 M_{\alpha\beta\gamma\mu} u_\mu} \cdot \boldsymbol{u} + \overbrace{\sum_i \omega \frac{\boldsymbol{c}_i \otimes \boldsymbol{c}_i \otimes \boldsymbol{c}_i \otimes \boldsymbol{c}_i \otimes \boldsymbol{c}_i}{2c_s^4}}^{\mathbf{0}} : (\boldsymbol{u} \otimes \boldsymbol{u}) \\
&= c_s^2 M_{\alpha\beta\gamma\mu} u_\mu. \qquad \text{(D.30)}
\end{aligned}$$

Now, we calculate $M_{\alpha\beta\gamma\mu}u_\mu$ using (2.27e):

$$\begin{aligned}
M_{\alpha\beta\gamma\mu}u_\mu &= (\delta_{\alpha\beta}\delta_{\gamma\mu} + \delta_{\alpha\gamma}\delta_{\beta\mu} + \delta_{\alpha\mu}\delta_{\beta\gamma})\, u_\mu \\
&= \delta_{\alpha\beta}\delta_{\gamma\mu}u_\mu + \delta_{\alpha\gamma}\delta_{\beta\mu}u_\mu + \delta_{\alpha\mu}\delta_{\beta\gamma}u_\mu \\
&= \delta_{\alpha\beta}u_\gamma + \delta_{\alpha\gamma}u_\beta + \delta_{\beta\gamma}u_\alpha. \qquad \text{(D.31)}
\end{aligned}$$

Therefore, injecting (D.31) in (D.30) leads to:

$$\left[\sum_i s_i(\boldsymbol{u})(\boldsymbol{c}_i \otimes \boldsymbol{c}_i \otimes \boldsymbol{c}_i)\right]_{\alpha\beta\gamma} = c_s^2 \left(\delta_{\alpha\beta}u_\gamma + \delta_{\alpha\gamma}u_\beta + \delta_{\beta\gamma}u_\alpha\right). \qquad \text{(D.32)}$$

We can now calculate $\boldsymbol{\nabla}_1 \cdot \sum_i f_i^{\text{eq}}(\boldsymbol{c}_i \otimes \boldsymbol{c}_i \otimes \boldsymbol{c_i})$:

$$
\begin{aligned}
\left[\boldsymbol{\nabla}_1 \cdot \sum_i f_i^{\text{eq}}(\boldsymbol{c}_i \otimes \boldsymbol{c}_i \otimes \boldsymbol{c}_i)\right]_{\alpha\beta} =& \boldsymbol{\nabla}_1 \cdot \left(p \overbrace{\sum_{i=1}^{q-1} \frac{\boldsymbol{c}_i \otimes \boldsymbol{c}_i \otimes \boldsymbol{c}_i}{c_s^2}}^{\mathbf{0}} \right) \\
&+ \boldsymbol{\nabla}_1 \cdot \left(\frac{p}{c_s^2}(\omega_0 - 1) \overbrace{\boldsymbol{c}_0}^{\mathbf{0}} \otimes \overbrace{\boldsymbol{c}_0}^{\mathbf{0}} \otimes \overbrace{\boldsymbol{c}_0}^{\mathbf{0}} \right) \\
&+ \overbrace{\boldsymbol{\nabla}_1}^{\partial_\gamma} \cdot \left[\rho \overbrace{\sum_i s_i(\boldsymbol{u})(\boldsymbol{c}_i \otimes \boldsymbol{c}_i \otimes \boldsymbol{c}_i)}^{N_{\alpha\beta\gamma}} \right] \\
=& \partial_\gamma(\rho N_{\alpha\beta\gamma}) \\
=& \rho\partial_\gamma N_{\alpha\beta\gamma} + N_{\alpha\beta\gamma}\partial_\gamma\rho \\
=& c_s^2\rho\partial_\gamma \left(\delta_{\alpha\beta}u_\gamma + \delta_{\alpha\gamma}u_\beta + \delta_{\beta\gamma}u_\alpha\right) \\
&+ c_s^2 \left(\delta_{\alpha\beta}u_\gamma + \delta_{\alpha\gamma}u_\beta + \delta_{\beta\gamma}u_\alpha\right)\partial_\gamma\rho \\
=& c_s^2\rho \left(\delta_{\alpha\beta}\partial_\gamma u_\gamma + \delta_{\alpha\gamma}u_\beta\partial_\gamma + \delta_{\beta\gamma}u_\alpha\partial_\gamma\right) \\
&+ c_s^2 \left(\delta_{\alpha\beta}u_\gamma\partial_\gamma\rho + \delta_{\alpha\gamma}u_\beta\partial_\gamma\rho + \delta_{\beta\gamma}u_\alpha\partial_\gamma\rho\right) \\
=& c_s^2\rho \left(\delta_{\alpha\beta}\partial_\gamma u_\gamma + u_\beta\partial_{\alpha 1}\rho + u_\alpha\partial_{\beta 1}\rho\right) \\
&+ c_s^2 \left(\delta_{\alpha\beta}u_\gamma\partial_\gamma\rho + u_\beta\partial_{\alpha 1}\rho + u_\alpha\partial_{\beta 1}\rho\right) \\
=& c_s^2\rho \left(\boldsymbol{\nabla}_1 \cdot \boldsymbol{u}\boldsymbol{I} + \boldsymbol{\nabla}_1\boldsymbol{u} +^T \boldsymbol{\nabla}_1\boldsymbol{u}\right) \\
&+ c_s^2 \left(\boldsymbol{u} \cdot \boldsymbol{\nabla}_1\rho\boldsymbol{I} + \boldsymbol{u} \otimes \boldsymbol{\nabla}_1\rho\right. \\
&\left.+ \boldsymbol{\nabla}_1\rho \otimes \boldsymbol{u}\right) \\
=& c_s^2\rho \left(\boldsymbol{\nabla}_1\boldsymbol{u} +^T \boldsymbol{\nabla}_1\boldsymbol{u}\right) \\
&+ c_s^2 \left(\boldsymbol{u} \cdot \boldsymbol{\nabla}_1\rho\boldsymbol{I} + \boldsymbol{u} \otimes \boldsymbol{\nabla}_1\rho\right. \\
&\left.+ \boldsymbol{\nabla}_1\rho \otimes \boldsymbol{u}\right)
\end{aligned}
\tag{D.33}
$$

with $\boldsymbol{\nabla}_1 \cdot \boldsymbol{u}\boldsymbol{I} = \mathbf{0}$, because of the incompressibility condition (3.83).
Finally, $\boldsymbol{\nabla}_1 \cdot \sum_i f_i^{\text{eq}}(\boldsymbol{c}_i \otimes \boldsymbol{c}_i \otimes \boldsymbol{c_i})$ expresses:

$$
\begin{aligned}
\boldsymbol{\nabla}_1 \cdot \sum_i f_i^{\text{eq}}(\boldsymbol{c}_i \otimes \boldsymbol{c}_i \otimes \boldsymbol{c_i}) =& c_s^2\rho \left(\boldsymbol{\nabla}_1 \cdot \boldsymbol{u}\boldsymbol{I} + \boldsymbol{\nabla}_1\boldsymbol{u} +^T \boldsymbol{\nabla}_1\boldsymbol{u}\right) \\
&+ c_s^2 \left(\boldsymbol{u} \cdot \boldsymbol{\nabla}_1\rho\boldsymbol{I} + \boldsymbol{u} \otimes \boldsymbol{\nabla}_1\rho + \boldsymbol{\nabla}_1\rho \otimes \boldsymbol{u}\right)
\end{aligned}
\tag{D.34}
$$

Injecting (D.28), (D.29), and (D.34) in (D.24), leads to:

$$
\begin{aligned}
\partial_{t_2}(\rho\boldsymbol{u}) + \left(1 - \frac{\Delta t}{2\tau_f}\right) \boldsymbol{\nabla}_1 \cdot \left[\rho c_s^2 \left(\boldsymbol{\nabla}_1\boldsymbol{u} +^T \boldsymbol{\nabla}_1\boldsymbol{u}\right) - \rho c_s^2 \boldsymbol{\nabla}_1 \cdot \boldsymbol{u}\boldsymbol{I}\right. \\
\left. - \partial_{t_1}(\rho\boldsymbol{u} \otimes \boldsymbol{u} + p\boldsymbol{I})\right] = 0
\end{aligned}
\tag{D.35}
$$

D.2 Wetting angle

D.2.1 Trilinear interpolation

The equation for trilinear interpolation is given as

$$\phi_p = \phi(x, y, z) \approx a_0 + a_1 x + a_2 y + a_3 z + a_4 xy + a_5 xz + a_6 yz + a_7 xyz \tag{D.36}$$

where the coefficients are to be found by solving the linear system

$$\begin{bmatrix} 1 & x_i & y_i & z_i & x_i y_i & x_i z_i & y_i z_i & x_i y_i z_i \\ 1 & x_{i+1} & y_i & z_i & x_{i+1} y_i & x_{i+1} z_i & y_i z_i & x_{i+1} y_i z_i \\ 1 & x_i & y_{j+1} & z_i & x_i y_{j+1} & x_i z_i & y_{j+1} z_i & x_i y_{j+1} z_i \\ 1 & x_{i+1} & y_{j+1} & z_i & x_{i+1} y_{j+1} & x_{i+1} z_i & y_{j+1} z_i & x_{i+1} y_{j+1} z_i \\ 1 & x_i & y_i & z_{k+1} & x_i y_i & x_i z_{k+1} & y_i z_{k+1} & x_i y_i z_{k+1} \\ 1 & x_{i+1} & y_i & z_{k+1} & x_{i+1} y_i & x_{i+1} z_{k+1} & y_i z_{k+1} & x_{i+1} y_i z_{k+1} \\ 1 & x_i & y_{j+1} & z_{k+1} & x_i y_{j+1} & x_i z_{k+1} & y_{j+1} z_{k+1} & x_i y_{j+1} z_{k+1} \\ 1 & x_{i+1} & y_{j+1} & z_{k+1} & x_{i+1} y_{j+1} & x_{i+1} z_{k+1} & y_{j+1} z_{k+1} & x_{i+1} y_{j+1} z_{k+1} \end{bmatrix} \begin{bmatrix} a_0 \\ a_1 \\ a_2 \\ a_3 \\ a_4 \\ a_5 \\ a_6 \\ a_7 \end{bmatrix} = \begin{bmatrix} \phi_{(i,j,k)} \\ \phi_{(i+1,j,k)} \\ \phi_{(i,j+1,k)} \\ \phi_{(i+1,j+1,k)} \\ \phi_{(i,j,k+1)} \\ \phi_{(i+1,j,k+1)} \\ \phi_{(i,j+1,k+1)} \\ \phi_{(i+1,j+1,k+1)} \end{bmatrix}$$

D.2.2 Determination of solution of the wetting angle

The equations we are interested in are listed hereafter:

$$\boldsymbol{n_w} \cdot \boldsymbol{\nabla}\phi\big|_{x_w} = -\sqrt{\frac{2\beta}{k}} \cos\theta \left(\phi_w - \phi_w^2\right) \tag{D.37a}$$

$$\boldsymbol{n_w} \cdot \boldsymbol{\nabla}\phi\big|_{x_w} = \frac{\phi_p - \phi_{(i,j,k)}}{2h} \tag{D.37b}$$

$$\phi_w = \frac{\phi_{(i,j,k)} + \phi_p}{2}. \tag{D.37c}$$

Let us suppose at first that:

$$\begin{aligned} a &= hq \\ q &= -\sqrt{\frac{2\beta}{k}} \cos\theta \end{aligned} \tag{D.38}$$

Combining Eqs. (D.37a), (D.37b) and (D.37c) we get:

$$2a \left(\phi_w - \phi_w^2\right) = \phi_p - \phi_{(i,j,k)}. \tag{D.39}$$

Obviously, if $\theta = \dfrac{\pi}{2}$, the LHS of Eq. (D.39) is nil, which gives us:

$$\phi_{(i,j,k)} = \phi_p. \tag{D.40}$$

Whereas, for $\theta \neq \dfrac{\pi}{2}$, we replace Eq. (D.37c) in Eq. (D.39), and after regrouping the terms we get:

$$\phi_{(i,j,k)}^2 + 2\phi_{(i,j,k)} \left(\phi_p - 1 - \frac{1}{a}\right) + \phi_p^2 - 2\phi_p + 2\frac{\phi_p}{a} = 0. \tag{D.41}$$

Eq. (D.41) is a classical quadratic equation $\sum_{i=0}^{2} b_i x^i = 0$ of $\phi_{(i,j,k)}$ as unknown, with the discriminant of $\Delta' = \left(\frac{b_1}{2}\right)^2 - b_0 b_2 = 1 + \frac{1}{a^2} - \frac{4\phi_p}{a} + \frac{2}{a}$. The solutions of Eq. (D.41):

$$\begin{aligned} \phi_{(i,j,k)} &= \frac{-(b_1/2) \pm \sqrt{\Delta'}}{b_2} \\ \phi_{(i,j,k)} &= \frac{1}{a} + 1 - \phi_p \pm \sqrt{1 + \frac{1}{a^2} - \frac{4\phi_p}{a} + \frac{2}{a}}. \end{aligned} \tag{D.42}$$

After performing some mathematical manipulations, we recover Eq. (3.122):

$$\phi_{(i,j,k)} = \frac{1}{a}\left(1 + a \pm \sqrt{a^2 + 1 + 2a - 4\phi_p a}\right) - \phi_p \tag{D.43}$$

$$\phi_{(i,j,k)} = \frac{1}{a}\left(1 + a \pm \sqrt{(a+1)^2 - 4\phi_p a}\right) - \phi_p. \tag{D.44}$$

D.3 Determination of nodoid and unduloid shape

We recall here the main results reported in Gagneux and Millet (2014), used for the resolution of the Young-Laplace (4.11) as an inverse problem when the capillary pressure at the RHS is unknown.

D.3.1 Nodoid shape

If the geometric parameters verify the condition $r \sin\delta \sin(\delta + \theta) < y^* < r \sin\delta$ with $H > 0$ and $\lambda > 0$, the capillary bridge shape corresponds to a portion of nodoid, whose parametric equations are given by:

$$x(t) = \frac{b^2}{a} \int_0^t \frac{\cos u du}{(e + \cos u)\sqrt{e^2 - \cos^2 u}} \tag{D.45}$$

$$y(t) = b\sqrt{\frac{e - \cos t}{e + \cos t}}, \quad t \in [-\tau, \tau] \tag{D.46}$$

where

$$\tau = \arccos\left(e \frac{b^2 - r^2 \sin^2\delta}{b^2 + r^2 \sin^2\delta}\right) \tag{D.47}$$

$$e = \frac{\sqrt{a^2 + b^2}}{a} \tag{D.48}$$

τ is the unique solution in $[0, \pi/2]$ of the equation $y(\tau) = r \sin\delta$. The associated geometrical parameters are given by:

$$a = \frac{1}{2} \frac{r^2 \sin^2\delta - y^{*^2}}{y^* - r \sin\delta \sin(\delta + \theta)} \tag{D.49}$$

$$b^2 = y^* r \sin\delta \frac{r \sin\delta - y^* \sin(\delta + \theta)}{y^* - r \sin\delta \sin(\delta + \theta)} \tag{D.50}$$

The capillary pressure Δp and the mean curvature H can be calculated as follows:

$$\Delta p = -2\gamma \frac{y^* - r\sin\delta\sin(\delta+\theta)}{r^2\sin^2\delta - y^{*^2}} \tag{D.51}$$

$$H = -\frac{\Delta p}{\gamma} = \frac{1}{a} \tag{D.52}$$

D.3.2 Unduloid shape

If the geometric parameters verify the condition $0 < y^* < r\sin\delta\sin(\delta+\theta)$ with $H < 0$ and $\lambda > 0$, the capillary bridge shape corresponds to a portion of unduloid, whose geometrical parameters are given by

$$x(t) = \frac{b^2}{a}\int_0^t \frac{du}{(1+e\cos u)\sqrt{1-e^2\cos^2 u}} \tag{D.53}$$

$$y(t) = b\sqrt{\frac{1-e\cos t}{1+e\cos t}}, \quad t \in \left[-\tau^{'}, \tau^{'}\right] \tag{D.54}$$

where

$$\tau^{'} = \arccos\left(\frac{1}{e}\frac{b^2 - r^2\sin^2\delta}{b^2 + r^2\sin^2\delta}\right) \tag{D.55}$$

$$e = \frac{\sqrt{a^2+b^2}}{a} \tag{D.56}$$

$\tau^{'}$ is the unique solution in $[0, \pi/2]$ of the equation $y(\tau^{'}) = r\sin\delta$. The associated geometrical parameters are given by:

$$a = \frac{1}{2}\frac{r^2\sin^2\delta - y^{*^2}}{r\sin\delta\sin(\delta+\theta) - y^*} \tag{D.57}$$

$$b^2 = y^* r\sin\delta\frac{r\sin\delta - y^*\sin(\delta+\theta)}{r\sin\delta\sin(\delta+\theta) - y^*} \tag{D.58}$$

The capillary pressure Δp and the mean curvature H can be calculated as follows:

$$\Delta p = -2\gamma \frac{y^* - r\sin\delta\sin(\delta+\theta)}{r^2\sin^2\delta - y^{*^2}} \tag{D.59}$$

$$H = -\frac{\Delta p}{\gamma} = -\frac{1}{a} \tag{D.60}$$

Appendix E

Sensitivity Analysis

In this section, a sensitivity analysis of the liquid volume V and the LBM surface tension $\widetilde{\gamma}$ is provided. A single capillary bridge between 2 spherical particles is considered. It has already been proven in Chapter 4 that in LBM simulations, initialization of a droplet at the mid-distance between particles will ultimately converge to a capillary bridge as shown in Figure (E.1). The silicone oil is chosen whose surface tension is $\gamma = 0.0219$ N.m^{-1}, and viscosity is $\nu_{\text{oil}} = 10^{-6}$ m^2.s^{-1} at a temperature of $T = 20°$C. The domain size is $N_x \times N_y \times N_z = 160 \times 294 \times 160$, with the particles having a radius of $R = 5$ mm. The physical characteristic length is $L_c = 12$ mm in x-direction, therefore the mesh size $\Delta x = L_c/(N_x - 1) \approx 7.5 \times 10^{-5}$ m, where $N_x - 1$ is indeed the characteristic length in lattice units $\widetilde{L}_c$. A drop of silicone oil with a spherical shape is created at mid-distance between the two particles as illustrated in Figure (E.1a). The initialized spherical shape will converge at equilibrium to a capillary bridge as shown in Figure (E.1b). A contact angle $\theta = 20°$ at the solid-liquid-gas interphase is imposed using Eq. (3.120).

(a) Initialization of silicone oil droplet.

(b) Convergence of the capillary bridge.

Figure E.1: From initialization of oil silicone droplet at mid-distance to the convergence of the capillary bridge.

E.1 Influence of LBM surface tension $\widetilde{\gamma}$ on simulations convergence speed

As previously mentioned, the LBM time step is computed via the LBM surface tension $\widetilde{\gamma}$ as seen in Eq. (5.7). It is therefore important to investigate its influence on the results. Multiple LBM surface tension values are considered $\widetilde{\gamma} \in \{1; 5; 10; 20; 30\}$ for the same silicone oil volume $V = 4\,\mu$L and same separation distance $D = 0.7$ mm. Following the

procedure presented in 3.7, the corresponding air and water relaxation times are:

$$\widetilde{\gamma} = \begin{cases} 1 \\ 5 \\ 10 \\ 20 \\ 30 \end{cases} \xrightarrow{\text{Eq. (3.128)}} (\tilde{\tau}_h^{\ell}; \tilde{\tau}_h^{g}) = \begin{cases} (0.502; 0.542) \\ (0.505; 0.594) \\ (0.507; 0.633) \\ (0.510; 0.688) \\ (0.512; 0.731) \end{cases}. \tag{E.1}$$

Figure (E.2) depicts capillary forces for different values of LBM tension surface $\widetilde{\gamma} \in \{5; 10; 20; 30\}$ in terms of number of iterations.
It is important to mention that results of $\widetilde{\gamma} = 1$ are not presented because of the numerical instability induced by the correspondent relaxation times as previously calculated in Eq. (E.1). When the values of $(\tilde{\tau}_h^{\ell}, \tilde{\tau}_h^{g})$ are very close to $\dfrac{\widetilde{\Delta t}}{2}$, numerical instabilities may be observed (Krüger et al., 2017; Succi and Succi, 2018).

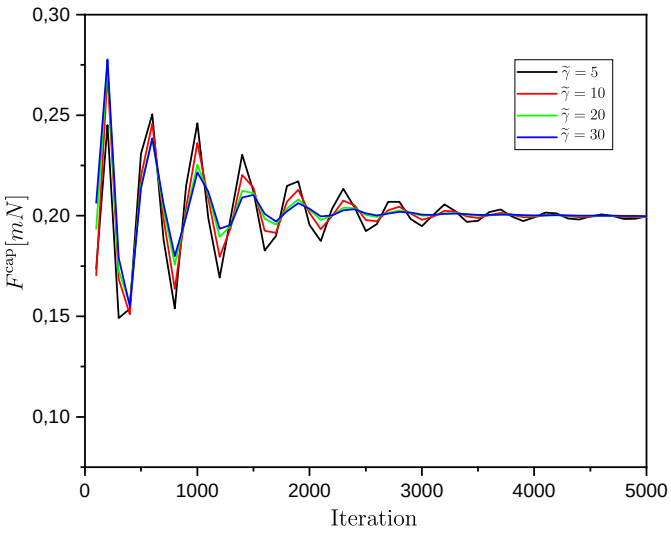

Figure E.2: Capillary forces F^{cap} for different LBM surface tension values $\widetilde{\gamma} \in \{5; 10; 20; 30\}$. From spherical drop initialization to converged capillary bridge.

It can be seen that $\widetilde{\gamma}$ has no effect on capillary force values because the same plateau is reached for all the simulations—$F^{\text{cap}} \approx 0.2$ mN. However, the main difference between these curves is the number of iterations at which the plateau is reached. The larger $\widetilde{\gamma}$, the faster the convergence. This can be explained by the fact that Δt_{LBM} depends on C_{γ} in Eq. (3.126). This also can be observed in Figure (E.5) where the relative error $\dfrac{|F_{i+1}^{\text{cap}} - F_i^{\text{cap}}|}{F_i^{\text{cap}}} \times 100$ with i is the i$^{\text{th}}$ iteration, is depicted in terms of the number of iterations. In fact, the relative error of $\widetilde{\gamma}$ tends to 0 faster than the other relative errors.

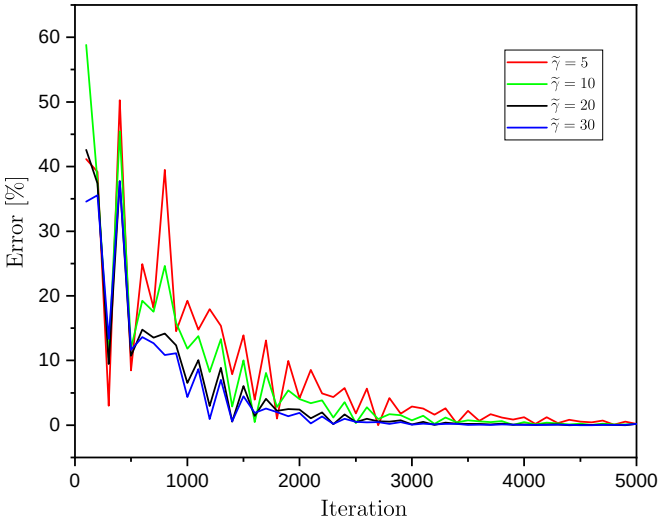

Figure E.3: Relative error between two consecutive capillary forces $\frac{|F_{i+1}^{\text{cap}} - F_i^{\text{cap}}|}{F_i^{\text{cap}}} \times 100$, where i is the i$^{\text{th}}$ iteration, in terms of number of iterations.

E.2 Influence of liquid volume V on simulations convergence speed

In this section, the separation distance is $D = 0.5$ mm, and several volumes are considered, $V \in \{1.79; 3.91; 10.68; 21.04\}$ µL. The LBM surface tension used is $\widetilde{\gamma} = 10$ lu. Figure (E.4) depicts the capillary forces F^{cap} of the four different oil volumes in terms of the number of iterations.
The present study confirms that the convergence of the aforementioned simulations does not happen at the same iteration. It is further validated with Figure (E.5), where the relative error between two consecutive iterations is plotted with respect to iteration numbers. A better visualization can be seen in Figure (E.5) in which the capillary bridge whose volume is the smallest $V = 1.79\mu$L, has the fastest convergence—at $n \approx 600$ iteration.

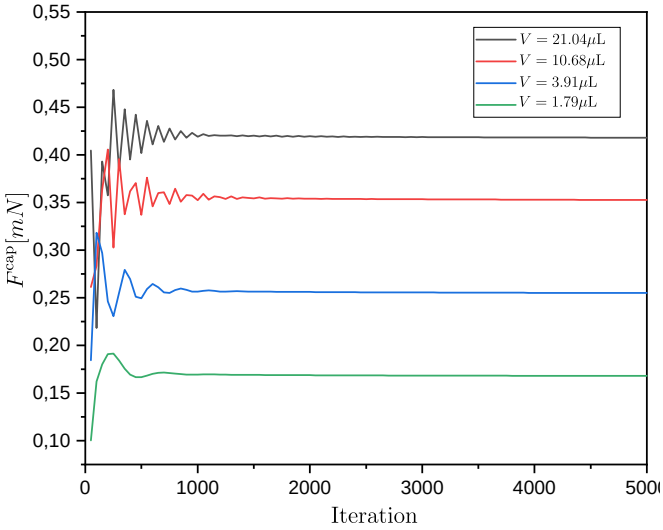

Figure E.4: Convergence of capillary forces F^{cap} for different volumes from spherical drop initialization to physically relevant capillary bridge shape

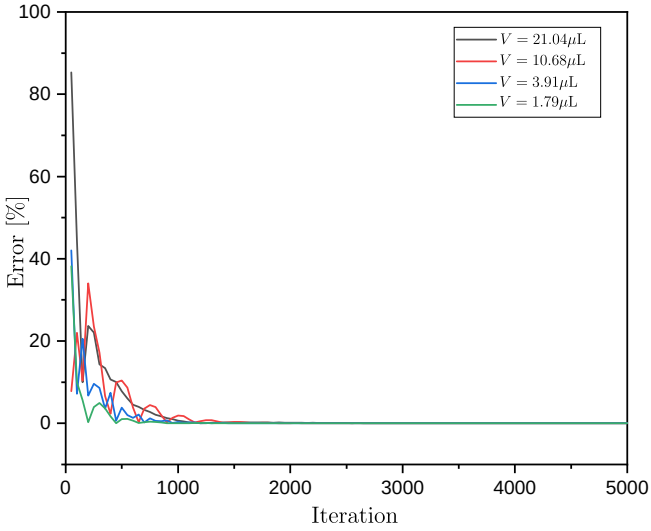

Figure E.5: Error between of capillary forces between two consecutive F^{cap}. The error is the so-called relative error between two consecutive iterations: $\frac{|F^{\text{cap}}_{i+1} - F^{\text{cap}}_{i}|}{F^{\text{cap}}_{i}} \times 100$, where i is the i^{th} iteration.

In the case of Chapter 5, the largest water volume can be found in the capillary regime, where the water phase is continuous which is around $V = 1.27\,\mu\text{L}$. As we have seen just before, for $V = 1.79\,\mu\text{L}$, we needed 600 iterations. Therefore, for $V = 1.27\,\mu\text{L}$, 500 iterations are enough to ensure the initial convergence.

Appendix F

List of publications

This research effort has led to the publication of three papers in international journals along with numerous presentations at both international and national conferences. Several additional papers are currently in preparation for submission.

Journal papers:

- **N. Younes**, A. Wautier, R. Wan, O. Millet, F. Nicot, and R. Bouchard. "DEM-LBM coupling for partially saturated granular assemblies." *Computers and Geotechnics* 162 (2023): 105677.
- **N. Younes**, Z. Benseghier, O. Millet, A. Wautier, F. Nicot, and R. Wan. "Phase-field Lattice Boltzmann model for liquid bridges and coalescence in wet granular media." *Powder Technology* 411 (2022): 117942.
- Z. Benseghier, O. Millet, P. Philippe, A.Wautier, **N. Younes**, and E. Liberge. "Relevance of capillary interfaces simulation with the Shan-Chen multiphase LB model." *Granular Matter* 24, no. 3 (2022): 82.
- **N. Younes**, A. Wautier, O. Millet, R. Wan, and F. Nicot. "Hysteresis phenomenon within unsaturated granular assemblies: capillary forces and matric suction." In preparation (2023).
- **N. Younes**, A. Wautier, R. Wan, O. Millet, and F. Nicot. "On the hysteresis phenomenon of unsaturated granular assemblies using DEM-LBM coupling". In Preparation (2023).
- **N. Younes**, O. Millet, and Z. Benseghier. "A relevant phase-field-based lattice-Boltzmann method for water-air capillary interfaces". In preparation (2023).

Conference proceedings:

- **N. Younes**, R. Wan, A. Wautier, O. Millet, F. Nicot. "Multiphase LBM-DEM Coupling for Unsaturated Granular Media." *Particles*, Milan, Italy. October 2023.
- **N. Younes**, R. Wan, A. Wautier, O. Millet, F. Nicot. " Hysteresis within unsaturated granular assemblies: DEM-LBM coupling" [Poster Presentation] *ALERT Workshop*, Aussois, France. September 2023.
- **N. Younes**, R. Wan, A. Wautier, O. Millet, F. Nicot. "On the capillary stress in unsaturated granular assemblies." *Méca-J*, France. August 2023.
- **N. Younes**, R. Wan, A. Wautier, O. Millet, F. Nicot. "Modeling capillary transitions in unsaturated media across all saturation regimes." *NANGE*, Assisi, Italy. May 2023
- **N. Younes**, Z. Benseghier, O. Millet, A. Wautier, F. Nicot, and R. Wan. "Multiscale modeling of maritime dikes under cyclic hydraulic loadings." [Poster Presentation] *ALERT Workshop*, Aussois, France. September 2022.

- **N. Younes**, Z. Benseghier, O. Millet, A. Wautier, F. Nicot, and R. Wan. "LBM approach for capillary bridges and associated forces in an air-water system." *CFM - Session: Mécanique des milieux granulaires*, Nantes, France. August 2022.

- **N. Younes**, Z. Benseghier, O. Millet, A. Wautier, F. Nicot, and R. Wan. "Multiphase Lattice-Boltzmann approach for capillary bridges and associated forces." *ICONSOM*, Sardinia, Italy. June 2022.

- **N. Younes**, Z. Benseghier, O. Millet, A. Wautier, F. Nicot, and R. Wan. "A relevant phase-field-based Lattice Boltzmann Method for water-air capillary interfaces." *Méca-J*, France. August 2021.

References (222)

G. D. Aitchison. Relationship of moisture and effective stress functions in unsaturated soils. *Pore pressure and suction in soils*, pages 47–52, 1961. Cited in pages 32, 33

G. D. Aitchison and P. Peter. Quantitative description of the stress deformation behaviour of expansive soils. 1973. Cited in page 32

M. Ajdari, G. Habibagahi, and A. Ghahramani. Predicting effective stress parameter of unsaturated soils using neural networks. *Computers and Geotechnics*, 40:89–96, 2012. Cited in page 35

H. M. B. Al-Hashemi and O. S. B. Al-Amoudi. A review on the angle of repose of granular materials. *Powder technology*, 330:397–417, 2018. Cited in page 122

A. Argilaga and C. Zhao. Rupture distances and capillary forces of liquid bridges: Closed-form expressions and anns-trained prediction models. *Powder Technology*, page 118702, 2023. Cited in page 19

Z. Benseghier, O. Millet, P. Philippe, A.Wautier, N. Younes, and E. Liberge. Relevance of capillary interfaces simulation with the shan-chen multiphase lb model. *Submitted to Granular Matter*, 2021. Cited in page 66

Z. Benseghier, O. Millet, P. Philippe, A. Wautier, and N. Younes. Relevance of capillary interfaces simulation with the shan–chen multiphase lb model. *Granular Matter*, 24(3): 82, 2022. Cited in pages XV, XVI, 20, 21, 22, 143

P. L. Bhatnagar, E. P. Gross, and M. Krook. A model for collision processes in gases. i. small amplitude processes in charged and neutral one-component systems. *Physical review*, 94(3):511, 1954. Cited in page 48

A. W. Bishop. The use of the slip circle in the stability analysis of slopes. *Geotechnique*, 5(1):7–17, 1955. Cited in page 3

A. W. Bishop. The principle of effective stress. *Teknisk ukeblad*, 39:859–863, 1959. Cited in page 32

A. W. Bishop and G. Blight. Some aspects of effective stress in saturated and partly saturated soils. *Geotechnique*, 13(3):177–197, 1963. Cited in pages 32, 133

A. W. Bishop and N. Morgenstern. Stability coefficients for earth slopes. *Geotechnique*, 10(4):129–153, 1960. Cited in page 3

S. Bonelli. *Erosion of geomaterials*. John Wiley & Sons, 2012. Cited in page 1

K. A. Brakke. The surface evolver. *Experimental mathematics*, 1(2):141–165, 1992. Cited in page 20

A. Briant. Lattice boltzmann simulations of contact line motion in a liquid-gas system. *Philosophical Transactions of the Royal Society of London. Series A: Mathematical, Physical and Engineering Sciences*, 360(1792):485–495, 2002. Cited in page 82

R. H. Brooks. *Hydraulic properties of porous media*. Colorado State University, 1965. Cited in page 30

M. Budhu. *Soil mechanics fundamentals*. John Wiley & Sons, 2015. Cited in page 1

S. Chapman and T. G. Cowling. *The mathematical theory of non-uniform gases: an account of the kinetic theory of viscosity, thermal conduction and diffusion in gases*. Cambridge university press, 1990. Cited in page 48

J. Cheng, M. Grossman, and T. McKercher. *Professional CUDA c programming*. John Wiley & Sons, 2014. Cited in pages 173, 177

P.-H. Chiu and Y.-T. Lin. A conservative phase field method for solving incompressible two-phase flows. *Journal of Computational Physics*, 230(1):185–204, 2011a. ISSN 0021-9991. doi: https://doi.org/10.1016/j.jcp.2010.09.021. URL https://www.sciencedirect.com/science/article/pii/S0021999110005243. Cited in pages 66, 67

P.-H. Chiu and Y.-T. Lin. A conservative phase field method for solving incompressible two-phase flows. *Journal of Computational Physics*, 230(1):185–204, 2011b. Cited in page 67

J. Chu, S. Yan, and W. Li. Innovative methods for dike construction–an overview. *Geotextiles and Geomembranes*, 30:35–42, 2012. Cited in page 1

T. J. Chung. *Computational fluid dynamics*. Cambridge university press, 2002. Cited in page 46

R. B. Clapp and G. M. Hornberger. Empirical equations for some soil hydraulic properties. *Water resources research*, 14(4):601–604, 1978. Cited in page 30

K. W. Connington, T. Lee, and J. F. Morris. Interaction of fluid interfaces with immersed solid particles using the lattice boltzmann method for liquid–gas–particle systems. *Journal of Computational Physics*, 283:453–477, 2015. ISSN 0021-9991. doi: https://doi.org/10.1016/j.jcp.2014.11.044. URL https://www.sciencedirect.com/science/article/pii/S0021999114008079. Cited in page 104

D. Croney, J. Coleman, and W. Black. Movement and distribution of water in soil in relation to highway design and performance. *Highway Research Board Special Report*, (40), 1958. Cited in page 32

P. A. Cundall and O. D. Strack. A discrete numerical model for granular assemblies. *geotechnique*, 29(1):47–65, 1979. Cited in pages 4, 114

B. M. Das. *Advanced soil mechanics*. CRC press, 2019. Cited in page 125

G. de Saxcé, J. Fortin, and O. Millet. About the numerical simulation of the dynamics of granular media and the definition of the mean stress tensor. *Mechanics of Materials*, 36(12):1175–1184, 2004. Cited in page 114

C. Delaunay. Sur la surface de révolution dont la courbure moyenne est constante. *Journal de Mathématiques Pures et Appliquées*, pages 309–314, 1841. URL http://eudml.org/doc/234757. Cited in page 16

J.-Y. Delenne, V. Richefeu, and F. Radjai. Capillary states of granular materials in the funicular state. In *AIP Conference Proceedings*, volume 1542, pages 1023–1026. American Institute of Physics, 2013. Cited in page 43

J.-Y. Delenne, V. Richefeu, and F. Radjai. Liquid clustering and capillary pressure in granular media. *Journal of Fluid Mechanics*, 762, 2015. Cited in pages 43, 66, 123

A. Di Renzo, G. Picarelli, and F. P. Di Maio. Numerical investigation of funicular liquid bridge interactions between spherical particles. *Chemical Engineering & Technology*, 43 (5):830–837, 2020. Cited in pages 27, 44

M. Dörmann and H.-J. Schmid. Distance-dependency of capillary bridges in thermodynamic equilibrium. *Powder technology*, 312:175–183, 2017. Cited in page 14

F. Dubois, V. Acary, and M. Jean. The contact dynamics method: A nonsmooth story. *Comptes Rendus Mécanique*, 346(3):247–262, 2018. Cited in page 114

J. Duriez and R. Wan. Stress in wet granular media with interfaces via homogenization and discrete element approaches. *Journal of Engineering Mechanics-ASCE*, 142(12), 2016. Cited in pages 36, 43, 44, 114, 121, 122, 125, 157, 162, 168

J. Duriez and R. Wan. Contact angle mechanical influence in wet granular soils. *Acta Geotechnica*, 12(1):67–83, 2017. Cited in pages 20, 36, 44, 103, 121, 122, 157, 162, 168

J. Duriez and R. Wan. A micromechanical μunsat effective stress expression for stress-strain behaviour of wet granular materials. *Geomechanics for Energy and the Environment*, 15:10–18, 2018. Cited in pages 36, 44, 157, 168

J. Duriez, M. Eghbalian, R. Wan, and F. Darve. The micromechanical nature of stresses in triphasic granular media with interfaces. *Journal of the Mechanics and Physics of Solids*, 99:495–511, 2017. Cited in pages 44, 114, 121, 122, 131, 162, 168

J. Duriez, R. Wan, M. Pouragha, and F. Darve. Revisiting the existence of an effective stress for wet granular soils with micromechanics. *International Journal for Numerical and Analytical Methods in Geomechanics*, 42(8):959–978, 2018. Cited in pages 130, 163

N. Edlefsen, A. Anderson, et al. Thermodynamics of soil moisture. *Hilgardia*, 15(2): 31–298, 1943. Cited in page 10

M. Eghbalian, M. Pouragha, and R. Wan. Micromechanical formulation of first-and second-order works in unsaturated granular media. *International Journal for Numerical and Analytical Methods in Geomechanics*, 47(7):1152–1174, 2023. Cited in pages 164, 170

F. Z. El Korchi. *Approche expérimentale multi-échelle de l'effondrement capillaire de sols granulaires.* PhD thesis, Université Montpellier, 2017. Cited in pages XVI, 23, 24, 25, 26, 27, 168

Encyclopedia Britannica. Sir Alfred Ewing, 2023. URL `https://www.britannica.com/biography/Alfred-Ewing`. Cited in page 12

E. U. Eyo, S. Ng'ambi, and S. J. Abbey. An overview of soil–water characteristic curves of stabilised soils and their influential factors. *Journal of King Saud University-Engineering Sciences*, 34(1):31–45, 2022. Cited in pages XVI, 27, 28, 29

A. Fakhari and D. Bolster. Diffuse interface modeling of three-phase contact line dynamics on curved boundaries: A lattice boltzmann model for large density and viscosity ratios. *Journal of Computational Physics*, 334:620–638, 2017. ISSN 0021-9991. doi: https://doi.org/10.1016/j.jcp.2017.01.025. URL https://www.sciencedirect.com/science/article/pii/S0021999117300414. Cited in page 69

A. Fakhari and T. Lee. Multiple-relaxation-time lattice boltzmann method for immiscible fluids at high reynolds numbers. *Physical Review E*, 87(2):023304, 2013. Cited in pages 50, 67

A. Fakhari and M. H. Rahimian. Phase-field modeling by the method of lattice boltzmann equations. *Physical Review E*, 81(3):036707, 2010. Cited in page 67

A. Fakhari, T. Mitchell, C. Leonardi, and D. Bolster. Improved locality of the phase-field lattice-boltzmann model for immiscible fluids at high density ratios. *Phys. Rev. E*, 96: 053301, Nov 2017a. Cited in page 67

A. Fakhari, T. Mitchell, C. Leonardi, and D. Bolster. Improved locality of the phase-field lattice-boltzmann model for immiscible fluids at high density ratios. *Physical Review E*, 96(5):053301, 2017b. Cited in page 67

M. Farahnak, R. Wan, and M. Pouragha. Anisotropic nature of the capillary stress tensor. In *EPJ Web of Conferences*, volume 249, page 11010. EDP Sciences, 2021. Cited in page 125

B. Fatahi, U. Pathirage, B. Indraratna, M. Pallewattha, and H. Khabbaz. The role of native vegetation in stabilizing formation soil for transport corridors: an australian experience. In *Ground Improvement Case Histories*, pages 591–628. Elsevier, 2015. Cited in page 28

R. Fisher. On the capillary forces in an ideal soil; correction of formulae given by wb haines. *The Journal of Agricultural Science*, 16(3):492–505, 1926. Cited in pages 17, 100

J. Fortin, O. Millet, and G. de Saxcé. Construction of an averaged stress tensor for a granular medium. *European Journal of Mechanics-A/Solids*, 22(4):567–582, 2003. Cited in page 114

J. Fortin, O. Millet, and G. de Saxcé. Numerical simulation of granular materials by an improved discrete element method. *International Journal for Numerical Methods in Engineering*, 62(5):639–663, 2005. Cited in page 114

D. G. Fredlund and H. Rahardjo. *Soil mechanics for unsaturated soils*. John Wiley & Sons, 1993. Cited in pages 2, 27

D. G. Fredlund and A. Xing. Equations for the soil-water characteristic curve. *Canadian geotechnical journal*, 31(4):521–532, 1994. Cited in pages 30, 125

U. Frisch, B. Hasslacher, and Y. Pomeau. Lattice-gas automata for the navier-stokes equation. In *Lattice Gas Methods for Partial Differential Equations*, pages 11–18. CRC Press, 2019. Cited in page 48

G. Gagneux and O. Millet. Analytic calculation of capillary bridge properties deduced as an inverse problem from experimental data. *Transport in Porous Media*, 105:117–139, 2014. Cited in pages 15, 16, 20, 97, 103, 161, 189

G. Gagneux and O. Millet. An analytical framework for evaluating the cohesion effects of coalescence between capillary bridges. *Granular matter*, 18(2):1–13, 2016. Cited in pages 126, 138, 139, 162, 169

G. Gagneux, O. Millet, B. Mielniczuk, and M. S. E. Youssoufi. Theoretical and experimental study of pendular regime in unsaturated granular media. *European Journal of Environmental and Civil Engineering*, 21(7-8):840–853, Apr. 2016. doi: 10.1080/19648189.2016.1167782. URL https://doi.org/10.1080/19648189.2016.1167782. Cited in pages 23, 98, 99

P.-G. Gennes, F. Brochard-Wyart, D. Quéré, et al. *Capillarity and wetting phenomena: drops, bubbles, pearls, waves*. Springer, 2004. Cited in page 12

H. Grad. On the kinetic theory of rarefied gases. *Communications on pure and applied mathematics*, 2(4):331–407, 1949a. Cited in page 51

H. Grad. Note on n-dimensional hermite polynomials. *Communications on Pure and Applied Mathematics*, 2(4):325–330, 1949b. Cited in page 51

J.-P. Gras. *Approche micromécanique de la capillarité dans les milieux granulaires: rétention d'eau et comportement mécanique*. PhD thesis, Université Montpellier II-Sciences et Techniques du Languedoc, 2011. Cited in pages XVI, 22, 23, 26, 138, 140, 162, 169

J.-P. Gras, J.-Y. Delenne, and M. S. El Youssoufi. Study of capillary interaction between two grains: a new experimental device with suction control. *Granular Matter*, 15(1):49–56, 2013. Cited in page 16

Z. Grof, C. J. Lawrence, and F. Štěpánek. The strength of liquid bridges in random granular materials. *Journal of Colloid and Interface Science*, 319(1):182–192, 2008. Cited in page 14

Z. Guo and C. Shu. *Lattice Boltzmann method and its application in engineering*, volume 3. World Scientific, 2013. Cited in page 57

W. Haines. The hysteresis effect in capillary properties and the mode of moisture distribution associated therewith. *J. Agric. Science*, 20:7, 1929. Cited in page 13

W. B. Haines. Studies in the physical properties of soils: Ii. a note on the cohesion developed by capillary forces in an ideal soil1. *The Journal of Agricultural Science*, 15(4):529–535, 1925. Cited in page 17

J. Hardy, Y. Pomeau, and O. De Pazzis. Time evolution of a two-dimensional classical lattice system. *Physical Review Letters*, 31(5):276, 1973. Cited in page 48

O. Harireche, A. Faramarzi, and A. M. Alani. A toroidal approximation of capillary forces in polydisperse granular assemblies. *Granular matter*, 15:573–581, 2013. Cited in page 17

Q. He, Y. Li, W. Huang, Y. Hu, and Y. Wang. Phase-field-based lattice boltzmann model for liquid-gas-solid flow. *Physical Review E*, 100(3):033314, 2019. Cited in page 67

X. He, S. Chen, and R. Zhang. A lattice boltzmann scheme for incompressible multiphase flow and its application in simulation of rayleigh–taylor instability. *Journal of computational physics*, 152(2):642–663, 1999. Cited in pages XVII, 88, 89, 90

R. Hill. Elastic properties of reinforced solids: some theoretical principles. *Journal of the Mechanics and Physics of Solids*, 11(5):357–372, 1963. Cited in page 114

D. Hornbaker, R. Albert, I. Albert, A.-L. Barabási, and P. Schiffer. What keeps sandcastles standing? *Nature*, 387(6635):765–765, 1997. Cited in page 14

R. Hosseini, K. Kumar, and J.-Y. Delenne. Investigating the effect of porosity on the soil water retention curve using the multiphase lattice boltzmann method. In *EPJ Web of Conferences*, volume 249, page 09007. EDP Sciences, 2021. Cited in page 125

K. Hotta, K. Takeda, and K. Iinoya. The capillary binding force of a liquid bridge. *Powder Technology*, 10(4-5):231–242, 1974. Cited in page 17

H. Huang, M. Krafczyk, and X. Lu. Forcing term in single-phase and shan-chen-type multiphase lattice boltzmann models. *Phys. Rev. E*, 84:046710, Oct 2011. doi: 10.1103/PhysRevE.84.046710. URL https://link.aps.org/doi/10.1103/PhysRevE.84.046710. Cited in page 20

H. Huang, M. Sukop, and X. Lu. Multiphase lattice boltzmann methods: Theory and application. 2015. Cited in pages 20, 50, 59, 66

T. Hueckel, B. Mielniczuk, and M. S. El Youssoufi. Adhesion-force micro-scale study of desiccating granular material. *Géotechnique*, 70(12):1133–1144, 2020. Cited in pages XVI, 26, 27, 140

D. Jacqmin. Calculation of two-phase navier–stokes flows using phase-field modeling. *Journal of Computational Physics*, 155(1):96–127, Oct. 1999. Cited in page 66

N. Janbu, L. Bjerrum, and B. Kjaernsli. *Soil mechanics applied to some engineering problems*. Norwegian Geotechnical Institute, 1956. Cited in page 3

M. Jean. The non-smooth contact dynamics method. *Computer methods in applied mechanics and engineering*, 177(3-4):235–257, 1999. Cited in page 114

J. Jennings. A revised effective stress law for use in the prediction of the behaviour of unsaturated soils. *Pore pressure and suction in soils*, pages 26–30, 1961. Cited in page 32

J. Jennings and J. Burland. Limitations to the use of effective stresses in partly saturated soils. *Géotechnique*, 12(2):125–144, 1962. Cited in pages XVI, 34

N. Khalili and M. Khabbaz. A unique relationship for χ for the determination of the shear strength of unsaturated soils. *Geotechnique*, 48(5):681–687, 1998. Cited in page 33

N. Khalili, R. Witt, L. Laloui, L. Vulliet, and A. Koliji. Effective stress in double porous media with two immiscible fluids. *Geophysical research letters*, 32(15), 2005. Cited in page 31

M. I. Khan and S. Wang. Comparing the various slope stability methods to find the optimum method for calculating factor of slope safety. In *IOP Conference Series: Earth and Environmental Science*, volume 480, page 012003. IOP Publishing, 2020. Cited in page 3

T. Krueger, H. Kusumaatmaja, A. Kuzmin, O. Shardt, G. Silva, and E. Viggen. *The Lattice Boltzmann Method: Principles and Practice*. Graduate Texts in Physics. Springer, 2016. ISBN 978-3-319-44647-9. Cited in page 53

T. Krüger, H. Kusumaatmaja, A. Kuzmin, O. Shardt, G. Silva, and E. M. Viggen. The lattice boltzmann method. *Springer International Publishing*, 10(978-3):4–15, 2017. Cited in page 192

N. P. Kruyt and O. Millet. An analytical theory for the capillary bridge force between spheres. *Journal of fluid mechanics*, 812:129–151, 2017. Cited in page 19

L. Laloui and M. Nuth. On the use of the generalised effective stress in the constitutive modelling of unsaturated soils. *Computers and Geotechnics*, 36(1-2):20–23, 2009. Cited in page 130

H. G. Lee and J. Kim. An efficient and accurate numerical algorithm for the vector-valued allen–cahn equations. *Computer Physics Communications*, 183(10):2107–2115, 2012. ISSN 0010-4655. Cited in page 67

S. Lee, S. R. Lee, and Y. Kim. An approach to estimate unsaturated shear strength using artificial neural network and hyperbolic formulation. *Computers and Geotechnics*, 30 (6):489–503, 2003. Cited in page 35

T. Lee and L. Liu. Wall boundary conditions in the lattice boltzmann equation method for nonideal gases. *Physical Review E*, 78(1):017702, 2008. Cited in page 82

E.-C. Leong and H. Abuel-Naga. Contribution of osmotic suction to shear strength of unsaturated high plasticity silty soil. *Geomechanics for Energy and the Environment*, 15:65–73, 2018. Cited in page 28

Q. Li, Y. Yu, and K. H. Luo. Implementation of contact angles in pseudopotential lattice boltzmann simulations with curved boundaries. *Phys. Rev. E*, 100:053313, Nov 2019. Cited in page 69

H. Liang, B. Shi, Z. Guo, and Z. Chai. Phase-field-based multiple-relaxation-time lattice boltzmann model for incompressible multiphase flows. *Physical Review E*, 89(5):053320, 2014. Cited in page 76

H. Liang, J. Xu, J. Chen, H. Wang, Z. Chai, and B. Shi. Phase-field-based lattice boltzmann modeling of large-density-ratio two-phase flows. *Phys. Rev. E*, 97:033309, Mar 2018. Cited in pages 5, 50, 67, 69, 70, 71, 76, 77

H. Liang, H. Liu, Z. Chai, and B. Shi. Lattice boltzmann method for contact-line motion of binary fluids with high density ratio. *Phys. Rev. E*, 99:063306, Jun 2019. Cited in pages 5, 50, 67, 70, 76, 82

W. J. Likos and N. Lu. Hysteresis of capillary stress in unsaturated granular soil. *Journal of Engineering mechanics*, 130(6):646–655, 2004a. Cited in page 13

W. J. Likos and N. Lu. Unsaturated soil mechanics. *ed: John Wiley and Sons Inc., New Jersey*, 2004b. Cited in pages XV, 2, 13, 14

S. Liu, Z. Su, M. Li, and L. Shao. Slope stability analysis using elastic finite element stress fields. *Engineering Geology*, 273:105673, 2020a. Cited in page 3

X. Liu, A. Zhou, S.-l. Shen, J. Li, and D. Sheng. A micro-mechanical model for unsaturated soils based on dem. *Computer Methods in Applied Mechanics and Engineering*, 368: 113183, 2020b. Cited in pages XVI, XIX, 34, 43, 44, 132, 133

H. Louati, D. Oulahna, and A. de Ryck. Effect of the particle size and the liquid content on the shear behaviour of wet granular material. *Powder Technology*, 315:398–409, 2017. Cited in page 14

A. E. H. Love. *A treatise on the mathematical theory of elasticity*. Cambridge university press, 2013. Cited in pages 35, 121

N. Lu, B. Wu, and C. P. Tan. Tensile strength characteristics of unsaturated sands. *Journal of Geotechnical and Geoenvironmental Engineering*, 133(2):144–154, 2007. Cited in page 14

C. Mancuso, C. Jommi, F. D'Onza, et al. *Unsaturated soils: research and applications*. Springer, 2012. Cited in page 124

J. R. Maranha, C. Pereira, and R. Cardoso. Effective stress in unsaturated soils: Lessons from capillarity in regular sphere arrangements. *Geomechanics for Energy and the Environment*, 32:100341, 2022. Cited in pages XV, 3

S. Matlan, M. Mukhlisin, and M. Taha. Statistical assessment of models for determination of soil–water characteristic curves of sand soils. *International Journal of Geological and Environmental Engineering*, 8(12):797–802, 2014a. Cited in page 125

S. J. Matlan, M. Mukhlisin, and M. R. Taha. Performance evaluation of four-parameter models of the soil-water characteristic curve. *The Scientific World Journal*, 2014, 2014b. Cited in page 125

C. McKee and A. Bumb. The importance of unsaturated flow parameters in designing a monitoring system for hazardous wastes and environmental emergencies. In *Proceedings of the Hazardous Materials Control Research Institute, National Conference*, pages 50–58, 1984. Cited in page 30

C. McKee and A. Bumb. Flow-testing coalbed methane production wells in the presence of water and gas. *SPE formation Evaluation*, 2(04):599–608, 1987. Cited in page 30

G. G. McNamara and G. Zanetti. Use of the boltzmann equation to simulate lattice-gas automata. In *Lattice Gas Methods For Partial Differential Equations*, pages 289–296. CRC Press, 2019. Cited in page 48

I. S. McQueen and R. F. Miller. Approximating soil moisture characteristics from limited data: Empirical evidence and tentative model. *Water Resources Research*, 10(3):521–527, 1974. Cited in page 30

K. Melnikov, R. Mani, F. K. Wittel, M. Thielmann, and H. J. Herrmann. Grain-scale modeling of arbitrary fluid saturation in random packings. *Physical Review E*, 92(2): 022206, 2015. Cited in page 43

K. Melnikov, F. K. Wittel, and H. J. Herrmann. Micro-mechanical failure analysis of wet granular matter. *Acta Geotechnica*, 11(3):539–548, 2016. Cited in page 43

J. C. Melrose. Model calculations for capillary condensation. *AIChE Journal*, 12(5): 986–994, 1966. Cited in page 17

R. L. Michalowski. Stability charts for uniform slopes. *Journal of Geotechnical and Geoenvironmental Engineering*, 128(4):351–355, 2002. Cited in page 3

R. L. Michalowski and S. S. Nadukuru. Three-dimensional limit analysis of slopes with pore pressure. *Journal of Geotechnical and Geoenvironmental Engineering*, 139(9):1604–1610, 2013. Cited in page 3

B. Mielniczuk, T. Hueckel, and M. S. El Youssoufi. Laplace pressure evolution and four instabilities in evaporating two-grain liquid bridges. *Powder Technology*, 283:137–151, 2015. Cited in page 14

B. Mielniczuk, O. Millet, G. Gagneux, and M. S. El Youssoufi. Characterisation of pendular capillary bridges derived from experimental data using inverse problem method. *Granular Matter*, 20(1):14, 2018. Cited in pages 20, 97, 98, 99, 100, 108, 109, 140, 143, 168

M. Miot, G. Veylon, A. Wautier, P. Philippe, F. Nicot, and F. Jamin. Numerical analysis of capillary bridges and coalescence in a triplet of spheres. *Granular Matter*, 23(3):1–18, 2021. Cited in pages XVIII, 20, 27, 44, 108, 109, 110, 111, 112, 143, 161, 168

N. Mitarai and F. Nori. Wet granular materials. *Advances in physics*, 55(1-2):1–45, 2006. Cited in pages XVI, 30, 124

A. Mohamad. *Lattice Boltzmann Method*, volume 70. Springer, 2011. Cited in page 57

F. Molenkamp and A. Nazemi. Interactions between two rough spheres, water bridge and water vapour. *Geotechnique*, 53(2):255–264, 2003. Cited in page 10

J. J. Moreau. Unilateral contact and dry friction in finite freedom dynamics. In *Nonsmooth mechanics and Applications*, pages 1–82. Springer, 1988. Cited in page 114

F. Moukalled, L. Mangani, M. Darwish, F. Moukalled, L. Mangani, and M. Darwish. *The finite volume method*. Springer, 2016. Cited in page 46

H. N. G. Nguyen, O. Millet, and G. Gagneux. On the capillary bridge between spherical particles of unequal size: analytical and experimental approaches. *Continuum Mechanics and Thermodynamics*, 31(1):225–237, 2019a. Cited in page 98

H. N. G. Nguyen, O. Millet, and G. Gagneux. On the capillary bridge between spherical particles of unequal size: analytical and experimental approaches. *Continuum Mechanics and Thermodynamics*, 31(1):225–237, 2019b. Cited in pages XV, 19, 20, 94

H. N. G. Nguyen, O. Millet, and G. Gagneux. Exact calculation of axisymmetric capillary bridge properties between two unequal-sized spherical particles. *Mathematics and Mechanics of Solids*, 24(9):2767–2784, 2019c. Cited in pages 20, 94, 98

H. N. G. Nguyen, O. Millet, and G. Gagneux. Liquid bridges between a sphere and a plane-classification of meniscus profiles for unknown capillary pressure. *Mathematics and Mechanics of Solids*, 24(10):3042–3060, 2019d. Cited in pages 19, 20, 98

H. N. G. Nguyen, O. Millet, C.-F. Zhao, and G. Gagneux. Theoretical and experimental study of capillary bridges between two parallel planes. *European Journal of Environmental and Civil Engineering*, pages 1–11, 2020a. Cited in pages XV, 19, 20, 94

H. N. G. Nguyen, C.-F. Zhao, O. Millet, and G. Gagneux. An original method for measuring liquid surface tension from capillary bridges between two equal-sized spherical particles. *Powder Technology*, 363:349–359, 2020b. Cited in pages XV, 19, 20

H. N. G. Nguyen, C.-F. Zhao, O. Millet, and A. Selvadurai. Effects of surface roughness on liquid bridge capillarity and droplet wetting. *Powder Technology*, 378:487–496, 2021. Cited in page 20

F. Nicot, N. Hadda, M. Guessasma, J. Fortin, and O. Millet. On the definition of the stress tensor in granular media. *International Journal of Solids and Structures*, 50 (14-15):2508–2517, 2013. Cited in page 121

X. Nie, S. Chen, M. Robbins, et al. A continuum and molecular dynamics hybrid method for micro-and nano-fluid flow. *Journal of Fluid Mechanics*, 500:55–64, 2004. Cited in page 47

M. Nijmeijer, C. Bruin, A. Van Woerkom, A. Bakker, and J. Van Leeuwen. Molecular dynamics of the surface tension of a drop. *The Journal of chemical physics*, 96(1): 565–576, 1992. Cited in page 47

C. Nouguier-Lehon, B. Cambou, and E. Vincens. Influence of particle shape and angularity on the behaviour of granular materials: a numerical analysis. *International journal for numerical and analytical methods in geomechanics*, 27(14):1207–1226, 2003. Cited in page 114

A. Nur and J. Byerlee. An exact effective stress law for elastic deformation of rock with fluids. *Journal of geophysical research*, 76(26):6414–6419, 1971. Cited in page 32

M. Nuth and L. Laloui. Effective stress concept in unsaturated soils: Clarification and validation of a unified framework. *International journal for numerical and analytical methods in Geomechanics*, 32(7):771–801, 2008. Cited in pages XVI, 34, 130

S. Oh and N. Lu. Uniqueness of the suction stress characteristic curve under different confining stress conditions. *Vadose Zone Journal*, 13(5), 2014. Cited in page 125

M. Pakpour, M. Habibi, P. Møller, and D. Bonn. How to construct the perfect sandcastle. *Scientific reports*, 2(1):549, 2012. Cited in page 14

O. Penrose and P. C. Fife. Thermodynamically consistent models of phase-field type for the kinetic of phase transitions. *Physica D: Nonlinear Phenomena*, 43(1):44–62, 1990. ISSN 0167-2789. Cited in page 66

F. Perales, F. Dubois, Y. Monerie, B. Piar, and L. Stainier. A nonsmooth contact dynamics-based multi-domain solver: code coupling (xper) and application to fracture. *European Journal of Computational Mechanics/Revue Européenne de Mécanique Numérique*, 19(4):389–417, 2010. Cited in page 114

O. Pitois, P. Moucheront, and X. Chateau. Liquid bridge between two moving spheres: An experimental study of viscosity effects. *Journal of Colloid and Interface Science*, 231 (1):26 – 31, 2000. ISSN 0021-9797. doi: https://doi.org/10.1006/jcis.2000.7096. URL http://www.sciencedirect.com/science/article/pii/S0021979700970966. Cited in pages 18, 161

S. Popinet. Numerical models of surface tension. *Annual Review of Fluid Mechanics*, 50: 49–75, 2018. Cited in page 104

M. Pouragha, M. Eghbalian, R. Wan, and T. Wong. Derivation of soil water retention curve incorporating electrochemical effects. *Acta Geotechnica*, 16(4):1147–1160, 2021. Cited in page 31

P. Pressure. Suction in soils conference. *London, i960*, pages 4–16, 1960. Cited in page 32

Y.-H. Qian, D. d'Humières, and P. Lallemand. Lattice bgk models for navier-stokes equation. *Europhysics letters*, 17(6):479, 1992. Cited in page 48

F. Radjai and V. Richefeu. Contact dynamics as a nonsmooth discrete element method. *Mechanics of Materials*, 41(6):715–728, 2009. Cited in page 114

F. Radjai, L. Brendel, and S. Roux. Nonsmoothness, indeterminacy, and friction in two-dimensional arrays of rigid particles. *Physical review E*, 54(1):861, 1996. Cited in page 114

F. Radjai, D. E. Wolf, M. Jean, and J.-J. Moreau. Bimodal character of stress transmission in granular packings. *Physical review letters*, 80(1):61, 1998. Cited in page 114

M. Renouf, F. Dubois, and P. Alart. A parallel version of the non smooth contact dynamics algorithm applied to the simulation of granular media. *Journal of Computational and Applied Mathematics*, 168(1-2):375–382, 2004. Cited in page 114

B. Richards. The significance of moisture flow and equilibria in unsaturated soils in relation to the design of engineering structures built on shallow foundations in australia. 1966. Cited in page 32

V. Richefeu. *Approche par éléments discrets 3D du comportement de matériaux granulaires cohésifs faiblement contraints*. PhD thesis, Université Montpellier II-Sciences et Techniques du Languedoc, 2005. Cited in pages XVII, 41, 42

V. Richefeu, F. Radjai, and M. El Youssoufi. Stress transmission in wet granular materials. *European Physical Journal E*, 21(4):359–369, 2006a. doi: 10.1140/epje/i2006-10077-1. Cited in page 66

V. Richefeu, F. Radjaı, and M. S. El Youssoufi. Stress transmission in wet granular materials. *The European Physical Journal E*, 21:359–369, 2006b. Cited in page 18

V. Richefeu, M. S. El Youssoufi, E. Azéma, and F. Radjai. Force transmission in dry and wet granular media. *Powder Technology*, 190(1-2):258–263, 2009. Cited in page 14

A. Russell and N. Khalili. A unified bounding surface plasticity model for unsaturated soils. *International Journal for Numerical and Analytical Methods in Geomechanics*, 30 (3):181–212, 2006. Cited in page 33

R. Scardovelli and S. Zaleski. Direct numerical simulation of free-surface and interfacial flow. *Annual review of fluid mechanics*, 31(1):567–603, 1999. Cited in pages 70, 104

L. Scholtès. *Modélisation micromécanique des milieux granulaires partiellement saturés*. PhD thesis, Institut National Polytechnique de Grenoble-INPG, 2008. Cited in pages XVII, 42, 43, 44, 162, 168

L. Scholtes, B. Chareyre, F. Nicot, and F. Darve. Micromechanics of granular materials with capillary effects. *International journal of engineering science*, 47(1):64–75, 2009. Cited in pages 44, 114, 121, 122, 131, 162, 168

L. Scholtès, P.-Y. Hicher, F. Nicot, B. Chareyre, and F. Darve. On the capillary stress tensor in wet granular materials. *International journal for numerical and analytical methods in geomechanics*, 33(10):1289–1313, 2009. Cited in pages 35, 42, 44, 121, 122, 162, 168

X. Shan and H. Chen. Lattice boltzmann model for simulating flows with multiple phases and components. *Physical review E*, 47(3):1815, 1993. Cited in page 66

X. Shan and H. Chen. Simulation of nonideal gases and liquid-gas phase transitions by the lattice boltzmann equation. *Physical Review E*, 49(4):2941, 1994. Cited in page 66

X. Shan and G. Doolen. Multicomponent lattice-boltzmann model with interparticle interaction. *Journal of statistical physics*, 81(1):379–393, 1995. Cited in page 66

X. Shan, X.-F. Yuan, and H. Chen. Kinetic theory representation of hydrodynamics: a way beyond the navier–stokes equation. *Journal of Fluid Mechanics*, 550:413–441, 2006. Cited in page 51

D. H. Sharp. Overview of rayleigh-taylor instability. 1983. Cited in page 88

A. Shivamanth, S. S. Athani, M. Desai, and G. Dodagoudar. Stability analysis of dyke using limit equilibrium and finite element methods. *Aquatic Procedia*, 4:884–891, 2015. Cited in page 3

A. Skempton. Effective stress in soils, concrete and rocks. *Selected papers on soil mechanics*, 1032:4–16, 1984. Cited in page 32

V. Šmilauer, E. Catalano, B. Chareyre, S. Dorofeenko, J. Duriez, A. Gladky, J. Kozicki, C. Modenese, L. Scholtès, L. Sibille, et al. Yade reference documentation. *Yade Documentation 3rd ed.*, (1), 2021. URL http://yadedem.org/doc/. Cited in pages 115, 168

J. Sorgatz and T. Nuber. Numerical investigation of the stability of sea dikes: Verification and plausibility approaches for a fluid-mechanical coupled fdm-model. In *Conference Proceedings of the Workshop on Numerical Methods in Geotechnics Hamburg*, pages 281–292, 2017. Cited in page 4

F. Soulié. *Cohésion par capillarité et comportement mécanique de milieux granulaires*. PhD thesis, Université Montpellier II-Sciences et Techniques du Languedoc, 2005. Cited in pages XVII, 40, 41

F. Soulie, M. S. El Youssoufi, F. Cherblanc, and C. Saix. Capillary cohesion and mechanical strength of polydisperse granular materials. *The European Physical Journal E*, 21: 349–357, 2006. Cited in page 18

T. Steward, N. Sivakugan, S. Shukla, and B. Das. Taylor's slope stability charts revisited. *International Journal of Geomechanics*, 11(4):348–352, 2011. Cited in page 3

S. Succi and S. Succi. *The lattice Boltzmann equation: for complex states of flowing matter*. Oxford university press, 2018. Cited in page 192

K. Suga, Y. Kuwata, K. Takashima, and R. Chikasue. A d3q27 multiple-relaxation-time lattice boltzmann method for turbulent flows. *Computers & Mathematics with Applications*, 69(6):518–529, 2015. Cited in page 50

M. Sukop. Dt thorne, jr. lattice boltzmann modeling lattice boltzmann modeling. 2006. Cited in pages 46, 57

X. Sun and M. Sakai. Direct numerical simulation of gas-solid-liquid flows with capillary effects: An application to liquid bridge forces between spherical particles. *Physical Review E*, 94(6):063301, 2016. Cited in page 20

Y. Sun and C. Beckermann. Sharp interface tracking using the phase-field equation. *Journal of Computational Physics*, 220(2):626–653, 2007. ISSN 0021-9991. doi: https://doi.org/10.1016/j.jcp.2006.05.025. URL https://www.sciencedirect.com/science/article/pii/S0021999106002531. Cited in pages 66, 67

G. Taubin. Estimation of planar curves, surfaces, and nonplanar space curves defined by implicit equations with applications to edge and range image segmentation. *IEEE Transactions on Pattern Analysis and Machine Intelligence*, 13(11):1115–1138, 1991. doi: 10.1109/34.103273. Cited in page 99

K. Terzaghi. *Erdbaumechanik auf bodenphysikalischer Grundlage*. F. Deuticke, 1925. Cited in page 31

K. Timm, H. Kusumaatmaja, A. Kuzmin, O. Shardt, G. Silva, and E. Viggen. The lattice boltzmann method: principles and practice. *Springer International Publishing AG Switzerland, ISSN*, pages 1868–4521, 2016. Cited in pages 46, 48, 50, 55, 57, 59, 62, 67, 86, 118, 119, 121

B. Tuomanen. *Hands-On GPU Programming with Python and CUDA: Explore high-performance parallel computing with CUDA*. Packt Publishing Ltd, 2018. Cited in page 173

M. T. Van Genuchten. A closed-form equation for predicting the hydraulic conductivity of unsaturated soils. *Soil science society of America journal*, 44(5):892–898, 1980. Cited in pages XIX, 31, 124

S. K. Vanapalli. *Simple test procedures and their interpretation in evaluating the shear strength of an unsaturated soil*. PhD thesis, 1996. Cited in page 28

S. K. Vanapalli, D. G. Fredlund, and D. E. Pufahl. The influence of soil structure and stress history on the soil–water characteristics of a compacted till. *Géotechnique*, 49(2): 143–159, 1999. Cited in page 28

W. Visser. An empirical expression for the desorption curve. In *Proceedings of the Wageningen Symposium: Water in the unsaturated zone*. Cited in page 30

I. Vlahinić, H. M. Jennings, J. E. Andrade, and J. J. Thomas. A novel and general form of effective stress in a partially saturated porous material: The influence of microstructure. *Mechanics of Materials*, 43(1):25–35, 2011. Cited in page 131

R. Wan, F. Nicot, and F. Darve. *Failure in geomaterials: a contemporary treatise*. Elsevier, 2017. Cited in pages 161, 164, 167, 170

R. Wan, M. Pouragha, M. Eghbalian, J. Duriez, and T. Wong. A probabilistic approach for computing water retention of particulate systems from statistics of grain size and tessellated pore network. *International Journal for Numerical and Analytical Methods in Geomechanics*, 43(5):956–973, 2019. Cited in page 31

H. Wang, Z. Chai, B. Shi, and H. Liang. Comparative study of the lattice boltzmann models for allen-cahn and cahn-hilliard equations. *Physical Review E*, 94(3):033304, 2016. Cited in page 67

H. Wang, X. Yuan, H. Liang, Z. Chai, and B. Shi. A brief review of the phase-field-based lattice boltzmann method for multiphase flows. *Capillarity*, 2(3):33–52, June 2019. doi: 10.26804/capi.2019.03.01. URL https://doi.org/10.26804/capi.2019.03.01. Cited in page 67

J.-P. Wang, E. Gallo, B. François, F. Gabrieli, and P. Lambert. Capillary force and rupture of funicular liquid bridges between three spherical bodies. *Powder Technology*, 305:89–98, 2017. Cited in page 14

Q. Wang, D. Pufahl, and D. Fredlund. A study of critical state on an unsaturated silty soil. *Canadian Geotechnical Journal*, 39(1):213–218, 2002. Cited in pages XVI, XVII, 38, 39, 40, 41

A. Wautier, S. Bonelli, and F. Nicot. Dem investigations of internal erosion: Grain transport in the light of micromechanics. *International Journal for Numerical and Analytical Methods in Geomechanics*, 43(1):339–352, 2019. Cited in page 114

J. Weber. Recherches concernant les contraintes intergranulaires dans les milieux pulvérulents. *Bulletin de liaison des Ponts et Chaussées*, 20:1–20, 1966. Cited in pages 35, 121

C. D. Willett, M. J. Adams, S. A. Johnson, and J. P. Seville. Capillary bridges between two spherical bodies. *Langmuir*, 16(24):9396–9405, 2000. Cited in page 18

J. Williams, R. Prebble, W. Williams, and C. Hignett. The influence of texture, structure and clay mineralogy on the soil moisture characteristic. *Soil Research*, 21(1):15–32, 1983. Cited in page 30

D. A. Wolf-Gladrow. *Lattice-gas cellular automata and lattice Boltzmann models: an introduction*. Springer, 2004. Cited in page 48

Z. Yan, X. Yang, S. Li, and M. Hilpert. Two-relaxation-time lattice boltzmann method and its application to advective-diffusive-reactive transport. *Advances in water resources*, 109:333–342, 2017. Cited in page 50

J. Yang, Z.-Y. Yin, P.-Y. Hicher, and F. Laouafa. A finite element modeling of the impact of internal erosion on the stability of a dike. In *Poromechanics VI*, pages 354–361. 2017. Cited in page 3

X. Yang and S. VANAPALLI. Slope stability analyses of outang landslide based on the peak and residual shear strength behavior. *Adv. Eng. Sci.*, 51(004):55–68, 2019. Cited in page 3

T. Yasuda, T. Hashimoto, I. Tanno, Y. Tanaka, H. Minagawa, K. Morinishi, and N. Satofuka. Effect of collision and velocity model of lattice boltzmann model on three-dimensional turbulent flow simulation. *International Journal of Computational Fluid Dynamics*, 31(4-5):258–268, 2017. Cited in page 50

N. Younes, Z. Benseghier, O. Millet, A. Wautier, F. Nicot, and R. Wan. Phase-field lattice boltzmann model for liquid bridges and coalescence in wet granular media. *Powder Technology*, 411:117942, 2022. Cited in pages 6, 69, 70, 71, 76, 119, 143, 162

N. Younes, O. Millet, and Z. Benseghier. A relevant phase-field-based lattice-boltzmann method for water-air capillary interfaces. *Submitted*, 2023a. Cited in pages 6, 69, 70, 76, 94, 140, 161

N. Younes, A. Wautier, O. Millet, R. Wan, and F. Nicot. On the hysteresis phenomenon of unsaturated granular assemblies using dem-lbm coupling. *In preparation*, 2023b. Cited in pages 6, 163

N. Younes, A. Wautier, O. Millet, R. Wan, and F. Nicot. Hysteresis phenomenon within unsaturated granular assemblies: capillary forces and matric suction. *In preparation*, 2023c. Cited in pages 6, 163

N. Younes, A. Wautier, R. Wan, O. Millet, F. Nicot, and R. Bouchard. Dem-lbm coupling for partially saturated granular assemblies. *Computers and Geotechnics*, 162:105677, 2023d. Cited in pages 6, 71, 114, 162

T. Young. Iii. an essay on the cohesion of fluids. *Philosophical transactions of the royal society of London*, (95):65–87, 1805. Cited in page 11

C. Yuan, B. Chareyre, and F. Darve. Deformation and stresses upon drainage of an idealized granular material. *Acta Geotechnica*, 13(4):961–972, 2018. Cited in page 34

M. I. Zerhouni. Role de la pression interstitielle negative dans le comportement des sols: Application au calcul des routes. 1994. Cited in pages XVI, 34

Q. Zhai and H. Rahardjo. Determination of soil–water characteristic curve variables. *Computers and Geotechnics*, 42:37–43, 2012. Cited in page 28

X. Zhang, H. Liu, and J. Zhang. A new capillary force model implemented in lattice boltzmann method for gas–liquid–solid three-phase flows. *Physics of Fluids*, 32(10): 103301, 2020. doi: 10.1063/5.0021473. URL https://doi.org/10.1063/5.0021473. Cited in page 104

C.-F. Zhao, N. P. Kruyt, and O. Millet. Capillary bridge force between non-perfectly wettable spherical particles: an analytical theory for the pendular regime. *Powder technology*, 339:827–837, 2018. Cited in page 19

C.-F. Zhao, N. P. Kruyt, and O. Millet. Capillary bridges between unequal-sized spherical particles: Rupture distances and capillary forces. *Powder technology*, 346:462–476, 2019. Cited in page 19

L. Zheng, S. Zheng, and Q. Zhai. Lattice boltzmann equation method for the cahn-hilliard equation. *Physical Review E*, 91(1):013309, 2015. Cited in page 67

O. C. Zienkiewicz, R. L. Taylor, and P. Nithiarasu. *The finite element method for fluid dynamics*. Butterworth-Heinemann, 2013. Cited in page 46

Q. Zou and X. He. On pressure and velocity boundary conditions for the lattice boltzmann bgk model. *Physics of fluids*, 9(6):1591–1598, 1997. Cited in page 57

Y. Zu and S. He. Phase-field-based lattice boltzmann model for incompressible binary fluid systems with density and viscosity contrasts. *Physical Review E*, 87(4):043301, 2013. Cited in pages XVII, 50, 88, 89, 90